Dark matter bound states in the early universe

The role of scalar mediators

Oncala Mesa, R.

Publication date
2021

Document Version
Final published version

Dark matter bound states in the early universe
The role of scalar mediators

ACADEMISCH PROEFSCHRIFT

ter verkrijging van de graad van doctor
aan de Universiteit van Amsterdam
op gezag van de Rector Magnificus
prof. dr. ir. K.I.J. Maex
ten overstaan van een door het College voor Promoties ingestelde commissie,
in het openbaar te verdedigen
op woensdag 9 juni 2021, te 10.00 uur

door Ruben Oncala Mesa
geboren te Sant Andreu De La Barca

Promotiecommissie

Promotor:	prof. dr. E.L.M.P. Laenen	Universiteit van Amsterdam
Copromotor:	prof. dr. K. Petraki	Université Paris Sorbonne (Paris IV)
Overige leden:	prof. dr. J. de Boer	Universiteit van Amsterdam
	prof. dr. M.P. Decowski	Universiteit van Amsterdam
	prof. dr. G. Bertone	Universiteit van Amsterdam
	prof. dr. A. Achúcarro	Universiteit Leiden
	dr. M.E.J. Postma	Nikhef
	dr. A. Goudelis	CNRS, France

Faculteit der Natuurwetenschappen, Wiskunde en Informatica

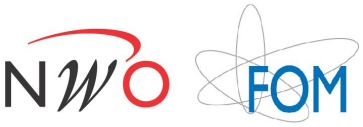

This work is part of the research programme of the Foundation for Fundamental Research on Matter (FOM), which is part of the Netherlands Organisation for Scientific Research (NWO). It has been part of the NWO Vidi project "Self-interacting asymmetric dark matter". The research has been carried out at the National Institute for Subatomic Physics Nikhef and the Laboratory of Theoretical and High Energy Physics (Laboratoire de Physique Théorique et Hautes Énergies –LPTHE) of the Sorbonne University.

Publications

This thesis is based on the following publications

[1] R. Oncala and K. Petraki
"Dark matter bound states via emission of scalar mediators"
JHEP, 01:070, 2019, arXiv: 1808.04854;

[2] R. Oncala and K. Petraki
"Dark matter bound state formation via emission of a charged scalar"
JHEP, 02:036, 2020; arXiv: 1911.02605;

[3] R. Oncala and K. Petraki
"Bound states of WIMP dark matter in Higgs-portal models I: cross-sections and transition rates"
arXiv: 2101.08666, under review;

[4] R. Oncala and K. Petraki.
"Bound states of WIMP dark matter in Higgs-portal models II: thermal decoupling"
arXiv: 2101.08667, under review.

Previous publications

[5] R. Oncala and J. Soto
"Heavy Quarkonium Hybrids: Spectrum, Decay and Mixing"
Phys. Rev. D, 96(1):014004, 2017, arXiv: 1702.03900;

[6] R. Oncala and J. Soto *"Heavy Hybrids: decay to and mixing with Heavy Quarkonium"*
EPJ Web Conf., 137:06025, 2017, arXiv: 1611.04761.

Contents

Chapter 1

Introduction

Our current knowledge of fundamental particles and interactions is summarised in the so-called Standard Model (SM) of particle physics. While the SM describes very well the properties of ordinary matter, precision measurements of the cosmic microwave background radiation (CMB) show that ordinary matter makes up only 4.9% of the energy density of our universe; 26.8% is made of a yet-unknown type of matter that gravitates but does not interact electromagnetically (or it does so very weakly), known as dark matter (DM), while 68.3% is dark energy that makes the universe expand at an accelerated rate [7].

This thesis focuses on DM. Besides the cosmological evidence for its existence, DM is necessary to explain many astrophysical observations. Elucidating the nature of DM would allow us to understand better the evolution and the structure of our universe. It would also correspond to discovering unknown fundamental physics. The importance of DM for particle physics, cosmology and astrophysics has placed it in the forefront of theoretical and experimental research in these fields. Indeed, a great number of plausible theories for the fundamental properties of DM have been proposed, and a large experimental program has been developed to identify its nature.

1.1 Evidence for dark matter

Dark matter was first inferred from the rotational curves of the Milky Way. They seemed to indicate that must be some hidden mass creating a gravitational potential to explain the observed stellar orbits. Other more recent investigations [8] include gravitational lensing, the cosmic microwave background and other astronomical observations. In the following we summarize some of this evidence.

Galactic rotation curves: The first evidence for DM comes after observing the trajectories of the stars in the Milky Way. The luminosity of the spiral galaxy decreases from the center to outside. If luminous mass were all of the matter, we can model the galaxy as the solar system, with a big mass in the center and other masses orbiting around. From the second Kepler's law, we expect[1] that the rotational velocities decreases with the distance to the center, however this is not observed [9]. The obvious way to solve this discrepancy is to conclude that the mass distribution in spiral galaxies is not similar to the light distribution. Today we can use gravitational lensing to determine the total mass of other similar spiral galaxies, independently

[1]The rotation speed is found to be constant with increasing distance, implying that the mass distribution is unlike the light distributions. From $v_{rot}^2 \sim GM/r$, we infer that M increases proportionally to r.

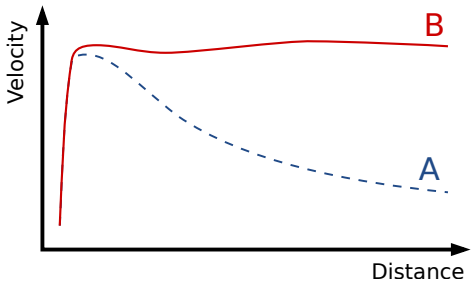

Figure 1.1: Rotation velocity curve in a typical spiral galax: predicted by just luminous matter (A) and observed (B). Dark matter may explain the discrepancy of the rotation velocity curves for long distances to the galactic center.

of their luminosity. We know that the problem of the rotational curves in the Milky Way is common to most of the observed galaxies [10].

Cosmic microwave background (CMB): In the early universe ordinary matter was ionized, and interacted strongly with radiation via Thomson scattering. In the meantime DM was not interacting directly with radiation, but it affected the CMB by its gravitational potential. The regions with higher DM density create gravitational potential wells that distort the space

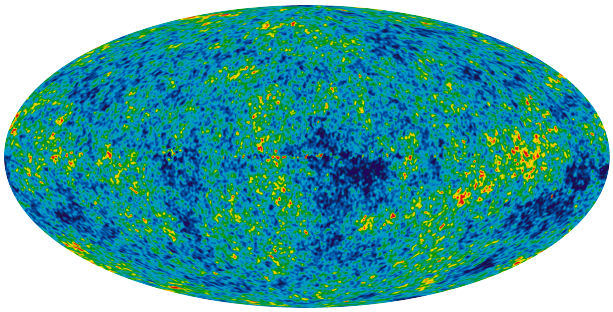

Figure 1.2: The CMB temperature fluctuations from the 7-year WMAP data seen over the full sky [11]. The image is a projection of temperature variations over the celestial sphere. The average temperature is 2.725K, and the colors represent temperature fluctuations of about 0.002K.

and produce temperature fluctuations[2] in the CMB. At the same time, the same gravitational potential affects the density and velocity of ordinary matter [12].

The Bullet Cluster is the result of a collision of two galaxy clusters. Galaxies are made of about 2% of stars; 5-15% of intergalactic gas and plasma, and the rest is DM (hypothetically at least). During collisions stars rarely collide, the gas and plasma interacts through gravity as well as electromagnetic friction-like interactions, and the DM is expected to interact by gravity but to be (almost) collision-less and pass right through at high velocities. Galaxy plasma emits radiation in the X-ray regime. Stars emit optical and infrared light. Finally, gravitational lensing of background galaxies allows us to spatially place the mass within the cluster. Putting all these measurements together we conclude that the mass distribution after the collision is far displaced

[2]The anisotropies can be predicted for any assumed set of cosmological parameters by modern computational models (such as CMBFAST or CAMB): they constrain cosmological parameters. The models predict that some peaks mostly show the density of baryonic matter while others show the density of DM.

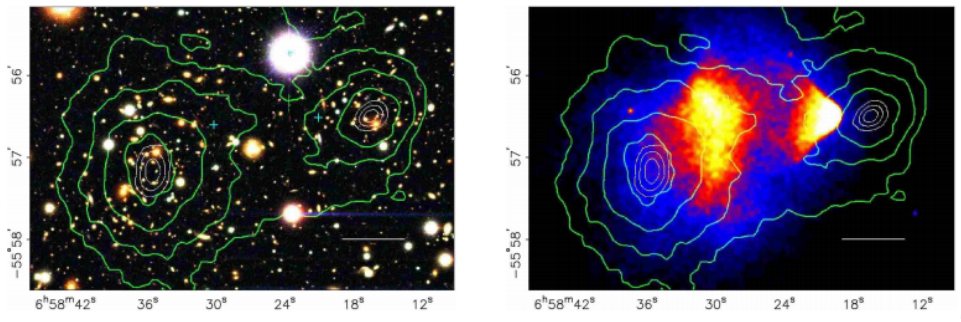

Figure 1.3: Left: Optical images of luminous stars from the Magellan telescope with overlayed contours of spatial distribution of mass (green lines) from gravitational lensing. Right: The same mass contours overlayed over Chandra X-ray data that traces the intergalactic gas (blue-red regions).

from the baryonic matter [13], i.e. the intergalactic gas, plasma and astrophysical bodies. In the right panel of fig. 1.3 we can see that most of the mass resides in a location different from the baryonic gas, which underwent frictional interactions during the merger and slowed down.

1.2 Dark matter candidates and production mechanisms

As we have seen in the previous section, the evidence for DM is compelling at all observed astrophysical scales. It is therefore natural to ask what is DM made of [14–16]. We summarize in this section the general features for particle DM candidates in the mass range of fig. 1.4, and then restrict ourselves to the keV – multiTeV window. The candidates in this window may be generated thermally with the standard cosmology, and are the ones invoked in this thesis.

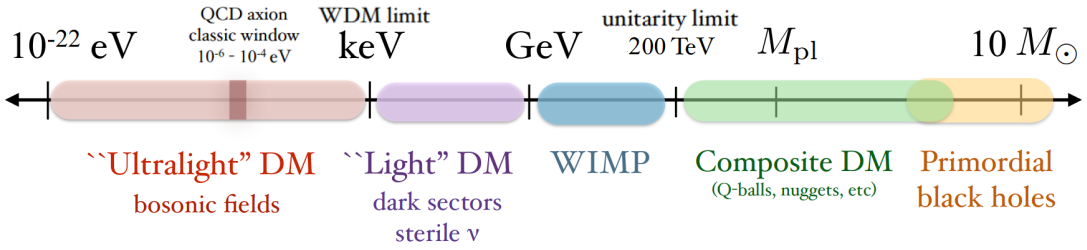

Figure 1.4: Candidates for particle DM and primordial black holes within the full mass range, image from [15].

Ultralight DM candidates are the set of DM candidates with mass lower than $\sim$ keV. This mass value refers to the *Warm DM bound*: all the particles that in the early universe were in thermal equilibrium with the photon bath are relativistic if $m_{\rm DM} <$ keV, which leads to a non-hierarchical growth of cosmological structures[3]. Of course this is not a hard bound for non-thermal DM. Among the ultralight candidates we find the **axion** [18], a hypothetical elementary

[3]Non-hierarchical growth of cosmological structures refers to large matter aggregations forming earlier, and subsequent fragmentation into separated galaxies. The Λ-CDM model, and in particular the CMB are solid arguments to conclude that cosmic structures grow hierarchically. Dwarf galaxies are in agreement with this theory [17]: they were formed for small density fluctuations in the early universe and they are considered as natural building blocks for the formation of larger structures.

particle introduced as an attempt to solve the problem of strong force CP violation in particle physics.

Superheavy DM includes candidates with masses heavier than the unitarity limit $m_{\rm DM} \gtrsim 200$ TeV. This is the maximum DM mass allowed for a thermal candidate. Otherwise its annihilation cross-section would surpass the geometric cross-section limit. Superheavy candidates up to the Planck mass are known as **WIMPzillas** [19]: such particles would have been generated via gravitational production or through another non-thermal channel at the end of the inflation. For masses heavier than the Planck mass we may fined **nuggets** [20]: they are conglomerated bound states of multiple lighter particles. Another possibility is the **Q-ball** [21], a soliton state that carries a baryon number and appears in supersymmetric models. Finally **primordial black holes** (PBHs) [22] are DM candidates that have been formed before recombination. Massive PBHs can accrete matter in the early universe, emitting ionized radiation that is strongly constrained by the CMB. At the low mass end, light PBHs can disintegrate through Hawking radiation [23] in times comparable to the age of the universe, consequently they are not good candidates either. Between $10M_\odot$ and $50M_\odot$ there are searches with gravitational lensing for PBHs in the Milky Way. Constraints on PBH are discussed in [23–25].

Thermal DM candidates are in the range of mass of keV $\lesssim m_{\rm DM} \lesssim$ 200 TeV. They are assumed to be non-relativistic and in equilibrium with the SM thermal bath at early times. As the universe get cold, DM is too heavy to be produced by the thermal bath. The system departs from the equilibrium and the total number of DM particles starts to decrease. At some point, the expansion of the universe separates the particles so much that they cannot interact. The remaining amount of DM particles **"freezes out"** [26], leaving the relic abundance that is observed today. Using the Boltzmann equation we can determine this relic abundance, and find relations with the parameters of the DM candidate. Furthermore the assumption of thermal equilibrium implies some level of interaction or **dark portal** [27] between DM and the SM, which has a variety of interesting and testable signatures. Two interesting thermal DM candidates are:

1. Weakly interacting massive particles (**WIMPs**) [28, 29] are the candidates in the mass range of 10 GeV − 200 TeV. For this mass, the couplings with the SM weak bosons suffice to explain the DM relic density. This is known as the WIMP miracle [30]: a numerical coincidence within two physical scales that suggests WIMPs as promising candidates for DM.

2. **Dark sector** [31, 32] models propose candidates for the keV − 200 TeV scale. This mass range requires some new non-SM mediator. Typically the dark sector features its own interactions and a potentially rich particle content; it is a generalization of thermal candidates beyond WIMPs. Within the dark sector we have DM coupled to **light mediators** [33], which manifest with long-range interactions. This is today an active area of DM experimental detection searches.

Besides thermal DM, the subGeV range has others interesting candidates. An example is **sterile neutrinos** [34], hypothetical particles similar to the SM neutrinos but without the SM weak interactions. Sterile neutrinos could simultaneously explain the small mass of neutrino and produce DM with the correct relic density. Another non-thermal DM production mechanism arise when DM has an small coupling with the SM thermal bath. In **"freeze in"** [35], DM was not produced as the other elements during the universe inflation, but it is the product of SM interactions. We can imagine the freeze-in production by the s-channel annihilation of two SM particles, such as $e^+e^- \to \text{DM} + \text{DM}$. The DM abundance slowly increases in the early universe

until it "freezes in" the observed relic abundance. The coupling of DM with the SM particle is assumed to be sufficiently feeble that the reaction is never in equilibrium.

Modified general relativity [36] is an interesting alternative for particle DM hypotheses. General relativity is well-tested on solar system scales, but its validity on galactic or cosmological scales has not been proved yet. A modification to general relativity that affects long distances may eliminate the need for DM in spiral galaxies. A challenge for modified gravity theories is the bullet cluster [13] because its apparent center of mass is displaced from the baryonic matter. As we saw in the previous section, particle DM candidates can easily explain this observation. A problem with alternative hypotheses is that observational evidence for DM comes from so many independent approaches: explaining some individual observations is possible, but to justify all of them is very difficult. The prevailing opinion today is that modifications to general relativity might explain part of the DM problem, however there is enough data to conclude there must be some form of particle DM.

1.3 Long-range interactions and bound states

Most of the thermal DM research in the past focused on DM interactions mediated by a force with a mass similar to DM. For example, in the prototypical version of DM coupled to the weak interactions of the SM, dark matter was hypothesized to have a similar mass to the weak gauge bosons, $m_{\rm DM} \sim m_{Z,W} \sim 100$ GeV. In this case, the DM interactions are *contact-type*.

By contrast, if DM couples to force mediators that are much lighter than itself, its interactions manifest as *long-range*. Long-range effects appear when the de Broglie wavelength (or Bohr radius) of the interacting particles[4] are of the same order or shorter than the range of the interaction, i.e. $\mu v_{\rm rel}$ or $\mu\alpha \gtrsim m_{\rm med}$. Even the weak interactions of the SM can be long-range if the interacting particles are heavier than a few TeV[5]. More generally, DM coupled to lighter force mediators is a generic possibility for multi-TeV DM. It may couple to the SM particles via the weak interaction or some other yet-unknown force from the dark sector.

Long-range interactions give rise to non-perturbative effects. On the one hand, they distort the wavefunctions of the scattering states, a phenomenon known as the Sommerfeld effect [37, 38]. This affects the cross-sections of all processes, elastic and inelastic, to which the particles participate. On the other hand, long-range interactions imply the existence of bound states. The formation of DM bound states, which is also affected by the Sommerfeld effect, can have very significant implications for DM phenomenology. The main ones are:

a. In the early universe, the formation of metastable bound states (e.g. particle-antiparticle bound states) and their subsequent decay can decrease the DM density, thereby changing the predicted DM couplings and/or mass that reproduce the observed DM relic density [39]. This in turn affects all DM experimental signatures.

b. Inside galactic haloes today, the formation and decay of metastable bound states contributes to the expected radiative signals searched for indirect detection [40–48].

[4]Here μ is the reduced mass of the interacting species ($\mu = m_{\rm DM}/2$ for a DM particle-antiparticle pair), and $v_{\rm rel}$ is their relative velocity. α stands for the DM coupling to the force mediators (to be defined more precisely in the following chapters), and $m_{\rm med}$ is the mediator mass.

[5]Considering the $SU_L(2)$ gauge coupling $\alpha_2 \simeq 0.03$, we find that $\alpha_2 m_{\rm DM}/2 \gtrsim m_{Z,W}$ for $m_{\rm DM} \gtrsim 5$ TeV. In the following chapters we get more precise determinations: they depend on the $SU_L(2) \times U_Y(1)$ representation of the interacting particles.

c. The formation of stable DM bound states in the early universe alters the DM self-scattering inside haloes which affects the galactic structure [49], and may give rise to novel direct detection signatures [50, 51].

In this thesis we focus on scalar force mediators. We investigate the formation of metastable DM bound states in the early universe, and how they may affect the DM relic density.

1.4 Outline

In the following chapters we study thermal DM candidates coupled to light scalar mediators, and we explore the DM bound states formation (BSF) via light scalar emission. We investigate the effect of metastable bound states on the DM relic density. We find that BSF can dramatically affect the DM thermal decoupling in the early universe, and consequently the predictions for the DM mass and couplings. This is expected to affect all experimental signatures, and suggests that DM may be much heavier than previously anticipated. We are thereby solidifying the physics for the experimental exploration in the multi-TeV regime.

In chapter 2, based on [1], we shall see that BSF in models with (neutral) scalar mediators appears to be less severe – or relevant to a limited parameter space – than via vector mediator. In such models, the radiative capture into bound states suffers from two suppression mechanisms:

i. The lowest order s-wave contribution to the BSF amplitude vanishes due to the orthogonality of the incoming and outgoing wavefunction, thus abdicating the leading order to the p-wave.

ii. The previous p-wave term of the BSF amplitude cancel for particle-antiparticle or particle-particle pair, yielding to s- and d-wave contributions that are suppressed by higher orders in the coupling.

Such cancellations concern the contributions to the radiative part of the amplitude that arise from the trilinear DM-DM-mediator coupling alone. However, the self-couplings of the mediator, as well as the biquadratic couplings between DM and the mediator also contribute to the BSF amplitude and may, in turn, enhance the capture cross-sections. Nevertheless, we find that for natural values of the parameters, the cross-sections remain mostly small. Even so, BSF may have some important implications since it contains an s-wave component: it results in CMB constraints for fermionic DM, whose direct annihilation is p-wave and thus unconstrained by indirect probes [52].

In chapter 3, based on [2], we point out that the situation is markedly different if the emission of the scalar boson alters the potential between the interacting particles, this may occur if the scalar mediator is charged under either a local or a global symmetry. For charged scalar mediators, the leading-order contributions to the BSF amplitude are proportional to the overlap of the initial-state and final-state wavefunctions, which now are not orthogonal since they are subject to different potentials. The large overlap between the incoming and outgoing states gives rise to strikingly large BSF cross-sections. This is akin to atomic transitions precipitated by "sudden perturbations", such as ionisation caused by a beta decay of the nucleus [53].

Models with charged scalars are a particularly compelling possibility in view of the discovery of the 125 GeV Higgs boson, which may provide a portal to DM via an extended scalar sector, or may itself be the mediator between TeV-scale particles. If DM has a sizeable coupling to the SM Higgs, then it affects their annihilation rate and can bind DM into bound states [54, 55].

This renders the dynamics of light scalar force carriers relevant, and impacts the phenomenology of DM consisting of weakly interacting massive particles.

Finally, in Chapter 4 based on [3, 4], we investigate the role of the Higgs doublet in the thermal decoupling of multi-TeV DM coupled to the weak interactions of the Standard Model (WIMPs). WIMPs have been arguably the most widely considered candidates for DM in the past decades. Among the archetypical WIMP models are Higgs-portal scenarios where DM is a linear combination of the neutral components of electroweak multiplets that couple to the Higgs doublet. The Higgs doublet can mediate a long-range force for DM, which affects the annihilation processes and binds DM into bound states. More importantly, the emission of a Higgs doublet by a pair of DM particles can give rise to extremely rapid monopole BSF processes and bound-state to bound-state transitions. We compute these effects in the unbroken electroweak phase, and we show that the formation of metastable DM bound states via Higgs-doublet emission and their decay decreases the relic density very significantly. We give new constraints for the WIMPs parameters, solidifying them at the multi-TeV scale.

Chapter 2

Bound state formation via emission of neutral scalar mediator

While the importance of bound-state formation for DM is now well established for weakly coupled theories with vector mediators [39–47, 49, 56–67], and of course in confining DM theories [68–72], in models with scalar mediators bound-state effects appear to be either less severe, or relevant to a limited parameter space. In such models, the radiative capture into bound states suffers from two cancellations: (i) The lowest order s-wave contribution vanishes due to the orthogonality of the incoming and outgoing wavefunctions, thus abdicating the leading order to the p-wave. (ii) The leading order p-wave terms cancel for particle-antiparticle or identical-particle pairs, yielding to s- and d-wave contributions that are suppressed by higher orders in the coupling with respect to the capture via vector emission and possibly to the annihilation cross-section [43, 59, 73]. Even so, BSF has some important implications. Since it contains an s-wave component, it results in CMB constraints for fermionic DM, whose direct annihilation is p-wave and thus unconstrained by indirect probes [52]. Moreover, asymmetric DM coupled to a light scalar may form stable multiparticle bound states, provided that the coupling is large enough to overcome the two-particle capture bottleneck [73–75] (or BSF is facilitated by a parametric resonance [76]).

In the present chapter 2 we go one step forward in the study of BSF mediated by neutral scalar forces. The above results take into account only the trilinear DM-DM-mediator coupling. However, given the cancelations mentioned above, there are also other couplings that contribute to the LO of the BSF amplitude. It is thus important to consider all relevant contributions, particularly if they are generic within a theory. Theories with scalar mediators include a scalar potential whose couplings can contribute to the radiative part of the capture process. In this work, we investigate the impact of the various couplings in the scalar potential to the radiative BSF.

This chapter is organised as follows. In section 2.1.1, we introduce the interaction Lagrangians, review the computation of radiative transitions, and summarise the past results on BSF with scalar emission via the trilinear DM-DM-mediator coupling. In section 2.2, we compute the contributions to the radiative BSF from other scalar couplings. We consider both scalar and fermionic DM, and compute BSF via one and two scalar emission (BSF1 and BSF2 respectively). We discuss the features of the resulting cross-sections and compare them with the past results. We conclude in section 2.3, with a discussion of their potential implications. Various technical computations are included in the appendices.

2.1 Bound state formation via trilinear couplings

2.1.1 Preliminaries

We consider two particles X_1 and X_2 with masses m_1 and m_2 respectively, that interact via a light scalar mediator φ of mass m_φ. We shall allow X_1 and X_2 to be real or complex scalars, or Dirac fermions. The relevant interactions are described by the following Lagrangians,

$$\begin{aligned}\mathcal{L}_{\Re,sc} = &\frac{1}{2}\partial_\mu X_1 \partial^\mu X_1 + \frac{1}{2}\partial_\mu X_2 \partial^\mu X_2 + \frac{1}{2}\partial_\mu \varphi \partial^\mu \varphi - \frac{1}{2}m_1^2 X_1^2 - \frac{1}{2}m_2^2 X_2^2 - \frac{1}{2}m_\varphi^2 \varphi^2 \\ &- \frac{1}{2}g_1 m_1 \varphi X_1^2 - \frac{1}{2}g_2 m_2 \varphi X_2^2 - \frac{\lambda_{1\varphi}}{4}X_1^2\varphi^2 - \frac{\lambda_{2\varphi}}{4}X_2^2\varphi^2 - \frac{\rho_\varphi}{3!}\varphi^3 - \frac{\lambda_\varphi}{4!}\varphi^4 \\ &- \frac{\lambda_1}{4!}X_1^4 - \frac{\lambda_2}{4!}X_2^4 - \frac{\lambda_{12}}{4}X_1^2 X_2^2 \,,\end{aligned} \tag{2.1.1}$$

$$\begin{aligned}\mathcal{L}_{\Im,sc} = &\partial_\mu X_1^\dagger \partial^\mu X_1 + \partial_\mu X_2^\dagger \partial^\mu X_2 + \frac{1}{2}\partial_\mu \varphi \partial^\mu \varphi - m_1^2|X_1|^2 - m_2^2|X_2|^2 - \frac{1}{2}m_\varphi^2\varphi^2 \\ &- g_1 m_1 \varphi |X_1|^2 - g_2 m_2 \varphi |X_2|^2 - \frac{\lambda_{1\varphi}}{2}|X_1|^2\varphi^2 - \frac{\lambda_{2\varphi}}{2}|X_2|^2\varphi^2 - \frac{\rho_\varphi}{3!}\varphi^3 - \frac{\lambda_\varphi}{4!}\varphi^4 \\ &- \frac{\lambda_1}{2}|X_1|^4 - \frac{\lambda_2}{2}|X_2|^2 - \lambda_{12}|X_1|^2|X_2|^2 \,,\end{aligned} \tag{2.1.2}$$

and

$$\begin{aligned}\mathcal{L}_f = &\bar{X}_1 i\partial\!\!\!/ X_1 + \bar{X}_2 i\partial\!\!\!/ X_2 + \frac{1}{2}\partial_\mu\varphi\partial^\mu\varphi - m_1\bar{X}_1 X_1 - m_2 \bar{X}_2 X_2 - \frac{1}{2}m_\varphi^2\varphi^2 \\ &- g_1\varphi\bar{X}_1 X_1 - g_2\varphi\bar{X}_2 X_2 - \frac{\rho_\varphi}{3!}\varphi^3 - \frac{\lambda_\varphi}{4!}\varphi^4 \,.\end{aligned} \tag{2.1.3}$$

Note that, since we are interested in the application of our results to DM, we shall assume that the interacting particles X_1, X_2 carry a $\mathbb{Z}_2$ symmetry. For later convenience, we define the total and the reduced mass of the two interacting particles

$$M \equiv m_1 + m_2, \qquad \mu \equiv \frac{m_1 m_2}{m_1 + m_2} \,, \tag{2.1.4}$$

and the dimensionless factors

$$\eta_1 \equiv \frac{m_1}{m_1 + m_2}, \qquad \eta_2 \equiv \frac{m_2}{m_1 + m_2} \,. \tag{2.1.5}$$

In the non-relativistic regime, the interaction between X_1 and X_2 is described to leading order by a static Yukawa potential that arises from the resummation of the one-boson-exchange diagrams,

$$V_Y(\mathbf{r}) = -\frac{\alpha}{r}e^{-m_\varphi r}, \tag{2.1.6}$$

with $\alpha = \alpha_{sc}$ or $\alpha = \alpha_f$, depending on whether the interacting particles are scalars or fermions, where

$$\alpha_{sc} \equiv \frac{g_1 g_2}{16\pi} \qquad \text{and} \qquad \alpha_f \equiv \frac{g_1 g_2}{4\pi} \,. \tag{2.1.7}$$

We derive the Yukawa potential and α_{sc}, α_f in appendix A.1. The long-range interaction between X_1 and X_2 described by the potential (2.1.6) distorts the wavefunction of the scattering (unbound) states – a phenomenon known as the Sommerfeld effect [37, 38] – and gives rise to bound states. Bound states exist if the mediator is sufficiently light. For the ground state to exist,

$$\mu\alpha/m_\varphi > 0.84 \,, \tag{2.1.8}$$

while stronger conditions apply for excited states [43]. The condition (2.1.8) also roughly marks the regime where the Sommerfeld effect is significant.

The capture into bound states necessitates the dissipation of the binding energy and the kinetic energy of the relative motion of the X_1X_2 pair, which may occur radiatively. In section 2.1.2, we review the computation of radiative BSF amplitudes. The capture via emission of one scalar mediator, $X_1 + X_2 \to \mathcal{B}(X_1X_2) + \varphi$, has been previously considered in Refs. [43, 52, 59, 73], where only the trilinear φX_j^2 couplings were taken into account. We review the main results in section 2.1.3. As we shall see, for a particle-antiparticle pair or a pair of identical particles, the dipole contribution – which is the leading order term for X_1, X_2 with different masses and couplings – vanishes identically.

2.1.2 Radiative transition amplitude

We consider the radiative transitions

$$X_1(k_1) + X_2(k_2) \to X_1(p_1) + X_2(p_2) + \text{radiation}\,, \tag{2.1.9}$$

where the parentheses denote the 4-momenta of the incoming and outgoing X_1 and X_2 fields. We will be interested in particular in the case where the incoming X_1, X_2 particles form a scattering state, while the outgoing X_1, X_2 are captured into a bound state. In order to separate the motion of the CM from the relative motion, we make the following transformation in the momenta [59, 77]

$$k_1 \equiv \eta_1 K + q, \qquad k_2 \equiv \eta_2 K - q\,, \tag{2.1.10}$$

$$p_1 \equiv \eta_1 P + p, \qquad p_2 \equiv \eta_2 P - p\,, \tag{2.1.11}$$

where $\eta_{1,2}$ are defined in eq. (2.1.5).

In the presence of a long-range interaction, the relative motion of X_1, X_2 is not well approximated by a plane wave. It is described more generally by wavefunctions, which in momentum space we shall denote as $\tilde{\phi}_{\mathbf{k}}(\mathbf{q})$ and $\tilde{\psi}_{n\ell m}(\mathbf{p})$ for the scattering and the bound states respectively. The wavefunctions obey the Schrödinger equation with the potential (2.1.6). The continuous spectrum is characterised by the momentum $\mathbf{k} = \mu\mathbf{v}_{\rm rel}$, which is the expectation value of $\mathbf{q}$ and parametrises the energy of the relative motion in the scattering states, $\epsilon_{\mathbf{k}} = \mathbf{k}^2/(2\mu) = \mu v_{\rm rel}^2/2$. The bound states are characterised by the standard discrete principal and angular momentum quantum numbers $\{n\ell m\}$, which determine the expectation value of $\mathbf{p}$ and the binding energy $\epsilon_{n\ell}$. As is well known, for a Coulomb potential, $\epsilon_{n\ell} = \kappa^2/(2n^2\mu) = \mu\alpha^2/(2n^2)$, where $\kappa \equiv \mu\alpha$ is the Bohr momentum; a non-negligible mediator mass suppresses $\epsilon_{n\ell}$ and introduces a dependence on ℓ. We review the wavefunctions in appendix B (see Ref. [43] for a more detailed discussion). For the purpose of evaluating the leading order contributions to the transition amplitude, we shall keep in mind that the wavefunctions impose $|\mathbf{q}| \sim |\mathbf{k}| = \mu v_{\rm rel}$ and $|\mathbf{p}| \sim \kappa = \mu\alpha$.

In the non-relativistic regime, the total 4-momenta of the scattering and the bound states are

$$K \simeq \left(M + \frac{\mathbf{K}^2}{2M} + \epsilon_{\mathbf{k}},\ \mathbf{K}\right)\,, \tag{2.1.12}$$

$$P \simeq \left(M + \frac{\mathbf{P}^2}{2M} - \epsilon_{n\ell},\ \mathbf{P}\right)\,. \tag{2.1.13}$$

We will work in the CM frame, $\mathbf{K} = \mathbf{0}$. Then, taking into account that $\epsilon_{\mathbf{k}}, \epsilon_{n\ell} \ll M$ (or equivalently $\alpha, v_{\rm rel} \ll 1$), the total energy available to be dissipated is

$$\omega \simeq \epsilon_{\mathbf{k}} + \epsilon_{n\ell}\,. \tag{2.1.14}$$

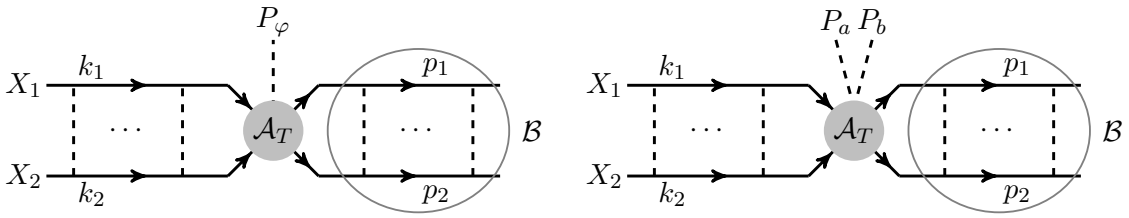

Figure 2.1: The amplitude for the radiative capture into bound states via emission of one or two scalars consists of the initial and final state wavefunctions, and the perturbative radiative amplitude $\mathcal{M}_T$ that includes the radiative vertices.

Evidently, the bound state acquires momentum $|\mathbf{P}| \sim \omega$. The full amplitude for the radiative capture into a bound state depends on the overlap of the initial (scattering) and final (bound) state wavefunctions and the radiative vertex. The diagrammatic representation for transitions with emission of one or two scalars is shown in fig. 2.1. In the instantaneous and non-relativistic approximations, the amplitude is [59]

$$\mathcal{M}_{\mathbf{k}\to\{n\ell m\}} \simeq \frac{1}{\sqrt{2\mu}} \int \frac{d^3p}{(2\pi)^3} \frac{d^3q}{(2\pi)^3} \left[1 - \frac{\mathbf{p^2}+\mathbf{q^2}}{4\mu^2}\left(1-\frac{3\mu}{M}\right)\right] \tilde{\psi}^*_{n\ell m}(\mathbf{p}) \tilde{\phi}_{\mathbf{k}}(\mathbf{q}) \mathcal{A}_T(\mathbf{q},\mathbf{p}) \,, \quad (2.1.15)$$

where $\mathcal{A}_T(\mathbf{q},\mathbf{p})$ is the radiative amplitude for the (off-shell) transition (2.1.9), under the transformations of eqs. (2.1.10) and (2.1.11). The fully connected diagrams contributing to $\mathcal{A}_T$ can be evaluated at leading order by setting the incoming and outgoing X_1, X_2 on-shell. For any non-fully-connected diagrams contributing to $\mathcal{A}_T$, the virtuality of X_1 and X_2 has to be integrated out. This can be done starting from the off-shell amplitude as described in [59] (see also [62, section 2.3] for a brief summary), or by adopting an effective field theory approach [78–89].[1] The dominant contributions to the capture with emission of a vector or scalar mediator via the trilinear coupling arise from non-fully-connected diagrams [43, 59]. (However, in non-Abelian theories, a leading order contribution to capture via gluon emission arises also from a fully connected diagram [42].) In the computations of this chapter in section 2.2, we will consider only fully connected diagrams.

In eq. (2.1.15), the factor inside the square brackets includes the leading order corrections in $\mathbf{p^2}, \mathbf{q^2}$ arising from the relativistic normalisation of states [59]. Upon the convolution with the wavefunctions and integration over $\mathbf{p}$ and $\mathbf{q}$, these terms amount to corrections in α^2 and $v_{\rm rel}^2$. They become important when the leading order contribution from $\mathcal{A}_T$ alone cancels, as is the case for the capture of particle-antiparticle or identical-particle pairs with emission of a scalar mediator via the trilinear coupling.

2.1.3 Capture via one scalar mediator: only trilinear couplings

The leading contributions to capture with emission of a scalar via the trilinear coupling only are shown in fig. 2.2. Starting from eq. (2.1.15), and neglecting the correction arising from the normalisation of states, these diagrams yield[2] [43, 59]

$$\mathcal{M}^{\rm TC}_{\mathbf{k}\to n\ell m} \simeq -M\sqrt{2\mu} \int d^3r \; \psi^*_{n\ell m}(\mathbf{r}) \; \phi_{\mathbf{k}}(\mathbf{r}) \left(g_1 \, e^{-i\eta_2 \mathbf{P}_\varphi\cdot\mathbf{r}} + g_2 \, e^{i\eta_1 \mathbf{P}_\varphi\cdot\mathbf{r}}\right) \,, \quad (2.1.16)$$

where $\mathbf{P}_\varphi$ is the momentum of the emitted boson, with $\mathbf{P}^2_\varphi + m^2_\varphi = \omega^2$ and ω given in eq. (2.1.14). The wavefunctions imply that the integrand is significant in the region $r \lesssim 1/\max(\mu\alpha/n, \mu v_{\rm rel}) \ll$

[1] For a comparison of quantum and classical approaches, see [90].

[2] We use the superscript TC to denote contributions that arise from the trilinear coupling alone, and in section 2.2 we will use the superscript SC to denote contributions in which other scalar couplings participate.

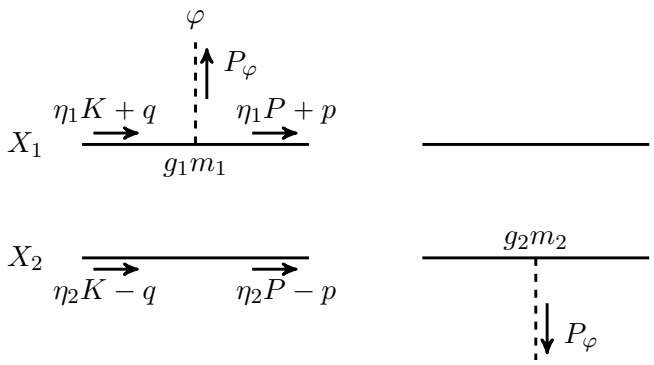

Figure 2.2: The contribution of the trilinear DM-DM-mediator couplings to the radiative part of bound-state formation via emission of one scalar mediator.

$1/\omega$, therefore we may evaluate eq. (2.1.16) by expanding in $\mathbf{P}_\varphi \cdot \mathbf{r} \sim \max(\alpha/n, v_{\rm rel})$ (cf. ref. [43, appendix B]). Clearly, the zeroth order terms vanish due to the orthogonality of the wavefunctions.

For a pair of particles with different masses and/or couplings to the scalar mediator, the leading order contributions arise from the $\mathbf{P}_\varphi \cdot \mathbf{r}$ terms in the expansion of eq. (2.1.16). The cross-section for capture into the ground state $\{n\ell m\} = \{100\}$ is [43, 59]

$$\sigma^{\rm TC}_{\rm BSF1} v_{\rm rel} \simeq \left[\frac{(g_1\eta_2 - g_2\eta_1)^2}{16\pi\alpha}\right] \frac{\pi\alpha^2}{\mu^2}\, S^{\rm TC}_{\rm BSF1}\,, \tag{2.1.17}$$

where $S^{\rm TC}_{\rm BSF1}$ depends on the dimensionless parameters $\alpha/v_{\rm rel}$ and $\mu\alpha/m_\varphi$. In the Coulomb approximation, which is valid at $m_\varphi \lesssim \mu v_{\rm rel}$, $S^{\rm TC}_{\rm BSF1}$ depends only on the parameter $\zeta \equiv \alpha/v_{\rm rel}$ as follows [43, 59]

$$S^{\rm TC}_{\rm BSF1}(\zeta) = \left(\frac{2\pi\zeta}{1-e^{-2\pi\zeta}}\right) \times \frac{2^6}{3}\left(\frac{\zeta^2}{1+\zeta^2}\right)^2 e^{-4\zeta {\rm arccot}\,\zeta}\,. \tag{2.1.18}$$

For the more general case that includes the effect of the mediator mass, we refer to [43]. We note that eqs. (2.1.17) and (2.1.18) correspond to dipole emission ($\ell_S = 1$ mode of the scattering state wavefunction). In eq. (2.1.17), the factor in the square brackets reduces to 1 for a pair of scalar particles with $g_1 = g_2$ and $\eta_1 \gg \eta_2$. In eq. (2.1.18), the first factor inside the brackets is responsible for the characteristic $\sigma v_{\rm rel} \propto 1/v_{\rm rel}$ scaling of the Sommerfeld-enhanced processes at low velocities ($\zeta \gtrsim 1$), while the remaining factors tend to a constant.

Evidently, for a particle-antiparticle pair or a pair of identical particles ($g_1 = g_2 = g$ and $\eta_1 = \eta_2 = 1/2$), the two terms proportional to $\mathbf{P}$, in the expansion of eq. (2.1.16) cancel. This cancellation persists even for capture into bound states of non-zero angular momentum ($\ell > 0$), as is evident from eq. (2.1.16), and implies that the next order contributions should be considered.

For a scalar particle-antiparticle pair the next order terms, which include also the leading order correction from the normalisation of states shown in eq. (2.1.15), yield [43]

$$\sigma^{\rm TC}_{\rm BSF1} v_{\rm rel} \simeq \frac{\pi\alpha_{sc}^4}{\mu^2}\, S^{\rm TC}_{{\rm BSF1},XX^*}\,, \tag{2.1.19}$$

where in the Coulomb regime $S^{\rm TC}_{{\rm BSF1},XX^*}$ depends on $\zeta = \alpha_{sc}/v_{\rm rel}$ as follows

$$S^{\rm TC}_{{\rm BSF1},XX^*}(\zeta) = \left(\frac{2\pi\zeta}{1-e^{-2\pi\zeta}}\right) \times \frac{2^6}{15}\frac{\zeta^2(3+2\zeta^2)}{(1+\zeta^2)^2}\, e^{-4\zeta {\rm arccot}\,\zeta}\,. \tag{2.1.20}$$

(For a pair of identical scalars, an extra factor of 2 arises from the symmetrization of the scattering state wavefunction.) The case of fermionic DM was considered in ref. [73]. In the Coulomb regime and for $\zeta \gtrsim 1$, the cross-section was found to be

$$\sigma^{\rm TC}_{{\rm BSF1},X\bar{X}}\, v_{\rm rel} \simeq \frac{\pi\alpha_f^4}{\mu^2}\left(\frac{2\pi\alpha_f}{v_{\rm rel}}\right)\frac{2^4 e^{-4}}{3^2}\,. \tag{2.1.21}$$

Note that both eq. (2.1.19) and eq. (2.1.21) are suppressed by α^2 with respect to eq. (2.1.17).

2.2 The contribution of scalar potential couplings to the radiative capture

In this section, we investigate how the scalar couplings $\lambda_{1\varphi}$, $\lambda_{2\varphi}$, λ_φ and ρ_φ in eqs. (2.1.1) to (2.1.3) – which do not affect the long-range potential between X_1 and X_2 – contribute to the radiative capture of X_1, X_2 pairs into bound states. In order to exhibit the leading order contribution from all couplings, we consider BSF via one and two scalar emission,

$$\text{BSF1:}\quad X_1 + X_2 \to \mathcal{B}(X_1X_2) + \varphi\,, \tag{2.2.1}$$

$$\text{BSF2:}\quad X_1 + X_2 \to \mathcal{B}(X_1X_2) + 2\varphi\,. \tag{2.2.2}$$

It is important to note that in most diagrams we will consider, the trilinear couplings g_j also participate in the radiative part of the process (cf. figs. 2.3 to 2.6). In fact, it may naively seem that these diagrams are of the same or higher order in α than those giving rise to the cross-sections of section 2.1.3 (even ignoring the additional suppression introduced by the new couplings). However, the momentum transfer along the mediators exchanged in these diagrams and the off-shellness of the interacting particles scale also with α, thereby reducing the order of dependence of the diagrams on α.[3]

For convenience, we first define in section 2.2.1 the wavefunction overlaps integrals that we will use for the BSF cross-sections. We provide some analytic approximations for capture into the ground state, and describe their features that are of course inherited by the BSF cross-sections. Then, in sections 2.2.2 and 2.2.3 we compute the contributions to BSF1 from the couplings in the scalar potential, for scalar and fermionic interacting particles, respectively, and discuss in which regimes they are important. We finish with considering BSF2 in section 2.2.4.

2.2.1 Overlap integrals

We define the overlap integrals

$$\mathcal{V}_{\mathbf{k},\{n\ell m\}} \equiv (8\pi\kappa)^{1/2}\int\frac{d^3q}{(2\pi)^3}\frac{d^3p}{(2\pi)^3}\frac{\tilde{\phi}_{\mathbf{k}}(\mathbf{q})\tilde{\psi}^*_{n\ell m}(\mathbf{p})}{(\mathbf{q}-\mathbf{p})^2+m_\varphi^2}\,, \tag{2.2.3}$$

$$\mathcal{R}_{\mathbf{k},\{n\ell m\}} \equiv (8\pi\kappa^5)^{1/2}\int\frac{d^3q}{(2\pi)^3}\frac{d^3p}{(2\pi)^3}\frac{\tilde{\phi}_{\mathbf{k}}(\mathbf{q})\tilde{\psi}^*_{n\ell m}(\mathbf{p})}{[(\mathbf{q}-\mathbf{p})^2+m_\varphi^2]^2}\,, \tag{2.2.4}$$

$$\mathcal{I}_{\mathbf{k},\{n\ell m\}}(\mathbf{\Gamma}) \equiv \int\frac{d^3p}{(2\pi)^3}\tilde{\phi}_{\mathbf{k}}(\mathbf{p}+\mathbf{\Gamma})\tilde{\psi}^*_{n\ell m}(\mathbf{p}) = \int\frac{d^3p}{(2\pi)^3}\phi_{\mathbf{k}}(\mathbf{r})\psi^*_{n\ell m}(\mathbf{r})\,e^{-i\mathbf{\Gamma}\cdot\mathbf{r}}\,. \tag{2.2.5}$$

The prefactors in eqs. (2.2.3) and (2.2.4) have been chosen such that $\mathcal{V}_{\mathbf{k},\{n\ell m\}}$ and $\mathcal{R}_{\mathbf{k},\{n\ell m\}}$ are dimensionless, and the definition of $\mathcal{I}_{\mathbf{k},\{n\ell m\}}$ follows refs. [43, 59].

[3] This is of course also the reason for the emergence of the non-perturbative effects we consider, the Sommerfeld enhancement and the existence of bound states.

The integrals eqs. (2.2.3) to (2.2.5) depend on the two dimensionless parameters

$$\zeta \equiv \frac{\alpha}{v_{\rm rel}} \quad \text{and} \quad \xi \equiv \frac{\mu\alpha}{0.84 m_\varphi} \,. \tag{2.2.6}$$

As stated in section 2.1.1, for the Yukawa potential (2.1.6) the ground state exists if $\xi > 1$ [43].[4] However, BSF1 is kinematically possible only if

$$m_\varphi < (\mu/2)[\alpha^2(1-1/\xi)^2 + v_{\rm rel}^2] \,, \tag{2.2.7}$$

where we used the Hulthen approximation for the binding energy (cf. appendix B). In the regime where BSF is important, $v_{\rm rel} \lesssim \alpha$ (see e.g. section 2.1.3), this condition reduces roughly to $m_\varphi \lesssim \mu\alpha^2/2$ or equivalently $\xi \gtrsim \xi_{\rm min} \simeq 2.4/\alpha \gg 1$, i.e. it is much stronger than the requirement for the existence of bound states. This in turn ensures that the bound-state wavefunction can be approximated by its Coulomb value. (For the validity of the Coulomb limit for the overlap integrals and the BSF cross-sections, see below.)

We derive analytical expressions for the $\mathcal{V}_{\mathbf{k},\{100\}}$ and $\mathcal{R}_{\mathbf{k},\{100\}}$ integrals in appendix C, using an appropriate approximation. The integral (2.2.5) has been considered in ref. [43]. For the BSF cross-sections of interest, $|\mathbf{\Gamma}| \sim |\mathbf{P}_\varphi| \ll \langle|\mathbf{p}|\rangle \sim \kappa$, thus $\mathcal{I}_{\mathbf{k}\to\{n\ell m\}}$ can be computed by expanding in $\mathbf{\Gamma}$. Here we shall keep up to first order terms in Γ/κ. For capture into the ground state,

$$\mathcal{V}_{\mathbf{k},\{100\}} \simeq \sqrt{8 S_0(\zeta,\xi)} \left(\frac{\zeta^2}{1+\zeta^2}\right) \, e^{-2\zeta \,\mathrm{arccot}\,\zeta} \,, \tag{2.2.8}$$

$$\mathcal{R}_{\mathbf{k},\{100\}} \simeq \sqrt{8 S_0(\zeta,\xi)} \left(\frac{\zeta^2}{1+\zeta^2}\right)^2 \, e^{-2\zeta \,\mathrm{arccot}\,\zeta} \,, \tag{2.2.9}$$

$$\mathcal{I}_{\mathbf{k},\{100\}}(\mathbf{\Gamma}) \simeq \sqrt{\frac{2^8\pi S_1(\zeta,\xi)}{\kappa^3}} \left[\frac{\zeta^5}{(1+\zeta^2)^3}\right] \, e^{-2\zeta \,\mathrm{arccot}\,\zeta} \, \frac{\Gamma\cos(\theta_{\mathbf{k},\mathbf{\Gamma}})}{\kappa} \,, \tag{2.2.10}$$

where $S_0(\zeta,\xi)$ and $S_1(\zeta,\xi)$ are the Sommerfeld factors for s- and p-wave annihilation respectively. In the Hulthen approximation,

$$S_0(\zeta,\xi) = \frac{2\pi\zeta\sinh(\pi\xi/\zeta)}{\cosh(\pi\xi/\zeta) - \cosh[(\pi\xi/\zeta)\sqrt{1-4\zeta^2/\xi}]} \,, \tag{2.2.11}$$

which in the Coulomb limit reduces to $S_0^C(\zeta) = 2\pi\zeta/(1-e^{-2\pi\zeta})$. While there is no analytical approximation for $S_1(\zeta,\xi)$ for finite ξ, in the Coulomb limit $\xi \to \infty$ it becomes $S_1^C(\zeta) = (1+\zeta^2)S_0^C(\zeta)$. The Coulomb limit remains a good approximation as long the average momentum transfer between the interacting particles is larger than the mediator mass,

$$m_\varphi \lesssim \mu v_{\rm rel} \,, \tag{2.2.12}$$

or equivalently $\xi > \zeta$ (see e.g. [43]).

Outside this range, i.e. at low velocities $v_{\rm rel} \lesssim m_\varphi/\mu$, both S_0 and S_1 exhibit parametric resonances at discrete values of ξ that correspond to the thresholds for the existence of $\ell = 0$ and $\ell = 1$ bound states respectively. For S_0 in the Hulthen approximation, these are $\xi = n^2$ with $n \in$ integers. At non-resonant parametric points, S_0 and S_1 follow the Coulomb approximation as long as (2.2.12) is satisfied, but saturate to their respective Coulomb values at $v_{\rm rel} \approx m_\varphi/\mu$ as the velocity decreases. In contrast, if close to a resonant parametric point, S_0 and S_1 grow faster

[4] Note that in ref. [43], the parameter ξ was defined as $\mu\alpha/m_\varphi$. The reason we prefer the definition (2.2.6) here is to simplify the expressions for the wavefunctions and the binding energies in the Hulthen approximation of the Yukawa potential.

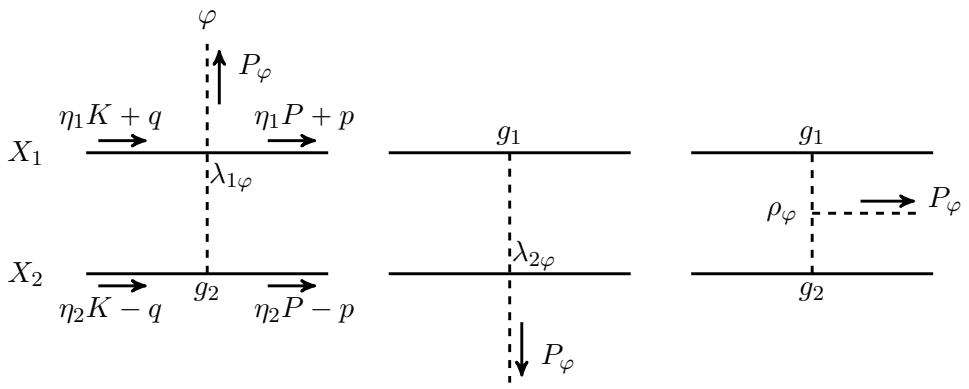

Figure 2.3: The contribution of the scalar couplings to the radiative part of bound-state formation via emission of one scalar mediator. For fermionic X_1, X_2, only the diagram to the right exists.

than $1/v_{\rm rel}$ and $1/v_{\rm rel}^3$ respectively at $v_{\rm rel} \lesssim m_\varphi/\mu$ (in particular $S_0 \propto \zeta^2 \propto 1/v_{\rm rel}^2$), to eventually saturate to a constant value at a lower velocity that depends on the proximity to the resonant point. For S_0 in the Hulthen approximation, the saturated value is $S_0(\zeta, \xi) \simeq \pi^2\xi/\sin^2\sqrt{\pi^2\xi}$ [cf. eq. (2.2.11)].

This behaviour implies that an s-wave cross-section times relative velocity saturates to a constant value at low velocities, while a p-wave recovers the velocity suppression that appears in perturbative cross-sections, $\sigma^{p-\rm wave} v_{\rm rel} \propto v_{\rm rel}^2$, albeit is enhanced with respect to its value if the Sommerfeld effect were neglected. This point will be important in our discussion of the new contributions to BSF that we compute in the following.

2.2.2 Capture via emission of one mediator: scalar dark matter

Amplitude

The leading order diagrams in $\lambda_{1\varphi}$, $\lambda_{2\varphi}$ and ρ_φ that contribute to the radiative part of the transition amplitude due to the scalar couplings in eqs. (2.1.1) to (2.1.3) are shown in fig. 2.3. We find

$$\begin{aligned} i\mathcal{A}_T^{\rm SC} &= (-i\lambda_{1\varphi})\frac{i}{(\eta_2 P_\varphi - q + p)^2 - m_\varphi^2}(-ig_2 m_2) \\ &+ (-i\lambda_{2\varphi})\frac{i}{(\eta_1 P_\varphi + q - p)^2 - m_\varphi^2}(-ig_1 m_1) \\ &+ (-ig_1 m_1)\frac{i}{(\eta_1 P_\varphi + q - p)^2 - m_\varphi^2}\,(-i\rho_\varphi)\,\frac{i}{(\eta_2 P_\varphi - q + p)^2 - m_\varphi^2}(-ig_2 m_2)\,. \end{aligned} \tag{2.2.13}$$

Then according to the discussion in section 2.1.2 on the scaling of the momenta,

$$\mathcal{A}_T^{\rm SC} \simeq \frac{(\lambda_{1\varphi} g_2 \eta_2 + \lambda_{2\varphi} g_1 \eta_1) M}{(\mathbf{q} - \mathbf{p})^2 + m_\varphi^2} - \frac{g_1 g_2 M \mu\, \rho_\varphi}{[(\mathbf{q} - \mathbf{p})^2 + m_\varphi^2]^2}\,. \tag{2.2.14}$$

The contribution from the diagrams of fig. 2.2 is [43, 59]

$$\mathcal{A}_T^{\rm TC} \simeq -2M\mu\left[g_1 (2\pi)^3 \delta^3(\mathbf{q} - \mathbf{p} - \eta_2 \mathbf{P}_,) + g_2 (2\pi)^3 \delta^3(\mathbf{q} - \mathbf{p} + \eta_1 \mathbf{P}_,)\right]\,. \tag{2.2.15}$$

Inserting eqs. (2.2.14) and (2.2.15) in eq. (2.1.15), and neglecting the corrections arising from the relativistic normalisation of states, we find

$$\mathcal{M}^{\rm SC}_{\mathbf{k}\to\{n\ell m\}} \simeq \frac{M}{\mu}\left[\frac{\lambda_{1\varphi}g_2\eta_2+\lambda_{2\varphi}g_1\eta_1)}{\sqrt{16\pi\alpha_{sc}}}\,\mathcal{V}_{\mathbf{k},\{n\ell m\}} - \left(\frac{\rho_\varphi}{\mu\alpha_{sc}^2/2}\right)\sqrt{4\pi\alpha_{sc}}\,\mathcal{R}_{\mathbf{k},\{n\ell m\}}\right], \tag{2.2.16}$$

$$\mathcal{M}^{\rm TC}_{\mathbf{k}\to\{nlm\}} \simeq -M\sqrt{2\mu}\left[g_1\mathcal{I}_{\mathbf{k},\{nlm\}}(\eta_2\mathbf{P}_\varphi) + g_2\mathcal{I}_{\mathbf{k},\{nlm\}}(-\eta_1\mathbf{P}_\varphi)\right]. \tag{2.2.17}$$

Equation (2.2.17) of course agrees with eq. (2.1.16)

Cross-section for capture into the ground state

The cross-section for capture into the ground state is

$$v_{\rm rel}\,\frac{d\sigma_{\rm BSF1}}{d\Omega} \simeq \frac{|\mathbf{P},|}{64\pi^2M^2\mu}|\mathcal{M}_{\mathbf{k}\to\{100\}}|^2\,. \tag{2.2.18}$$

The momentum of the emitted scalar is found from the conservation of energy [cf. eq. (2.1.14)]

$$\sqrt{\mathbf{P}_\varphi^2+m_\varphi^2} \simeq \frac{\mu}{2}(\alpha^2+v_{\rm rel}^2)\,, \tag{2.2.19}$$

where we adopted the Coulomb value for the binding energy since $\xi \gg 1$.

Taking into account the contributions of eqs. (2.2.16) and (2.2.17) to the amplitude, and the overlap integrals of eqs. (2.2.8) to (2.2.10) for capture into the ground state, we obtain

$$\begin{aligned}\sigma^{\rm tot}_{\rm BSF1}v_{\rm rel} \simeq{}& \frac{\alpha_{sc}^2}{\mu^2}\,s_{ps}^{\rm BSF1}\left(\frac{\zeta^2}{1+\zeta^2}\right)e^{-4\zeta\,\mathrm{arccot}\,\zeta}\\ &\times\left\{\left[\frac{\lambda_{1\varphi}\,g_2\eta_2+\lambda_{2\varphi}\,g_1\eta_1}{\sqrt{64\pi^2\alpha_{sc}}} - \sqrt{\alpha_{sc}}\left(\frac{\rho_\varphi}{\mu\alpha_{sc}^2/2}\right)\left(\frac{\zeta^2}{1+\zeta^2}\right)\right]^2 S_0(\zeta,\xi)\right.\\ &\left.+\frac{2^6\pi}{3}\frac{(g_1\eta_2-g_2\eta_1)^2}{16\pi\alpha_{sc}}\left(\frac{\zeta^2}{1+\zeta^2}\right)\frac{S_1(\zeta,\xi)}{(1+\zeta^2)}\right\},\end{aligned} \tag{2.2.20}$$

where $s_{ps}^{\rm BSF1}$ is the phase-space suppression factor for BSF1,

$$s_{ps}^{\rm BSF1} \equiv \left(1-\left[\frac{2m_\varphi}{\mu(\alpha^2+v_{\rm rel}^2)}\right]^2\right)^{1/2}. \tag{2.2.21}$$

As can be seen from eq. (2.2.20), the ρ_φ contribution to the BSF1 cross-section scales as $\sigma_{\rm BSF1}v_{\rm rel} \propto (1/\alpha)(\rho_\varphi/\mu)^2$. This is clearly of lower order in α than the cross-sections of section 2.1.3, however it is suppressed by the square of the ratio of the mediator scale to the DM scale. Assuming that $\rho_\varphi \sim m_\varphi$, the kinematic threshold $m_\varphi \lesssim \mu\alpha^2/2$ implies that this contribution scales at best as $\sigma_{\rm BSF1}v_{\rm rel} \propto \alpha^3$. While this is of higher order in α than eq. (2.1.17), it is still of lower order than eqs. (2.1.19) and (2.1.21). It is of course important to keep in mind that ρ_φ may differ significantly from m_φ and/or the binding energy.[5]

We shall now simplify and adapt the above expression – which has been derived for a pair of distinguishable scalars – to various cases.

[5] We note that the third diagram of fig. 2.3, from where the ρ_φ contribution to BSF1 arises, resembles the diagram that appears in the radiative capture via one gluon emission in non-Abelian theories due to the trilinear gluon coupling [42]. That coupling is momentum dependent, with the relevant momentum scale in the capture process being κ. We may recover the scaling of the non-Abelian BSF cross-section on α [62] by mapping $\rho_\varphi \to g\,\kappa \propto \alpha^{3/2}$.

Different scalars species

Let us consider for simplicity the limiting case where the couplings of the two particles are equal, $\lambda_{1\varphi} = \lambda_{2\varphi} = \lambda_{X\varphi}$ and $g_1 = g_2 = g$, while their masses are very different, $\eta_1 \gg \eta_2$. Then, eq. (2.2.20) simplifies to

$$\sigma^{\rm tot}_{\rm BSF1} v_{\rm rel} \simeq \frac{\alpha_{sc}^2}{\mu^2} s_{ps}^{\rm BSF1} \left(\frac{\zeta^2}{1+\zeta^2}\right) e^{-4\zeta \,{\rm arccot}\,\zeta} \times \left\{ \left[\frac{\lambda_{X\varphi}}{\sqrt{4\pi}} - \sqrt{\alpha_{sc}} \left(\frac{\rho_\varphi}{\mu\alpha_{sc}^2/2}\right) \left(\frac{\zeta^2}{1+\zeta^2}\right) \right]^2 S_0(\zeta,\xi) + \frac{2^6\pi}{3} \left(\frac{\zeta^2}{1+\zeta^2}\right) \frac{S_1(\zeta,\xi)}{(1+\zeta^2)} \right\}. \tag{2.2.22}$$

In the regime where BSF is important and the Coulomb approximation is valid, i.e. for $m_\varphi \lesssim \mu v_{\rm rel} \lesssim \mu\alpha_{sc}$, we recall that $S_1 \simeq (1+\zeta^2) S_0$, thus all contributions exhibit the same velocity scaling, $\sigma v_{\rm rel} \propto 1/v_{\rm rel}$. For perturbative $\lambda_{X\varphi}$ and for $\rho_\varphi \sim m_\varphi \lesssim \mu\alpha_{sc}^2/2$, the s-wave contributions are subdominant, and we recover the cross-section arising from the diagrams of fig. 2.2 [cf. eq. (2.1.17)].

However, outside the Coulomb regime, i.e. for $\mu v_{\rm rel} \lesssim m_\varphi \lesssim \mu\alpha_{sc}$, the p-wave term becomes velocity suppressed (cf. discussion in the end of section 2.2.1). This implies that at sufficiently low velocities, the $\lambda_{X\varphi}$ and ρ_φ contributions dominate.

Particle-antiparticle pair

For a particle-antiparticle pair, $\lambda_{1\varphi} = \lambda_{2\varphi} \equiv \lambda_{X\varphi}$, $g_1 = g_2 \equiv g$ and $m_1 = m_2 \equiv m_X$ (or $\eta_1 = \eta_2$). In this case, the p-wave term in eq. (2.2.20) vanishes. The contribution from the $\lambda_{X\varphi}$ and ρ_φ couplings becomes

$$\sigma^{\rm SC}_{\rm BSF1} v_{\rm rel} \simeq \frac{\alpha_{sc}^2}{\mu^2} \left[\frac{\lambda_{X\varphi}}{\sqrt{4\pi}} - \sqrt{\alpha_{sc}} \left(\frac{\rho_\varphi}{\mu\alpha_{sc}^2/2}\right) \left(\frac{\zeta^2}{1+\zeta^2}\right) \right]^2 s_{ps}^{\rm BSF1} \; S_0(\zeta,\xi) \left(\frac{\zeta^2}{1+\zeta^2}\right) e^{-4\zeta \,{\rm arccot}\,\zeta}. \tag{2.2.23}$$

However, as discussed in section 2.1.3, the trilinear $\varphi X X^\dagger$ coupling gives rise also to s- and d-wave contributions that are suppressed by higher orders in α_{sc} [43]. Comparing eq. (2.2.23) with eq. (2.1.19) in the Coulomb regime, we find the following.

- The $\lambda_{X\varphi}$ contribution to eq. (2.2.23) dominates over eq. (2.1.19) if

$$\lambda_{X\varphi} \gtrsim 18\alpha_{sc}\,. \tag{2.2.24}$$

  Note that if the mediator φ is the radial component of a complex scalar Φ that obtains a vacuum expectation value v_φ and breaks a local symmetry, i.e. $\Phi = (v_\varphi + \varphi) e^{i a_\varphi}/\sqrt{2}$, then the trilinear DM-DM-mediator coupling g arises from the quartic coupling of this scalar to DM after spontaneous symmetry breaking, i.e.

$$\delta\mathcal{L} = -\lambda_{X\varphi} |\Phi|^2 |X|^2 \supset -\lambda_{X\varphi}\, v_\varphi\, \varphi |X|^2 - \frac{\lambda_{X\varphi}}{2}\, \varphi^2 |X|^2\,. \tag{2.2.25}$$

  In this case, $\lambda_{X\varphi}$ and g are related via $\lambda_{X\varphi} v_\varphi = g m_X$. Note that m_X receives a contribution from v_φ, but remains an independent parameter. The above implies $\alpha_{sc} = \lambda_{X\varphi}^2 v_\varphi^2/(16\pi m_X^2)$, and the condition (2.2.24) becomes $\lambda_{X\varphi} \lesssim (16\pi/18)(m_X/v_\varphi)^2$, which encompasses the entire regime where $\lambda_{X\varphi}$ is perturbative if $v_\varphi \sim m_\varphi \ll m_X$ (or more generally, if $v_\varphi \lesssim m_X$). In this case, the $\lambda_{X\varphi}$ contribution to BSF1 dominates.

- The ρ_φ contribution to eq. (2.2.23) dominates over eq. (2.1.19) if

$$\frac{\rho_\varphi}{\mu\alpha_{sc}^2/2} \gtrsim 3\sqrt{\alpha_{sc}}\,, \tag{2.2.26}$$

  which encompasses significant parameter space.

Note that outside the Coulomb regime, the $\lambda_{X\varphi}$ and ρ_φ contributions dominate over eq. (2.1.19) in a broader parameter ranges than those designated by the conditions (2.2.24) and (2.2.26), since the d-wave component of eq. (2.1.19) becomes suppressed at low $v_{\rm rel}$ while the s-wave terms saturate to constant values.

Identical scalars

For a pair of identical scalars, the total wavefunction has to be symmetric in the interchange of the two particles. Thus the scattering state wavefunction is

$$\left[\phi_{\mathbf{k}}(\mathbf{r}) + \phi_{-\mathbf{k}}(\mathbf{r})\right]/\sqrt{2}\,, \tag{2.2.27}$$

This implies that the contribution of the even-ℓ_S modes participating in a process is doubled with respect to the case of distinguishable scalars, while the contribution of the odd-ℓ_S modes vanishes. Similarly, there are only $\ell =$ even bound states of two identical bosons. Since eq. (2.2.23) includes only s-wave terms, the cross-section for a pair of identical scalars is twice as large as that given by eq. (2.2.23).

2.2.3 Capture via emission of one mediator: fermionic dark matter

Amplitude

For fermions, there are no renormalisable $\lambda_{j\varphi}$ couplings and only the third diagram in fig. 2.3 contributes. The amplitude is related to that for scalars as follows. The Dirac propagators S_j^D can be expressed in terms of the scalar propagators $S_j(p)$ and the spinors $u, \bar{u}$

$$S_j^D(p) = \frac{i(\not{p} + m_j)}{p^2 - m_j^2} = S_j(p)(\not{p} + m_j) = S_j(p)\sum_r u_j^r(p)\bar{u}_j^r(p)\,, \tag{2.2.28}$$

where r denotes the spin and $j = 1, 2$ refers to the particle species. In order to compute the fermionic BSF diagrams, we insert a factor $\sum_{r_i} u_j^{r_i}(p_i)\bar{u}_j^{r_i}(p_i)$ for each propagator and contract $\bar{u}_j^{r_{i+1}}(p_{i+1})u_j^{r_i}(p_i)$ across each vertex i. Since all the fermion-fermion-scalar vertices in the BSF diagrams are either soft or ultrasoft, we can use the identity

$$\bar{u}_j^{s_{i+1}}(p_{i+1})u^{s_i}(p_i) \simeq \bar{u}_j^{s_{i+1}}(p_i)u_j^{s_i}(p_i) = +2m_j\delta^{s_i s_{i+1}}\,, \tag{2.2.29}$$

as also in appendix A.1. The spin Kronecker deltas in eq. (2.2.29), upon summation over the internal spin indices, ensure that the spin of each particle is conserved across the entire diagram, including both the ladders and the vertices in the radiative parts of the diagrams. With this, we find

$$\begin{aligned} i\mathcal{A}_T^{\rm SC} &= (-ig_1)\frac{i\bar{u}_1^{r_1'}(\eta_1 K + q)u_1^{r_1}(\eta_1 P + p)}{(\eta_1 P_\varphi + q - p)^2 - m_\varphi^2}\ (-i\rho_\varphi)\ \frac{i\bar{u}_2^{r_2'}(\eta_1 K + q)u_2^{r_2}(\eta_1 P + p)}{(\eta_2 P_\varphi - q + p)^2 - m_\varphi^2}(-ig_2) \\ &= \frac{-i4M\mu g_1 g_2\rho_\varphi}{[(\mathbf{q}-\mathbf{p})^2 + m_\varphi^2]^2}\ \delta^{r_1 r_1'}\,\delta^{r_2 r_2'}\,, \end{aligned} \tag{2.2.30}$$

where r_1, r_1' and r_2, r_2' are the spins of the incoming and outgoing X_1 and X_2 particles. Comparing eq. (2.2.30) to (2.2.14), we see that the ρ_φ contribution to $\mathcal{A}_T$ is larger by a factor 4 for a fermionic pair than for a scalar pair. However, taking into account that for fermions $\alpha_f = g_1 g_2/(4\pi)$, the full amplitude for fermions looks the same as the ρ_φ contribution to eq. (2.2.16), up to the spin conservation factors,

$$\mathcal{M}^{\rm SC}_{\mathbf{k}\to\{n\ell m\}} \simeq -\frac{M}{\mu}\left(\frac{\rho_\varphi}{\mu\alpha_f^2/2}\right)\sqrt{4\pi\alpha_f}\,\mathcal{R}_{\mathbf{k},\{n\ell m\}}\;\delta^{r_1 r_1'}\,\delta^{r_2 r_2'}\,, \tag{2.2.31}$$

where we used eqs. (2.1.15) and (2.2.4). Similarly, the contribution to the amplitude from the diagrams of fig. 2.2 is

$$\mathcal{M}^{\rm TC}_{\mathbf{k}\to\{nlm\}} \simeq -2M\sqrt{2\mu}\left[g_1\mathcal{I}_{\mathbf{k},\{n\ell m\}}(\eta_2\mathbf{P}_\varphi) + g_2\mathcal{I}_{\mathbf{k},\{n\ell m\}}(-\eta_1\mathbf{P}_\varphi)\right]\,\delta^{r_1 r_1'}\,\delta^{r_2 r_2'}\,, \tag{2.2.32}$$

where the extra factor 2 with respect to eq. (2.2.17) arises from the spinor contraction along the leg that contains the radiative vertex.

Cross-section for capture into the ground state

Upon squaring the amplitudes (2.2.31) and (2.2.32), summing over the final-state spins and averaging over the spin of the initial particles, the spin factors simply yield 1. Using eqs. (2.2.18) and (2.2.19) and the overlap integrals (2.2.9) and (2.2.10), we find the spin-averaged BSF1 cross-section to be

$$\begin{aligned}\sigma^{\rm tot}_{\rm BSF1} v_{\rm rel} \simeq{}& \frac{\alpha_f^2}{\mu^2}\,s_{ps}^{\rm BSF1}\left(\frac{\zeta^2}{1+\zeta^2}\right)^2 e^{-4\zeta\,\mathrm{arccot}\,\zeta}\\ &\times\left\{\alpha_f\left(\frac{\rho_\varphi}{\mu\alpha_f^2/2}\right)^2\left(\frac{\zeta^2}{1+\zeta^2}\right)S_0(\zeta,\xi) + \frac{2^6\pi}{3}\frac{(g_1\eta_2 - g_2\eta_1)^2}{4\pi\alpha_f}\frac{S_1(\zeta,\xi)}{(1+\zeta^2)}\right\}.\end{aligned} \tag{2.2.33}$$

As in the previous section, we shall now consider some specific cases.

Different fermion species

We consider again the limiting case $g_1 = g_2 \equiv g$ and $\eta_1 \gg \eta_2$. Equation (2.2.33) simplifies to

$$\begin{aligned}\sigma^{\rm tot}_{\rm BSF1} v_{\rm rel} \simeq{}& \frac{\alpha_f^2}{\mu^2}\,s_{ps}^{\rm BSF1}\left(\frac{\zeta^2}{1+\zeta^2}\right)^2 e^{-4\zeta\,\mathrm{arccot}\,\zeta}\\ &\times\left\{\alpha_f\left(\frac{\rho_\varphi}{\mu\alpha_f^2/2}\right)^2\left(\frac{\zeta^2}{1+\zeta^2}\right)S_0(\zeta,\xi) + \frac{2^6\pi}{3}\frac{S_1(\zeta,\xi)}{(1+\zeta^2)}\right\}.\end{aligned} \tag{2.2.34}$$

As in the case of scalar $X_{1,2}$, in the regime $m_\varphi < \mu v_{\rm rel} < \mu\alpha$ where the Coulomb approximation holds, $S_1 = (1+\zeta^2)S_0$, and both terms in eq. (2.2.34) scale as $\sigma v_{\rm rel} \propto 1/v_{\rm rel}$. For $\rho_\varphi \sim m_\varphi \lesssim \mu\alpha_f^2/2$, the s-wave term is subdominant for perturbative α_f. However, at lower velocities $v_{\rm rel} < m_\varphi/\mu$, the p-wave term dwindles and the ρ_φ contribution dominates.

Particle-antiparticle pair

For a particle-antiparticle pair, the p-wave contribution in eq. (2.2.33) vanishes, and the BSF cross-section becomes

$$\sigma^{\rm SC}_{\rm BSF1} v_{\rm rel} = \frac{\alpha_f^3}{\mu^2}\left(\frac{\rho_\varphi}{\mu\alpha_f^2/2}\right)^2 s_{ps}^{\rm BSF1}\times S_0(\zeta,\xi)\left(\frac{\zeta^2}{1+\zeta^2}\right)^3 e^{-4\zeta\,\mathrm{arccot}\,\zeta}\,. \tag{2.2.35}$$

We recall that there are also s- and d-wave contributions of higher order in α_f from the trilinear $\varphi X\bar{X}$ coupling alone. Comparing eq. (2.2.35) with eq. (2.1.21), we find that the ρ_φ term is more significant if

$$\frac{\rho_\varphi}{\mu\alpha_f^2/2} \gtrsim 2.4\sqrt{\alpha_f}\,. \tag{2.2.36}$$

Identical fermions

For a pair of identical fermions, the total wavefunction has to be antisymmetric in the interchange of the two particles. This implies that the spatial wavefunction depends on their total spin. A pair of identical spin-1/2 particles may be either in the antisymmetric spin-0 state, or in the symmetric spin-1 state. Their spatial wavefunction should then be symmetric or antisymmetric, respectively,

$$\text{fermions with total spin 0:} \qquad \left[\phi_{\mathbf{k}}(\mathbf{r}) + \phi_{-\mathbf{k}}(\mathbf{r})\right]/\sqrt{2}\,, \tag{2.2.37}$$

$$\text{fermions with total spin 1:} \qquad \left[\phi_{\mathbf{k}}(\mathbf{r}) - \phi_{-\mathbf{k}}(\mathbf{r})\right]/\sqrt{2}\,. \tag{2.2.38}$$

As for identical bosons, the wavefunction (2.2.37) implies that the contribution of the even-ℓ_S modes participating in a process is doubled with respect to the case of distinguishable particles, while the contribution of the odd-ℓ_S modes vanishes. The opposite holds for the wavefunction (2.2.38). Similarly, there are only $\ell =$ even bound states of two identical total-spin-0 fermions, and only $\ell =$ odd bound states of two identical total-spin-one fermions. Since eq. (2.2.35) is an s-wave process, the spin-averaged cross-section for capture of two identical fermions is half of that given in eq. (2.2.35), with the entire contribution arising from the spin-0 state.

2.2.4 Capture via emission of two scalar mediators

The scalar couplings appearing in eqs. (2.1.1) to (2.1.3) raise the possibility that the radiative part of the capture into bound states may carry a lower suppression in α if two mediators are emitted. On the other hand, the emission of two mediators, which share the available energy $\omega \simeq \mu(\alpha^2 + v_{\rm rel}^2)/2$, implies that the BSF2 cross-section picks up additional suppression in powers of α (for $\alpha > v_{\rm rel}$) due the phase space of the second mediator. To determine which diagrams may contribute significantly, we first work out the phase-space integration.

Phase-space integration

The cross-section for capture via emission of two mediators with momenta $\mathbf{P}_a$ and $\mathbf{P}_b$ is

$$d\sigma_{\rm BSF2} = \frac{1}{2E_1 2E_2 v_{\rm rel}} \frac{1}{2} \int \frac{d^3P}{(2\pi)^3 2P^0} \frac{d^3P_a}{(2\pi)^3 2P_a^0} \frac{d^3P_b}{(2\pi)^3 2P_b^0} \left|\mathcal{M}_{\mathbf{k}\to\{n\ell m\}}\right|^2 (2\pi)^4 \delta^4(K - P - P_a - P_b), \tag{2.2.39}$$

where the factor (1/2) is due to the two identical particles in the final state. We work in the CM frame, $\mathbf{K} = \mathbf{0}$, and use the three-momentum delta function to integrate over the momentum of the bound state $\mathbf{P} = -(\mathbf{P}_a + \mathbf{P}_b)$. The energy delta function yields the condition

$$\sqrt{\mathbf{P}_a^2 + m_\varphi^2} + \sqrt{\mathbf{P}_b^2 + m_\varphi^2} + \frac{\mathbf{P^2}}{2M} \simeq \epsilon_{n\ell} + \epsilon_{\mathbf{k}}. \tag{2.2.40}$$

For convenience, we define the dimensionless parameters

$$x_a = \frac{|\mathbf{P}_a|}{\epsilon_{n\ell} + \epsilon_{\mathbf{k}}}, \qquad x_b = \frac{|\mathbf{P}_b|}{\epsilon_{n\ell} + \epsilon_{\mathbf{k}}} \tag{2.2.41}$$

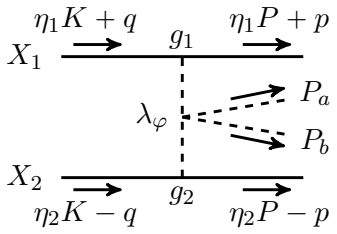

Figure 2.4: Capture via emission of two scalar mediators: the contribution of the mediator quartic self-coupling to the radiative amplitude.

and

$$\delta \equiv \frac{\epsilon_{n\ell} + \epsilon_{\mathbf{k}}}{2M}, \qquad d \equiv \frac{m_\varphi}{\epsilon_{n\ell} + \epsilon_{\mathbf{k}}}\,. \tag{2.2.42}$$

Then, combining energy and momentum conservation, we obtain the phase space condition for the momenta of the emitted scalars,

$$\sqrt{x_a^2 + d^2} + \sqrt{x_b^2 + d^2} + (x_a^2 + x_b^2 + 2x_a x_b \cos\theta_{ab})\delta = 1\,, \tag{2.2.43}$$

where θ_{ab} is the angle between $\mathbf{P}_a$ and $\mathbf{P}_b$. Because $\delta \ll 1$, the phase-space encompassed by eq. (2.2.43) extends on the $x_a - x_b$ plane essentially along the line

$$\sqrt{x_a^2 + d^2} + \sqrt{x_b^2 + d^2} = 1\,, \tag{2.2.44}$$

with $0 \leqslant x_a \leqslant \sqrt{1-2d}$, and a small width along the x_b direction, due to $\cos\theta_{ab}$ ranging in $[-1, 1]$. Note that for the capture process to be kinematically allowed, $2d < 1$. The x_b width can be estimated by differentiating eq. (2.2.43) with respect to x_b and $\cos\theta_{ab}$. We find

$$x_b^{\max} - x_b^{\min} \simeq 4x_a \left(1 - \sqrt{x_a^2 + d^2}\right)\delta\,. \tag{2.2.45}$$

For the diagrams of interest, the amplitude is independent of $\mathbf{P}_{a,b}$ (cf. section 2.2.4). Thus, putting everything together, eq. (2.2.39) yields

$$\sigma_{\rm BSF2} v_{\rm rel} \simeq \frac{(\epsilon_{n\ell} + \epsilon_{\mathbf{k}})^3}{2^8 3\pi^3 M^2 \mu}\ \left|\mathcal{M}_{\mathbf{k}\to\{n\ell m\}}\right|^2\ s_{ps}^{\rm BSF2}(d)\,, \tag{2.2.46}$$

where $s_{ps}^{\rm BSF2}$ is the phase-space suppression factor due to the kinematic threshold for BSF2,

$$s_{ps}^{\rm BSF2}(d) \equiv 6\int_0^{\sqrt{1-2d}} dx\ x^2\ \sqrt{\frac{1 + x^2 - 2\sqrt{x^2+d^2}}{x^2+d^2}}\,, \tag{2.2.47}$$

with $s_{ps}^{\rm BSF2} = 1$ for $d = 0$. Comparing eq. (2.2.46) with eq. (2.2.18), we observe that the BSF2 cross-section is proportional to two extra powers of the available energy to be dissipated, $\omega \simeq \epsilon_{n\ell} + \epsilon_{\mathbf{k}}$, with respect to BSF1, as expected from the phase-space element for the second mediator $d^3P_b/(2P_b^0) \propto \omega^2$. This implies an extra suppression by α^4 in the regime where BSF is important, $\alpha > v_{\rm rel}$. We also note the suppression of BSF2 with respect to BSF1 by the numerical factor $1/(2^4 3\pi^2) \simeq 2 \times 10^{-3}$.

Amplitude and cross-section

In figs. 2.4 to 2.6, we show various contributions to BSF2 arising from the mediator self-couplings and the mediator-DM quartic coupling for scalar DM. The diagram of fig. 2.4 yields the most important contribution. We shall first compute the cross-section arising from this diagram and then discuss why we neglect the other contributions.

The amplitude for the λ_φ contribution can be obtained from the second term in eq. (2.2.16) by replacing ρ_φ with λ_φ. Taking into account the discussion in section 2.2.3, we find it to be the same for both bosons and fermions,

$$\mathcal{M}^{\mathrm{SC}}_{\mathbf{k}\to\{n\ell m\}} \simeq \lambda_\varphi \sqrt{\frac{16\pi}{\alpha^3}\frac{M}{\mu^2}}\, \mathcal{R}_{\mathbf{k},\{n\ell m\}}\,, \tag{2.2.48}$$

where $\mathcal{R}_{\mathbf{k},\{n\ell m\}}$ is defined in eq. (2.2.4). From eqs. (2.2.9) and (2.2.46) we obtain the (spin-averaged) cross-section for capture into the ground state,

$$\sigma^{\mathrm{SC}}_{\mathrm{BSF2}} v_{\mathrm{rel}} \simeq f\, \frac{\lambda_\varphi^2 \alpha^3}{48\pi^2\mu^2}\, s_{ps}^{\mathrm{BSF2}}\, S_0 \left(\frac{\zeta^2}{1+\zeta^2}\right) e^{-4\zeta\, \mathrm{arccot}\,\zeta}\,, \tag{2.2.49}$$

where s_{ps}^{BSF2} and S_0 are given in eqs. (2.2.47) and (2.2.11) respectively. The factor f follows from the discussion in sections 2.2.2 and 2.2.3, with

$$f = \begin{cases} 1, & \text{distinguishable scalars,} \\ 2, & \text{identical scalars,} \\ 1/4, & \text{distinguishable fermions,} \\ 1/2, & \text{identical fermions.} \end{cases} \tag{2.2.50}$$

The cross-section (2.2.49) becomes comparable to the ρ_φ contribution to BSF1 computed in sections 2.2.2 and 2.2.3 for

$$\frac{\lambda_\varphi}{4\sqrt{3}\pi} \sim \frac{\rho_\varphi}{\mu\alpha^2/2}\,. \tag{2.2.51}$$

Comparing with the BSF1 contributions from the trilinear coupling alone (2.1.19) and (2.1.21), the λ_φ contribution to BSF2 is more significant for

$$\lambda_\varphi \gtrsim 10^2\sqrt{\alpha}\,. \tag{2.2.52}$$

The perturbativity of the couplings implies that the above condition may be meaningfully satisfied only for small coupling $\alpha \lesssim 10^{-3}$.

Other subdominant contributions

In figs. 2.5 and 2.6, we display various diagrams arising from ρ_φ and $\lambda_{j\varphi}$. Their contributions to BSF2 are subdominant compared to the contributions of the same couplings to BSF1 for reasonable choices of the parameters, as we discuss below. Since for phenomenological purposes, we are interested mostly in the total capture rate, we do not compute these contributions in detail.

Because part of the suppression arises from the phase space density of the second mediator (cf. section 2.2.4), we will consider directly the contributions of these diagrams to the cross-section rather than the amplitude, thus neglecting any cross-terms between different diagrams (except in the cases where there is a cancellation between them). It is straightforward to verify that the cross-terms do not alter our conclusions. We focus on particle-antiparticle or identical-particle pairs. Our comparisons refer to the regime $\alpha > v_{\mathrm{rel}}$ where BSF is important, setting aside the ζ-dependent factors that yield the same v_{rel} dependence between BSF1 and BSF2 in this regime.

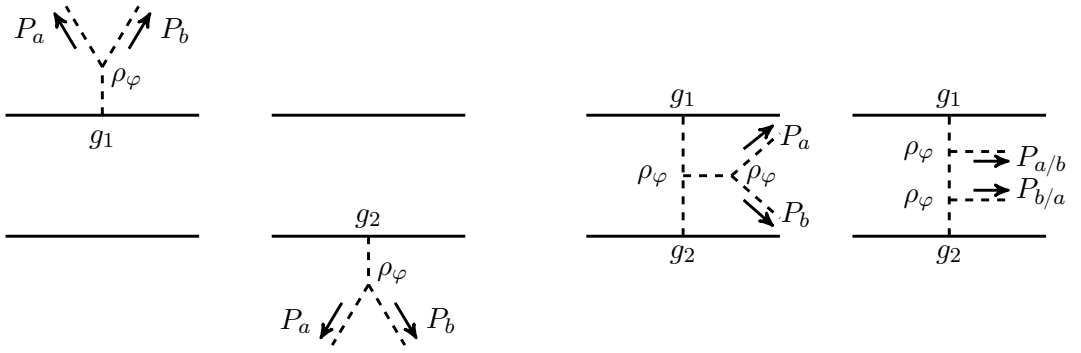

Figure 2.5: Capture via emission of two scalar mediators: the contributions of the mediator trilinear self-coupling to the radiative amplitude.

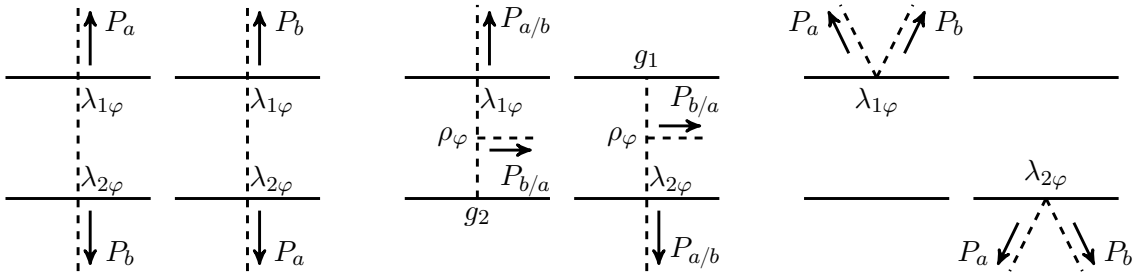

Figure 2.6: Capture via emission of two scalar mediators: the contribution of the quartic DM-mediator coupling to the radiative amplitude. These diagrams exist for scalar DM only.

- For particle-antiparticle or identical-particle pairs, the sum of the two diagrams on the left in fig. 2.5 suffers from the same cancellation as the diagrams of fig. 2.2 (cf. section 2.1.3). This introduces a α^4 suppression in the corresponding cross-section, while the phase-space density of the second emitted mediator implies an additional suppression by $(\mu\alpha^2/2)^2$ as discussed in section 2.2.4. These suppressions are balanced by the propagator of the off-shell mediator, which introduces a factor $\sim (P_a^0 + P_b^0)^{-4} \propto (\mu\alpha^2/2)^{-4}$. Thus, the contribution of these diagrams to the cross-section scales as $\sigma_{\text{BSF2}} v_{\text{rel}} \propto (\rho_\varphi/\mu)^2$. This is suppressed by α with respect to the ρ_φ contribution to BSF1, $\sigma_{\text{BSF1}} v_{\text{rel}} \propto (1/\alpha)(\rho_\varphi/\mu)^2$ [see e.g. eq. (2.2.35)], as well as by the numerical factor $\sim 2 \times 10^{-3}$ due to the three-body phase space.

- The third and forth diagrams in fig. 2.5 can be estimated starting from the ρ_φ contribution to BSF1 [cf. third diagram in fig. 2.3 and eq. (2.2.35)].

  For the third diagram, the off-shell mediator yields a factor $\propto (\mu\alpha^2/2)^{-4}$. Taking into account the phase-space suppression $\propto (\mu\alpha^2/2)^2$, we find that the contribution to the BSF2 cross-section scales as $\sigma_{\text{BSF2}} v_{\text{rel}} \propto (1/\alpha^5)(\rho_\varphi/\mu)^4$. Assuming that $\rho_\varphi \sim m_\varphi \lesssim \mu\alpha^2/4$ (cf. footnote 5), effectively this yields at best $\sigma_{\text{BSF2}} v_{\text{rel}} \propto \alpha^3$, similarly to the BSF1 cross-section (2.2.35). Still, the numerical suppression of BSF2 due to the three-body phase space ensures that the BSF2 contribution is subdominant to BSF1. However, if there is a large hierarchy between m_φ and ρ_φ with $\rho_\varphi \gg m_\varphi$, then the diagram under consideration may be significant.[6]

  For the forth diagram, the off-shell mediator between the two emitted scalars yields a

[6] We note that the three left diagrams in fig. 2.5 exhibit a collinear divergence at $m_\varphi \to 0$ that would have to be treated appropriately.

factor $\propto (\mu\alpha)^{-4}$. It follows that it is subdominant to the third diagram in fig. 2.5 and to the ρ_φ contribution to BSF1.

- For the two diagrams on the left in fig. 2.6, we start from the first term of eq. (2.2.23), replace one factor of α with $\lambda_{X\varphi}^2$ and introduce the phase-space suppression $\propto \alpha^4$. We obtain $\sigma_{\text{BSF2}} v_{\text{rel}} \propto \alpha^5 \lambda_{X\varphi}^4$.

- For the two middle diagrams in fig. 2.6, we start from the second term of eq. (2.2.23), replace one power of α with $\lambda_{X\varphi}^2$ and introduce the phase-space suppression $\propto \alpha^4$. We obtain $\sigma_{\text{BSF2}} v_{\text{rel}} \propto \alpha^2 \lambda_{X\varphi}^2 (\rho_\varphi/\mu)^2$, which is subdominant to the first term of eq. (2.2.23) for $\rho_\varphi \ll \mu$.

- The two diagrams on the right in fig. 2.6 suffer from the cancellations of the BSF1 diagrams of fig. 2.2. Replacing one factor of α with $\lambda_{X\varphi}^2$ results in the suppression $\lambda_{X\varphi}^2 \alpha^3$ for particle-antiparticle or identical-particle pairs. Introducing also the phase-space suppression yields $\sigma_{\text{BSF2}} v_{\text{rel}} \propto \lambda_{X\varphi}^2 \alpha^7$.

2.3 Conclusion

While the trilinear coupling determines the long-range interaction between the DM particles, it is not necessarily the only contributor to the radiative part of the transition. Quite generically, in theories with scalar mediators the couplings in the scalar potential also contribute. In the present chapter, we investigated the contribution of the mediator self-couplings, as well as the DM-mediator quartic coupling in the case of scalar DM, to the radiative capture into bound states. We considered capture both via one and two scalar mediator emission. Our main results include eqs. (2.2.22) and (2.2.23) for BSF1 by scalar particles, eqs. (2.2.34) and (2.2.35) for BSF1 by fermionic particles, and in eq. (2.2.49) for BSF2. We have found that the newly considered couplings can enhance or dominate the capture rate in sizeable parts of the parameter space, described in part by eqs. (2.2.24), (2.2.26), (2.2.36), (2.2.51) and (2.2.52).

Importantly, the new contributions are s-wave and remain significant even at very low velocities, thereby enhancing the radiative signals that can be probed in the indirect searches. This can potentially strengthen the resulting constraints. While models with light mediators and s-wave annihilation are severely constrained by the CMB and other indirect probes [44, 91, 92], models with p-wave annihilation – such as fermionic DM coupled to a scalar mediator – remain largely unconstrained. In this case, the formation and subsequent decay of unstable bound states offers a source of detectable indirect signals [52]. (Bremsstrahlung of dark mediators has also been invoked to lift the p-wave suppression [93].) Moreover, s-wave annihilation processes may lead to a period of reannihilation in the early universe, after DM kinetic decoupling [94].

Besides the signals produced from the decay of unstable bound states, the radiation emitted during the capture process is another source of indirect signals even in the case of stable bound states [95]. This is particularly important for asymmetric DM [96], whose annihilation signals are suppressed due to the asymmetry (albeit can still be significant due to the Sommerfeld effect [46]). Asymmetric DM, in turn, offers an excellent host of self-interacting DM, both because it allows for large couplings to light mediators, and it evades the indirect detection constraints, provided that the asymmetry is sufficiently large [47]. The enhanced radiative signals expected due to the contributions computed here can improve the prospects of probing asymmetric and self-interacting DM.

In this chapter, we focused on scalar mediators that do not carry any conserved charge. In chapter 3 we go one step forward in the model to and we study how the situation changes when a scalar mediator is charged under a low-energy symmetry.

Chapter 3

Bound state formation via emission of charged scalar mediator

As we studied in the previous chapter 2, for a particle-antiparticle pair or a pair of identical particles, the radiative capture via emission of a scalar boson is rather suppressed due to cancellations in the amplitude that reflect in part the angular momentum selection rules of the process (cf. section 3.1.2) [43, 73]. These cancellations concern the contributions to the radiative part of the amplitude that arise from the trilinear DM-DM-mediator coupling alone. The couplings of the scalar potential — the self-couplings of the mediator, as well as the biquadratic couplings between DM and the mediator if DM is bosonic — also contribute to the radiative amplitude and may enhance the capture cross-sections [1]. However for natural values of the parameters, the cross-sections remain mostly small. The radiative capture via emission of a scalar boson suppressed due to cancellations in the amplitude: (i) The lowest order s-wave contribution vanishes due to the orthogonality of the incoming and outgoing wavefunctions, thus abdicating the leading order to the p-wave. (ii) The leading order p-wave terms cancel for particle-antiparticle or identical-particle pairs, yielding to s- and d-wave contributions that are suppressed by higher orders in the coupling with respect to the capture via vector emission and possibly to the annihilation cross-section [43, 59, 73].

In this chapter we point out that the situation is markedly different if the emission of the scalar boson alters the potential between the interacting particles. This may occur if the scalar is charged under *either a local or a global* symmetry. As we shall see, in this case, the leading-order contributions to the amplitude are proportional to the overlap of the initial-state and final-state wavefunctions, which now are not orthogonal since they are subject to different potentials. The large overlap between the incoming and outgoing states gives rise to strikingly large BSF cross-sections. This is akin to atomic transitions precipitated by "sudden perturbations", such as ionisation caused by a beta decay of the nucleus [53].

To demonstrate the phenomenological importance of the transitions we consider, we calculate the chemical decoupling of DM in the early universe taking into account the formation of particle-antiparticle bound states via charged-scalar emission, and their subsequent decay into radiation. The formation of metastable bound states in the early universe has been shown to deplete the DM abundance [39], with the effect being generally more pronounced if the bound states have sizeable binding energy. Then, they form and decay efficiently already at high temperatures, when the DM density is large [39, 55, 62]. Here we find that, because of the largeness of the BSF cross-sections, shallow bound states can cause a second period of rapid DM depletion at low temperatures (of the order of their binding energy), much later than the traditional

freeze-out. This alters the predicted couplings of DM to other species very significantly, thereby affecting its observable signatures.

For simplicity, in the present work, we carry out our computations in an Abelian model with scalar DM that is singly-charged under a dark $U(1)_D$ gauge force and is coupled to a doubly-charged light scalar via a trilinear coupling. We shall not assume that the light scalar obtains a vacuum expectation value (VEV). Even in models where it does, our computation remains essentially valid, provided that the VEV of the scalar is not much larger than its mass. Then, if the scalar mediator is light enough to be emitted during BSF, its mass and VEV must be smaller than all other relevant scales, and the symmetry is only mildly broken. Our results are also readily applicable to non-Abelian models, whose dynamics in the unbroken phase can be reduced to the Abelian case by an appropriate decomposition of the representations of the interacting particles [97].

The chapter is organized as follows. In section 3.1, we introduce the model, compute the cross-sections for BSF via emission of a charged scalar, provide analytical results in the Coulomb limit for capture into *any* bound level, and discuss their features. We confront our results with partial-wave unitarity and discuss the resolution to its apparent violation where it occurs. In section 3.2, we consider the DM freeze-out in the presence of BSF via emission of a charged scalar, and show the effect on the DM relic density and predicted couplings. We conclude in section 3.4 with an outlook on the implications of our results.

3.1 Bound state formation via charged scalar emission

3.1.1 The model

We assume that DM consists of a complex scalar field X that couples to a dark Abelian gauge force $U(1)_D$ with V being the gauge boson, as well as to a light complex scalar Φ that is doubly charged under the same force. The interaction Lagrangian is

$$\begin{aligned}\mathcal{L} = &-\frac{1}{4}F_{\mu\nu}F^{\mu\nu} + (D_\mu X)^\dagger (D^\mu X) + (D_\mu \Phi)^\dagger (D^\mu \Phi) - m_X^2|X|^2 - m_\Phi^2|\Phi|^2 \\ &- \frac{y\, m_X}{2}\left(X^2\Phi^\dagger + {X^\dagger}^2\Phi\right) - \frac{\lambda_X}{4}|X|^4 - \frac{\lambda_\Phi}{4}|\Phi|^4 - \lambda_{X\Phi}|X|^2|\Phi|^2,\end{aligned} \tag{3.1.1}$$

with $F^{\mu\nu} \equiv \partial^\mu V^\nu - \partial^\nu V^\mu$ and $D_j^\mu \equiv \partial^\mu + \mathbb{i} q_j g V^\mu$, where the index j denotes the particle of charge q_j. The charges are $q_X = 1$ and $q_\Phi = 2$ for X and Φ fields respectively. The quartic terms stabilize the scalar potential at large field values. It is possible that the dark sector couples also to the SM, via biquadratic couplings of the scalars to the Higgs, and/or kinetic mixing of V with the Hypercharge gauge boson. Here we do not attempt a detailed phenomenological study of the model, but instead focus on computing the radiative capture into bound states via emission of a charged scalar, and simply showcasing its implications. We thus do not consider any couplings to the SM and do not derive any observational constraints.

We define the parameters that will appear in the non-relativistic potential,

$$\alpha_V \equiv \frac{g^2}{4\pi} \qquad \text{and} \qquad \alpha_\Phi \equiv \frac{y^2}{16\pi}\,. \tag{3.1.2}$$

For convenience, we also define the total mass M and the reduced mass μ of a pair of interacting particles; in our case $M = 2m_X$ and $\mu = m_X/2$.

We emphasise here that we are interested in $m_\Phi \ll m_X$. This hierarchy remains stable for momentum flows $Q < m_X$, which encompass the momentum transfer along the off-shell Φ bosons

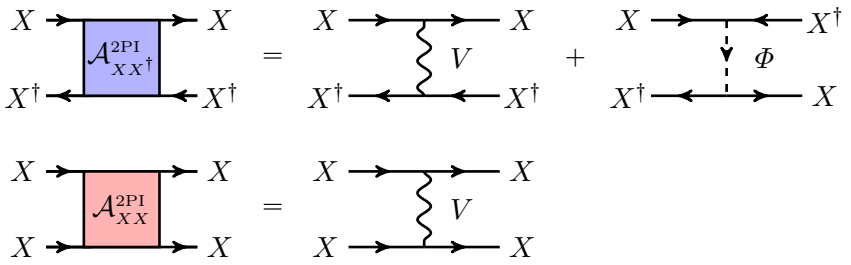

Figure 3.1: The 2PI diagrams contributing to the non-relativistic potential for $XX^\dagger$ pairs (upper) and XX or $X^\dagger X^\dagger$ pairs (lower). The arrows denote the flow of the $U(1)_D$ charge.

exchanged in the scattering and bound states (cf. section 3.1.1). At $Q \gtrsim m_X$, X loops generate corrections to the running mass of Φ, $\delta(m_\Phi^2) \propto \alpha_\Phi m_X^2$, that may far exceed its low-energy value. Seen from a high-energy perspective, this amounts to a near cancellation between the high-energy value of the running Φ mass and the running contribution. While this may be fine-tuned, the value of the running Φ mass at high energies does not affect our computations. Moreover, eq. (3.1.1) can be viewed as an effective theory valid below $\sim m_X$, that is potentially stabilised by additional physics at higher scales, such as supersymmetry.

Non-relativistic potential

The long-range potential of XX, $X^\dagger X^\dagger$ and $XX^\dagger$ pairs is generated by the one-boson-exchange diagrams shown in fig. 3.1. Because the Φ-exchange diagram for $XX^\dagger$ pairs is u-channel, the Φ-generated potential depends on the angular momentum mode of the eigenstate; we clarify this subtlety in appendix A.2. Combining this with well-known results for vector-mediated and scalar-mediated potentials [1, 43, 59], we obtain

$$V_{XX}(r) = V_{X^\dagger X^\dagger}(r) = +\frac{\alpha_V}{r}\,, \tag{3.1.3a}$$

$$V_{XX^\dagger}(r) = -\frac{\alpha_V}{r} - (-1)^\ell\,\frac{\alpha_\Phi}{r}\,e^{-m_\Phi r}\,, \tag{3.1.3b}$$

where α_V and α_Φ are defined in eq. (3.1.2). The potentials (3.1.3) distort the wavefunctions of pairs of unbound particles, a phenomenon known as the Sommerfeld effect [37, 38]. For $\alpha_V + (-1)^\ell \alpha_\Phi > 0$, they also give rise to $XX^\dagger$ bound states.[1]

Radiative capture processes

The capture of unbound particles into bound states can occur radiatively, via emission of a vector or scalar boson, according to the processes

$$X + X^\dagger \to \mathcal{B}(XX^\dagger) + V, \tag{3.1.4}$$

and

$$X + X \to \mathcal{B}(XX^\dagger) + \Phi, \tag{3.1.5a}$$

$$X^\dagger + X^\dagger \to \mathcal{B}(XX^\dagger) + \Phi^\dagger. \tag{3.1.5b}$$

[1] In fact, the condition for the existence of $XX^\dagger$ bound levels is somewhat more relaxed since the repulsive contribution to the potential (3.1.3b) arising from Φ exchange for ℓ odd is of finite range, while the attractive term is of infinite range.

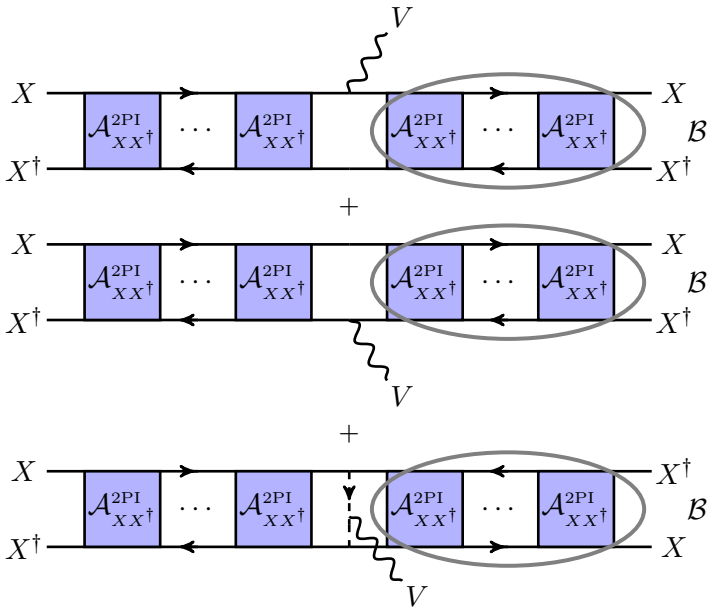

Figure 3.2: The capture into bound states via emission of a vector boson (BSF_V), $X + X^\dagger \to \mathcal{B}(XX^\dagger) + V$. While the bottom diagram appears to be naively of higher order, the momentum exchange along the two Φ propagators scales with the couplings, and renders this diagram of the same order as the two upper diagrams. We refer to appendix D.1 for the computation.

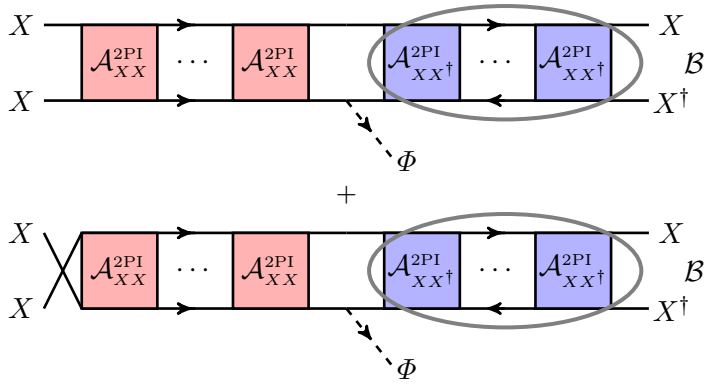

Figure 3.3: The capture into bound states via emission of a charged scalar (BSF_Φ), $X + X \to \mathcal{B}(XX^\dagger) + \Phi$. There is also the conjugate process, $X^\dagger + X^\dagger \to \mathcal{B}(XX^\dagger) + \Phi^\dagger$. The arrows denote the flow of the $U(1)_D$ charge. Note that in this case, the diagrams in which the incoming XX particles emit off-shell V and Φ that fuse to produce the final state Φ are of higher order, and we do not consider them here.

We shall refer to the processes (3.1.4) and (3.1.5) as BSF_V and BSF_Φ respectively. The leading order Feynman diagrams are shown in figs. 3.2 and 3.3.

BSF_V has been computed in [43, 59] (see [62] for non-Abelian generalisations), and a number of papers have considered its effects on the DM relic density [39, 46, 47, 55, 62, 98, 99] and indirect signals [40, 41, 44, 46, 47, 58, 98]. Here, the coupling of DM to the light scalar gives rise to an additional contribution to the BSF_V amplitude at leading order, shown in fig. 3.2. We review and adapt the computation of BSF_V to the present model in appendix D.1.

In the rest of this section, we focus on the BSF_Φ cross-sections.

Momentum decomposition and wavefunctions

We focus on the processes (3.1.5). For simplicity, in the following we neglect the mass of Φ, except in the phase-space integration. This will allow us to obtain analytical expressions for the BSF$_\Phi$ cross-sections, and gain important insight. Taking fully into account the mass of Φ (and potentially also a non-zero mass for V) requires computing the wavefunctions numerically, as done in [43] for a Yukawa potential and [54, 55] for mixed Coulomb and Yukawa potentials. In the Coulomb approximation, the XX, $X^\dagger X^\dagger$ scattering states and the $XX^\dagger$ bound states are governed respectively by the potentials

$$V_S = -\alpha_S/r \qquad \text{and} \qquad V_B = -\alpha_B/r, \tag{3.1.6}$$

with

$$\alpha_S = -\alpha_V, \qquad \alpha_B = \alpha_V + (-1)^\ell \alpha_\Phi. \tag{3.1.7}$$

The momentum assignments for the particles participating in BSF$_\Phi$ are shown in fig. 3.4. In order to separate the motion of the center-of-momentum from the relative motion in the scattering and bound states, we decompose the momenta as follows [59]

$$k_1^{(\prime)} \equiv K/2 + k^{(\prime)}, \qquad k_2^{(\prime)} \equiv K/2 - k^{(\prime)}, \tag{3.1.8a}$$

$$p_X \equiv P/2 + p, \qquad p_{X^\dagger} \equiv P/2 - p. \tag{3.1.8b}$$

Scattering states. In eq. (3.1.8a), the unprimed momenta correspond to infinite separation of XX, while the primed momenta denote the corresponding values in the XX wavepacket, which is distorted by the long-range interaction; this is the well-known Sommerfeld effect [37, 38]. It is easy to see from eq. (3.1.8a) that in the non-relativistic regime, $\mathbf{k} = \mu \mathbf{v}_{\rm rel}$, with $\mathbf{v}_{\rm rel}$ being the relative velocity of the incoming XX pair. The non-relativistic on-shell relations for k_1^0 and k_2^0 imply that the total energy of the scattering state is $K^0 \simeq M + \mathcal{E}_\mathbf{k} + \mathbf{K^2}/(2M)$, with $\mathcal{E}_\mathbf{k} = \mathbf{k^2}/(2\mu) = \mu v_{\rm rel}^2/2$. The scattering states are described by the wavefunctions $\phi_\mathbf{k}^{XX}(\mathbf{r})$ in position space and $\tilde{\phi}_\mathbf{k}^{XX}(\mathbf{k}')$ in momentum space; $\mathbf{k}$ is the expectation value of $\mathbf{k}'$. The wavefunctions $\phi_\mathbf{k}^{XX}(\mathbf{r})$ obey the Schrödinger equation with the potential (3.1.3a) and energy eigenvalue $\mathcal{E}_\mathbf{k}$.

Bound states. They are described by the wavefunctions $\psi_{n\ell m}^{XX^\dagger}(\mathbf{r})$ and $\tilde{\psi}_{n\ell m}^{XX^\dagger}(\mathbf{p})$ in position and momentum space respectively, where $n\ell m$ are the standard principal and angular momentum quantum numbers in a central potential that determine the expectation value of $\mathbf{p}$. The energy of the bound states is $P^0 \simeq M - |\mathcal{E}_n| + \mathbf{P^2}/(2M)$, where the binding energies can be parametrised as $\mathcal{E}_n = -\kappa_B^2/(2n^2\mu)$, with $\kappa_B \equiv \mu\alpha_B$ being the Bohr momentum of the system. Note that p_1^0 and p_2^0 do *not* obey on-shell relations individually. The wavefunctions $\psi_{n\ell m}^{XX^\dagger}(\mathbf{r})$ obey the Schrödinger equation with the potential (3.1.3b) and energy eigenvalue $\mathcal{E}_n$.

Hierarchy of scales. The emergence of non-perturbative phenomena – the Sommerfeld effect and the existence of bound states – is largely due to the different scales involved in the XX and $XX^\dagger$ scattering. For the scattering states and the bound states,

$$\mu v_{\rm rel}^2/2 \ll \mu v_{\rm rel} \ll \mu \lesssim M, \tag{3.1.9a}$$

$$\mu \alpha_B^2/(2n^2) \ll \mu\alpha_B/n \ll \mu \lesssim M, \tag{3.1.9b}$$

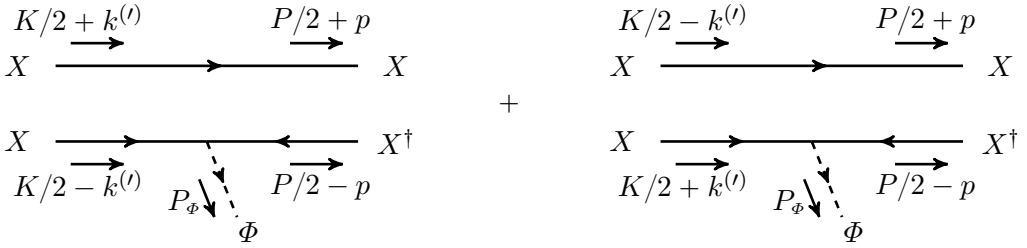

Figure 3.4: The radiative part of transitions via emission of a charged scalar, $XX \to XX^\dagger + \Phi$. The arrows on the field lines denote the flow of the $U(1)_D$ charge.

or equivalently,

$$\mathcal{E}_{\mathbf{k}} \ll |\mathbf{k}| \sim |\mathbf{k}'| \ll K^0 \tag{3.1.10a}$$

$$|\mathcal{E}_n| \ll \kappa_{\mathcal{B}}/n \sim |\mathbf{p}| \ll P^0 \tag{3.1.10b}$$

In our computations, we make approximations based on these hierarchies.

Energy-momentum conservation. Taking into account the above relations, the conservation of energy and momentum, $K = P + P_\Phi$, implies that Φ takes away the kinetic energy of the relative motion in the scattering state and the binding energy of the bound state [43, 59],

$$\sqrt{|\mathbf{P}_\Phi|^2 + m_\Phi^2} = \omega \equiv \mathcal{E}_{\mathbf{k}} - \mathcal{E}_n = \frac{\mathbf{k}^2 + \kappa_{\mathcal{B}}^2/n^2}{2\mu} = \frac{\mu}{2}(\alpha_{\mathcal{B}}^2/n^2 + v_{\rm rel}^2), \tag{3.1.11}$$

where we neglected the recoil of the bound state, as per (3.1.9). Equation (3.1.11) can be recast as $|\mathbf{P}_\Phi| = \omega\, s_{ps}^{1/2}$, with the phase-space suppression factor being

$$s_{ps} \equiv 1 - m_\Phi^2/\omega^2. \tag{3.1.12}$$

Parametrisation. Throughout, we shall thus assume and use the well-known analytical solutions for the energy eigenstates and eigenvalues in a Coulomb potential (see e.g. ref. [100]), which we review in appendix B. We discuss the range of validity of the Coulomb approximation in section 3.3, in the context of the phenomenological application of BSF_Φ on the DM freeze-out, that we present in section 3.2. In the Coulomb regime, we need the following two variables to parametrise the cross-sections in a minimal fashion [59],

$$\zeta_{\mathcal{S}} \equiv \alpha_{\mathcal{S}}/v_{\rm rel}, \qquad \zeta_{\mathcal{B}} \equiv \alpha_{\mathcal{B}}/v_{\rm rel}. \tag{3.1.13}$$

Taking the couplings (3.1.7) into account, $\zeta_{\mathcal{S}}$ and $\zeta_{\mathcal{B}}$ can be re-expressed in terms of

$$\zeta_V \equiv \alpha_V/v_{\rm rel}, \qquad \zeta_\Phi \equiv \alpha_\Phi/v_{\rm rel}. \tag{3.1.14}$$

Outside the Coulomb regime, the wavefunctions can be computed as in ref. [43] (see [54, 55] for results in a mixed Coulomb and Yukawa potential).

3.1.2 Amplitude

The amplitude for BSF_Φ is [59]

$$\text{i}\mathcal{M}^{\Phi}_{\mathbf{k}\to n\ell m} \simeq \int \frac{d^3\mathbf{k}'}{(2\pi)^3}\frac{d^3\mathbf{p}}{(2\pi)^3}\; \tilde{\phi}^{XX}_{\mathbf{k}}(\mathbf{k}')\; \text{i}\mathcal{A}^{\Phi}_T(\mathbf{k}',\mathbf{p})\; \frac{[\tilde{\psi}^{XX^\dagger}_{n\ell m}(\mathbf{p})]^*}{\sqrt{2\mu}}, \tag{3.1.15}$$

where the factor $1/\sqrt{2\mu}$ has arisen in switching from the relativistic to the non-relativistic normalisation for the fields participating in the bound state [59]. $\mathcal{A}_T^{\Phi}$ is the (amputated) amplitude of the radiative part of the process,

$$X(K/2+k')+X(K/2-k')\to X(P/2+p)+X^\dagger(P/2-p)+\Phi(P_\Phi), \tag{3.1.16}$$

where the parentheses denote the momenta of each field; K and P are the total 4-momenta of the XX scattering state and the $XX^\dagger$ bound state respectively. The leading order diagrams with the precise momentum assignments are shown in fig. 3.4. Because these diagrams are not fully connected, the virtuality of the $X, X^\dagger$ fields has to be integrated out as described in [59] (see [62] for a more recent summary). Adapting the result of [59], we find the leading order contributions to be

$$\mathbb{i}\mathcal{A}_T^{\Phi}(\mathbf{k}',\mathbf{p})\simeq -\mathbb{i}2y\,M\mu\,(2\pi)^3\left[\delta^3(\mathbf{k}'-\mathbf{p}+\mathbf{P}_\Phi/2)+\delta^3(\mathbf{k}'+\mathbf{p}-\mathbf{P}_\Phi/2)\right]. \tag{3.1.17}$$

Combining eqs. (3.1.15) and (3.1.17), Fourier transforming the wavefunctions, and taking into account that $\psi_{n\ell m}(-\mathbf{r})=(-1)^\ell\psi_{n\ell m}(\mathbf{r})$, we obtain

$$\mathbb{i}\mathcal{M}^{\Phi}_{\mathbf{k}\to n\ell m}\simeq -\mathbb{i}y\,M\sqrt{2\mu}\int d^3\mathbf{r}\;\phi^{XX}_{\mathbf{k}}(\mathbf{r})\;[\psi^{XX^\dagger}_{n\ell m}(\mathbf{r})]^*\left[e^{+\mathbb{i}\mathbf{P}_\Phi\cdot\mathbf{r}/2}+(-1)^\ell\,e^{-\mathbb{i}\mathbf{P}_\Phi\cdot\mathbf{r}/2}\right]. \tag{3.1.18}$$

Amplitudes of this type can be computed by expanding in powers of $\mathbf{P}_\Phi\cdot\mathbf{r}/2$ [43]. Indeed, the bound-state wavefunction is exponentially suppressed at $r\gtrsim n/\kappa_{\mathcal{B}}$. Moreover, the scattering state wavefunction oscillates at $r>1/k$. Thus the integrand is significant roughly only for $r\lesssim 1/\sqrt{\kappa_{\mathcal{B}}^2/n^2+\mathbf{k}^2}$. Taking eq. (3.1.11) into account, this implies $\mathbf{P}_\Phi\cdot\mathbf{r}/2\lesssim\sqrt{\kappa_{\mathcal{B}}^2/n^2+\mathbf{k}^2}/(4\mu)=\sqrt{\alpha_{\mathcal{B}}^2/n^2+v_{\rm rel}^2}/4\ll 1$. If the scattering and the bound states were subject to the same potential, the zeroth order term in this expansion would vanish due to the orthogonality of the wavefunctions.[2]

The essential point of our calculation is that because Φ carries away charge, the scattering and bound state wavefunctions are governed by different potentials and thus are not orthogonal.[3] Therefore, to lowest order, eq. (3.1.18) becomes

$$\mathbb{i}\mathcal{M}^{\Phi}_{\mathbf{k}\to n\ell m}\simeq -\mathbb{i}\,\delta_{\ell,\rm even}\,2yM\sqrt{2\mu}\int d^3\mathbf{r}\;\phi^{XX}_{\mathbf{k}}(\mathbf{r})\;[\psi^{XX^\dagger}_{n\ell m}(\mathbf{r})]^*. \tag{3.1.19}$$

Since the scattering state consists of a pair of identical bosons XX, the wavefunction is related to that of two distinguishable particles (DP), $\phi^{\rm DP}_{\mathbf{k}}(\mathbf{r})$, as follows

$$\phi^{XX}_{\mathbf{k}}(\mathbf{r})=\frac{\phi^{\rm DP}_{\mathbf{k}}(\mathbf{r})+\phi^{\rm DP}_{\mathbf{k}}(-\mathbf{r})}{\sqrt{2}}=\frac{\phi^{\rm DP}_{\mathbf{k}}(\mathbf{r})+\phi^{\rm DP}_{-\mathbf{k}}(\mathbf{r})}{\sqrt{2}}=\sqrt{2}\sum_{\ell_{\mathcal{S}}=\rm even}\phi^{\rm DP}_{\mathbf{k},\ell_{\mathcal{S}}}(\mathbf{r}), \tag{3.1.20}$$

[2] For two particles X_1, X_2 coupled to a light *neutral* scalar φ via $\delta\mathcal{L}=-y_jm_jX_j^\dagger X_j\varphi$, the amplitude for the formation of X_1X_2 bound states via φ emission is [43, 59]

$$\mathbb{i}\mathcal{M}_{\mathbf{k}\to n\ell m}\simeq -\mathbb{i}\,M\sqrt{2\mu}\int d^3\mathbf{r}\;\phi_{\mathbf{k}}(\mathbf{r})\,\psi^*_{n\ell m}(\mathbf{r})\left[y_1e^{-\mathbb{i}\eta_2\mathbf{P}_\Phi\cdot\mathbf{r}}+y_2e^{\mathbb{i}\eta_1\mathbf{P}_\Phi\cdot\mathbf{r}}\right],$$

with $\eta_{1,2}\equiv m_{1,2}/(m_1+m_2)$. In the $\mathbf{P}_\Phi\cdot\mathbf{r}$ expansion, the zeroth order terms vanish due to the orthogonality of the wavefunctions, and for $y_1=y_2$ and $m_1=m_2$ also the first order terms cancel with each other. Then, the dominant contributions arise from the $(\mathbf{P}_\Phi\cdot\mathbf{r})^2$ terms (plus corrections of the same order that have been omitted in the above expression). Note that the second cancellation indicates the angular momentum selection rule $\Delta\ell=$ even. Thus, for a particle-antiparticle pair or a pair of identical particles, the capture cross-section is suppressed and becomes phenomenologically important mostly for large couplings.

[3] While this is inevitable in an Abelian theory, in non-Abelian theories it is possible for a pair of particles to emit a charged boson without changing their combined representation. For example, because adj $\otimes$ adj $\supset$ adj, two particles each transforming in the adjoint representation of a group, can begin from a combined adjoint configuration, emit an adjoint boson and end up again in an adjoint combined state.

where $\phi^{\rm DP}_{\mathbf{k},\ell_{\mathcal{S}}}(\mathbf{r})$ denotes the $\ell_{\mathcal{S}}$ angular mode of $\phi^{\rm DP}_{\mathbf{k}}(\mathbf{r})$. We now define the overlap integral of wavefunctions of distinguishable particles[4]

$$\mathcal{R}_{\mathbf{k},n\ell m} \equiv \kappa_{\mathcal{B}}^{3/2} \int d^3r \; [\psi^{\rm DP}_{n\ell m}(\mathbf{r})]^* \, \phi^{\rm DP}_{\mathbf{k}}(\mathbf{r}), \tag{3.1.21}$$

for scattering and bound states that are subject to the potentials (3.1.6). We calculate $\mathcal{R}_{\mathbf{k},n\ell m}$ analytically in appendix C.2 (without specifying the couplings $\alpha_{\mathcal{S}}$ and $\alpha_{\mathcal{B}}$). The angular integration in eq. (3.1.21) imposes the selection rule

$$\ell_{\mathcal{S}} = \ell. \tag{3.1.22}$$

Then, collecting eqs. (3.1.19) to (3.1.22), we find

$$\mathcal{M}^{\Phi}_{\mathbf{k}\to n\ell m} \simeq -\frac{4y}{\alpha_{\mathcal{B}}^{3/2}} \frac{M}{\mu} \mathcal{R}_{\mathbf{k},n\ell m} \; \delta_{\ell,\rm even}. \tag{3.1.23}$$

We will use eq. (3.1.23) to compute the BSF$_{\Phi}$ cross-section in section 3.1.3. Before doing so, some clarifications are important.

For $\ell =$ odd, we must keep the first order terms in the $(\mathbf{P}_{\Phi}\cdot\mathbf{r})$ expansion of the integrand of eq. (3.1.18). Then the amplitude becomes non-vanishing for $\ell =$ odd, and is proportional to the overlap integral $\int d^3\mathbf{r}\,(\mathbf{P}_{\Phi}\cdot\mathbf{r})\,\phi^{XX}_{\mathbf{k}}(\mathbf{r})\;[\psi^{XX^\dagger}_{n\ell m}(\mathbf{r})]^*$, which imposes the selection rule $|\ell-\ell_{\mathcal{S}}|=1$. As per eq. (3.1.20), the scattering state wavefunction contains only modes $\ell_{\mathcal{S}} =$ even. Thus, this contribution survives, and yields a cross-section that is larger than BSF via emission of a neutral scalar (cf. footnote 2) and of the equivalent order as BSF via emission of a vector boson.[5]

Nevertheless, the cancellation of the zeroth order terms in $(\mathbf{P}_{\Phi}\cdot\mathbf{r})$ for odd ℓ is a particularity of the model we are considering here, rather than a generic feature of BSF via charged scalar emission. For example, in a (coannihilation) scenario where the two incoming particles transform under different representations of the underlying symmetry (i.e. in the $U(1)$ case, they have different charges), there in no generic cancellation between the contributing diagrams. Thus, to remain focused on the main point of our computation, we shall consider only the lowest order contributions given by eq. (3.1.19).

The result (3.1.23) should also make evident that for BSF$_{\Phi}$, the diagrams in which the final-state Φ is produced from the fusion of off-shell V and Φ emitted by the incoming XX pair, are subleading. Diagrams where the radiated boson is emitted from an off-shell propagator exchanged between the two interacting particles, are known to give leading-order contributions to BSF$_V$ [42]. However, as shown here, the diagrams of fig. 3.4 for BSF$_{\Phi}$ yield lower order contributions than the corresponding diagrams for BSF$_V$, where the vector-emission vertices introduce a momentum suppression in the wavefuntion overlap integral and thus in the amplitude (see appendix D.1 for more details). Thus, with respect to the diagrams of fig. 3.4, the Φ emission from $V\Phi$ fusion must be subleading; in fact, it turns out to be even of higher order than the corresponding diagrams in BSF$_V$, due to the different Lorentz structure of the vertices involved.

[4] In the notation of refs. [43, 59], this is the overlap integral $\mathcal{I}_{\mathbf{k},n\ell m}(\mathbf{b})$, evaluated at $\mathbf{b}=\mathbf{0}$ and up to the overall constant $\kappa_{\mathcal{B}}^{3/2}$, here introduced to make $\mathcal{R}_{\mathbf{k},n\ell m}$ dimensionless.

[5] For fermionic DM, we find that the $(\mathbf{P}_{\Phi}\cdot\mathbf{r})^0$ contributions would survive for $\ell+s+1=$ even, with $s=0$ or 1 being the total spin. However, the XX wavefunctions contain only $\ell_{\mathcal{S}}+s+1=$ odd modes. Given the $\ell_{\mathcal{S}}=\ell$ selection rule (3.1.22), these contributions cancel. The $(\mathbf{P}_{\Phi}\cdot\mathbf{r})^1$ contributions have the same fate: they would survive for $\ell+s+1=$ odd, however the selection rule now becomes $|\ell-\ell_{\mathcal{S}}|=1$. Since $\ell_{\mathcal{S}}+s+1=$ odd, these contributions cancel as well.

3.1.3 Cross Section

The cross-section times relative velocity for the BSF_Φ processes (3.1.5) is

$$\sigma^{\Phi}_{n\ell m} v_{\rm rel} = \frac{|\mathbf{P}_\Phi|}{2^6\pi^2 M^2 \mu} \int d\Omega \; |\mathcal{M}^{\Phi}_{\mathbf{k}\to n\ell m}|^2 \,, \tag{3.1.24}$$

where the momentum of the emitted scalar $\mathbf{P}_\Phi$ is given by eq. (3.1.11).

Collecting eqs. (3.1.11), (3.1.23), (3.1.24) and (C.2.6), we find for the capture cross-section,

$$\sigma^{\Phi}_{n\ell} v_{\rm rel} \equiv \sum_{m=-\ell}^{\ell} \sigma^{\Phi}_{n\ell m} v_{\rm rel}, \tag{3.1.25}$$

the following

$$\begin{aligned} \sigma^{\Phi}_{n\ell} v_{\rm rel} \simeq\; & s_{ps}^{1/2} \, \frac{\pi}{\mu^2} \frac{\alpha_\Phi}{\alpha_{\mathcal{B}}} \left(1 - \frac{\alpha_{\mathcal{S}}}{\alpha_{\mathcal{B}}}\right)^2 \, \delta_{\ell,\rm even} \, \frac{2^{4\ell+9}\, n^2}{2\ell+1} \frac{(n+\ell)!}{(n-\ell-1)!} \left[\frac{\ell!}{(2\ell)!}\right]^2 \\ & \times S_\ell(\zeta_{\mathcal{S}}) \left[\frac{(\zeta_{\mathcal{B}}^2/n^2)^{\ell+3}}{(1+\zeta_{\mathcal{B}}^2/n^2)^{2\ell+3}}\right] e^{-4\zeta_{\mathcal{S}} \,\mathrm{arccot}(\zeta_{\mathcal{B}}/n)} \\ & \times \left| {}_2F_1\left(1+\ell-n;\; 1+\ell+\mathbb{i}\zeta_{\mathcal{S}};\; 2\ell+2;\; \frac{4\mathbb{i}\zeta_{\mathcal{B}}/n}{(1+\mathbb{i}\zeta_{\mathcal{B}}/n)^2}\right)\right|^2 , \end{aligned} \tag{3.1.26}$$

where $S_\ell(\zeta_{\mathcal{S}})$ is the Sommerfeld factor for ℓ-wave processes [101],

$$S_\ell(\zeta_{\mathcal{S}}) = \frac{2\pi\zeta_{\mathcal{S}}}{1-e^{-2\pi\zeta_{\mathcal{S}}}} \prod_{j=1}^{\ell} \left(1 + \frac{\zeta_{\mathcal{S}}^2}{j^2}\right), \tag{3.1.27}$$

and in our model

$$\alpha_{\mathcal{S}} = -\alpha_V, \qquad \zeta_{\mathcal{S}} \equiv \alpha_{\mathcal{S}}/v_{\rm rel} = -\zeta_V, \tag{3.1.28a}$$

$$\alpha_{\mathcal{B}} = +\alpha_V + (-1)^\ell \alpha_\Phi, \qquad \zeta_{\mathcal{B}} \equiv \alpha_{\mathcal{B}}/v_{\rm rel} = +\zeta_V + (-1)^\ell \zeta_\Phi, \tag{3.1.28b}$$

with α_V and α_Φ defined in eq. (3.1.2). ${}_2F_1$ is the (ordinary) hypergeometric function, and s_{ps} is the phase-space suppression factor defined in eq. (3.1.12).

The cross-sections (3.1.26) is the main result of this section. They are readily generalisable to unbroken perturbative non-Abelian theories: as in ref. [62], the appropriate colour factors arising in the amplitudes (3.1.23) upon projection of the initial and final states onto states of definite colour must be included, $\alpha_{\mathcal{S}}$ and $\alpha_{\mathcal{B}}$ have to be chosen according to the initial and final colour representations [97], and the (anti)symmetrisation of the wavefunctions in the case of identical particles must be taken into account. Considering the couplings (3.1.28), we illustrate eq. (3.1.26) in figs. 3.5 and 3.6, and compare BSF_Φ with BSF_V [43, 59].

A few remarks are in order.

- The computed contribution (3.1.26) to the BSF cross-section vanishes if $\alpha_{\mathcal{B}} = \alpha_{\mathcal{S}}$, as expected from the orthogonality of the wavefunctions.

- The hypergeometric function in eq. (3.1.26) is a finite polynomial in its last argument (which can be also cast as $1 + e^{\mathbb{i}4\mathrm{arccot}(\zeta_{\mathcal{B}}/n)}$) because its first argument is a non-positive integer, $1+\ell-n \leqslant 0$. For $\ell = n-1$, this factor reduces to 1. For an arbitrary ℓ, it tends to 1 both at large and at small velocities ($\zeta_{\mathcal{B}}, |\zeta_{\mathcal{S}}| \ll 1$ and $\zeta_{\mathcal{B}}, |\zeta_{\mathcal{S}}| \gg 1$). At intermediate velocities, it gives rise to cancellations, as seen for example in fig. 3.5.

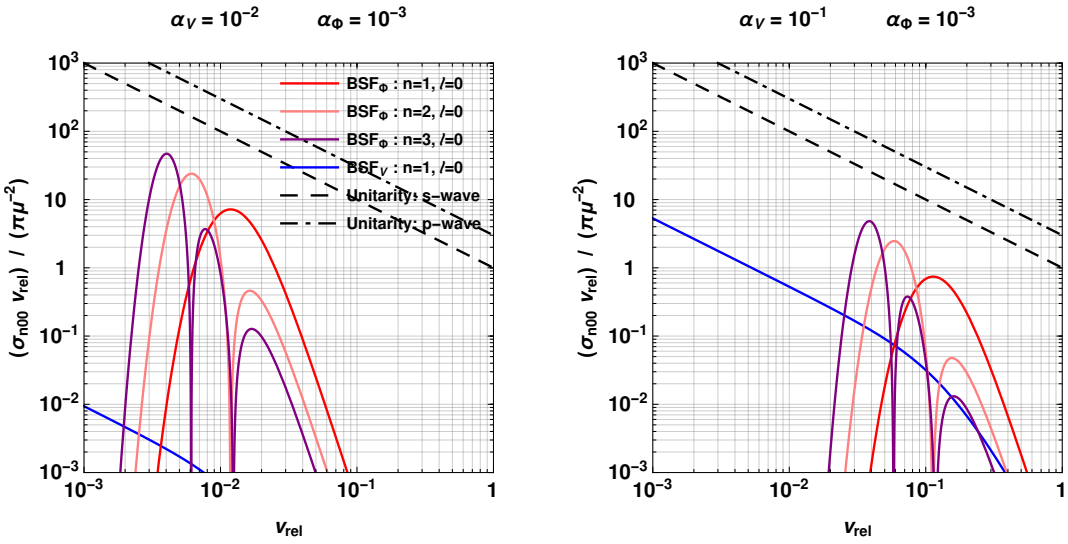

Figure 3.5: The velocity-weighted cross-section for capture into zero-angular momentum $XX^\dagger$ bound states, $n00$: $XX \to \mathcal{B}_{n00}(XX^\dagger) + \Phi$ for $n = 1, 2, 3$, and $XX^\dagger \to \mathcal{B}_{100}(XX^\dagger) + V$. For V emission, the capture into $n > 1$ states is subdominant to capture into $n = 1$ [43], and we do not show them here. Also shown are the s- and p-wave unitarity limits on inelastic cross-sections; for capture into $n00$, BSF$_\Phi$ is s-wave, while BSF$_V$ is p-wave. All cross-sections have been normalised to π/μ^2, with μ being the reduced mass of the interacting particles, and we have neglected any phase-space suppression due to the mass of Φ.

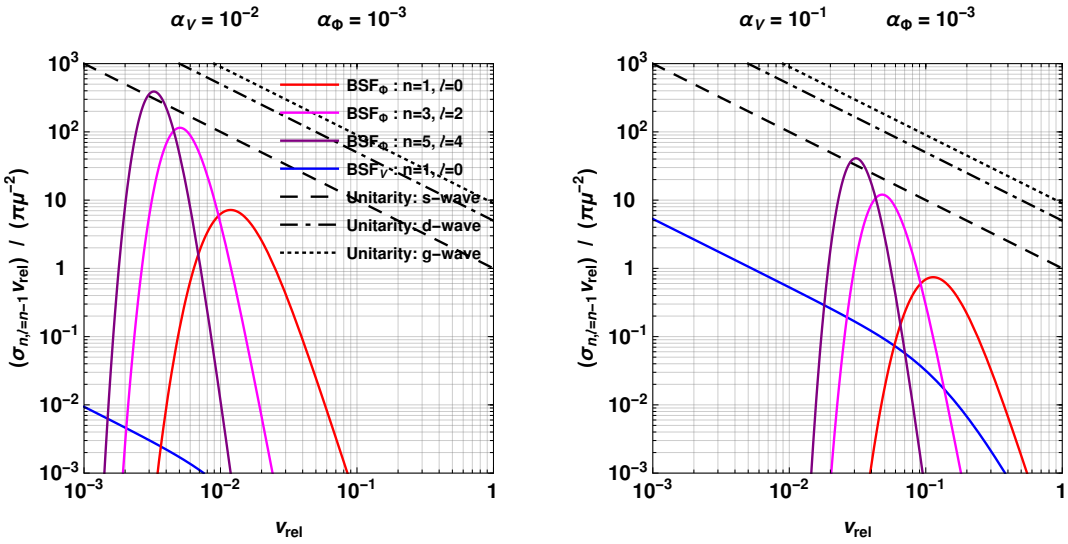

Figure 3.6: Same as in fig. 3.5, for capture into bound levels with $\ell = n - 1$, which have the highest multiplicity for a given n. We also show the respective unitarity limits for each process.

- At large velocities, $v_{\rm rel} \gg \alpha_{\mathcal{B}}/n = (\alpha_V + \alpha_\Phi)/n$ (i.e. $\zeta_{\mathcal{B}}/n \ll 1$), the overlap of the scattering and bound state wavefunctions is small, as seen from the term inside the square brackets in the second line of eq. (3.1.26). The BSF$_\Phi$ cross-sections are suppressed by $\zeta_{\mathcal{B}}^{2(\ell+3)} \ll 1$.
- At low velocities, $v_{\rm rel} \lesssim |\alpha_{\mathcal{S}}| = \alpha_V$ (i.e. $|\zeta_{\mathcal{S}}| \gtrsim 1$), the BSF$_\Phi$ cross-sections become sup-

pressed due to the repulsion in the scattering state, by the Sommerfeld factor $S_\ell(\zeta_{\mathcal{S}})$, with $\zeta_{\mathcal{S}} = -\zeta_V < 0$. The suppression becomes exponential at very low velocities $\zeta_{\mathcal{S}} \ll -1$.

- In between, the BSF_Φ cross-sections become very significant. While the velocity at which they peak depends on n, ℓ and the ratio $\alpha_{\mathcal{S}}/\alpha_{\mathcal{B}}$, it can be roughly approximated by $v_{\rm rel} \sim \alpha_{\mathcal{B}}/n = (\alpha_V + \alpha_\Phi)/n$, as seen in figs. 3.5 and 3.6.

- For $\zeta_{\mathcal{B}}/n = \alpha_{\mathcal{B}}/(n v_{\rm rel}) \gtrsim 1$, the factor in eq. (3.1.26) next to $S_\ell(\zeta_{\mathcal{S}})$ yields the characteristic behaviour $v_{\rm rel}^{2\ell}$ of ℓ-wave processes without Sommerfeld. Combined with $S_\ell(\zeta_{\mathcal{S}})$, we see that the velocity suppression of higher partial waves disappears, and all partial waves exhibit the velocity dependence of S_0.

Let us also now examine two different limits of eq. (3.1.26).

Limit $\boldsymbol{\alpha_V \to 0}$. In the limit of vanishing gauge coupling, the symmetry that is responsible for the dynamics we are considering becomes essentially global. This limit can be also effectively attained if the gauge boson has a very large mass $m_V \gg \mu\alpha_V$ such that it mediates a contact type interaction. In this case, V decouples from the low-energy effective theory, leaving a remnant unbroken global symmetry. In this regime, $\alpha_{\mathcal{B}} \to \alpha_\Phi$, $\zeta_{\mathcal{B}} \to \zeta_\Phi$ and $\alpha_{\mathcal{S}} \to 0$, $\zeta_{\mathcal{S}} \to 0$. Then, eq. (3.1.26) becomes

$$\sigma^{\Phi}_{n\ell} v_{\rm rel} \simeq s_{ps}^{1/2}\, \frac{\pi}{\mu^2}\, \delta_{\ell,\mathrm{even}}\, \frac{2^{4\ell+9} n^2}{2\ell+1} \frac{(n+\ell)!}{(n-\ell-1)!} \left[\frac{\ell!}{(2\ell)!}\right]^2 \times \left[\frac{(\zeta_\Phi^2/n^2)^{\ell+3}}{(1+\zeta_\Phi^2/n^2)^{2\ell+3}}\right] \times \left|{}_2F_1\left(1+\ell-n;\ 1+\ell;\ 2\ell+2;\ \frac{4\mathbb{i}\zeta_\Phi/n}{(1+\mathbb{i}\zeta_\Phi/n)^2}\right)\right|^2 . \tag{3.1.29}$$

Since there is now no repulsion in the scattering state, this cross-section is not exponentially suppressed at very low velocities. Nevertheless, because there is also no long-range attraction in the incoming state, the cross-section scales as $\sigma^{\Phi}_{n\ell} v_{\rm rel} \propto v_{\rm rel}^{2\ell}$ at $v_{\rm rel} \ll \alpha_{\mathcal{B}}/n$.

Limit $\boldsymbol{\alpha_V \gg \alpha_\Phi}$. In this regime, $\alpha_{\mathcal{B}} \to \alpha_V$, $\zeta_{\mathcal{B}} \to \zeta_V$. As always $\alpha_{\mathcal{S}} = -\alpha_V$, $\zeta_{\mathcal{S}} = -\zeta_V$. Then, eq. (3.1.26) becomes

$$\sigma^{\Phi}_{n\ell} v_{\rm rel} \simeq s_{ps}^{1/2}\, \frac{\pi(\alpha_\Phi/\alpha_V)}{\mu^2}\, \delta_{\ell,\mathrm{even}}\, \frac{2^{4\ell+11} n^2}{2\ell+1} \frac{(n+\ell)!}{(n-\ell-1)!} \left[\frac{\ell!}{(2\ell)!}\right]^2 S_\ell(-\zeta_V) \left[\frac{(\zeta_V^2/n^2)^{\ell+3}}{(1+\zeta_V^2/n^2)^{2\ell+3}}\right] \times e^{4\zeta_V \operatorname{arccot}(\zeta_V/n)} \left|{}_2F_1\left(1+\ell-n;\ 1+\ell-\mathbb{i}\zeta_V;\ 2\ell+2;\ \frac{4\mathbb{i}\zeta_V/n}{(1+\mathbb{i}\zeta_V/n)^2}\right)\right|^2 . \tag{3.1.30}$$

Despite the very small α_Φ, this can exceed the BSF_V cross-section for a significant velocity range, as seen in figs. 3.5 and 3.6.

Capture via scattering

While in this work we focus on radiative BSF, it is possible that the dissipation of energy necessary for the capture into bound states occurs via scattering on other particles through exchange of an off-shell mediator, if the mediator couples also to other light degrees of freedom. Although of higher order, such processes can be extremely efficient inside a relativistic thermal bath, where the density of the light particles is very high, as was recently shown in [102] and previously suggested in [61, 65, 103].

Reference [102] found that the rate of capture via scattering factorises into the radiative cross-section (albeit without any phase-space suppression due to the mass of the emitted scalar),

times a part that includes the kinematics and dynamics of the bath particles. The cross-sections (3.1.26) can then be recast to calculate BSF via off-shell exchange of a charged scalar. A corollary of this and the largeness of the radiative cross-sections (3.1.26) is that the corresponding bath scattering processes must also be very significant in the early universe in the presence of light relativistic particles coupled to the charged scalar. In the case of an unbroken or mildly broken gauge symmetry, the gauge bosons and charged scalars already provide the relativistic bath necessary for such scattering processes to occur, $XX + V \to \mathcal{B}(XX^\dagger) + \Phi$ and $XX + \Phi^\dagger \to \mathcal{B}(XX^\dagger) + V$.

In contrast to the radiative capture, BSF via bath scattering is not kinematically blocked if the mediator mass is larger than the energy available to be dissipated [cf. eq. (3.1.11)]. This implies that bound-state effects are not only enhanced, but also relevant to a broader parameter space.

3.1.4 Partial wave unitarity

The unitarity of the S matrix implies an upper bound on the partial wave inelastic cross-section [104]

$$\sigma^{(J)}_{\rm inel} v_{\rm rel} \leqslant \sigma^{(J)}_{\rm uni} v_{\rm rel} = \frac{\pi(2J+1)}{\mu^2 v_{\rm rel}}, \tag{3.1.31}$$

where J denotes the partial wave of the scattering state wavefunction that participates in the process. For BSF$_\Phi$, this is the same as that of the bound state formed, thus we consider the ratio

$$\sigma^{\Phi}_{n\ell}/\sigma^{(\ell)}_{\rm uni} = \alpha_\Phi \times \tilde{f}_{n\ell}(\zeta_{\mathcal{S}}, \zeta_{\mathcal{B}})\, \delta_{\ell,\rm even}, \tag{3.1.32}$$

with

$$\tilde{f}_{n\ell}(\zeta_{\mathcal{S}}, \zeta_{\mathcal{B}}) \equiv \frac{2^{4\ell+9}\, n^2\, (n+\ell)!}{(n-\ell-1)!} \left[\frac{\ell!}{(2\ell+1)!}\right]^2 \left(1 - \frac{\zeta_{\mathcal{S}}}{\zeta_{\mathcal{B}}}\right)^2 \frac{S_\ell(\zeta_{\mathcal{S}})}{\zeta_{\mathcal{B}}} \left[\frac{(\zeta^2_{\mathcal{B}}/n^2)^{\ell+3}}{(1+\zeta^2_{\mathcal{B}}/n^2)^{2\ell+3}}\right] \times e^{-4\zeta_{\mathcal{S}} \operatorname{arccot}(\zeta_{\mathcal{B}}/n)} \left|{}_2F_1\left(1+\ell-n;\ 1+\ell+\mathbb{i}\zeta_{\mathcal{S}};\ 2\ell+2;\ \frac{4\mathbb{i}\zeta_{\mathcal{B}}/n}{(1+\mathbb{i}\zeta_{\mathcal{B}}/n)^2}\right)\right|^2, \tag{3.1.33}$$

where we have neglected the phase-space suppression factor $s_{ps}^{1/2}$. As $v_{\rm rel}$ varies, $\zeta_{\mathcal{S}}$ and $\zeta_{\mathcal{B}}$ scan a range of values, but the ratio $r \equiv \zeta_{\mathcal{S}}/\zeta_{\mathcal{B}}$ of course remains constant (neglecting the possible running of the coupling, which may render $\alpha_{\mathcal{S}}$ mildly dependent on $v_{\rm rel}$). Unitarity must be respected for all $v_{\rm rel}$. We thus define

$$f_{n\ell;r}(\zeta_{\mathcal{B}}) \equiv \tilde{f}_{n\ell}(r\,\zeta_{\mathcal{B}}, \zeta_{\mathcal{B}}). \tag{3.1.34}$$

Then eq. (3.1.32) implies that unitarity is respected provided that α_Φ is sufficiently small,

$$\alpha_\Phi < 1/\max[f_{nl;r}(\zeta_{\mathcal{B}})], \tag{3.1.35}$$

where $f_{nl;r}$ is maximized with respect to $\zeta_{\mathcal{B}}$. (Note that $\zeta_{\mathcal{B}} > 0$ always for bound states to exist.)

In fig. 3.7, we present $f_{n\ell;r}(\zeta_{\mathcal{B}})$ vs. $\zeta_{\mathcal{B}}$ for $n = 1, \ell = 0$ and various values of r. In the present model, $r = -\alpha_V/(\alpha_V + \alpha_\Phi) \in [-1, 0]$. However, in any model where transitions of the type considered here occur, the BSF amplitudes will be proportional to the overlap integrals (3.1.21), and the cross-sections will be similar to eq. (3.1.26), up to a possible numerical factor. Thus, to get a broader insight into the implications of unitarity, in fig. 3.7 we consider a wider range of r values. As seen, $f_{n\ell;r}$ is bounded from above; this remains true for all n, ℓ. It is then

indeed possible to find a maximum value for α_Φ, below which our calculation is consistent with unitarity, but above which it evidently fails. We determine this numerically and present it in fig. 3.8. Notably, for $\alpha_\mathcal{S}/\alpha_\mathcal{B} < 0$, our computation fails already at rather small values of α_Φ. This is a consequence of the very large overlap between the initial and final states. The high peak of the BSF_Φ cross-sections at $v_{\mathrm{rel}} \sim \alpha_\mathcal{B}/n$, explained in section 3.1.3, results in a rather stringent upper bound on α_Φ.

What is the underlying reason for this apparent violation of unitarity, and how can unitarity be restored in the computation of the BSF_Φ cross-sections? At such low values of α_Φ it is unlikely that higher order corrections to the perturbative part of the amplitude $\mathcal{A}_T^\Phi$ [cf. eq. (3.1.17)] may have any significant effect on the cross-section. Moreover, it has been pointed out that the breakdown of unitarity in perturbative calculations at low energies suggests that the two-particle interactions at infinity must be resummed [46, section 5]. In our computation, this has been done at leading order, by the resummation of the one-boson exchange diagrams of fig. 3.1 that give rise to the potentials (3.1.3). However, by the optical theorem, all the inelastic processes to which the two interacting particles may participate also contribute to the self-energy of this two-particle state. Such contributions are typically neglected because they are of higher order than the one-boson exchange diagrams, and give rise to shorter-range (or contact) potentials that may have only limited impact on the large-distance behaviour of the wavefunctions. Still, the fact that the BSF_Φ cross-sections can become so large suggests that their contribution to the two-particle self-energy may be significant, thus it must be resummed. The effect of this resummation will likely be significant mostly for incoming momenta around the peak of the BSF_Φ cross-sections, k_{peak}. While the corrected BSF_Φ cross-sections should be consistent with unitarity, we expect them to remain very significant for $k \sim k_{\mathrm{peak}}$, and essentially unaffected for $k \gg k_{\mathrm{peak}}$ and $k \ll k_{\mathrm{peak}}$. Therefore, we still expect significant phenomenological implications. We leave this computation for future work.

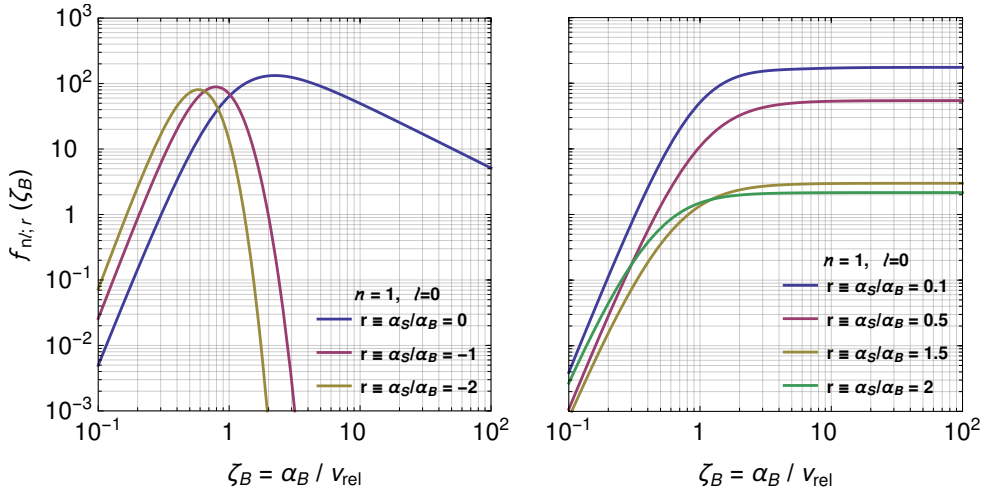

Figure 3.7: $f_{n\ell;r} \equiv \alpha_\Phi^{-1}(\sigma^\Phi_{n\ell}/\sigma^{(\ell)}_{\rm uni})$ vs $\zeta_\mathcal{B} \equiv \alpha_\mathcal{B}/v_{\rm rel}$, for $n = 1, \ell = 0$ and various values of $r \equiv \alpha_\mathcal{S}/\alpha_\mathcal{B}$. The coupling α_Φ must be sufficiently small, $\alpha_\Phi < \max(f_{n\ell;r})$, such that unitarity is respected for all velocities. This is possible because $f_{n\ell;r}$ is bounded from above.

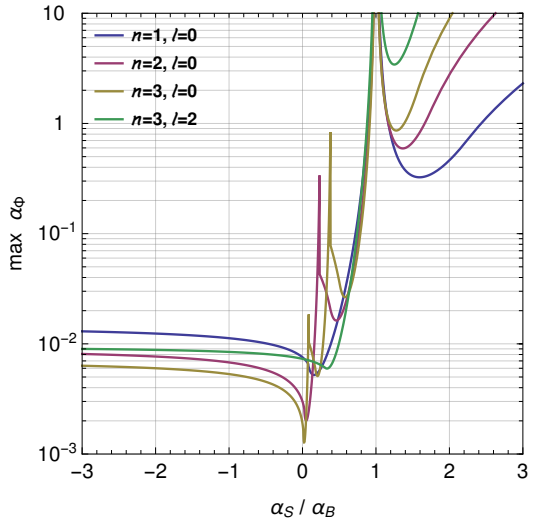

Figure 3.8: The maximum value of α_Φ vs. $r \equiv \alpha_\mathcal{S}/\alpha_\mathcal{B}$, for which the BSF$_\Phi$ cross-sections (3.1.26) remain below the unitarity limit for all velocities. In the model considered in this work $r = -\alpha_V/(\alpha_V + \alpha_\Phi)$, thus $-1 \leqslant r \leqslant 0$.

3.2 Freeze out of thermal relic dark matter

To showcase the phenomenological applications of the above, we consider the effect of BSF$_\Phi$ on the density of thermal-relic DM. Below, we list the pertinent cross-sections and rates, and present the Boltzmann equations that govern the evolution of the unbound and bound DM particle densities. We then describe how freeze-out is modified due to BSF$_\Phi$, and compute the couplings that reproduce the observed DM density. For simplicity, we assume that the DM particles and the radiation to which they couple are at the same temperature as the SM plasma, and use the standard time parameter

$$x = m_X/T. \tag{3.2.1}$$

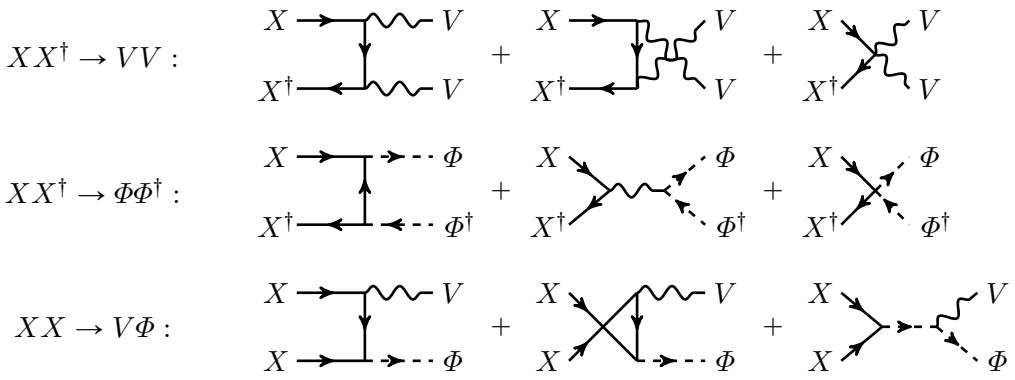

Figure 3.9a: The tree level diagrams contributing to the annihilation of $XX^\dagger$, XX and $X^\dagger X^\dagger$ pairs. Note that for the $XX^\dagger \to VV$ and $XX \to \Phi V$ annihilation processes, there are both t- and u-channel diagrams. In contrast, there is no u-channel diagram for $XX^\dagger \to \Phi\Phi^\dagger$. The arrows denote the flow of the $U(1)_D$ charge.

Figure 3.9b: The long-range interaction affects the rate of the annihilation processes, and necessitates the resummation of the 2PI interactions at infinity. The 2PI kernels are shown in fig. 3.1. The black blob stands for the tree-level annihilation diagrams of fig. 3.9a.

The generalisation to different dark sector and SM temperatures is straightforward, see e.g. [47].

3.2.1 Interaction rates

Annihilation

The tree-level annihilation channels for XX, $X^\dagger X^\dagger$ and $XX^\dagger$ pairs are shown in fig. 3.9a. The annihilation processes are affected by the Sommerfeld effect as depicted in fig. 3.9b. We consider only s-wave contributions, at leading order in each coupling and zeroth order in $v_{\rm rel}$. The full velocity-weighted cross-sections are

$$\sigma_{XX^\dagger \to VV}\, v_{\rm rel} \simeq \frac{2\pi\alpha_V^2}{m_X^2}\, S_0(\zeta_V + \zeta_\Phi), \tag{3.2.2a}$$

$$\sigma_{XX^\dagger \to \Phi\Phi^\dagger}\, v_{\rm rel} \simeq \frac{2\pi[\alpha_\Phi - \lambda_{X\Phi}/(8\pi)]^2}{m_X^2}\, S_0(\zeta_V + \zeta_\Phi), \tag{3.2.2b}$$

$$\sigma_{XX \to \Phi V}\, v_{\rm rel} = \sigma_{X^\dagger X^\dagger \to \Phi^\dagger V}\, v_{\rm rel} \simeq 0, \tag{3.2.2c}$$

where we recall that $\zeta_V \equiv \alpha_V/v_{\rm rel}$ and $\zeta_\Phi = \alpha_\Phi/v_{\rm rel}$, and $S_0(\zeta_\mathcal{S}) \equiv 2\pi\zeta_\mathcal{S}/(1 - e^{-2\pi\zeta_\mathcal{S}})$ is the s-wave Sommerfeld factor [cf. eqs. (3.1.14) and (3.1.27)]. Note that the cross-section (3.2.2a) for $XX^\dagger \to VV$ is twice as large as the spin-averaged cross-section for the annihilation of a fermionic particle-antiparticle pair into two Abelian vector bosons [39, 43]. For the $XX^\dagger \to \Phi\Phi^\dagger$ annihilation, the s-channel diagram (annihilation via off-shell V) is p-wave and we have neglected it in eq. (3.2.2b). For simplicity, in the following we shall also ignore the $\lambda_{X\Phi}$ contribution. This coupling does not affect BSF_Φ, and ignoring it will allow us to compare more easily the strength of the processes that arise from the essential couplings of the model, α_Φ and α_V.

Thus, the total velocity-weighted annihilation cross-section we will consider is

$$\sigma_{\rm ann} v_{\rm rel} \simeq \frac{2\pi(\alpha_V^2+\alpha_\Phi^2)}{m_X^2}\, S_0(\zeta_V+\zeta_\Phi), \tag{3.2.3}$$

with its thermal average being

$$\langle \sigma_{\rm ann} v_{\rm rel}\rangle = \frac{x^{3/2}}{2\sqrt{\pi}} \int_0^\infty dv_{\rm rel}\, v_{\rm rel}^2\, (\sigma_{\rm ann} v_{\rm rel})\, e^{-x v_{\rm rel}^2/4}. \tag{3.2.4}$$

Bound-state formation, ionisation and decay

Formation

As already discussed, $XX^\dagger$ bound states can form via emission of a V or a Φ boson, according to the processes (3.1.4) and (3.1.5), with the Feynman diagrams shown in figs. 3.2 and 3.3. For simplicity, we shall consider the capture into the ground state only, $n=1, \ell=m=0$, for both BSF_V and BSF_Φ. The larger binding energy and decay rate of the ground state render the ionisation processes unimportant earlier on, and imply that the capture into the ground state has a higher efficiency in depleting DM than the other BSF processes. Moreover, for BSF_V, the capture into the ground state is the dominant contribution [43, fig. 2]. On the other hand, for BSF_Φ, the rate of capture into excited states may exceed that of capture into the ground state in some velocity range, as seen in figs. 3.5 and 3.6. While we do expect that the capture into excited states plays an important role, here we only aim at showcasing the effect of BSF via emission of a charged scalar. We leave more detailed phenomenological studies for future work.

The effect of BSF_V on the DM relic density was shown in [39], in a setup where V was the sole mediator; the corresponding cross-sections have been computed in [43, 59, 62]. In appendix D.1, we review the computation and adapt it to the present model.

Taking the above into account, the BSF cross-sections we will consider are

$$\begin{aligned}\sigma_{100}^V v_{\rm rel} = {}& \frac{2^9\pi}{3m_X^2}\, \alpha_V(\alpha_V+\alpha_\Phi)\, \left(1+\frac{2\alpha_\Phi}{\alpha_V+\alpha_\Phi}\right)^2 \times \\ & \times S_0(\zeta_V-\zeta_\Phi)\,[1+(\zeta_V-\zeta_\Phi)^2]\, \frac{(\zeta_V+\zeta_\Phi)^4}{[1+(\zeta_V+\zeta_\Phi)^2]^3}\, e^{-4(\zeta_V-\zeta_\Phi)\text{arccot}(\zeta_V+\zeta_\Phi)}, \end{aligned} \tag{3.2.5a}$$

$$\sigma_{100}^\Phi v_{\rm rel} \simeq \frac{2^{11}\pi}{m_X^2}\, \frac{\alpha_\Phi(2\alpha_V+\alpha_\Phi)^2}{(\alpha_V+\alpha_\Phi)^3}\, S_0(-\zeta_V)\, \left[\frac{(\zeta_V+\zeta_\Phi)^2}{1+(\zeta_V+\zeta_\Phi)^2}\right]^3 e^{4\zeta_V\,\text{arccot}(\zeta_V+\zeta_\Phi)}, \tag{3.2.5b}$$

where $S_0(\zeta_{\mathcal{S}}) \equiv 2\pi\zeta_{\mathcal{S}}/(1-e^{-2\pi\zeta_{\mathcal{S}}})$ is the s-wave Sommerfeld factor [cf. eq. (3.1.27)], and we neglect any phase-space suppression due to the mass of the Φ (cf. section 3.3). The total BSF cross-section is then

$$\sigma_{\rm BSF} v_{\rm rel} = \sigma_{100}^\Phi v_{\rm rel} + \sigma_{100}^V v_{\rm rel}. \tag{3.2.6}$$

The thermally averaged BSF cross-section is

$$\langle \sigma_{\rm BSF} v_{\rm rel}\rangle = \frac{x^{3/2}}{2\sqrt{\pi}} \int_0^\infty dv_{\rm rel}\, v_{\rm rel}^2 (\sigma_{\rm BSF} v_{\rm rel}) e^{-x v_{\rm rel}^2/4} \left(1+\frac{1}{e^{x[v_{\rm rel}^2+(\alpha_V+\alpha_\Phi)^2]/4}-1}\right), \tag{3.2.7}$$

where the last factor accounts for the Bose enhancement due to the low-energy boson (V or Φ) emitted in the capture process; including the Bose enhancement is necessary in order to ensure detailed balance at large temperatures [39].

Ionization

The ionisation rate of the bound states can be found either by using the Milne relation between the capture and ionization cross-sections (see [62, appendix D] for the proof), or more directly, by invoking detailed balance,

$$\Gamma_{\mathcal{B}}^{\rm ion} = \langle \sigma_{\rm BSF} v_{\rm rel} \rangle \times (n_X^{\rm eq})^2 / n_{\mathcal{B}}^{\rm eq} = \langle \sigma_{\rm BSF} v_{\rm rel} \rangle \times s (Y_X^{\rm eq})^2 / Y_{\mathcal{B}}^{\rm eq}, \tag{3.2.8}$$

where s is the entropy density of the universe, and the equilibrium yields of the unbound particles and the bound states, $Y_X^{\rm eq} \equiv n_X^{\rm eq}/s$ and $Y_{\mathcal{B}}^{\rm eq} \equiv n_{\mathcal{B}}^{\rm eq}/s$, are given in section 3.2.2 below. Using these densities, we obtain

$$\Gamma_{\mathcal{B}}^{\rm ion} \simeq \langle \sigma_{\rm BSF} v_{\rm rel} \rangle \left(\frac{m_X T}{4\pi} \right)^{3/2} \, e^{-|\mathcal{E}_{\mathcal{B}}|/T}, \tag{3.2.9}$$

where $\mathcal{E}_{\mathcal{B}} = \mathcal{E}_{10}$ is the binding energy of the ground state.

Decay into radiation

The dominant decays of the ground state are

$$\mathcal{B}_{100}(XX^\dagger) \to VV, \; \Phi\Phi^\dagger, \tag{3.2.10}$$

with total rate

$$\Gamma_{\mathcal{B}}^{\rm dec} \simeq |\psi_{100}^{XX^\dagger}(0)|^2 (\sigma_{\rm ann} v_{\rm rel})_0^{\rm pert} \tag{3.2.11}$$

where $(\sigma_{\rm ann} v_{\rm rel})_0^{\rm pert}$ is the perturbative s-wave velocity-weighted annihilation cross-section (to zeroth order in $v_{\rm rel}$), which is contained in eq. (3.2.3). Then,

$$\Gamma_{\mathcal{B}}^{\rm dec} \simeq \frac{m_X^3 (\alpha_V + \alpha_\Phi)^3}{2^3 \pi} \left(\frac{2\pi\alpha_V^2}{m_X^2} + \frac{2\pi\alpha_\Phi^2}{m_X^2} \right) = \frac{m_X}{4} (\alpha_V + \alpha_\Phi)^3 (\alpha_V^2 + \alpha_\Phi^2). \tag{3.2.12}$$

3.2.2 Boltzmann equations and effective depletion rate

Let $Y_X = n_X/s$ and $Y_{\mathcal{B}} = n_{\mathcal{B}}/s$ be the yields of the unbound X particles and the bound states respectively. The Boltzmann equations that govern the evolution of the densities are [39][6]

$$\frac{dY_X}{dx} = -\sqrt{\frac{\pi}{45}} \frac{m_{\rm Pl}\, m_X\, g_{*,\rm eff}^{1/2}}{x^2} \left\{ \langle \sigma_{\rm ann} v_{\rm rel} \rangle \left[Y_X^2 - (Y_X^{\rm eq})^2 \right] + \langle \sigma_{\rm BSF}\, v_{\rm rel} \rangle \left[Y_X^2 - \frac{Y_{\mathcal{B}}}{Y_{\mathcal{B}}^{\rm eq}} (Y_X^{\rm eq})^2 \right] \right\}, \tag{3.2.13a}$$

$$\frac{dY_{\mathcal{B}}}{dx} = +\sqrt{\frac{\pi}{45}} \frac{m_{\rm Pl}\, m_X\, g_{*,\rm eff}^{1/2}}{x^2} \langle \sigma_{\rm BSF}\, v_{\rm rel} \rangle \left[Y_X^2 - \frac{Y_{\mathcal{B}}}{Y_{\mathcal{B}}^{\rm eq}} (Y_X^{\rm eq})^2 \right] - \sqrt{\frac{45}{4\pi^3}} \frac{m_{\rm Pl}}{m_X^2} \frac{g_{*,\rm eff}^{1/2}}{g_{*S}}\; x\, \Gamma_{\mathcal{B}}^{\rm dec} \left(Y_{\mathcal{B}} - Y_{\mathcal{B}}^{\rm eq} \right), \tag{3.2.13b}$$

where $\langle \sigma_{\rm ann} v_{\rm rel} \rangle$, $\langle \sigma_{\rm BSF} v_{\rm rel} \rangle$ and $\Gamma_{\mathcal{B}}^{\rm dec}$ have been given in section 3.2.1. In eqs. (3.2.13),

$$g_{*,\rm eff}^{1/2} \equiv \frac{g_{*S}}{\sqrt{g_*}} \left(1 - \frac{x}{3 g_{*S}} \frac{dg_{*S}}{dx} \right), \tag{3.2.14}$$

with g_* and g_{*S} being the energy and entropy relativistic degrees of freedom. We will take $g_* = g_{*S} = g_*^{\rm SM} + 4$ to account for the SM plus the V and Φ degrees of freedom, during the

[6] We use the Planck mass $m_{\rm Pl} = 1.22 \times 10^{19}$ GeV.

DM freeze-out. We recall that the entropy density of the universe is $s = (2\pi^2/45) g_{*S} T^3$. In the non-relativistic regime, the equilibrium yields $Y_X^{\rm eq}$ and $Y_{\mathcal{B}}^{\rm eq}$ are

$$Y_X^{\rm eq} \simeq \frac{90}{(2\pi)^{7/2}} \frac{1}{g_{*S}} \, x^{3/2} \, e^{-x} \,, \tag{3.2.15a}$$

$$Y_{\mathcal{B}}^{\rm eq} \simeq \frac{90}{(2\pi)^{7/2}} \frac{1}{g_{*S}} \, (2x)^{3/2} \, e^{-2x[1-(\alpha_V+\alpha_\Phi)^2/8]} \,. \tag{3.2.15b}$$

The relic density of the $X, X^\dagger$ particles is

$$\Omega_X = 2 m_X Y_X s_0 / \rho_c, \tag{3.2.16}$$

where $s_0 \simeq 2840 \text{ cm}^{-3}$ and $\rho_c \simeq 3.67 \times 10^{-47} \text{GeV}^4$ are the entropy and critical energy density of the universe today [7]. We require that $\Omega_X = \Omega_{\rm DM}$, where the observed DM density is $\Omega_{\rm DM} \simeq 0.264$ [7].

We note that in the minimal setup considered here, the Φ particles are stable, being the lightest degrees of freedom charged under $U(1)_D$. As such, they contribute to the DM density. However, due to their lightness, even a small α_V suffices to ensure that they annihilate into vector bosons efficiently, via the t/u-channel process $\Phi\Phi^\dagger \to VV$, thereby reaching a cosmologically negligible relic abundance. Moreover, the radiation density due to V evades the CMB and BBN constraints provided that the dark sector temperature is somewhat lower than that of the SM plasma at the corresponding times. If Φ acquires a VEV and/or the dark sector couples to the SM, then there are more possibilities for the cosmological abundance of Φ and V, as well as constraints. A complete phenomenological study is beyond the scope of this work.

Effective depletion cross-section

Instead of the system of coupled eqs. (3.2.13), the effect of bound states on the relic density can be described by a single Boltzmann equation for the DM particles and an *effective* annihilation cross-section that includes BSF weighted by the fraction of bound states that decay rather than being ionised. We define first the effective BSF cross-section

$$\langle \sigma_{\rm BSF} v_{\rm rel} \rangle_{\rm eff} \equiv \langle \sigma_{\rm BSF} v_{\rm rel} \rangle \times \left(\frac{\Gamma_{\mathcal{B}}^{\rm dec}}{\Gamma_{\mathcal{B}}^{\rm dec} + \Gamma_{\mathcal{B}}^{\rm ion}} \right). \tag{3.2.17}$$

The effective DM depletion cross-section is

$$\langle \sigma v_{\rm rel} \rangle_{\rm eff} = \langle \sigma_{\rm ann} v_{\rm rel} \rangle + \langle \sigma_{\rm BSF} v_{\rm rel} \rangle_{\rm eff}. \tag{3.2.18}$$

We may compute the X relic density by solving the Boltzmann equation [105]

$$\frac{dY_X}{dx} = -\sqrt{\frac{\pi}{45}} \frac{m_{\rm Pl} \, m_X \, g_{*,\rm eff}^{1/2}}{x^2} \, \langle \sigma v_{\rm rel} \rangle_{\rm eff} \left[Y_X^2 - (Y_X^{\rm eq})^2 \right]. \tag{3.2.19}$$

In figs. 3.10 and 3.11, we show the DM annihilation and BSF cross-sections, and their thermal averages. The BSF_Φ cross-sections can exceed both the BSF_V and annihilation cross-sections by orders of magnitude, even for very small values of the couplings. However, the effect on the DM density depends on the interplay among the bound-state formation, ionisation and decay processes. To anticipate the result, it is useful to discern between two phases during the DM chemical decoupling.

(a) While the temperature is large enough to ensure that $\Gamma_{\mathcal{B}}^{\rm ion} \gg \Gamma_{\mathcal{B}}^{\rm dec}$, the system is in a state of *ionization equilibrium* [106], where the effective DM depletion rate due to bound states is essentially independent of the BSF cross-section. Indeed, combining eqs. (3.2.9), (3.2.11) and (3.2.17) under the aforementioned condition, we obtain

$$\langle \sigma_{\rm BSF} v_{\rm rel} \rangle_{\rm eff} \simeq \langle \sigma_{\rm ann} v_{\rm rel} \rangle_0^{\rm pert} \times 8\sqrt{\pi} \left(\frac{|\mathcal{E}_{\mathcal{B}}|}{T} \right)^{3/2} e^{+|\mathcal{E}_{\mathcal{B}}|/T}. \tag{3.2.20}$$

Note that eq. (3.2.20) does not rely on the specific couplings or interactions of the model considered here, but is rather general. It is easy to check that (3.2.20) is small in comparison to the annihilation cross-section, unless or until the temperature approaches or drops below the binding energy. In a $U(1)$ model where DM couples only to the gauge boson, the ionization equilibrium ends at a temperature somewhat higher than the binding energy, thus (3.2.20) remains mostly small and most of the BSF effect on the DM density arises after that the end of ionisation equilibrium [39]. However, in the present model, the largeness of the BSF$_\Phi$ cross-section sustains ionization equilibrium down to temperatures below the binding energy (cf. fig. 3.11), thereby rendering the DM depletion significant during this phase. Clearly, while eq. (3.2.20) is independent of $\langle \sigma_{\rm BSF} v_{\rm rel} \rangle$, the duration of ionisation equilibrium depends on it.

(b) The ionisation equilibrium ends when the ionisation rate drops below the decay rate, $\Gamma_{\mathcal{B}}^{\rm ion} \lesssim \Gamma_{\mathcal{B}}^{\rm dec}$. Then, the DM depletion rate approaches rapidly the actual BSF rate, and is therefore sensitive to the exact BSF cross-section, $\langle \sigma_{\rm BSF} v_{\rm rel} \rangle_{\rm eff} \simeq \langle \sigma_{\rm BSF} v_{\rm rel} \rangle$.

Taking into account the above considerations, and in order to gain insight on whether BSF$_\Phi$ may affect the DM density, in figs. 3.12 and 3.13 we present the effective DM depletion cross-section for the following four cases:

AnnP: Perturbative annihilation only (diagrams shown in fig. 3.9a).

AnnS: Annihilation including the Sommerfeld effect due to both V and Φ exchange [cf. eq. (3.2.3)].

AnnS + BSF$_V$: Annihilation with Sommerfeld effect due to V and Φ exchange, plus BSF$_V$ [cf. eq. (3.2.5a)] with the ionization of the bound states [cf. eq. (3.2.8)] caused by V only.

AnnS + BSF$_V$ + BSF$_\Phi$: Annihilation with Sommerfeld effect due to V and Φ exchange, plus BSF$_V$ and BSF$_\Phi$ [cf. eq. (3.2.6)], with the ionization of the bound states [cf. eq. (3.2.8)] caused by V or Φ.

In fig. 3.12 we show the evolution of $\langle \sigma v_{\rm rel} \rangle_{\rm eff}$ as the temperature drops. We choose a small value for the DM coupling to the charged scalar, $\alpha_\Phi = 10^{-3}$, to be well within the range that is consistent with unitarity (cf. section 3.1.4). We observe that the BSF$_V$ and BSF$_\Phi$ contributions to the effective cross-section begin to rise at $T \sim |\mathcal{E}_{\mathcal{B}}|$, as implied by eq. (3.2.20). Later on, the ionisation equilibrium ends, and $\langle \sigma_{\rm BSF} v_{\rm rel} \rangle_{\rm eff}$ saturates to $\langle \sigma_{\rm BSF} v_{\rm rel} \rangle$; because this occurs at $T < |\mathcal{E}_{\mathcal{B}}|$, when $\sqrt{\langle v_{\rm rel}^2 \rangle} < \alpha_{\mathcal{B}} = \alpha_V + \alpha_\Phi < \alpha_V$, the effective BSF cross-section $\langle \sigma_{\rm BSF} v_{\rm rel} \rangle_{\rm eff}$ decreases beyond this point, due to the repulsive potential in the XX and $X^\dagger X^\dagger$ scattering states. The largeness of $\langle \sigma_{\rm BSF} v_{\rm rel} \rangle$ and consequently of $\langle \sigma_{\rm BSF} v_{\rm rel} \rangle_{\rm eff}$ around its peak, suggest that the DM depletion processes may recouple, even at a very low temperature, as we shall see in section 3.2.3.

Comparing the two plots of fig. 3.12, corresponding to $\alpha_V = 10^{-2}$ and $\alpha_V = 10^{-4}$, we also note that the rise and the peak of BSF$_\Phi$become more pronounced for smaller α_V values, which allow for the effective BSF$_\Phi$cross-sections to grow larger before the suppression due to the

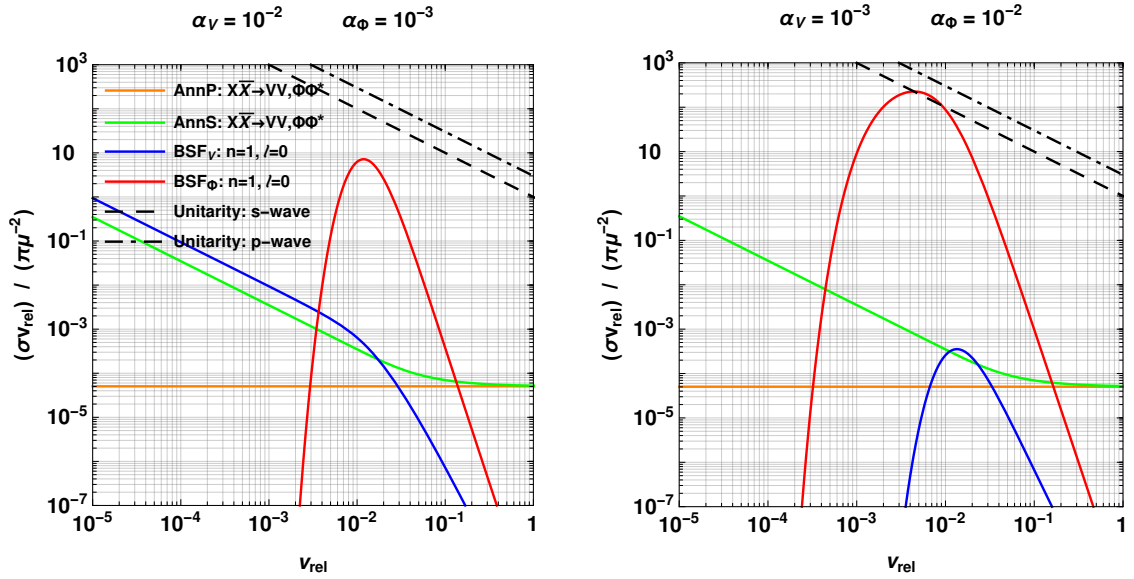

Figure 3.10: The BSF and annihilation velocity-weighted cross-sections that we consider in the computation of the DM freeze-out, vs. $v_{\rm rel}$. All cross-sections have been normalised to π/μ^2, with $\mu = m_X/2$ being the reduced mass of the interacting particles. Also shown, the unitarity limits on s-wave and p-wave inelastic processes, which have to be respected by BSF_Φ and BSF_V, respectively, for capture into the ground state.

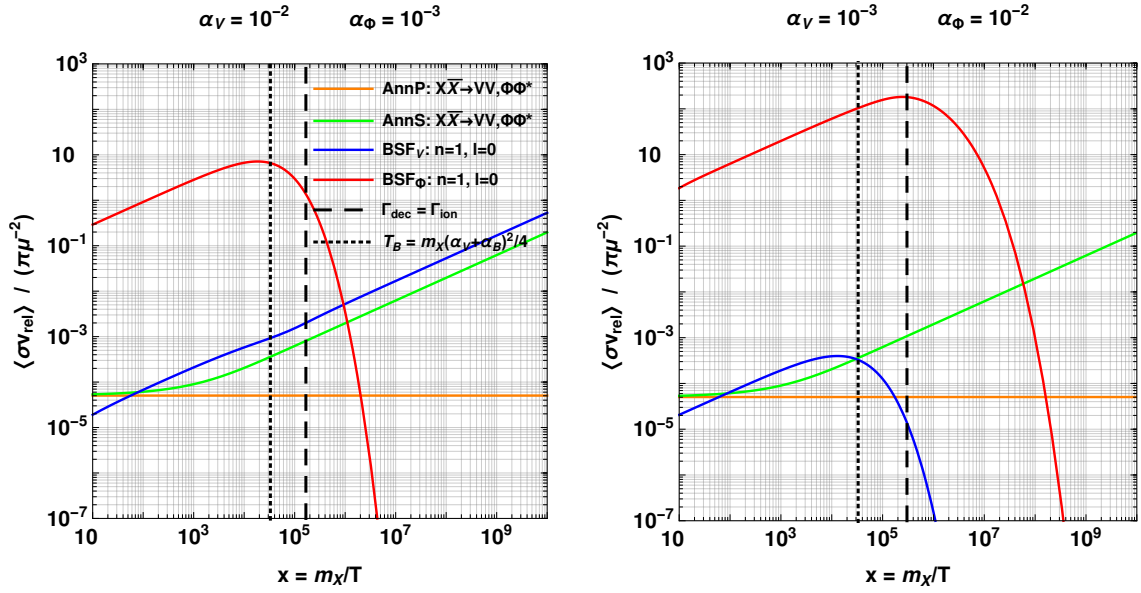

Figure 3.11: The thermally averaged BSF and annihilation velocity-weighted cross-sections that we consider in the computation of the DM freeze-out, vs. $x \equiv m_X/T$. All cross-sections have been normalised to π/μ^2, with $\mu = m_X/2$ being the reduced mass of the interacting particles. We also mark two important mileposts: (i) the time when the temperature equals the binding energy $T_B = m_X(\alpha_V + \alpha_\Phi)^2/4$, at and below which the equilibrium occupation number of the bound states becomes very significant, and (ii) the end of ionisation equilibrium, below which the DM depletion rate saturates to the BSF rate and thus becomes sensitive to the BSF cross-section.

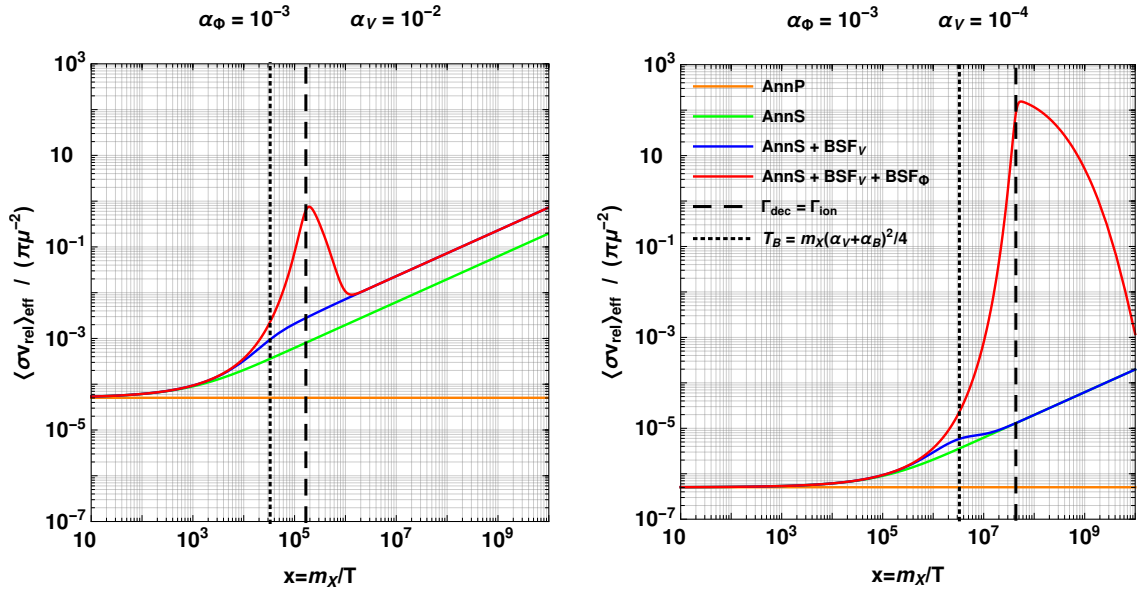

Figure 3.12: The thermally-averaged velocity-weighted effective cross-section as a function $x = m_X/T$, for fixed $\alpha_\Phi = 10^{-3}$ and two different values of α_V.

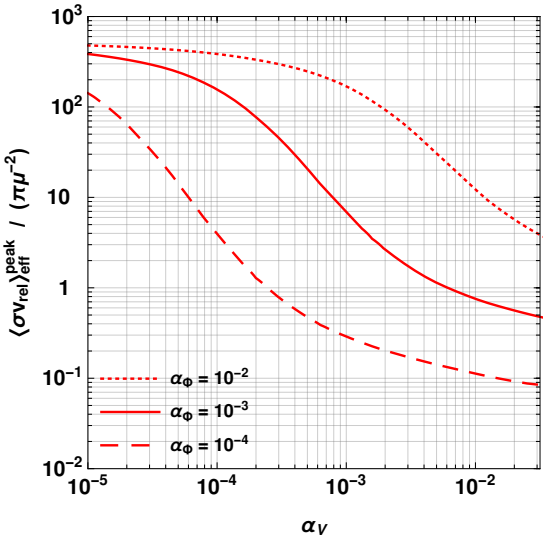

Figure 3.13: The value of the thermally averaged velocity-weighted effective cross-section at its peak as a function of α_V, for different values of α_Φ. Note that the time at which the peak occurs, $x = x_{\rm peak}$, depends on α_V and α_Φ, and is chosen accordingly. We observe that, by varying α_V, $\langle\sigma v_{\rm rel}\rangle_{\rm eff}^{\rm peak}$ rises at $\alpha_V \lesssim \alpha_\Phi$, and becomes most significant at the limit of global symmetry, $\alpha_V \to 0$.

repulsion in the scattering state settles in. To investigate this further, in fig. 3.13 we show the dependence of $\langle\sigma v_{\rm rel}\rangle_{\rm eff}$ evaluated at its peak, on α_V. We see that $\langle\sigma v_{\rm rel}\rangle_{\rm eff}^{\rm peak}$ rises at $\alpha_V \lesssim \alpha_\Phi$, and becomes most significant at $\alpha_V \to 0$, i.e. in the limit where the symmetry becomes global.

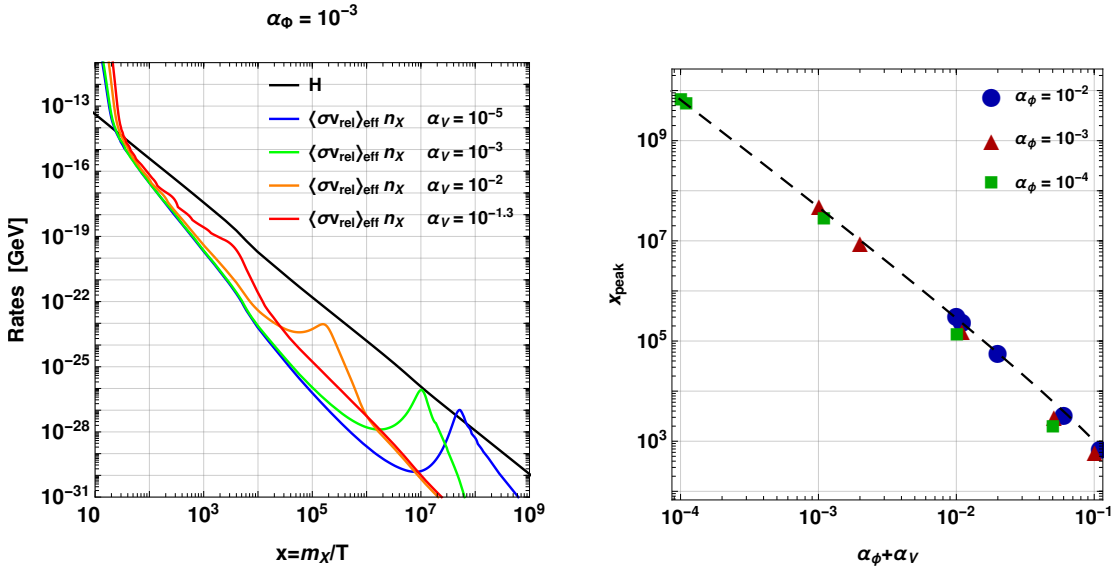

Figure 3.14: *Left:* The DM depletion rate $\Gamma_X = n_X\langle\sigma v_{\rm rel}\rangle_{\rm eff}$ compared to the Hubble parameter H, for $\alpha_\Phi = 10^{-3}$ and different values of α_V. We have used $m_X = 10^3$ GeV. *Right:* $x_{\rm peak}$ is the value of $x \equiv m_X/T$ at which $\langle\sigma v_{\rm rel}\rangle_{\rm eff}$ peaks. The symbols correspond to the values determined numerically, while the line is the semi-analytical prediction eq. (3.2.21).

3.2.3 Solutions of the Boltzmann equations

We now solve the Boltzmann eq. (3.2.19), discuss the qualitative features of the solutions and present numerical results. We focus mostly on small values of α_Φ, roughly $\alpha_\Phi \lesssim 10^{-2}$, in order to be consistent with unitarity (cf. section 3.1.4), and mark any parameter space where the BSF$_\Phi$ cross-section violates it.

Freeze-out and recoupling of DM depletion processes

The Boltzmann eq. (3.2.19) describes the balance between the DM depletion processes and the expansion of the universe. Motivated by the sharp increase of $\langle\sigma v_{\rm rel}\rangle_{\rm eff}$ at low temperatures seen in fig. 3.12, we compare the X depletion rate $\Gamma_X \equiv n_X\langle\sigma v_{\rm rel}\rangle_{\rm eff}$ with the expansion rate of the universe $H = \sqrt{4\pi^3 g_*/45}\, T^2/m_{\rm Pl}$ in the left plot of fig. 3.14. Then in fig. 3.15, we show the evolution of the DM density for different sets of parameters, in the four cases defined in section 3.2.2. The DM chemical decoupling is marked by two important events.

First freeze-out. As is standard, for $x \lesssim x_{\rm FO1} \approx 30$, the DM depletion and creation processes are in equilibrium, i.e. $\Gamma_X \gtrsim H$. Beyond this point, the $X, X^\dagger$ densities depart from their equilibrium values, their exponential drop is stalled, and they begin to freeze-out. However, because the annihilation and BSF cross-sections increase with decreasing temperature, the depletion of DM continues to be important until somewhat later, and may lead to the reduction of the DM density by a factor of a few. The Sommerfeld enhancement of the annihilation processes is important for $v_{\rm rel} \lesssim 10(\alpha_V + \alpha_\Phi)$, which upon thermal averaging implies $x \gtrsim 10^{-2}(\alpha_V + \alpha_\Phi)^{-2}$. Thus if $\alpha_V + \alpha_\Phi \gtrsim 10^{-2}$, the Sommerfeld enhancement becomes significant already at $x \sim 10^2$, i.e. soon after freeze-out, while the DM density is still quite large. For BSF, a somewhat larger coupling, $\alpha_V + \alpha_\Phi \gtrsim 0.03$, is required. In this range of couplings, the DM chemical decoupling is prolonged beyond freeze-out, as clearly seen in the bottom right plot of fig. 3.15.

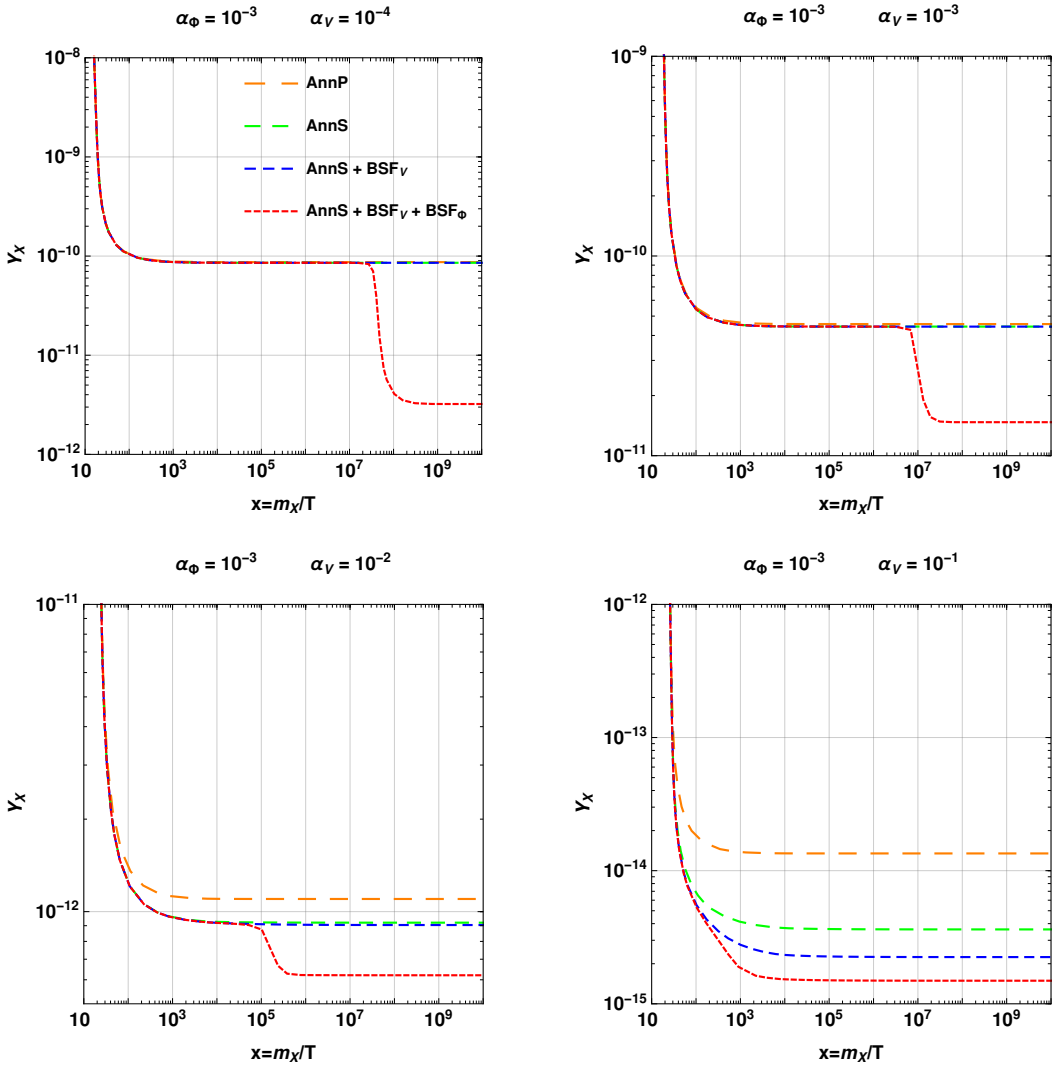

Figure 3.15: The evolution of the DM yield $Y_X \equiv n_X/s$ vs. $x \equiv m_X/T$ for the four cases defined in section 3.2.2. We have fixed $m_X = 10^3$ GeV.

Recoupling of DM depletion and second freeze-out. If $\alpha_V + \alpha_\Phi \lesssim 10^{-2}$, the ionisation processes impede the DM depletion via BSF until quite late, when the DM density is rather low. However, the largeness of the BSF$_\Phi$ cross-section may compensate for the smallness of the DM density, and result in the recoupling of the DM depletion processes around the time when $\langle\sigma v_{\rm rel}\rangle_{\rm eff}$ peaks, at $T \lesssim |\mathcal{E}_\mathcal{B}|$.[7] We may estimate if and when this occurs as follows. The $X, X^\dagger$ yield after the first freeze-out is estimated by the standard result, $m_X Y_X^{\rm FO1}\langle\sigma_{\rm ann} v_{\rm rel}\rangle^{\rm FO1} \sim 8\times 10^{-19}$ GeV^{-1} (see e.g. [108]), where we assumed that the direct annihilation dominates the DM depletion rate at that time; this is indeed true for the range of α_V, α_Φ where the recoupling may occur. The DM depletion recouples if $Y_X^{\rm FO1}\langle\sigma v_{\rm rel}\rangle_{\rm eff} \gtrsim H/s$, which implies $\langle\sigma v_{\rm rel}\rangle_{\rm eff}/\langle\sigma_{\rm ann} v_{\rm rel}\rangle^{\rm FO1} \gtrsim 0.4\, x/\sqrt{g_*}$. If this occurs, it does so shortly before DM exits the ionisation equilibrium, i.e. while eq. (3.2.20) is still approximately valid. (As already mentioned, at later times BSF$_\Phi$ decreases exponentially due to the repulsion in the scattering state.) Thus, the recoupling condition becomes $\sqrt{\pi/S_{\rm ann}^{\rm FO1}}(\alpha_V + \alpha_\Phi)^3\, x^{3/2}\, e^{x(\alpha_V+\alpha_\Phi)^2/4} \gtrsim 0.4\, x/\sqrt{g_*}$,

[7] Recoupling of the DM depletion at late times may occur also due to the strong velocity dependence of Sommerfeld-enhanced cross-sections at (or close to) parametric resonance points [94, 107]. The recoupling observed here is not due to resonant features, and applies to broader parameter space.

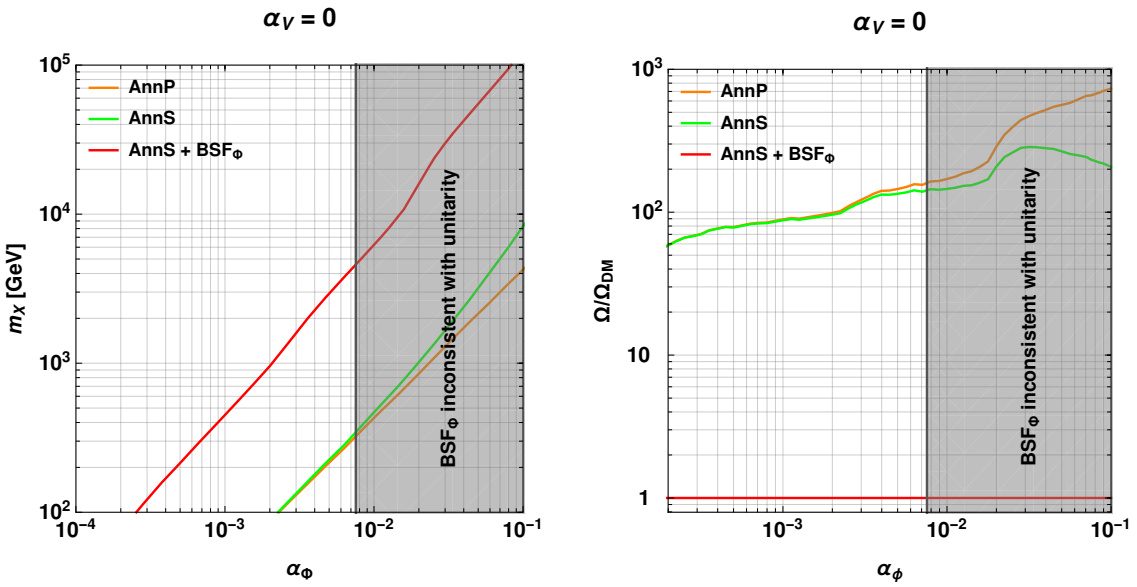

Figure 3.16: In the limit of the local symmetry becoming global, $\alpha_V = 0$, we show the relation between the DM mass m_X and the coupling α_Φ to the scalar mediator (*left*), and the effect of BSF$_\Phi$ on the DM density (*right*).

where $S_{\rm ann}^{\rm FO1} \sim \mathcal{O}(1)$ stands for the thermally averaged Sommerfeld factor of the annihilation processes around the time of the first freeze-out. For large $\alpha_V + \alpha_\Phi$, this condition yields a time close to the first freeze-out, and corresponds to the case when the DM chemical decoupling is simply delayed due to the BSF processes, as discussed above (cf. bottom right plot in fig. 3.15). However, for smaller couplings, we obtain the following estimate for the time of recoupling and approximately the peak of $\langle \sigma v_{\rm rel} \rangle_{\rm eff}$,

$$x_{\rm peak} \sim \frac{8 \, \ln(\alpha_V + \alpha_\Phi)^{-1}}{(\alpha_V + \alpha_\Phi)^2}, \tag{3.2.21}$$

where we kept the leading order logarithmic correction in $x_{\rm peak}$. Note that $x_{\rm peak}$ is independent of the DM mass m_X. In the right plot of fig. 3.14, we compare the semi-analytical prediction (3.2.21) with values of $x_{\rm peak}$ determined numerically, and we find them in very good agreement. For $\alpha_V + \alpha_\Phi \gtrsim 10^{-2}$, (3.2.21) occurs much after the first chemical decoupling. In the top and the bottom left plots of fig. 3.15, this manifests as a second plateau of the DM yield at large x. Clearly, the recoupling of the depletion processes at low temperatures results in very significant decrease of the DM abundance. This impels the re-determination of the couplings that give rise to the observed DM density.

Mass-coupling relation

We solve the Boltzmann eq. (3.2.19) numerically and determine the relation between α_V, α_Φ and m_X that reproduces the observed DM density. In figs. 3.16 to 3.18, we present our results.

From the previous discussion, we expect that the effect of BSF$_\Phi$ is more pronounced at small α_V, and in particular for $\alpha_V \lesssim \alpha_\Phi$. For this reason, in fig. 3.16, we focus on the limit of global symmetry, $\alpha_V = 0$, and determine the relation between m_X and α_Φ, while in figs. 3.17 and 3.18 we consider also the dependence on α_V.

In all cases, we see that taking BSF$_\Phi$ into account changes the predicted couplings or mass very significantly, even by an order of magnitude. The effect on the DM density is illustrated

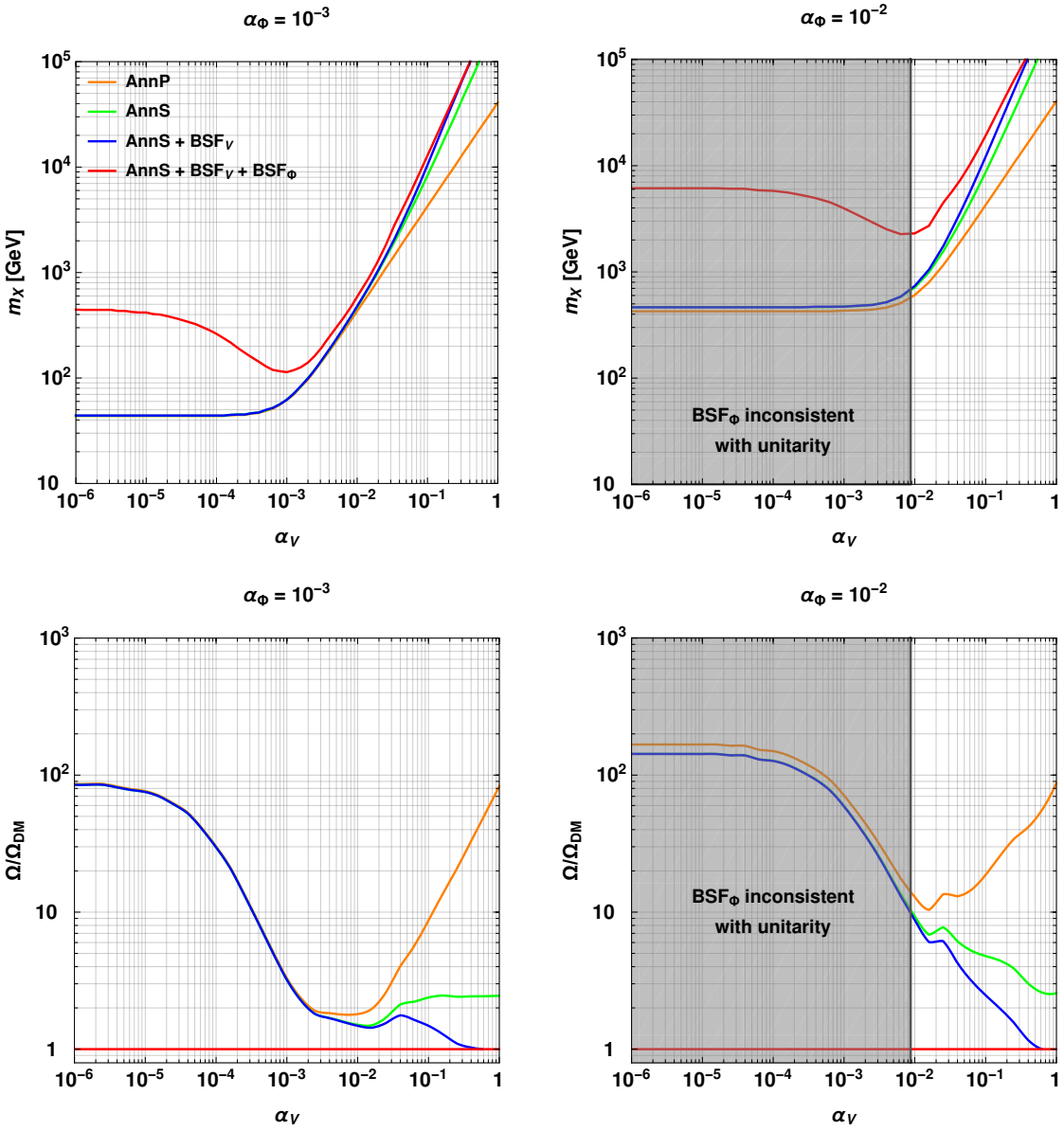

Figure 3.17: *Top:* The relation between the DM mass m_X and the coupling to the gauge boson α_V that reproduces the observed DM density, when considering different contributions to the DM depletion. In the gray-shaded region, our computation of the BSF$_\Phi$ cross-section violates unitarity within a range of velocities. *Bottom:* The $X, X^\dagger$ relic density when taking into account only some of the DM depletion processes, normalised to the observed DM density. For each value of α_V we have chosen m_X such that the observed DM density is reproduced by the AnnS+BSF$_V$+BSF$_\Phi$ calculation (red line in plots above).

in the right plot of fig. 3.16 and the bottom plots of fig. 3.17. We pick the combination of parameters that reproduce the observed DM abundance when considering AnnS+BSF$_V$+BSF$_\Phi$, and then calculate the final density attained if only AnnP, AnnS, or AnnS+BSF$_V$ are taken into account. We observe the BSF$_\Phi$ can deplete the DM density by more than two orders of magnitude.

Because of the interplay of the couplings α_V and α_Φ in $\langle\sigma v_{\rm rel}\rangle_{\rm eff}$, the DM relic density does not always vary monotonically with the parameters. In particular, for fixed m_X and α_Φ within

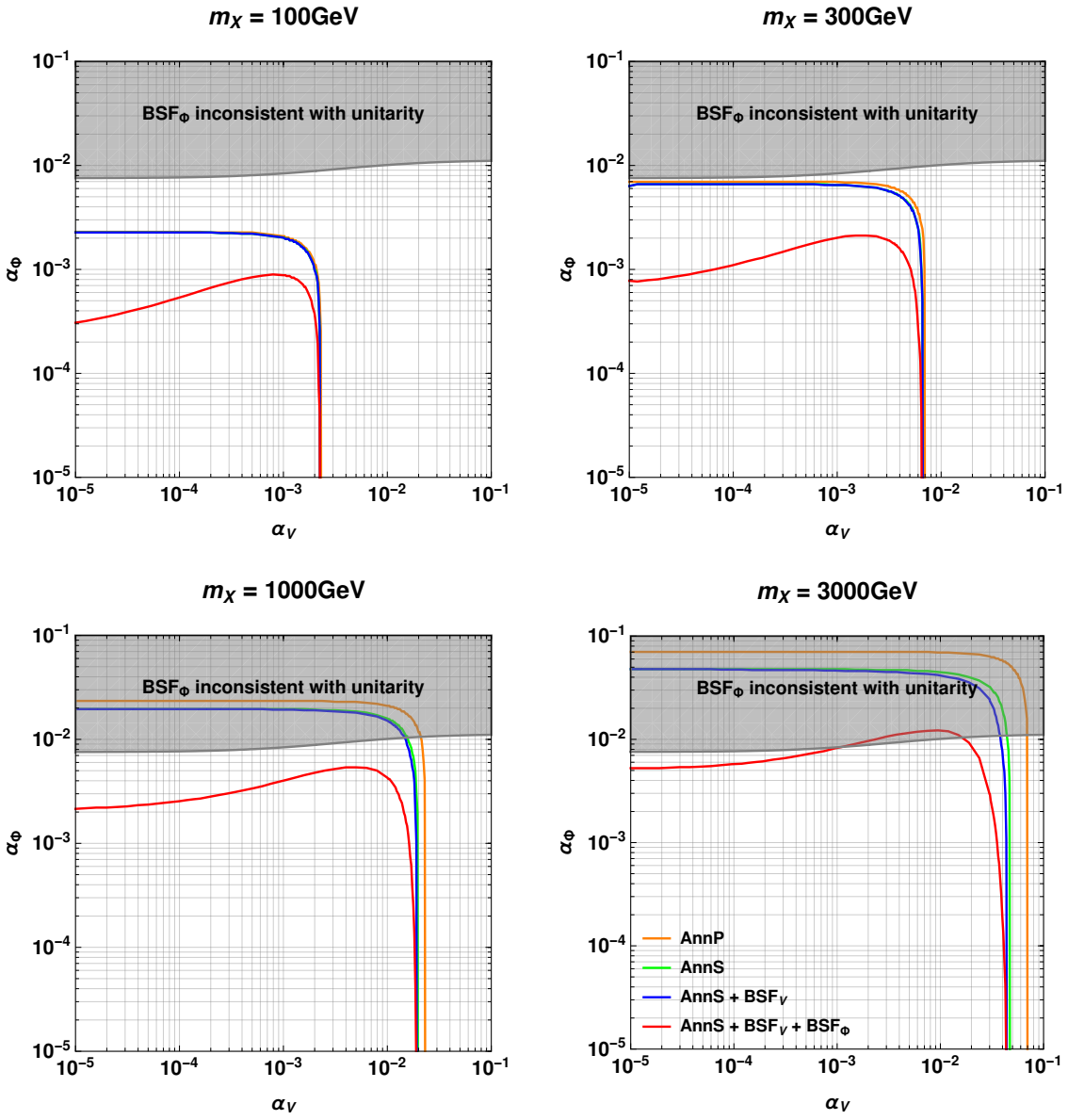

Figure 3.18: The combination of the couplings α_V, α_Φ that reproduces the observed DM abundance, for fixed values of the DM mass, when considering different contributions to the DM depletion.

some range, we observe in figs. 3.17 and 3.18 that there are two values of α_V that reproduce the observed DM density: a value in the range $\alpha_V > \alpha_\Phi$ where BSF$_\Phi$ has little effect, and a value in the range $\alpha_V < \alpha_\Phi$ where BSF$_\Phi$ has significant impact.

3.3 Validity of the Coulomb approximation

Throughout this chapter, we have neglected the mass of the charged scalar Φ (as well as the possibility of a non-vanishing V mass). The calculation of section 3.1 can be generalised to include non-zero masses for Φ and V by evaluating numerically the wavefunctions and the overlap integral, as in refs. [43, 54, 55]. Here we examine the validity of the Coulomb approximation in the computation of the DM relic density.

In the present model, m_Φ affects BSF_Φ via the bound-state wavefunction and the phase-space suppression due to Φ emission. Note that m_Φ does not affect the XX and $X^\dagger X^\dagger$ scattering states that participate in BSF_Φ. The conditions for the Coulomb approximation to be valid are as follows.

(i) For a pure Yukawa potential, the ground state is Coulombic if the mediator mass is much smaller than the Bohr momentum. In the absence of V, this would imply $m_\Phi \ll \mu\alpha_\Phi$ [43]. The presence of the V-mediated attractive Coulomb potential relaxes this condition [55]. Indicatively we note that, neglecting the V-generated potential, the binding energy is larger than 90% of its Coulomb value if $m_\Phi < \mu\alpha_\Phi/10$ [43, fig. 13]. On the other hand, for $\alpha_V = \alpha_\Phi$, this occurs if $m_\Phi < \mu\alpha_\Phi/2$ [55, fig. 6]. For simplicity, we shall thus assume the following condition for the Coulomb approximation

$$\text{few} \times m_\Phi \lesssim \mu\alpha_\mathcal{B} = \mu(\alpha_V + \alpha_\Phi). \tag{3.3.1}$$

(ii) BSF_Φ is kinematically accessible if $m_\Phi < \mathcal{E}_\mathbf{k} + |\mathcal{E}_\mathcal{B}| \simeq (\mu/2)[(\alpha_V+\alpha_\Phi)^2 + v_\mathrm{rel}^2]$. In the thermal bath, $\langle \mu v_\mathrm{rel}^2/2 \rangle = 3T/2$. During the first freeze-out the temperature is large, $T \gg |\mathcal{E}_\mathcal{B}|$, and $\mathcal{E}_\mathbf{k}$ dominates the energy available to be dissipated. However, the recoupling of the DM depletion processes occurs at $T \sim |\mathcal{E}_\mathcal{B}|$ (if at all), when $\langle \mathcal{E}_\mathbf{k} \rangle \sim |\mathcal{E}_\mathcal{B}|$. Therefore, we require

$$m_\Phi \lesssim \mu\alpha_\mathcal{B}^2/2 = (\mu/2)(\alpha_V + \alpha_\Phi)^2. \tag{3.3.2}$$

The condition (3.3.2) is stronger than (3.3.1). Particularly for the small values of α_Φ and α_V we have considered here, it ensures that the bound states are very nearly Coulombic.

For BSF_V, there is no kinematic blocking, provided that V is massless. However, a non-vanishing m_Φ affects the $XX^\dagger$ scattering state, as well as the $XX^\dagger$ bound state. For the latter, the condition for the Coulomb approximation is (3.3.1). We briefly discuss the scattering state. In the case of a pure attractive Yukawa potential, the Coulomb limit is obtained if the mediator mass is lower than the average momentum transfer, $m_\Phi \lesssim \mu v_\mathrm{rel}$ [43]. For a pure repulsive Yukawa potential the condition is somewhat stronger. On the other hand, this condition is relaxed by the superposition of the V-mediated attractive Coulomb force [54, fig. 2]. Since BSF_V can be important only at early times, when the average kinetic energy is still fairly large, and provided that $\alpha_V + \alpha_\Phi$ is sufficiently large, the Coulomb approximation is typically justified (see e.g. discussion in ref. [44]). Regardless of the validity of the approximation, BSF_V is not the focus of this study, thus we do not elaborate on this issue further.

Finally, we note that if the charged scalar obtains a VEV, v_Φ, the symmetry-breaking phase transition is expected to occur at temperature $T_\mathrm{PT} \lesssim v_\Phi$. Then, if $v_\Phi < |\mathcal{E}_\mathcal{B}|$, the DM chemical decoupling – including both the first freeze-out and the recoupling epoch – takes place essentially in the unbroken phase, and the computation of this section is applicable. Assuming that (3.3.2) holds, the condition $v_\Phi < |\mathcal{E}_\mathcal{B}|$ is satisfied in models where $v_\Phi \lesssim m_\Phi$. However, the DM chemical decoupling may occur in the unbroken phase even for $v_\Phi \gg m_\Phi$, if both v_Φ and m_Φ are much lower than $|\mathcal{E}_\mathcal{B}|$.

3.4 Conclusion

In this chapter 3, we computed the cross-sections for the radiative capture of non-relativistic particles into bound states via emission of a scalar that is charged under either a local or global symmetry. The emission of a charged scalar alters the Hamiltonian between the interacting particles, and precipitates extremely rapid transitions. We have provided analytical formulae in the Coulomb approximation for the capture into any bound level [cf. eq. (3.1.26)]. While we carried

out our calculations in the context of a minimal $U(1)$ model, our results are readily generalisable to more complex models, including perturbative non-Abelian theories, and can thus be relevant to the phenomenology of various scenarios, e.g. [54, 55, 68, 71, 109].

The phenomenological implications of the processes we computed can be striking. Here, we demonstrated that the formation of particle-antiparticle bound states via emission of a charged scalar and their subsequent decay can deplete the DM density by as much as two orders of magnitude. While for simplicity we considered only capture into the ground state, the computed cross-sections strongly suggest that the capture into excited states during the DM chemical decoupling should also be significant, thereby producing an even more important effect. The depletion of DM via these processes in the early universe alters the predicted relation between the DM mass and couplings rather dramatically. This in turn implies very different predictions for the DM signals in collider, direct and indirect detection experiments.

For indirect detection, the modification in the predicted relation between the DM mass and couplings implies that the signals arising from the direct annihilation processes and BSF via vector emission are very suppressed with respect to what expected when neglecting BSF via charged scalar emission during freeze-out. This essentially invalidates any existing constraints. On the other hand, BSF via charged scalar emission occurring during CMB or inside halos today may itself produce very significant radiative signals that result in strong constraints. For direct detection experiments, the implications are again varied. The larger predicted DM mass can bring a model previously thought to reside in the sub-GeV regime, within the threshold of current detectors. On the other hand, it can relax existing constraints for models already within the experimental sensitivity. Finally, the large BSF_Φ cross-sections may imply late kinetic decoupling of DM from radiation in the early universe, as well as strong DM self-interactions inside halos today; both features can potentially affect the galactic structure very significantly.

Our results can be recast to compute BSF via scattering on a bath of relativistic particles, through exchange of a charged scalar, according to ref. [102]. This can be particularly important for the chemical decoupling of multi-TeV WIMP DM coupled to the 125 GeV Higgs [109]; in this regime the Higgs can indeed act as a light mediator [54, 55], even if its on-shell emission in capture processes is not kinematically allowed. We study multi-TeV WIMP DM coupled to the 125 GeV Higgs in chapter 4.

Chapter 4

Bound states of WIMP dark matter in Higgs portal model

In the present chapter we study WIMP models - particles coupled to the weak interactions of the Standard Model - in a Higgs-portal scenario where DM is a linear combination of the neutral components of electroweak multiplets that couple to the Higgs doublet. The hierarchy between the multi-TeV and electroweak scales implies the emergence of *long-range* interactions, since the interaction range $l \sim (100\text{ GeV})^{-1}$ may be comparable or exceed the de Broglie wavelength $(\mu v_{\rm rel})^{-1}$ and/or the Bohr radius $(\mu\alpha)^{-1}$ of the interacting particles, where $\mu = m/2 \gtrsim$ TeV, $v_{\rm rel}$ and α are the reduced mass, relative velocity and coupling to the force mediators. The long-range nature of the interactions gives rise to non-perturbative phenomena, the Sommerfeld effect and the existence of bound states.

In chapter 3 we showed that the emission of a scalar boson charged under a symmetry alters the effective Hamiltonian between the interacting particles and renders BSF extremely rapid, even for small couplings [2]. For WIMPs, this implies that BSF via emission of a Higgs doublet may be a very significant inelastic process. Moreover, it has been shown in simplified models, that the 125 GeV Higgs boson can mediate a sizeable long-range force between TeV-scale particles, despite being heavier than all SM gauge bosons [54, 55].

The phenomenological importance of the above is rather large. It has been long known that the Sommerfeld effect [37, 38] – the distortion of the wavefunction of interacting particles due to a long-range force – affects the DM annihilation cross-sections at low relative velocities [110]. This, in turn, alters the DM chemical decoupling in the early universe, and consequently the predicted DM mass and couplings to other particles [111]. It also affects the radiative signals expected from the DM annihilations during CMB and inside galaxies today [112]. More recently, it has been realised that the formation and decay of metastable (e.g. particle-antiparticle) bound states in the early universe can decrease the DM density [39], and contribute to the DM indirect detection signals [40, 42, 44, 46–48, 52]. Importantly, BSF can be faster than annihilation in a variety of models [2, 43, 55, 59, 62], but it can also produce novel indirect signals even in models where annihilation is absent or suppressed [49, 57, 58, 95, 113–115].

Collecting the above considerations, in this chapter we consider bound states in Higgs portal models, and their effect on the DM relic density. We are interested in scenarios that feature a trilinear coupling between the DM and Higgs multiplets, i.e. $\delta\mathcal{L} \supset \bar{\chi}_n H \chi_{n+1} +$ h.c., where χ_n is a fermionic or bosonic n-plet under $SU_L(2)$, and DM is the lightest linear combination of the neutral χ_n and χ_{n+1} components after electroweak symmetry breaking. Such scenarios

have been considered extensively in the literature, and appear also in supersymmetry, e.g. Bino-Higgsino or Higgsino-Wino DM [109, 116–132]. For concreteness, we shall focus on the most minimal such model with a Majorana singlet and a Dirac doublet [109, 116–125].

The chapter is organized as follows. In section 4.1, we introduce the DM model and briefly review its basic properties in the broken electroweak phase. In section 4.2, we derive the long-range potentials between the DM multiplets in the unbroken electroweak phase. We identify the scattering and bound eigenstates of these potentials by appropriate spin and gauge projections, before computing the DM annihilation processes and bound-state decay rates. In section 4.3, we calculate all the radiative BSF cross-sections, while in section 4.4 we consider BSF via scattering on a relativistic thermal bath. Then, in sections 4.5 and 4.6, we compute the DM thermal decoupling in the early universe using an effective DM destruction cross-section that incorporates bound-state effects, and analyse the results. We conclude in section 4.9.

4.1 The model

We introduce a gauge-singlet Majorana fermion $S = (\psi_\alpha, \psi^{\dagger\dot{\alpha}})^T$ of mass m_S, as well as a Dirac fermion $D = (\xi_\alpha, \chi^{\dagger\dot{\alpha}})^T$ of mass m_D with SM gauge charges $SU_L(2) \times U_Y(1) = (2, 1/2)$. We assume that S and D are odd under a $\mathbb{Z}_2$ symmetry that leaves all the SM particles unaffected. Under these assignments, the new degrees of freedom (dof) allow to extend the SM Lagrangian by the following interactions

$$\delta\mathcal{L} = \frac{1}{2}\bar{S}(\mathbb{i}\not{\partial} - m_S)S + \overline{D}(\mathbb{i}\not{\mathcal{D}} - m_D)D - (y_L\bar{D}_L H S + y_R\bar{D}_R H S + \text{h.c.}), \tag{4.1.1}$$

where H is the SM Higgs doublet of mass m_H and hypercharge $Y_H = 1/2$, and $D_L \equiv P_L D = (\xi_\alpha, 0)^T$ and $D_R \equiv P_R D = (0, \chi^{\dagger\dot{\alpha}})^T$, with $P_{R,L} = (1 \pm \gamma_5)/2$ being the right-handed and left-handed projection operators. In the above, $\mathcal{D}_\mu \equiv \partial_\mu - \mathbb{i}g_1 Y B_\mu - \mathbb{i}g_2 W^a_\mu t^a$ is the covariant derivative, with $t^a = \frac{1}{2}(\sigma^1, \sigma^2, \sigma^3)$ and σ being the Pauli matrices. The particle content of eq. (4.1.1) is summarised in table 4.1.

field	$SU_L(2)$	$U_Y(1)$	$\mathbb{Z}_2$
S	1	0	-1
D	2	1/2	-1
H	2	1/2	$+1$

Table 4.1: Particle content and charge assignments

Here, we have taken the mass parameters m_S and m_D to be real. This can always be achieved by rephasing ψ and either ξ or χ. Rephasing the remaining spinor eliminates the phase of one of the Yukawa couplings. Thus the free parameters of the present model are 4 real couplings (two masses and two dimensionlesss Yukawa couplings), and a phase that allows for CP violation.

We are interested in the regime in which S and D can co-annihilate efficiently before the electroweak phase transition (EWPT) of the universe, which occurs if their masses are similar, within about 10%. This is because the number density of the heavier species in the non-relativistic regime is suppressed with respect to that of the lighter species by a factor $\exp[-(\delta m/m)x]$, with $x \equiv m/T \sim 30$ during DM freeze-out. For $\delta m/m \gtrsim 10\%$, the co-annihilations and the self-annihilations of the heavier species are subdominant to the self-annihilations of the lightest species, although their relative importance depends also on the corresponding cross-sections.

Such a small discrepancy in the masses does not significantly affect (most of) the cross-sections that we compute in the following; we shall thus take the masses to be equal, which greatly simplifies the computations and allows to obtain analytical results,

$$m_D = m_S \equiv m. \tag{4.1.2}$$

We will very often use the reduced mass of a pair of DM particles,

$$\mu \equiv m/2. \tag{4.1.3}$$

Moreover, in order to reduce the number of free parameters, we set

$$y_L = y_R \equiv y, \tag{4.1.4}$$

which we take to be real. (The CP violation is anyway not important for our purposes.) Our computations can of course be extended to more general Yukawa couplings. As is standard, we define the couplings

$$\alpha_1 \equiv \frac{g_1^2}{4\pi}, \qquad \alpha_2 \equiv \frac{g_2^2}{4\pi}, \qquad \alpha_H \equiv \frac{y^2}{4\pi}. \tag{4.1.5}$$

The model of eq. (4.1.1) and various aspects of its phenomenology have been considered for general parameters extensively in the past [109, 116–124]. Here we will only briefly review the mass eigenstates and their interactions after electroweak symmetry breaking for the choice of parameters denoted in eqs. (4.1.2) and (4.1.4).

Mass eigenstates in the broken electroweak phase

At electroweak symmetry breaking, the neutral component of the Higgs doublet acquires a vacuum expectation value. In terms of $SU_L(2)$ components, the H, ξ and χ fields are

$$H = \begin{pmatrix} \phi^+ \\ \frac{1}{\sqrt{2}}(v_H + h + \mathbb{i}\phi^0) \end{pmatrix}, \qquad \xi_\alpha = \begin{pmatrix} \xi_\alpha^+ \\ \xi_\alpha^0 \end{pmatrix}, \qquad \chi_\alpha = \begin{pmatrix} \chi_\alpha^0 \\ \chi_\alpha^- \end{pmatrix}, \tag{4.1.6}$$

with $v_H \simeq 246$ GeV.

We define the left-handed multiplet of the neutral states $\hat{N}_\alpha \equiv (\psi_\alpha, \xi_\alpha, \chi_\alpha)^T$. Then, by inserting eq. (4.1.6) into the Lagrangian (4.1.1), we find the corresponding mass terms,

$$\delta\mathcal{L}_{N,\text{mass}} = -\frac{1}{2}\hat{N}^\alpha \hat{M}_N \hat{N}_\alpha + \text{h.c.}, \tag{4.1.7}$$

with

$$\hat{M}_N = \begin{pmatrix} m & yv_H/\sqrt{2} & yv_H/\sqrt{2} \\ yv_H/\sqrt{2} & 0 & m \\ yv_H/\sqrt{2} & m & 0 \end{pmatrix}. \tag{4.1.8}$$

We diagonalise eq. (4.1.7) by setting

$$N_\alpha = U\hat{N}_\alpha, \qquad N^\alpha = \hat{N}^\alpha U^T, \qquad M_N = (U^T)^{-1}\hat{M}_N U^{-1}, \tag{4.1.9}$$

where U is the unitary matrix

$$U = \begin{pmatrix} -1/\sqrt{2} & 1/2 & 1/2 \\ 0 & \mathbb{i}/\sqrt{2} & -\mathbb{i}/\sqrt{2} \\ 1/\sqrt{2} & 1/2 & 1/2 \end{pmatrix}. \tag{4.1.10}$$

The corresponding mass eigenvalues are

$$m_1 \equiv m - yv_H, \qquad m_2 \equiv m, \qquad m_3 \equiv m + yv_H. \tag{4.1.11}$$

In addition to the neutral states, there is a charged Dirac fermion of mass m.

Interactions in the broken electroweak phase and constraints

The interactions among the neutral states, $N \equiv (N_1, N_2, N_3)^T$, are described by the Lagrangian [120]

$$\delta\mathcal{L}_{N,\text{inter}} = \frac{g_2}{2c_W} Z_\mu N_2^\dagger \bar{\sigma}^\mu \frac{\mathbb{i}}{2\sqrt{2}} (N_1 + N_3) - \frac{y}{2} h \left(N_1 N_1 - N_3 N_3 + N_1 N_3\right) + \text{h.c.}, \tag{4.1.12}$$

where $c_W = g_2/\sqrt{g_1^2 + g_2^2}$.

Since the coupling to Z_μ is non-diagonal, with the mass splitting being always much larger than $\sim \mathcal{O}(100$ keV) for the y values we will consider here (cf. section 4.5), the constraints from direct detection experiments due to this interaction are evaded. On the other hand, the coupling to the Higgs boson is expected to yield sizable DM-nucleus scattering and potentially strong constraints. Existing analyses of the direct detection data for this model do not extend to the multi-TeV regime that is of interest here. Moreover, the direct detection constraints on the model (4.1.1) are generally significantly relaxed around the so-called blind spots where the coupling to the Higgs vanishes, roughly when $y_L = -y_R$ (see e.g.[119, 120].) A detailed phenomenological analysis is beyond the scope of the present work. However, our results are important for interpreting the experimental constraints, since they imply a different relation between the DM mass and couplings in order for the observed DM density to be attained via thermal freeze-out.

4.2 Long-range dynamics in the unbroken electroweak phase

4.2.1 Static potentials

The D, $\bar{D}$ and S fermions interact with each other via the W, B and H boson exchanges that give rise to long-range potentials. The kernels generating these potentials are shown in fig. 4.1. To compute them, we decompose the incoming and outgoing momenta as follows

$$p_1 = P/2 + p, \qquad p_1' = P/2 + p', \tag{4.2.1a}$$
$$p_2 = P/2 - p, \qquad p_2' = P/2 - p'. \tag{4.2.1b}$$

For low momentum transfers, we find (see e.g. [1, 2, 43, 59, 62])

$$\mathbb{i}[\mathcal{K}_{D\bar{D}\leftrightarrow SS}]_{ij}^{s_1 s_2, s_1' s_2'} \simeq +\mathbb{i}4m^2 (y^2\delta_{ij}) \, \frac{1}{2}\left[\frac{\delta^{s_1 s_1'}\delta^{s_2 s_2'}}{(\mathbf{p}'-\mathbf{p})^2 + m_H^2} - \frac{\delta^{s_1 s_2'}\delta^{s_2 s_1'}}{(\mathbf{p}'+\mathbf{p})^2 + m_H^2}\right], \tag{4.2.2a}$$

$$\mathbb{i}[\mathcal{K}_{D\bar{D}\leftrightarrow D\bar{D}}]_{ij,i'j'}^{s_1 s_2, s_1' s_2'} \simeq +\frac{\mathbb{i}4m^2}{(\mathbf{p}'-\mathbf{p})^2} \left(g_1^2 Y_D^2 \delta_{ii'}\delta_{jj'} + g_2^2 t_{i'i}^a t_{jj'}^a\right) \delta^{s_1 s_1'}\delta^{s_2 s_2'}, \tag{4.2.2b}$$

$$\begin{aligned}\mathbb{i}[\mathcal{K}_{DD\leftrightarrow DD}]_{ij,i'j'}^{s_1 s_2, s_1' s_2'} \simeq -\mathbb{i}4m^2 \, \frac{1}{2}\Bigg[&\frac{\left(g_1^2 Y_D^2 \delta_{ii'}\delta_{jj'} + g_2^2 t_{i'i}^a t_{j'j}^a\right)\delta^{s_1 s_1'}\delta^{s_2 s_2'}}{(\mathbf{p}'-\mathbf{p})^2} \\ &- \frac{\left(g_1^2 Y_D^2 \delta_{ij'}\delta_{ji'} + g_2^2 t_{j'i}^a t_{i'j}^a\right)\delta^{s_1 s_2'}\delta^{s_2 s_1'}}{(\mathbf{p}'+\mathbf{p})^2}\Bigg],\end{aligned} \tag{4.2.2c}$$

$$\mathbb{i}[\mathcal{K}_{DS\leftrightarrow DS}]_{i,i'}^{s_1 s_2, s_1' s_2'} \simeq -\frac{\mathbb{i}4m^2}{(\mathbf{p}'+\mathbf{p})^2 + m_H^2} (y^2\delta_{ii'}) \delta^{s_1 s_2'}\delta^{s_2 s_1'}. \tag{4.2.2d}$$

In determining the sign of each contribution in the above, we have taken into account the number of fermion permutations needed to perform the Wick contractions. This is the origin of the relative minus sign between the t- and u-channels of the $D\bar{D} \leftrightarrow SS$ and $DD \leftrightarrow DD$

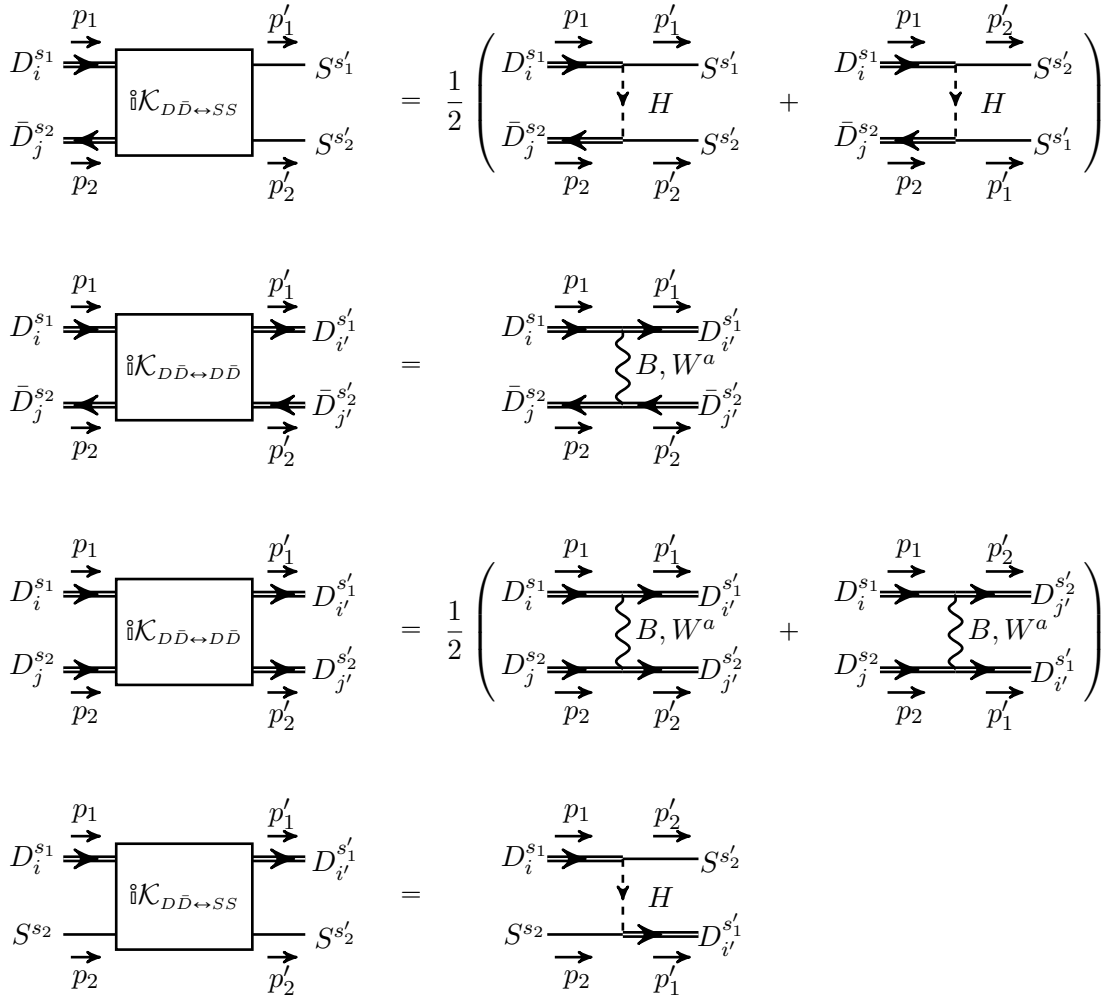

Figure 4.1: The kernels generating the long-range potentials between pairs of D, $\bar{D}$ and S fermions. The double lines represent the $SU_L(2) \times U_Y(1) = (2, 1/2)$ fermion D while the single lines stand for the gauge singlet S. The arrows on the fermion lines denote the flow of Hypercharge. The indices i, j, i', j' and s_1, s_2, s_1', s_2' are $SU_L(2)$ and spin indices, respectively. The factors $1/2$ in the interactions involving identical particles, $D\bar{D} \leftrightarrow SS$ and $DD \leftrightarrow DD$, ensure that the resummation of the kernels does not result in double-counting of loops (cf. appendix E.)

interactions. The factors 1/2 appearing in eqs. (4.2.2a) and (4.2.2c) ensure that the resummation of the kernels does not double-count the loop diagrams by exchanging identical particles in the loops; this is shown in appendix E.

To obtain the non-relativistic potentials, we must diagonalise the interactions (4.2.2) in momentum, spin, and gauge charge space.

Momentum space. The kernels of both the t- and u-channel diagrams depend only on the momentum transfer, which is however different in the two cases, $\mathcal{K}_t(\mathbf{p}-\mathbf{p}')$ and $\mathcal{K}_u(\mathbf{p}+\mathbf{p}')$. This implies that in position space, the u-channel potential depends on the orbital angular momentum mode ℓ of the state under consideration [2, appendix A]. Specifically, the static potentials generated by t- and u-channel diagrams are [2, 59]

$$V_t(r) = -\frac{1}{\mathbb{i}4m^2}\int \frac{d^3\mathbf{q}}{(2\pi)^3}\,\mathbb{i}\mathcal{K}_t(\mathbf{q})\,e^{\mathbb{i}\mathbf{q}\cdot\mathbf{r}}, \tag{4.2.3a}$$

$$V_u(r) = -\frac{(-1)^\ell}{\mathbb{i}4m^2}\int \frac{d^3\mathbf{q}}{(2\pi)^3}\,\mathbb{i}\mathcal{K}_u(\mathbf{q})\,e^{\mathbb{i}\mathbf{q}\cdot\mathbf{r}}. \tag{4.2.3b}$$

Inserting eqs. (4.2.2) into (4.2.3) yields the well-known Coulomb and Yukawa potentials.

Spin diagonalisation. The factor $\delta^{s_1 s_1'}\delta^{s_2 s_2'}$ and $\delta^{s_1 s_2'}\delta^{s_2 s_1'}$ arising from t- and u-channel exchanges respectively, can be written in matrix form in the basis $\{\uparrow\uparrow,\ \uparrow\downarrow,\ \downarrow\uparrow,\ \downarrow\downarrow\}$ as

$$t\text{-channel:}\quad \begin{pmatrix} 1&0&0&0\\ 0&1&0&0\\ 0&0&1&0\\ 0&0&0&1 \end{pmatrix}, \qquad u\text{-channel:}\quad \begin{pmatrix} 1&0&0&0\\ 0&0&1&0\\ 0&1&0&0\\ 0&0&0&1 \end{pmatrix}. \tag{4.2.4}$$

Clearly, the t-channel interactions conserve spin along each leg of the ladder, and the corresponding spin factor is simply the unity operator. On the other hand, the u-channel interactions conserve the total spin only. Indeed, the u-channel spin eigenvalues are $\{-1,1,1,1\}$, and correspond to the eigenvectors of total spin

$$\frac{1}{\sqrt{2}}(0,1,-1,0)^T, \quad (0,0,0,1)^T, \quad \frac{1}{\sqrt{2}}(0,1,1,0)^T, \quad (1,0,0,0)^T. \tag{4.2.5}$$

In the following, we shall therefore project the asymptotic states of pairs of $S, D, \bar{D}$ fermions onto eigenstates of total spin.

Gauge-charge diagonalisation. Since the interactions respect the $SU_L(2)$ symmetry, this amounts to projecting on $SU_L(2)$ representations of the incoming or outgoing pairs. For two multiplets transforming under the representations $\mathbb{R}_1$ and $\mathbb{R}_2$ of a gauge group, the Coulomb potential generated by the gauge-boson exchange in the configuration $\mathbb{R} \subset \mathbb{R}_1 \otimes \mathbb{R}_2$ of the pair is $V^{\mathbb{R}}(r) = -\alpha^{\mathbb{R}}/r$ with [97]

$$\alpha^{\mathbb{R}} = \frac{\alpha}{2}[C_2(\mathbb{R}_1) + C_2(\mathbb{R}_2) - C_2(\mathbb{R})], \tag{4.2.6}$$

where α is the fine structure constant of the group, and $C_2(\mathbb{R})$ is the quadratic Casimir operator of the representation $\mathbb{R}$. For $SU(2)$, $\mathbb{2}\otimes\mathbb{2} = \mathbb{1}+\mathbb{3}$, and $C_2(\mathbb{2}) = 3/4$, $C_2(\mathbb{3}) = 2$. Thus, the $D\bar{D}$, DD and $\bar{D}\bar{D}$ pairs appear in $SU_L(2)$ singlet and triplet configurations, with $\alpha_2^{\mathbb{1}} = 3\alpha_2/4$ and $\alpha_2^{\mathbb{3}} = -\alpha_2/4$ respectively. In the case of identical-particle pairs DD and $\bar{D}\bar{D}$, the (anti)symmetry of the $SU_L(2)$ (singlet) triplet states in gauge space generates also the factor $(-1)^{I+1}$ for the

u-channel diagrams, where here $I = 0, 1$ stands for the Weak isospin. Note that the $U_Y(1)$ potentials are of course not affected by the $SU_L(2)$ diagonalisation.[1]

The remaining task is the H-mediated interaction of eq. (4.2.2a). This occurs only in the $SU_L(2)$ singlet state. Projecting $D\bar{D}$ on the singlet, we obtain

$$\frac{\delta^{ij}}{\sqrt{2}}(y^2\delta_{ij}) = \sqrt{2}y^2. \tag{4.2.7}$$

Kernel (anti)symmetrisation. We close this discussion by noting the importance of considering properly both the t- and u-channel diagrams when identical particles are present in the initial and/or final states, as e.g. in the $D\bar{D} \leftrightarrow SS$ and $DD \leftrightarrow DD$ interactions of the present model. Using the correct kernel, as derived in appendix E, and taking into account the above yields the overall factor

$$[1 - (-1)^{\ell}(-1)^{s+1}(-1)^{I+1}]/2 \tag{4.2.8}$$

that enforces the proper particle statistics. This result is valid for pairs of fermions as well as pairs of scalars. Collecting the above, in table 4.2 we summarise the potentials generated by the one-boson-exchange diagrams of fig. 4.1.

Interaction	$U_Y(1)$	$SU_L(2)$	Potential	Sign of the potential	
				$\ell + s =$ even	$\ell + s =$ odd
$D\bar{D} \leftrightarrow SS$	0	$\mathbb{1}$	$-\left[\frac{1+(-1)^{\ell+s}}{2}\right] \sqrt{2}\alpha_H \frac{e^{-m_H r}}{r}$	attractive	0
$D\bar{D} \leftrightarrow D\bar{D}$	0	$\mathbb{1}$	$-\frac{(\alpha_1+3\alpha_2)/4}{r}$	attractive	attractive
		$\mathbb{3}$	$-\frac{(\alpha_1-\alpha_2)/4}{r}$	repulsive	repulsive
$DD \leftrightarrow DD$	1	$\mathbb{1}$	$\left[\frac{1-(-1)^{\ell+s}}{2}\right] \frac{(\alpha_1-3\alpha_2)/4}{r}$	0	attractive
		$\mathbb{3}$	$\left[\frac{1+(-1)^{\ell+s}}{2}\right] \frac{(\alpha_1+\alpha_2)/4}{r}$	repulsive	0
$SD \leftrightarrow SD$	1/2	$\mathbb{2}$	$-(-1)^{\ell+s} \alpha_H \frac{e^{-m_H r}}{r}$	attractive	repulsive

Table 4.2: The static potentials generated by the W, B and H-exchange diagrams shown in fig. 4.1. ℓ and s denote the orbital angular momentum mode and the total spin respectively.

[1] All these results can be easily recovered by organising the gauge factors of eqs. (4.2.2b) and (4.2.2c) in 4×4 matrices with elements $\{ij, i'j'\}$ and diagonalising them.

4.2.2 Asymptotic scattering and bound states

The potentials of table 4.2 determine the asymptotic states. For all gauge assignments except the singlet states, $SU_L(2) \times U_Y(1) = (\mathbb{1}, 0)$, finding the corresponding wavefunctions is rather straightforward; it amounts to solving a single Schrödinger equation with the corresponding potential, and antisymmetrising the wavefunction in the case of identical particles. For the gauge-singlet states, the $D\bar{D} \leftrightarrow SS$ interaction implies that a system of coupled Schrödinger equations must be solved. We work out this case in detail in section 4.2.2, after we discuss the general properties of the wavefunctions and the underlying hierarchy of scales in section 4.2.2. All the results on the wavefunctions of the scattering and bound states are summarised in tables 4.3 and 4.4.

Wavefunctions and hierarchy of scales

The non-relativistic potentials of table 4.2include both Coulomb and Yukawa contributions. The latter does not allow for analytical solutions. In order to obtain analytical expressions for the wavefunctions and ultimately the various cross-sections of interest, we shall neglect the Higgs mass in the potentials of table 4.2,

$$m_H \to 0, \tag{4.2.9}$$

although we will retain it in the phase-space suppression of BSF via H emission computed in section 4.3, as well as in the H propagator of BSF via off-shell H exchange with the thermal bath, computed in section 4.4. We discuss the validity of this approximation in section 4.2.2.

In the approximation (4.2.9), we can express all wavefunctions in terms of those for a Coulomb potential $V(r) = -\alpha/r$, which we shall denote as $\varphi(\mathbf{r};\ \alpha)$ and we now summarise. For clarity, we denote by $\alpha_{\mathcal{S}}$ and $\alpha_{\mathcal{B}}$ the couplings of the scattering and bound states. The momentum of each particle in the CM frame in the scattering states is $\mathbf{k} \equiv \mu \mathbf{v}_{\rm rel}$, with $\mathbf{v}_{\rm rel}$ being the relative velocity. The Bohr momenta in the scattering and bound states are $\kappa_{\mathcal{S}} \equiv \mu\alpha_{\mathcal{S}}$ and $\kappa_{\mathcal{B}} \equiv \mu\alpha_{\mathcal{B}}$. For convenience, we define the parameter $\zeta_{\mathcal{S}} \equiv \kappa_{\mathcal{S}}/k = \alpha_{\mathcal{S}}/v_{\rm rel}$ (in section 4.3 we will also use $\zeta_{\mathcal{B}} \equiv \kappa_{\mathcal{B}}/k = \alpha_{\mathcal{B}}/v_{\rm rel}$), and the variables $x_{\mathcal{S}} \equiv kr$ and $x_{\mathcal{B}} \equiv \kappa r$. The energy eigenvalues of the scattering and bound states are

$$\mathcal{E}_{\mathbf{k}} = \frac{\mathbf{k^2}}{2\mu} = \frac{\mu v_{\rm rel}^2}{2}, \qquad \mathcal{E}_n = -\frac{\kappa^2}{2\mu\, n^2} = -\frac{\mu\alpha_{\mathcal{B}}^2}{2n^2}. \tag{4.2.10}$$

The scattering state wavefunctions can be decomposed in partial waves,

$$\varphi_{\mathbf{k}}(\mathbf{r};\ \alpha_{\mathcal{S}}) = \sum_{\ell_{\mathcal{S}}=0}^{\infty} (2\ell_{\mathcal{S}}+1) \left[\frac{\varphi_{|\mathbf{k}|,\ell_{\mathcal{S}}}(x_{\mathcal{S}};\ \alpha_{\mathcal{S}})}{x_{\mathcal{S}}}\right] P_{\ell_{\mathcal{S}}}(\hat{\mathbf{k}}\cdot\hat{\mathbf{r}}), \tag{4.2.11}$$

where

$$\begin{aligned}\varphi_{|\mathbf{k}|,\ell_{\mathcal{S}}}(x_{\mathcal{S}};\ \alpha_{\mathcal{S}}) = &-\frac{\sqrt{S_0(\zeta_{\mathcal{S}})}}{(2\ell_{\mathcal{S}}+1)!}\,\frac{\Gamma(1+\ell_{\mathcal{S}}-\mathbb{i}\zeta_{\mathcal{S}})}{\Gamma(1-\mathbb{i}\zeta_{\mathcal{S}})} \\ &\times e^{-ix_{\mathcal{S}}}\, x_{\mathcal{S}}\, (2\mathbb{i}x_{\mathcal{S}})^{\ell_{\mathcal{S}}}\, {}_1F_1(1+\ell_{\mathcal{S}}+\mathbb{i}\zeta_{\mathcal{S}};\ 2\ell_{\mathcal{S}}+2;\ 2\mathbb{i}x_{\mathcal{S}}),\end{aligned} \tag{4.2.12}$$

and

$$S_0(\zeta_{\mathcal{S}}) \equiv \frac{2\pi\zeta_{\mathcal{S}}}{1-e^{-2\pi\zeta_{\mathcal{S}}}} \tag{4.2.13}$$

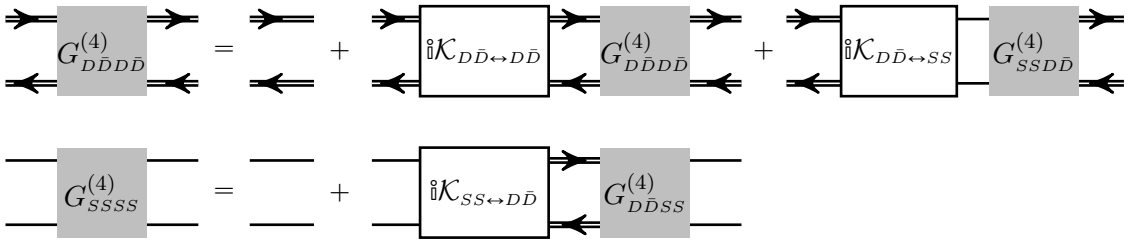

Figure 4.2: The resummation of 2PI diagrams for the gauge-singlet states, $SU_L(2) \times U_Y(1) = (\mathbb{1}, 0)$. Single and double lines correspond to S and D respectively.

is the well-known s-wave Sommerfeld factor. The bound-state wavefunctions are

$$\begin{aligned}\varphi_{n\ell m}(\mathbf{r};\alpha_{\mathcal{B}}) = \kappa^{3/2} Y_{\ell m}(\Omega_{\mathbf{r}})\ \frac{2}{n^2(2\ell+1)!}\left[\frac{(n+\ell)!}{(n-\ell-1)!}\right]^{1/2} \\ \times\, e^{-x_{\mathcal{B}}/n}\ (2x_{\mathcal{B}}/n)^{\ell}\ {}_1F_1\left(-n+\ell+1;\ 2\ell+2;\ 2x_{\mathcal{B}}/n\right),\end{aligned} \tag{4.2.14}$$

where the normalisation of the spherical harmonics is $\int d\Omega\, Y_{\ell m}(\Omega) Y^*_{\ell' m'}(\Omega) = \delta_{\ell\ell'}\delta_{mm'}$.

The emergence of the Sommerfeld effect and the existence of bound states emanate from the different scales involved in the interactions of the D, $\bar{D}$ and S particles,

$$\mu v_{\rm rel}^2/2 \ll \mu v_{\rm rel} \ll \mu < m \qquad \text{and} \qquad \mu\alpha^2/(2n^2) \ll \mu|\alpha|/n \ll \mu < m, \tag{4.2.15}$$

where here $\alpha = \alpha_{\mathcal{S}}$ or $\alpha_{\mathcal{B}}$. (Note that $\alpha_{\mathcal{S}}$ may be negative.) In computing the BSF cross-sections in sections 4.3 and 4.4, we make approximations based on these hierarchies.

The hierarchies (4.2.15) imply that the couplings (4.1.5) must be evaluated at the appropriate momentum transfer in every occurrence. The average momentum transfers in the annihilation vertices, the scattering-state potentials, the bound-state potentials, and the emission vertices for BSF and bound-to-bound transitions are respectively

$$Q \ \approx\ m,\ \ \mu v_{\rm rel},\ \ \mu\alpha_{\mathcal{B}},\ \ (\mu/2)(\alpha_{\mathcal{B}}^2/n^2 + v_{\rm rel}^2),\ \ (\mu/2)|\alpha_{\mathcal{B}}^2/n^2 - {\alpha'_{\mathcal{B}}}^2| \tag{4.2.16}$$

(cf. section 4.3 for the last two.) Here for simplicity we will neglect the running of the couplings (although it is easy to restore the scale dependence in all of our analytical results.) In computing the DM freeze-out in section 4.5, we adopt the values of the gauge couplings α_1 and α_2 at the Z pole, $\alpha_1(m_Z) \simeq 0.00973$ and $\alpha_2(m_Z) \simeq 0.0339$. Since α_H increases with Q, we consider the quoted values of α_H to correspond to the highest relevant scale, $Q = m$, such that the theory remains well-defined at all $Q \leqslant m$. For large values of α_H, a Landau pole appears at fairly low energies (but larger than m); however this may be cured by other new physics around those scales. For the renormalisation group equations in the present model, we refer to [124].

Mixed $SU_L(2) \times U_Y(1) = (\mathbb{1}, 0)$ states

The H exchange mixes SS and $D\bar{D}$ Fock states. The coupled resummation of the $D\bar{D} \leftrightarrow D\bar{D}$ and $D\bar{D} \leftrightarrow SS$ potentials is shown schematically in fig. 4.2. We define the wavefunctions of the gauge-singlet states

$$\Phi^j(\mathbf{r}) = \begin{pmatrix} [\phi(\mathbf{r})]^j_{SS} \\ [\phi(\mathbf{r})]^j_{D\bar{D}} \end{pmatrix}, \tag{4.2.17}$$

where the component wavefunctions are

$$[\phi(\mathbf{x})]^j_{SS} \equiv \langle \Omega | T\, S(x/2) S(-x/2) | \mathcal{S}^j_{(\mathbb{1},0)} \rangle_{x^0=0}, \tag{4.2.18a}$$

$$[\phi(\mathbf{x})]^j_{D\bar{D}} \equiv \langle \Omega | T\, D(x/2) \bar{D}(-x/2) | \mathcal{S}^j_{(\mathbb{1},0)} \rangle_{x^0=0}. \tag{4.2.18b}$$

Here, $\mathcal{S}^j_{(\mathbb{1},0)}$ denotes the gauge-singlet states. Along with their wavefunctions Φ^j, they carry quantum numbers that define their energy, angular momentum and spin, and that we have here left implicit. The superscript j aims to differentiate between states with the same quantum numbers but different boundary conditions. Ω stands for the vacuum of the interacting theory, T is the time ordering operator, S, D and $\bar{D}$ are the field operators.

The resummation sketched in fig. 4.2 implies that Φ obey the Schrödinger equations

$$\left[-\frac{\nabla^2}{2\mu} + \mathbb{V}_{(\mathbb{1},0)}(r) \right] \Phi(\mathbf{r}) = \mathcal{E} \Phi(\mathbf{r}), \tag{4.2.19}$$

where $\mathbb{V}_{(\mathbb{1},0)}$ is the 2×2 potential matrix of the gauge-singlet states

$$\mathbb{V}_{(\mathbb{1},0)}(r) = -\frac{1}{r} \begin{pmatrix} 0 & \delta_{\ell+s,\text{even}} \sqrt{2} \alpha_H \, \exp(-m_H r) \\ \delta_{\ell+s,\text{even}} \sqrt{2} \alpha_H \, \exp(-m_H r) & (\alpha_1 + 3\alpha_2)/4 \end{pmatrix}. \tag{4.2.20}$$

In the limit $m_H \to 0$, the system (4.2.19) easily decouples. We first define the couplings

$$\alpha_R \equiv \frac{1}{2} \left[\sqrt{[(\alpha_1 + 3\alpha_2)/4]^2 + 8\alpha_H^2 \, \delta_{\ell+s,\text{even}}} - (\alpha_1 + 3\alpha_2)/4 \right], \tag{4.2.21a}$$

$$\alpha_A \equiv \frac{1}{2} \left[\sqrt{[(\alpha_1 + 3\alpha_2)/4]^2 + 8\alpha_H^2 \, \delta_{\ell+s,\text{even}}} + (\alpha_1 + 3\alpha_2)/4 \right], \tag{4.2.21b}$$

noting that $\alpha_R, \alpha_A \geqslant 0$, as well as the unitary matrix

$$P \equiv \frac{1}{\sqrt{\alpha_A + \alpha_R}} \begin{pmatrix} \sqrt{\alpha_A} & \sqrt{\alpha_R} \\ -\sqrt{\alpha_R} & \sqrt{\alpha_A} \end{pmatrix}, \tag{4.2.22}$$

whose columns are the normalised $\mathbb{V}_{(\mathbb{1},0)}$ eigenvectors with eigenvalues $-\alpha_R$ and α_A. Then, the rotated wavefunctions $\hat{\Phi} \equiv P^\dagger \Phi$ obey the Schrödinger equations

$$\left[-\frac{\nabla^2}{2\mu} + \hat{\mathbb{V}}_{(\mathbb{1},0)}(r) \right] \hat{\Phi}(\mathbf{r}) = \mathcal{E} \hat{\Phi}(\mathbf{r}), \tag{4.2.23}$$

with the potential

$$\hat{\mathbb{V}}_{(\mathbb{1},0)} = P^\dagger \mathbb{V}_{(\mathbb{1},0)} P = -\frac{1}{r} \begin{pmatrix} -\alpha_R & 0 \\ 0 & \alpha_A \end{pmatrix}. \tag{4.2.24}$$

We now seek scattering and bound state solutions to eq. (4.2.23).

Scattering states. The scattering state solutions of eq. (4.2.23) are given by eq. (4.2.11), albeit the normalisation of each component is allowed to vary and will be determined by the boundary conditions on Φ^j. Analysing eq. (4.2.23) in partial waves, the solutions are

$$\hat{\Phi}^j_{|\mathbf{k}|,\ell}(x_\mathcal{S}) = \begin{pmatrix} N^j_R \, \varphi_{|\mathbf{k}|,\ell}(x_\mathcal{S};\ -\alpha_R) \\ N^j_A \, \varphi_{|\mathbf{k}|,\ell}(x_\mathcal{S};\ \alpha_A) \end{pmatrix}, \tag{4.2.25}$$

where at $x_{\mathcal{S}} \to \infty$, the wavefunctions $\varphi_{\mathbf{k},\ell}(x_{\mathcal{S}};\ \alpha)$ obey

$$\frac{d\varphi_{|\mathbf{k}|,\ell}(x_{\mathcal{S}};\ \alpha)}{dx_{\mathcal{S}}} - \mathbb{i}\varphi_{|\mathbf{k}|,\ell}(x_{\mathcal{S}};\ \alpha) = e^{-\mathbb{i}(x_{\mathcal{S}}-\ell\pi)}. \tag{4.2.26}$$

We seek scattering-state solutions to eq. (4.2.19) that asymptote at $r \to \infty$ to a pure SS or $D\bar{D}$ state. In terms of partial waves, this implies that at $r \to \infty$,

$$SS\text{-like state:} \qquad \frac{d[\phi_\ell(x_{\mathcal{S}})]_i^{SS}}{dx_{\mathcal{S}}} - \mathbb{i}[\phi_\ell(x_{\mathcal{S}})]_i^{SS} = \delta_i^{SS} e^{-\mathbb{i}(x_{\mathcal{S}}-\ell\pi)} \times \sqrt{2}\delta_{\ell+s,\text{even}}, \tag{4.2.27a}$$

$$D\bar{D}\text{-like state:} \qquad \frac{d[\phi_\ell(x_{\mathcal{S}})]_i^{D\bar{D}}}{dx_{\mathcal{S}}} - \mathbb{i}[\phi_\ell(x_{\mathcal{S}})]_i^{D\bar{D}} = \delta_i^{D\bar{D}} e^{-\mathbb{i}(x_{\mathcal{S}}-\ell\pi)}, \tag{4.2.27b}$$

where $i = SS, D\bar{D}$ denotes the component. In eq. (4.2.27a), we included the antisymmetrisation factor due to the identical particles in the SS-like state, with $s = 0$ or 1 being the total spin (cf. appendix E.2).

Since $\hat{\Phi}_{|\mathbf{k}|,\ell}(x_{\mathcal{S}}) = P^\dagger \Phi_{|\mathbf{k}|,\ell}(x_{\mathcal{S}})$, the asymptotic behaviours (4.2.26) and (4.2.27) imply

$$\begin{pmatrix} N_R^{SS} \\ N_A^{SS} \end{pmatrix} = P^\dagger \begin{pmatrix} \sqrt{2}\delta_{\ell+s,\text{even}} \\ 0 \end{pmatrix} = \frac{\sqrt{2}\delta_{\ell+s,\text{even}}}{\sqrt{\alpha_A + \alpha_R}} \begin{pmatrix} \sqrt{\alpha_A} \\ \sqrt{\alpha_R} \end{pmatrix}, \tag{4.2.28a}$$

$$\begin{pmatrix} N_R^{D\bar{D}} \\ N_A^{D\bar{D}} \end{pmatrix} = P^\dagger \begin{pmatrix} 0 \\ 1 \end{pmatrix} = \frac{1}{\sqrt{\alpha_A + \alpha_R}} \begin{pmatrix} -\sqrt{\alpha_R} \\ \sqrt{\alpha_A} \end{pmatrix}. \tag{4.2.28b}$$

We recall that α_R and α_A depend on $\ell + s$, and note that while the $D\bar{D}$-like state should *not* be antisymmetrised, the SS components of the symmetric $\ell + s =$ odd modes do vanish due to the antisymmetrisation of the kernel ($\alpha_R = 0$ for $\ell + s =$ odd). Equivalently, we could have required that the SS components of both of the SS-like and $D\bar{D}$-like states are antisymmetrised. Combining eqs. (4.2.25) and (4.2.28), we obtain the wavefunctions $\Phi^j_{|\mathbf{k}|,\ell}(\mathbf{r}) = P\hat{\Phi}^j_{|\mathbf{k}|,\ell}(\mathbf{r})$. The results are summarised in table 4.3.

Bound states. It is easy to see that eq. (4.2.23) has only one set of bound-state solutions, $\hat{\Phi}_{n\ell m}(\mathrm{r}) = (0,\quad \varphi_{n\ell m}(\mathbf{r};\ \alpha_A))^T$, with $\mathcal{E}_n = -\mu\alpha_A^2/(2n^2)$. The unrotated wavefunctions are $\Phi_{n\ell m}(\mathrm{r}) = P\hat{\Phi}_{n\ell m}(\mathrm{r})$.

Validity of the Coulomb approximation $m_H \to 0$

Scattering states. The scattering states are listed in table 4.3. The DS states with $\ell + s =$ even are subject to an attractive Higgs-mediated potential, and the Coulomb approximation is good as long as [43]

$$\mu v_{\text{rel}} \gtrsim m_H. \tag{4.2.29}$$

The condition becomes stronger for the DS scattering states with $\ell + s =$ odd, where the Higgs-mediated potential is repulsive. Moreover, it is relaxed or strengthened in the presence of an additional attractive or repulsive Coulomb potential due to B or W exchange, as is the case with the SS-like and $D\bar{D}$-like scattering states for $\ell + s =$ even [54, figs. 2, 3].

Bound states. The bound states of the present model are listed in table 4.4. The DS states with $\ell + s =$ even are bound only by the Higgs-mediated potential; they exist if $(\mu\alpha_H/n)/m_H > 0.84$, and become essentially Coulombic if this condition is strengthened only by a factor of a few [43]. (For example, the binding energy of the ground state exceeds 80% of its Coulomb

$U_Y(1)$	$SU_L(2)$	State	Component	Partial-wave wavefunctions
0	$\mathbb{1}$	SS-like	SS	$\delta_{\ell+s,\text{even}}\ \dfrac{\sqrt{2}}{\alpha_A+\alpha_R}\ \Big[\alpha_R\varphi_{\lvert\mathbf{k}\rvert,\ell}(x_{\mathcal{S}};\alpha_A)+\alpha_A\varphi_{\lvert\mathbf{k}\rvert,\ell}(x_{\mathcal{S}};-\alpha_R)\Big]$
			$D\bar{D}$	$\delta_{\ell+s,\text{even}}\ \dfrac{\sqrt{2\alpha_A\alpha_R}}{\alpha_A+\alpha_R}\ \Big[\varphi_{\lvert\mathbf{k}\rvert,\ell}(x_{\mathcal{S}};\alpha_A)-\varphi_{\lvert\mathbf{k}\rvert,\ell}(x_{\mathcal{S}};-\alpha_R)\Big]$
0	$\mathbb{1}$	$D\bar{D}$-like	SS	$\dfrac{\sqrt{\alpha_A\alpha_R}}{\alpha_A+\alpha_R}\ \Big[\varphi_{\lvert\mathbf{k}\rvert,\ell}(x_{\mathcal{S}};\alpha_A)-\varphi_{\lvert\mathbf{k}\rvert,\ell}(x_{\mathcal{S}};-\alpha_R)\Big]$
			$D\bar{D}$	$\dfrac{1}{\alpha_A+\alpha_R}\ \Big[\alpha_A\varphi_{\lvert\mathbf{k}\rvert,\ell}(x_{\mathcal{S}};\alpha_A)+\alpha_R\varphi_{\lvert\mathbf{k}\rvert,\ell}(x_{\mathcal{S}};-\alpha_R)\Big]$
0	$\mathbb{3}$	$D\bar{D}$	$D\bar{D}$	$\varphi_{\lvert\mathbf{k}\rvert,\ell}\left(x_{\mathcal{S}};\ (\alpha_1-\alpha_2)/4\right)$
1	$\mathbb{1}$	DD	DD	$\delta_{\ell+s,\text{odd}}\ \sqrt{2}\quad \varphi_{\lvert\mathbf{k}\rvert,\ell}\left(x_{\mathcal{S}};\ (-\alpha_1+3\alpha_2)/4\right)$
1	$\mathbb{3}$	DD	DD	$\delta_{\ell+s,\text{even}}\ \sqrt{2}\quad \varphi_{\lvert\mathbf{k}\rvert,\ell}\left(x_{\mathcal{S}};\ -(\alpha_1+\alpha_2)/4\right)$
1/2	$\mathbb{2}$	DS	DS	$\varphi_{\lvert\mathbf{k}\rvert,\ell}\left(x_{\mathcal{S}};\ (-1)^{\ell+s}\alpha_H\right)$

Table 4.3: The scattering states and their wavefunctions in the limit $m_H \to 0$. Here, $\varphi_{|\mathbf{k}|,\ell}(x_{\mathcal{S}};\ \alpha)$ denotes the ℓ mode of a scattering state with momentum $\mathbf{k}$ for a Coulomb potential $V(r) = -\alpha/r$; the position variable is $x_{\mathcal{S}} \equiv kr$. The couplings α_A and α_R, defined in eqs. (4.2.21), depend on $\ell + s$. For $\ell + s =$ odd, the $(\mathbb{1}, \mathbb{0})$ mixed states decouple.

$U_Y(1)$	$SU_L(2)$	Binding energy	Bound state/ component	Wavefunctions
0	$\mathbb{1}$	$\dfrac{\mu\alpha_A^2}{2n^2}$	SS	$\sqrt{\dfrac{\alpha_R}{\alpha_A+\alpha_R}}\quad \varphi_{n\ell m}(\mathbf{r};\ \alpha_A)$
			$D\bar{D}$	$\sqrt{\dfrac{\alpha_A}{\alpha_A+\alpha_R}}\quad \varphi_{n\ell m}(\mathbf{r};\ \alpha_A)$
1	$\mathbb{1}$	$\dfrac{\mu\left[(-\alpha_1+3\alpha_2)/4\right]^2}{2n^2}$	DD	$\delta_{\ell+s,\text{odd}}\sqrt{2}\quad \varphi_{n\ell m}\left(\mathbf{r};\ (-\alpha_1+3\alpha_2)/4\right)$
1/2	$\mathbb{2}$	$\dfrac{\mu\alpha_H^2}{2n^2}$	DS	$\delta_{\ell+s,\text{even}}\quad \varphi_{n\ell m}(\mathbf{r};\ \alpha_H)$

Table 4.4: The bound states and their wavefunctions in the limit $m_H \to 0$. Here $\varphi_{n\ell m}(\mathbf{r};\ \alpha)$ denotes the bound state wavefunction with quantum numbers $\{n\ell m\}$ for a Coulomb potential $V(r) = -\alpha/r$. The couplings α_A and α_R are defined in eqs. (4.2.21), and depend on $\ell + s$. For $\ell + s =$ odd, the $(\mathbb{1}, \mathbb{0})$ state becomes purely $D\bar{D}$.

value if $\mu\alpha_H/m_H > 10$ [43, fig. 13].) The mixed $SS/D\bar{D}$ states are bound by the combined attraction of the B, W and H bosons, which removes the condition of existence and relaxes the condition for the Coulomb approximation [55, fig. 6]. Thus, the strongest condition for the

Coulomb approximation to be satisfactory is

$$\mu\alpha_H/n > \text{few} \times m_H. \tag{4.2.30}$$

We note that this condition is essentially satisfied everywhere BSF via Higgs emission is phenomenologically significant (cf. section 4.3.) Indeed, the energy available to be dissipated must exceed the Higgs mass, $(\mu/2)[(\alpha_H/n)^2 + v_{\rm rel}^2] > m_H$, while BSF is most significant when $v_{\rm rel} \lesssim \alpha_H/n$. Since $\alpha_H < 1$, this yields a stronger condition. Bound states can also form via B or W emission, however we shall see that these processes are less significant.

We further discuss the Coulomb approximation for the DM freeze-out in section 4.7.

4.2.3 Annihilation

The S, D and $\bar{D}$ fermions annihilate into SM particles via various processes that we list in table 4.5 together with their tree-level cross-sections and Sommerfeld factors. We consider s-wave contributions only. Because the non-relativistic potentials between the annihilating particles depend in many cases on their spin and gauge representations, we project the initial state on eigenstates of total spin and Weak isospin. With the help of table 4.3, it is straightforward to obtain the Sommerfeld factors for all states except the spin-0 $(\mathbb{1}, 0)$ ones, which involve mixing of the SS and $D\bar{D}$ channels nd we discuss in detail below. The Sommerfeld factors are expressed in term of the $S_0(\zeta)$ function defined in eq. (4.2.13), and the variables

$$\zeta_1 \equiv \alpha_1/v_{\rm rel}, \quad \zeta_2 \equiv \alpha_2/v_{\rm rel}, \quad \zeta_H \equiv \alpha_H/v_{\rm rel}, \quad \zeta_A \equiv \alpha_A/v_{\rm rel}, \quad \zeta_R \equiv \alpha_R/v_{\rm rel}, \tag{4.2.31}$$

where the couplings α_1, α_2, α_H, α_A and α_R have been defined in eqs. (4.1.5) and (4.2.21). In fig. 4.3, we present the total s-wave 2-to-2 annihilation cross-section, averaged over the dof of the incoming particles.

Mixed $(\mathbb{1}, 0)$ spin-0 states

The annihilation amplitudes of the SS-like and $D\bar{D}$-like states (denoted by $\mathcal{M}$) are related to the perturbative amplitudes (denoted by $\mathcal{A}$) as follows

$$\text{i}\mathcal{M}^{SS\text{-like}\to f}(\mathbf{k}) = \int \frac{d^3\mathbf{k}'}{(2\pi)^3} \left[[\tilde{\phi}_{\mathbf{k}}(\mathbf{k}')]^{SS}_{SS}\ \text{i}\mathcal{A}_{SS\to f}(\mathbf{k}') + [\tilde{\phi}_{\mathbf{k}}(\mathbf{k}')]^{SS}_{D\bar{D}}\ \text{i}\mathcal{A}_{D\bar{D}\to f}(\mathbf{k}') \right], \tag{4.2.32a}$$

$$\text{i}\mathcal{M}^{D\bar{D}\text{-like}\to f}(\mathbf{k}) = \int \frac{d^3\mathbf{k}'}{(2\pi)^3} \left[[\tilde{\phi}_{\mathbf{k}}(\mathbf{k}')]^{D\bar{D}}_{SS}\ \text{i}\mathcal{A}_{SS\to f}(\mathbf{k}') + [\tilde{\phi}_{\mathbf{k}}(\mathbf{k}')]^{D\bar{D}}_{D\bar{D}}\ \text{i}\mathcal{A}_{D\bar{D}\to f}(\mathbf{k}') \right], \tag{4.2.32b}$$

where f stands for the final state, and $[\tilde{\phi}_{\mathbf{k}}(\mathbf{k}')]^j_i$ are the momentum-space wavefuntions, with the j and i indices denoting the state and the component respectively, as in section 4.2.2. Since the perturbative s-wave SS annihilation vanishes, in our approximation there is no interference between SS and $D\bar{D}$ channels. Considering that the perturbative s-wave annihilation amplitudes are independent of the momentum to lowest order in $v_{\rm rel}$, we obtain as is standard,

$$(\sigma v_{\rm rel})^{SS\text{-like}\to f} = \left| [\phi_{\mathbf{k}}(\mathbf{0})]^{SS}_{D\bar{D}} \right|^2 (\sigma v_{\rm rel})_{D\bar{D}\to f}, \tag{4.2.33a}$$

$$(\sigma v_{\rm rel})^{D\bar{D}\text{-like}\to f} = \left| [\phi_{\mathbf{k}}(\mathbf{0})]^{D\bar{D}}_{D\bar{D}} \right|^2 (\sigma v_{\rm rel})_{D\bar{D}\to f}, \tag{4.2.33b}$$

where $[\phi_{\mathbf{k}}(\mathbf{r})]_i^j$ are the position-space wavefunctions computed in section 4.2.2. Using the results quoted in table 4.3, we find

$$\left|[\phi_{\mathbf{k}}(\mathbf{0})]^{SS}_{D\bar{D}}\right|^2_{\text{spin-0}} = \frac{2\alpha_A\alpha_R\left[\sqrt{S_0(\zeta_A)}-\sqrt{S_0(-\zeta_R)}\right]^2}{(\alpha_A+\alpha_R)^2}, \tag{4.2.34a}$$

$$\left|[\phi_{\mathbf{k}}(\mathbf{0})]^{D\bar{D}}_{D\bar{D}}\right|^2 = \frac{\left[\alpha_A\sqrt{S_0(\zeta_A)}+\alpha_R\sqrt{S_0(-\zeta_R)}\right]^2}{(\alpha_A+\alpha_R)^2}. \tag{4.2.34b}$$

Note that eq. (4.2.34a) includes the symmetry factor of the spin-0 SS-like state, and that $\left|[\phi_{\mathbf{k}}(\mathbf{0})]^{SS}_{D\bar{D}}\right|^2_{\text{spin-1}} = 0$.

We are ultimately interested in the reduction of the DM density via the various annihilation processes. For the spin-0 $(\mathbb{1},0)$ states, the rate is (cf. section 4.5)

$$(n_S n_S)^{\text{spin-0}}_{(\mathbb{1},0)}\langle\sigma v_{\text{rel}}\rangle^{SS\text{-like}\to f} + 2(n_D n_{\bar{D}})^{\text{spin-0}}_{(\mathbb{1},0)}\langle\sigma v_{\text{rel}}\rangle^{D\bar{D}\text{-like}\to f}, \tag{4.2.35}$$

where n and $\langle\cdot\rangle$ denote densities and thermal averages. In the limit $m_S = m_D$, the densities are $(n_S n_S)^{\text{spin-0}}_{(\mathbb{1},0)} = (n_D n_{\bar{D}})^{\text{spin-0}}_{(\mathbb{1},0)}$, thus the DM density reduction rate can be computed by regarding that the spin-0 $(\mathbb{1},0)$ $D\bar{D}$ perturbative annihilation cross-sections are enhanced by the factor

$$\frac{1}{2}\left|[\phi_{\mathbf{k}}(\mathbf{0})]^{SS}_{D\bar{D}}\right|^2 + \left|[\phi_{\mathbf{k}}(\mathbf{0})]^{D\bar{D}}_{D\bar{D}}\right|^2 = \frac{\alpha_A S_0(\zeta_A)+\alpha_R S_0(-\zeta_R)}{\alpha_A+\alpha_R}. \tag{4.2.36}$$

We quote this result in table 4.5, but emphasise that $(n_S n_S)^{\text{spin-0}}_{(\mathbb{1},0)}$ and $(n_D n_{\bar{D}})^{\text{spin-0}}_{(\mathbb{1},0)}$ depend exponentially on the corresponding masses, thus eq. (4.2.36) ceases to be a good approximation already for fairly small mass differences $|m_D - m_S|$.

4.2.4 Ground-level bound states and their decay rates

Besides annihilating directly into radiation, the S, D and $\bar{D}$ fermions can form unstable bound states that decay rapidly into radiation, thereby enhancing the DM destruction rate. However, the DM annihilation via BSF is impeded by the inverse (ionisation) processes. The latter become inefficient as the temperature drops around or below the binding energy. This occurs earlier for the most deeply bound states, which therefore have the greatest effect on the DM density. Thus, for our purposes, we shall consider the ground level of each bound state species only, $\{n\ell m\} = \{100\}$, which has the largest binding energy.[2] We list the ground-level bound states in table 4.6.

Decay into radiation

The decay rate of bound states with zero angular momentum into radiation is

$$\Gamma_{\mathcal{B}(X_1X_2)\to f} = (\sigma_0 v_{\text{rel}})_{X_1X_2\to f} \times |\psi_{n00}(0)|^2, \tag{4.2.37}$$

where X_1X_2 represent the constituent fields of the bound state and f stands for the final state particles. $(\sigma_0 v_{\text{rel}})_{X_1X_2\to f}$ is the s-wave annihilation cross-section of an X_1X_2 state with the

[2] In addition to its ionisation becoming inefficient earlier, the cross-section for capture into the ground state is typically larger than those of excited states, if BSF occurs via vector emission [39, 43, 59, 62]. This strengthens the argument for considering only the ground states of each bound species. However, in ref. [2] it was shown that if BSF occurs via emission of a charged scalar (here the Higgs doublet), the capture into excited states can be comparable to the capture into the ground state. It is thus possible that excited states have substantial impact in the present model. We leave this investigation for future work.

Channel	$U_Y(1)$	$SU_L(2)$	Spin	dof	$(\sigma_0 v_{\rm rel})/(\pi m^{-2})$	Sommerfeld factor
$SS \to HH^\dagger$	0	$\mathbb{1}$	$0,1$	4	0	–
$D\bar{D} \to HH^\dagger$	0	$\mathbb{1}$	0	1	0	–
			1	3	$(\alpha_1 + 2\alpha_H)^2/12$	$S_0\left[(\zeta_1 + 3\zeta_2)/4\right]$
		$\mathbb{3}$	0	3	0	–
			1	9	$(\alpha_2 + 2\alpha_H)^2/12$	$S_0\left[(\zeta_1 - \zeta_2)/4\right]$
$D\bar{D} \to WW$	0	$\mathbb{1}$	0	1	$3\alpha_2^2/2$	$\dfrac{\alpha_A S_0(\zeta_A) + \alpha_R S_0(-\zeta_R)}{\alpha_A + \alpha_R}$
			1	3	0	–
		$\mathbb{3}$	0	3	0	–
			1	9	$\alpha_2^2/12$	$S_0\left[(\zeta_1 - \zeta_2)/4\right]$
$D\bar{D} \to BB$	0	$\mathbb{1}$	0	1	$\alpha_1^2/2$	$\dfrac{\alpha_A S_0(\zeta_A) + \alpha_R S_0(-\zeta_R)}{\alpha_A + \alpha_R}$
			1	3	0	–
		$\mathbb{3}$	$0,1$	12	0	–
$D\bar{D} \to WB$	0	$\mathbb{1}$	$0,1$	4	0	–
		$\mathbb{3}$	0	3	$\alpha_1\alpha_2$	$S_0\left[(\zeta_1 - \zeta_2)/4\right]$
			1	9	0	–
$D\bar{D} \to F_L\bar{F}_L$	0	$\mathbb{1}$	0	1	0	–
			1	3	$2Y_L^2\alpha_1^2/3$, $\sum Y_L^2 = 1$	$S_0\left[(\zeta_1 + 3\zeta_2)/4\right]$
		$\mathbb{3}$	0	3	0	–
			1	9	$N_L \times \alpha_2^2/6$ $N_L = 12$	$S_0\left[(\zeta_1 - \zeta_2)/4\right]$
$D\bar{D} \to f_R\bar{f}_R$	0	$\mathbb{1}$	0	1	0	–
			1	3	$Y_R^2\alpha_1^2/3$, $\sum Y_R^2 = 8$	$S_0\left[(\zeta_1 + 3\zeta_2)/4\right]$
		$\mathbb{3}$	$0,1$	12	0	–
$DD \to HH$	1	$\mathbb{1}$	0	1	0	–
			1	3	$4\alpha_H^2/3$	$S_0\left[(-\zeta_1 + 3\zeta_2)/4\right]$
		$\mathbb{3}$	$0,1$	12	0	–
$DS \to WH$	1/2	2	0	2	0	–
			1	6	$\alpha_2\alpha_H/2$	$S_0(-\zeta_H)$
$DS \to BH$	1/2	2	0	2	0	–
			1	6	$\alpha_1\alpha_H/6$	$S_0(-\zeta_H)$
$DS \to f_R\bar{F}_L,\ F_L\bar{f}_R$	1/2	2	$0,1$	8	0	–

Table 4.5: Annihilation processes, their tree-level s-wave velocity-weighted cross-sections $\sigma_0 v_{\rm rel}$ and Sommerfeld factors. All $\sigma_0 v_{\rm rel}$ are averaged over the degrees of freedom of the corresponding *projected* scattering state (5th column). For DD, $\sigma_0 v_{\rm rel}$ includes the symmetry factor due to the identical initial-state particles. For the gauge-singlet spin-0 $D\bar{D}$ channels, see text for discussion. $S_0(\zeta)$ and the various ζ parameters are defined in eqs. (4.2.13) and (4.2.31).

same quantum numbers (spin, gauge and global) as the bound state, averaged over the dof that correspond to those quantum numbers only (rather than all the dof of an X_1X_2 scattering

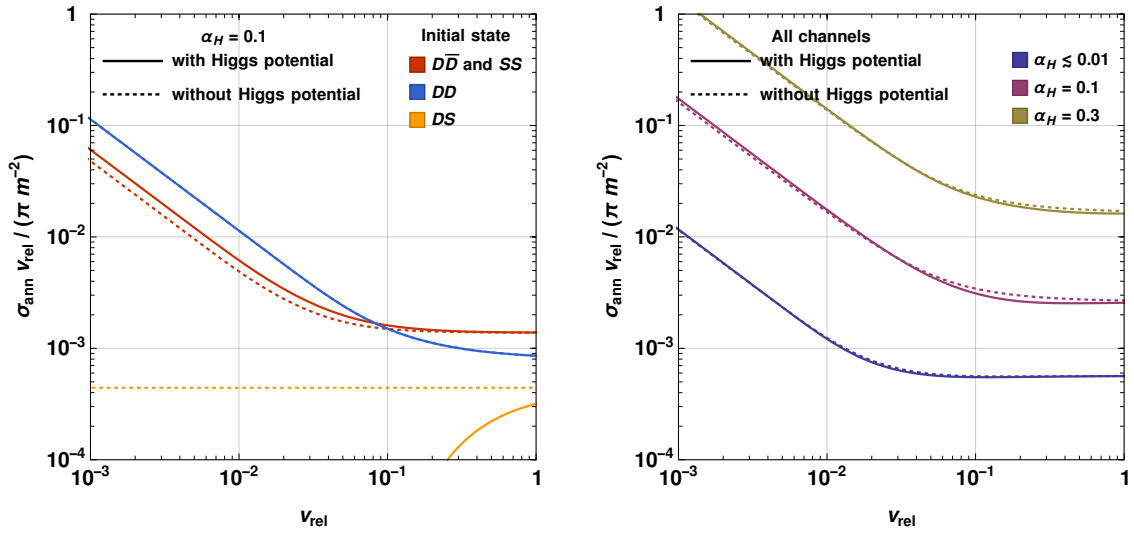

Figure 4.3: The s-wave annihilation cross-sections, by initial state (*left*) and total (*right*), averaged over the dof of the incoming particles, with and without the Higgs-mediated potential (cf. table 4.5). Because the processes affected by the latter have either low multiplicity or small perturbative cross-sections, the Sommerfeld effect at low velocities arises mostly due to the B^μ and W^μ gauge bosons. Note that we have weighted the contribution of each annihilation channel with the number of DM particles eliminated in each process as estimated upon thermal averaging (cf. section 4.5.)

state.) For an attractive Coulomb potential of strength α, the squared ground-state wavefunction evaluated at the origin is $|\psi_{n00}(0)|^2 = \kappa_{\mathcal{B}}^3/\pi = \mu^3\alpha^3/\pi$, where $\kappa_{\mathcal{B}} = \mu\alpha$ is the Bohr momentum.

Taking into account the s-wave annihilation processes of table 4.5, we compute the total decay rates of the ground states and list them in table 4.6. The decay of the mixed $SS/D\bar{D}$ bound state occurs via its $D\bar{D}$ component, and the rate is computed analogously to the annihilation of the mixed scattering states described in section 4.2.3. For the DD bound state, a factor 2 due to the antisymmetrisation of the wavefunction has already been included in the corresponding $\sigma_0 v_{\rm rel}$ in table 4.5 and should not be included twice when computing the decay rate of the bound state. As seen in table 4.5, the DS bound state cannot decay into two particles. It may decay instead into three bosons, however the corresponding rates are suppressed by higher powers of the couplings, $\mathcal{O}(\alpha_1^2\alpha_H^4,\ \alpha_2^2\alpha_H^4,\ \alpha_1\alpha_2\alpha_H^4,\ \alpha_H^6)$, as well as the three-body final-state phase space. The DS bound state instead decays much faster into the tighter $SS/D\bar{D}$ bound state, as we shall now see.

Transitions into deeper bound levels

Besides decaying directly into radiation, bound states may transition into lower-lying bound levels via dissipation of energy. The bound-to-bound transition rates are computed in a similar fashion to BSF processes, as we shall see in sections 4.3 and 4.4. Here we note that in radiative transitions (either scattering-to-bound or bound-to-bound), spin is conserved at leading order in the non-relativistic regime. Spin-flipping transitions can occur via emission of a vector boson, but rely on spin-orbit interaction and are suppressed by higher powers of the couplings. Consequently, they are subdominant to the direct bound-state decay rates into two relativistic species.

Considering the bound states of table 4.6, there are only two spin-conserving transitions, of

Bound state ($\mathcal{B}$)	$U_Y(1)$	$SU_L(2)$	Spin	dof (g_B)	Bohr momentum ($\kappa_\mathcal{B}$)	Decay rate (Γ_B)
$SS/D\bar{D}$	0	$\mathbb{1}$	0	1	$\frac{m\alpha_A}{2}$	$\frac{m\alpha_A^3(\alpha_1^2+3\alpha_2^2)}{16}\left(\frac{\alpha_A}{\alpha_A+\alpha_R}\right)$
$D\bar{D}$	0	$\mathbb{1}$	1	3	$\frac{m(\alpha_1+3\alpha_2)}{8}$	$\frac{m(\alpha_1+3\alpha_2)^3[(\alpha_1+2\alpha_H)^2+40\alpha_1^2]}{2^{11}\cdot 3}$
DD	1	$\mathbb{1}$	1	3	$\frac{m(-\alpha_1+3\alpha_2)}{8}$	$\frac{m(-\alpha_1+3\alpha_2)^3\alpha_H^2}{2^7\cdot 3}$
DS	1/2	$\mathbb{2}$	0	2	$\frac{m\alpha_H}{2}$	Negligible. Transition to $\mathcal{B}(SS/D\bar{D})$: eq. (4.3.26), eqs. (4.4.12) and (4.4.19) to (4.4.21)

Table 4.6: The ground-level bound states, $\{n\ell m\} = \{100\}$, and their rates of decay into radiation, in the limit $m_H \to 0$. The decay rate of the DS bound state is suppressed, and we reference instead the formulae for its transition rate to the $SS/D\bar{D}$ bound state. In the first row, α_A and α_R are found from eqs. (4.2.21) for $\ell = s = 0$. The binding energy of each bound state is $|\mathcal{E}_B| = \kappa_\mathcal{B}^2/m$.

which only one may occur with emission of a single boson contained in the theory. Noting that $\alpha_A \geqslant \alpha_H$ (cf. eq. (4.2.21b)), this transition is

$$\mathcal{B}(DS) \to \mathcal{B}(SS/D\bar{D}) + H. \tag{4.2.38}$$

In fact, much like BSF, bound-to-bound transitions may occur either radiatively or via scattering on the relativistic thermal bath. In sections 4.3 and 4.4, we compute the corresponding rates for the transition (4.2.38) and reference the results in table 4.6.

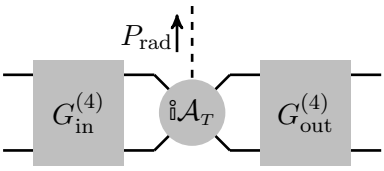

Figure 4.4: Radiative bound-state formation and bound-to-bound transitions.

4.3 Radiative bound-state formation and bound-to-bound transitions

We now compute the cross-sections for the radiative formation of the ground-level bound states of table 4.6. We first outline the elements of the computation, explain the approximations involved, and define some useful quantities. Then we proceed with the computation of the amplitudes and cross-sections. The final results are listed in tables 4.7 to 4.10 and illustrated in fig. 4.9.

4.3.1 Preliminaries

Full amplitudes $\mathcal{M}_{\mathbf{k}\to n\ell m}$ and $\mathcal{M}_{n'\ell'm'\to n\ell m}$. As depicted schematically in fig. 4.4, the full amplitudes consist of the radiative transition part $\mathcal{A}_T$ computed perturbatively and convoluted with the initial and final-state wavefunctions [59],

$$\mathbb{i}\mathcal{M}_{\mathbf{k}\to n\ell m} = \int \frac{d^3\mathbf{k}'}{(2\pi)^3}\frac{d^3\mathbf{p}}{(2\pi)^3}\;\tilde{\phi}_{\mathbf{k}}(\mathbf{k}')\;\mathbb{i}\mathcal{A}_T(\mathbf{k}',\mathbf{p})\;\frac{[\tilde{\psi}_{n\ell m}(\mathbf{p})]^\dagger}{\sqrt{2\mu}}. \tag{4.3.1a}$$

$$\mathbb{i}\mathcal{M}_{n'\ell'm'\to n\ell m} = \int \frac{d^3\mathbf{p}'}{(2\pi)^3}\frac{d^3\mathbf{p}}{(2\pi)^3}\;\frac{\tilde{\psi}_{n'\ell'm'}(\mathbf{p}')}{\sqrt{2\mu}}\;\mathbb{i}\mathcal{A}_T(\mathbf{p}',\mathbf{p})\;\frac{[\tilde{\psi}_{n\ell m}(\mathbf{p})]^\dagger}{\sqrt{2\mu}}. \tag{4.3.1b}$$

Equations (4.3.1) can accommodate the possibility that the incoming and/or outgoing states are superpositions of different Fock states, as is the case with the mixed $SS/D\bar{D}$ states discussed in section 4.2.2. Then, the wavefunctions are vectors and $\mathcal{A}_T$ becomes a matrix.

Transition amplitudes $\mathcal{A}_T$. The radiative parts of the BSF and transition diagrams are shown in figs. 4.5 to 4.8. Following refs. [2, 59, 62], we compute the amplitudes $\mathcal{A}_T$, applying the standard approximations due to the hierarchy of scales and retaining only the leading order terms. Among else, we shall use the following approximate spinor identities valid for low momentum changes, $p \simeq p'$,

$$\bar{u}(p,s)\,u(p',s') \simeq +2m\;\delta^{ss'}, \qquad \bar{u}(p,s)\,\gamma^\mu\,u(p',s') \simeq +2p^\mu\delta^{ss'}, \tag{4.3.2a}$$

$$\bar{v}(p,s)\,v_2(p',s') \simeq -2m\;\delta^{ss'}, \qquad \bar{v}(p,s)\,\gamma^\mu\,v(p',s') \simeq +2p^\mu\delta^{ss'}. \tag{4.3.2b}$$

Moreover, we emphasise that the signs arising from the fermion permutations needed to perform the Wick contractions must be carefully taken into account, as they often differ among various diagrams contributing to the same amplitude. An example calculation is presented in detail in appendix D.2.

Overlap integrals. The scattering and bound state wavefunctions are listed in tables 4.3 and 4.4. To express $\mathcal{M}_{\mathbf{k}\to n\ell m}$ and $\mathcal{M}_{n'\ell'm'\to n\ell m}$ compactly, we define the Coulombic overlap

integrals [2, 43, 59, 62]

$$\mathcal{R}_{\mathbf{k},n\ell m}(\alpha_{\mathcal{S}},\alpha_{\mathcal{B}}) \equiv (\mu\alpha_{\mathcal{B}})^{3/2}\int\frac{d^3\mathbf{p}}{(2\pi)^3}\;\tilde{\varphi}_{\mathbf{k}}(\mathbf{p};\alpha_{\mathcal{S}})\;\tilde{\varphi}^*_{n\ell m}(\mathbf{p};\alpha_{\mathcal{B}}), \tag{4.3.3a}$$

$$\boldsymbol{\mathcal{J}}_{\mathbf{k},n\ell m}(\alpha_{\mathcal{S}},\alpha_{\mathcal{B}}) \equiv \int\frac{d^3\mathbf{p}}{(2\pi)^3}\;\mathbf{p}\;\tilde{\varphi}_{\mathbf{k}}(\mathbf{p};\alpha_{\mathcal{S}})\;\tilde{\varphi}^*_{n\ell m}(\mathbf{p};\alpha_{\mathcal{B}}), \tag{4.3.3b}$$

$$\boldsymbol{\mathcal{Y}}^W_{\mathbf{k},n\ell m}(\alpha_{\mathcal{S}},\alpha_{\mathcal{B}}) \equiv 8\pi\mu\alpha_2\int\frac{d^3\mathbf{k}'}{(2\pi)^3}\frac{d^3\mathbf{p}}{(2\pi)^3}\frac{\mathbf{k}'-\mathbf{p}}{(\mathbf{k}'-\mathbf{p})^4}\,\tilde{\varphi}_{\mathbf{k}}(\mathbf{k}';\alpha_{\mathcal{S}})\,\tilde{\varphi}^*_{n\ell m}(\mathbf{p};\alpha_{\mathcal{B}}), \tag{4.3.3c}$$

$$\boldsymbol{\mathcal{Y}}^H_{\mathbf{k},n\ell m}(\alpha_{\mathcal{S}},\alpha_{\mathcal{B}}) \equiv 8\pi\mu\alpha_H\int\frac{d^3\mathbf{k}'}{(2\pi)^3}\frac{d^3\mathbf{p}}{(2\pi)^3}\frac{\mathbf{k}'-\mathbf{p}}{[(\mathbf{k}'-\mathbf{p})^2+m_H^2]^2}\tilde{\varphi}_{\mathbf{k}}(\mathbf{k}';\alpha_{\mathcal{S}})\tilde{\varphi}^*_{n\ell m}(\mathbf{p};\alpha_{\mathcal{B}}), \tag{4.3.3d}$$

and

$$\mathcal{R}_{n'\ell'm,n\ell m}(\alpha'_{\mathcal{B}},\alpha_{\mathcal{B}}) \equiv \int\frac{d^3\mathbf{p}}{(2\pi)^3}\;\tilde{\varphi}_{n'\ell'm'}(\mathbf{p};\alpha'_{\mathcal{B}})\;\tilde{\varphi}^*_{n\ell m}(\mathbf{p};\alpha_{\mathcal{B}}), \tag{4.3.3e}$$

where $\tilde{\varphi}_{n\ell m}$ and $\tilde{\varphi}_{\mathbf{k}}$ are Fourier transforms of the Coulomb wavefunctions (4.2.11) and (4.2.14).[3] In the Coulomb regime, the overlap integrals can be computed analytically, after Fourier transforming into position space. The scattering-bound integrals of eqs. (4.3.3a) to (4.3.3d) have been computed in refs. [2, 43, 59, 62]. We compute the bound-bound integral (4.3.3e) in appendix C.3. For the ground-level bound states, $\{n\ell m\} = \{100\}$, the results are

$$\mathcal{R}_{\mathbf{k},100}(\alpha_{\mathcal{S}},\alpha_{\mathcal{B}}) = \left[2^6\pi\left(1-\frac{\zeta_{\mathcal{S}}}{\zeta_{\mathcal{B}}}\right)^2\left(\frac{\zeta_{\mathcal{B}}^2}{1+\zeta_{\mathcal{B}}^2}\right)S_{\rm scl}(\zeta_{\mathcal{S}},\zeta_{\mathcal{B}})\right]^{1/2}, \tag{4.3.4a}$$

$$\boldsymbol{\mathcal{J}}_{\mathbf{k},100}(\alpha_{\mathcal{S}},\alpha_{\mathcal{B}}) = \hat{\mathbf{k}}\left[\frac{2^6\pi}{\mu\alpha_{\mathcal{B}}}\left(\frac{\zeta_{\mathcal{B}}^2}{1+\zeta_{\mathcal{B}}^2}\right)S_{\rm vec}(\zeta_{\mathcal{S}},\zeta_{\mathcal{B}})\right]^{1/2}, \tag{4.3.4b}$$

$$\boldsymbol{\mathcal{Y}}^W_{\mathbf{k},100}(\alpha_{\mathcal{S}},\alpha_{\mathcal{B}}) = (\alpha_2/\alpha_{\mathcal{B}})\boldsymbol{\mathcal{J}}_{\mathbf{k},100}(\alpha_{\mathcal{S}},\alpha_{\mathcal{B}}), \tag{4.3.4c}$$

$$\lim_{m_H\to 0}[\boldsymbol{\mathcal{Y}}^H_{\mathbf{k},100}(\alpha_{\mathcal{S}},\alpha_{\mathcal{B}})] = (\alpha_H/\alpha_{\mathcal{B}})\;\boldsymbol{\mathcal{J}}_{\mathbf{k},100}(\alpha_{\mathcal{S}},\alpha_{\mathcal{B}}), \tag{4.3.4d}$$

and

$$\mathcal{R}_{100,100}(\alpha'_{\mathcal{B}},\alpha_{\mathcal{B}}) = 8(\alpha_{\mathcal{B}}\alpha'_{\mathcal{B}})^{3/2}/(\alpha_{\mathcal{B}}+\alpha'_{\mathcal{B}})^3, \tag{4.3.4e}$$

where

$$\zeta_{\mathcal{S}} \equiv \alpha_{\mathcal{S}}/v_{\rm rel} \quad \text{and} \quad \zeta_{\mathcal{B}} \equiv \alpha_{\mathcal{B}}/v_{\rm rel} \tag{4.3.5}$$

entail the coupling strengths $\alpha_{\mathcal{S}}$ and $\alpha_{\mathcal{B}}$ of the potential in the scattering and bound states respectively, and we have defined the functions [2, 39, 43, 59, 62]

$$S_{\rm scl}(\zeta_{\mathcal{S}},\zeta_{\mathcal{B}}) \equiv \left(\frac{2\pi\zeta_{\mathcal{S}}}{1-e^{-2\pi\zeta_{\mathcal{S}}}}\right)\left[\frac{\zeta_{\mathcal{B}}^6 e^{-4\zeta_{\mathcal{S}}\,\mathrm{arccot}(\zeta_{\mathcal{B}})}}{(1+\zeta_{\mathcal{B}}^2)^3}\right]. \tag{4.3.6a}$$

$$S_{\rm vec}(\zeta_{\mathcal{S}},\zeta_{\mathcal{B}}) \equiv \left(\frac{2\pi\zeta_{\mathcal{S}}}{1-e^{-2\pi\zeta_{\mathcal{S}}}}\right)(1+\zeta_{\mathcal{S}}^2)\left[\frac{\zeta_{\mathcal{B}}^4 e^{-4\zeta_{\mathcal{S}}\,\mathrm{arccot}(\zeta_{\mathcal{B}})}}{(1+\zeta_{\mathcal{B}}^2)^3}\right]. \tag{4.3.6b}$$

Note that $S_{\rm scl}$ and $S_{\rm vec}$ include the s- and p-wave Sommerfeld factors, $S_0(\zeta_{\mathcal{S}}) \equiv 2\pi\zeta_{\mathcal{S}}/(1+e^{-2\pi\zeta_{\mathcal{S}}})$ and $S_1(\zeta_{\mathcal{S}}) = S_0(\zeta_{\mathcal{S}})(1+\zeta_{\mathcal{S}}^2)$, respectively. Indeed, eq. (4.3.4a) arises from the $\ell_{\mathcal{S}} = 0$ and eqs. (4.3.4b) to (4.3.4d) arise from the $\ell_{\mathcal{S}} = 1$ modes of the scattering state wavefunctions. In eq. (4.3.4d) we took the limit $m_H \to 0$ to be consistent with our approximations, although it is easy to obtain an analytical result for $m_H \neq 0$ (but using the Coulomb wavefunctions.)

[3] Note that $\mathcal{R}_{\mathbf{k},n\ell m}$, $\mathcal{R}_{n'\ell'm,n\ell m}$ are dimensionless, while $\boldsymbol{\mathcal{J}}_{\mathbf{k},n\ell m}$ and $\boldsymbol{\mathcal{Y}}_{\mathbf{k},n\ell m}$ have mass-dimension $-1/2$.

BSF cross-sections. The cross-sections for BSF via emission of a massless vector (B or W) or scalar (H or $H^\dagger$) boson are, respectively [43, 59]

$$v_{\rm rel}\,\frac{d\sigma^V_{\mathbf{k}\to n\ell m}}{d\Omega} = \frac{|\mathbf{P}_{_V}|}{2^7\pi^2 m^3}\;|\boldsymbol{\mathcal{M}}_{\mathbf{k}\to n\ell m}|^2\left[1-\left(\hat{\mathbf{P}}_{_V}\cdot\hat{\boldsymbol{\mathcal{M}}}_{\mathbf{k}\to n\ell m}\right)^2\right], \tag{4.3.7a}$$

$$v_{\rm rel}\,\frac{d\sigma^H_{\mathbf{k}\to n\ell m}}{d\Omega} = \frac{|\mathbf{P}_{_H}|}{2^7\pi^2 m^3}|\mathcal{M}_{\mathbf{k}\to n\ell m}|^2, \tag{4.3.7b}$$

where $\mathbf{P}_{_V}$ and $\mathbf{P}_{_H}$ are the momenta of the emitted bosons, which dissipate the kinetic energy of the relative motion and the binding energy, $|\mathbf{P}_{_V}|$ or $\sqrt{\mathbf{P}_{_H}^2+m_{_H}^2}=\omega_{\mathbf{k}\to n\ell m}$, where

$$\omega_{\mathbf{k}\to n\ell m}\simeq\mathcal{E}_{\mathbf{k}}-\mathcal{E}_{n\ell m}\simeq(m/4)\left(\alpha_{\mathcal{B}}^2/n^2+v_{\rm rel}^2\right). \tag{4.3.8}$$

In eq. (4.3.7a), we have summed over polarisations of the emitted vector. As we shall see in the following, to working order, the amplitudes for BSF via vector emission are $\boldsymbol{\mathcal{M}}_{\mathbf{k}\to 100}\propto\mathbf{k}$, while the amplitudes for BSF via scalar emission are independent of Ω. Then, eqs. (4.3.7) simplify to [43, 59]

$$\sigma^V_{\mathbf{k}\to n\ell m}v_{\rm rel} = \frac{\alpha_{\mathcal{B}}^2}{2^6\cdot 3\pi m^2}\left(\frac{1+\zeta_{\mathcal{B}}^2}{\zeta_{\mathcal{B}}^2}\right)\;|\boldsymbol{\mathcal{M}}_{\mathbf{k}\to n\ell m}|^2, \tag{4.3.9a}$$

$$\sigma^H_{\mathbf{k}\to n\ell m}v_{\rm rel} = \frac{\alpha_{\mathcal{B}}^2}{2^7\pi m^2}\left(\frac{1+\zeta_{\mathcal{B}}^2}{\zeta_{\mathcal{B}}^2}\right)\;|\mathcal{M}_{\mathbf{k}\to n\ell m}|^2\;h_{_H}(\omega_{\mathbf{k}\to n\ell m}), \tag{4.3.9b}$$

where $h_{_H}\equiv|\mathbf{P}_{_H}|/E_{_H}$ is the phase-space suppression due to the Higgs mass,

$$h_{_H}(\omega)\equiv\left(1-m_{_H}^2/\omega^2\right)^{1/2}. \tag{4.3.10}$$

Bound-to-bound transition rates. Similarly to the above, the rates for the radiative de-excitation of bound states are

$$\frac{d\Gamma^V_{n'\ell'm'\to n\ell m}}{d\Omega} = \frac{|\mathbf{P}_{_V}|}{2^7\pi^2 m^2}\;|\boldsymbol{\mathcal{M}}_{n'\ell'm'\to n\ell m}|^2\left[1-\left(\hat{\mathbf{P}}_{_V}\cdot\hat{\boldsymbol{\mathcal{M}}}_{n'\ell'm'\to n\ell m}\right)^2\right], \tag{4.3.11a}$$

$$\frac{d\Gamma^H_{n'\ell'm'\to n\ell m}}{d\Omega} = \frac{|\mathbf{P}_{_H}|}{2^7\pi^2 m^2}|\mathcal{M}_{n'\ell'm'\to n\ell m}|^2, \tag{4.3.11b}$$

where $|\mathbf{P}_{_V}|$ and $|\mathbf{P}_{_H}|$ are determined again by the amount of dissipated energy, which is now the difference between the binding energies of the two states,

$$\omega_{n'\ell'm'\to n\ell m}\simeq\mathcal{E}_{n'\ell'm'}-\mathcal{E}_{n\ell m}\simeq(m/4)\left(\alpha_{\mathcal{B}}^2/n^2-\alpha_{\mathcal{B}}'^2/n'^2\right). \tag{4.3.12}$$

For monopole transitions via H or $H^\dagger$ emission, the amplitude is independent of the $\mathbf{P}_{_H}$ direction, and eq. (4.3.11b) simplifies to

$$\Gamma^H_{n'\ell'm'\to n\ell m} = \frac{\alpha_{\mathcal{B}}'^2/n'^2-\alpha_{\mathcal{B}}^2/n^2}{2^7\pi m}\;|\mathcal{M}_{n'\ell'm'\to n\ell m}|^2\;h_{_H}(\omega_{n'\ell'm'\to n\ell m}), \tag{4.3.13}$$

where the phase-space suppression $h_{_H}$ is defined in eq. (4.3.10).

4.3.2 $SS/D\bar{D}$ bound states: $(\mathbb{1},0)$, spin 0, $n\ell m=\{100\}$

The BSF processes are listed in table 4.7, and the radiative part of the diagrams contributing to these processes are shown in fig. 4.5. We project the bound-state fields on the spin-0 state via $[U^{-1}_{\text{spin-0}}]^{r_2r_1}=\epsilon^{r_1r_2}/\sqrt{2}$, and the $D\bar{D}$ component on the $SU_{_L}(2)$ singlet via $\delta_{i'j'}/\sqrt{2}$.

Bound state $SS/D\bar{D}$: $(\mathbb{1},\mathbf{0})$, spin 0, $\{n\ell m\} = \{100\}$

Scattering state (spin 0)					Rad	Cross-section
State	$U_Y(1)$	$SU_L(2)$	dof	ℓ_S	boson	$(\sigma_{\rm BSF} v_{\rm rel})/(\pi m^{-2})$
$D\bar{D}$	0	$\mathbb{1}$	1	1	B	$\frac{2^7}{3}\frac{\alpha_1\alpha_A^2}{\alpha_A+\alpha_R}\left[1+\frac{\alpha_H}{\alpha_A}\sqrt{\frac{8\alpha_R}{\alpha_A}}\right]^2 \quad S_{\rm vec}\left(\frac{\zeta_1+3\zeta_2}{4},\zeta_A\right)$
SS	0	$\mathbb{1}$	1	1	B	0 (due to antisymmetry of SS scattering state)
$D\bar{D}$	0	$\mathbb{3}$	3	1	W	$\frac{2^5}{3}\frac{\alpha_2\alpha_A^2}{\alpha_A+\alpha_R}\left[1+\frac{\alpha_2}{\alpha_A}+\frac{\alpha_H}{\alpha_A}\sqrt{\frac{8\alpha_R}{\alpha_A}}\right]^2 \quad S_{\rm vec}\left(\frac{\zeta_1-\zeta_2}{4},\zeta_A\right)$
DS	$+1/2$	$\mathbb{2}$	2	0	H	$\frac{2^7\alpha_H}{\alpha_A}\frac{\left(\sqrt{\alpha_A}+\sqrt{8\alpha_R}\right)^2}{\alpha_A+\alpha_R}\left(1-\frac{\alpha_H}{\alpha_A}\right)^2 \quad S_{\rm scl}\left(\zeta_H,\zeta_A\right)\, h_H(\omega)$
$\bar{D}S$	$-1/2$	$\mathbb{2}$	2	0	$H^\dagger$	same as above

Table 4.7: Radiative processes and cross-sections for capture into the ground level of the $SS/D\bar{D}$ bound states. Here, α_A, α_R are obtained from eqs. (4.2.21) for $\ell = s = 0$. Each cross-section is averaged over the dof of the corresponding scattering state (4th column.) $S_{\rm vec}$ and $S_{\rm scl}$ are defined in eqs. (4.3.6), and h_H in eq. (4.3.10). Here, $\omega = m(\alpha_A^2 + v_{\rm rel}^2)/4$.

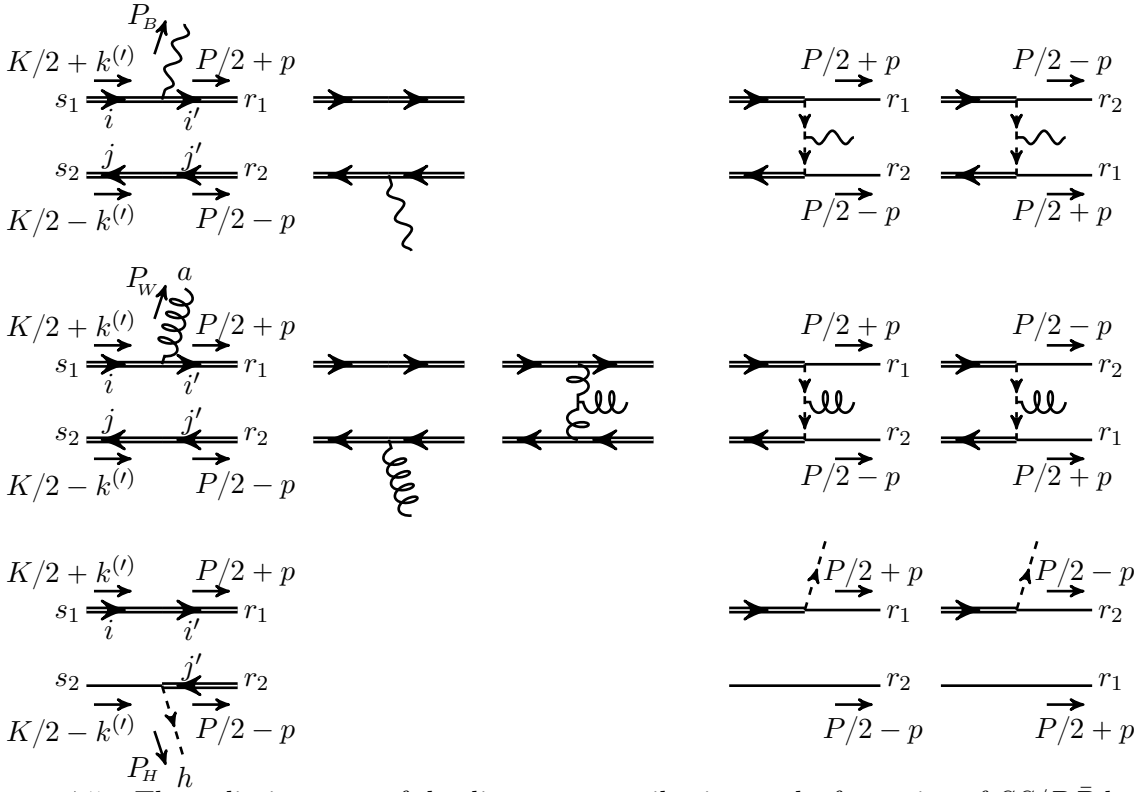

Figure 4.5: The radiative parts of the diagrams contributing to the formation of $SS/D\bar{D}$ bound states. *Top row:* $D\bar{D} \to \mathcal{B}(SS/D\bar{D}) + B$. *Middle row:* $D\bar{D} \to \mathcal{B}(SS/D\bar{D}) + W$. *Bottom row:* $DS \to \mathcal{B}(SS/D\bar{D}) + H$, which has also a conjugate counterpart (not shown.) Single and double lines correspond to S and D fermions, while vector, gluon and dashed lines to B, W and H bosons. The arrows on the field lines denote the flow of Hypercharge. Wherever not shown, the momenta, spins and gauge indices of the external particles can be deduced from the other graphs.

$D\bar{D} \to \mathcal{B}(SS/D\bar{D}) + B$

The perturbative parts of the amplitude are

$$\begin{aligned}
&\mathbb{i}\boldsymbol{\mathcal{A}}_{ij}^{s_1 s_2}\left[D\bar{D} \to (SS)^{\text{spin-0}}_{(\mathbb{1},0)} + B\right] \simeq \\
&\qquad \simeq \mathbb{i}\,\delta_{ij}\,\frac{\epsilon^{s_1 s_2}}{\sqrt{2}}\,y^2\,g_1 Y_H\,4m^2\left[\frac{2(\mathbf{k}'-\mathbf{p})}{[(\mathbf{k}'-\mathbf{p})^2+m_H^2]^2}+\frac{2(\mathbf{k}'+\mathbf{p})}{[(\mathbf{k}'+\mathbf{p})^2+m_H^2]^2}\right], \qquad (4.3.14a)\\
&\mathbb{i}\boldsymbol{\mathcal{A}}_{ij}^{s_1 s_2}\left[D\bar{D} \to (D\bar{D})^{\text{spin-0}}_{(\mathbb{1},0)} + B\right] \simeq \\
&\qquad \simeq \mathbb{i}\,\frac{\delta_{ij}}{\sqrt{2}}\,\frac{\epsilon^{s_1 s_2}}{\sqrt{2}}\,g_1 Y_D\,2m\,2\mathbf{p}\,(2\pi)^3\left[\delta^3(\mathbf{k}'-\mathbf{p}-\mathbf{P}_B/2)+\delta^3(\mathbf{k}'-\mathbf{p}+\mathbf{P}_B/2)\right], \qquad (4.3.14b)
\end{aligned}$$

In eq. (4.3.14a), the fermion permutations introduced factors (-1) and $(+1)$ for the t- and u-channel diagrams. The projection on the antisymmetric spin-0 eigenstate alloted another factor (-1) to the u-channel. The full amplitude (4.3.1a) is

$$\begin{aligned}
\mathbb{i}\boldsymbol{\mathcal{M}}_{ij}^{s_1 s_2} = \frac{1}{\sqrt{2\mu}}\int\frac{d^3\mathbf{k}'}{(2\pi)^3}\frac{d^3\mathbf{p}}{(2\pi)^3}\;\tilde{\varphi}_{\mathbf{k}}\left(\mathbf{k}';\frac{\alpha_1+3\alpha_2}{4}\right)\\
\times\left[\mathbb{i}\boldsymbol{\mathcal{A}}_{ij}^{s_1 s_2}\left[D\bar{D}\to(SS)^{\text{spin-0}}_{(\mathbb{1},0)}+B\right]\sqrt{\frac{\alpha_R}{\alpha_A+\alpha_R}}\;\tilde{\varphi}^{\dagger}_{100}(\mathbf{p};\alpha_A)\right.\\
\left.+\,\mathbb{i}\boldsymbol{\mathcal{A}}_{ij}^{s_1 s_2}\left[D\bar{D}\to(D\bar{D})^{\text{spin-0}}_{(\mathbb{1},0)}+B\right]\sqrt{\frac{\alpha_A}{\alpha_A+\alpha_R}}\;\tilde{\varphi}^{\dagger}_{100}(\mathbf{p};\alpha_A)\right], \qquad (4.3.15)
\end{aligned}$$

where only the $\ell_{\mathcal{S}}=1$ component of the scattering state wavefunction is meant to be kept, and here α_A and α_R should be evaluated from eqs. (4.2.21) for $\ell=s=0$. This becomes

$$\begin{aligned}
\mathbb{i}\boldsymbol{\mathcal{M}}_{ij}^{s_1 s_2} \simeq \mathbb{i}\delta_{ij}\epsilon^{s_1 s_2}\left(\frac{4\pi\alpha_1}{\alpha_A+\alpha_R}\;4m\right)^{1/2}\times\\
\times\left\{\sqrt{8\alpha_R}\,\boldsymbol{\mathcal{Y}}^H_{\mathbf{k},100}\left(\frac{\alpha_1+3\alpha_2}{4},\alpha_A\right)+\sqrt{\alpha_A}\,\boldsymbol{\mathcal{J}}_{\mathbf{k},100}\left(\frac{\alpha_1+3\alpha_2}{4},\alpha_A\right)\right\}. \qquad (4.3.16)
\end{aligned}$$

Note that we have neglected the $\pm\mathbf{P}_B/2$ terms inside the δ-functions of eq. (4.3.14b) that give rise to higher order corrections [43, 59]. Squaring and summing over the initial-state gauge indices and spins selects the $(\mathbb{1},0)$ spin-0 $D\bar{D}$ scattering state, which has one dof. Using the overlap integrals (4.3.4), we find

$$\sum_{s_1,s_2}\sum_{i,j}\left|\boldsymbol{\mathcal{M}}_{ij}^{s_1 s_2}\right|^2 \simeq 2^{13}\pi^2\left(\frac{\alpha_1}{\alpha_A+\alpha_R}\right)\left(1+\frac{\alpha_H}{\alpha_A}\sqrt{\frac{8\alpha_R}{\alpha_A}}\right)^2\left(\frac{\zeta_A^2}{1+\zeta_A^2}\right)S_{\text{vec}}\left(\frac{\zeta_1+3\zeta_2}{4},\zeta_A\right). \qquad (4.3.17)$$

The cross-section is obtained from eq. (4.3.9a) setting $\alpha_{\mathcal{B}}\to\alpha_A$, and is shown in table 4.7.

$D\bar{D} \to \mathcal{B}(SS/D\bar{D}) + W$

The perturbative parts of the amplitude are

$$\begin{aligned}
\mathbb{i}(\boldsymbol{\mathcal{A}}^{s_1 s_2})_{ij}^{a}\left[D\bar{D}\to(SS)^{\text{spin-0}}_{(\mathbb{1},0)}+W\right] \simeq \mathbb{i}\,t^a_{ji}\,\frac{\epsilon^{s_1 s_2}}{\sqrt{2}}\,y^2\,g_2\,4m^2\times\\
\times\left[\frac{2(\mathbf{k}'-\mathbf{p})}{[(\mathbf{k}'-\mathbf{p})^2+m_H^2]^2}+\frac{2(\mathbf{k}'+\mathbf{p})}{[(\mathbf{k}'+\mathbf{p})^2+m_H^2]^2}\right], \qquad (4.3.18a)\\
\mathbb{i}(\boldsymbol{\mathcal{A}}^{s_1 s_2})_{ij}^{a}\left[D\bar{D}\to(D\bar{D})^{\text{spin-0}}_{(\mathbb{1},0)}+W\right] \simeq \mathbb{i}\,\frac{t^a_{ji}}{\sqrt{2}}\,\frac{\epsilon^{s_1 s_2}}{\sqrt{2}}\,g_2\,2m\times\left\{2m\;4\pi\alpha_2\;\frac{2(\mathbf{k}'-\mathbf{p})}{(\mathbf{k}'-\mathbf{p})^4}\right. \qquad (4.3.18b)\\
\left.+2\mathbf{p}\,(2\pi)^3\left[\delta^3(\mathbf{k}'-\mathbf{p}-\mathbf{P}_W/2)+\delta^3(\mathbf{k}'-\mathbf{p}+\mathbf{P}_W/2)\right]\right\},
\end{aligned}$$

where the signs of the t- and u-channel diagrams in eq. (4.3.18a) are as in $D\bar{D} \to SS + B$ above, and the first factor 2 in the first term of eq. (4.3.18b) is the quadratic Casimir of $SU_L(2)$ (see ref. [62] for details of this computation.) The full amplitude (4.3.1a) is

$$\begin{aligned}\mathbb{i}(\boldsymbol{\mathcal{M}}^{s_1 s_2})^a_{ij} \simeq \mathbb{i}(t^a)_{ij}\epsilon^{s_1 s_2}\left(\frac{4\pi\alpha_2}{\alpha_A+\alpha_R}\,4m\right)^{1/2}\times\Bigg\{\sqrt{8\alpha_R}\,\boldsymbol{\mathcal{Y}}^H_{\mathbf{k},100}\left(\frac{\alpha_1-\alpha_2}{4},\alpha_A\right)\\ +\sqrt{\alpha_A}\left[\boldsymbol{\mathcal{J}}_{\mathbf{k},100}\left(\frac{\alpha_1-\alpha_2}{4},\alpha_A\right)+\boldsymbol{\mathcal{Y}}^W_{\mathbf{k},100}\left(\frac{\alpha_1-\alpha_2}{4},\alpha_A\right)\right]\Bigg\},\end{aligned} \tag{4.3.19}$$

where again α_A and α_R should be evaluated from eqs. (4.2.21) for $\ell = s = 0$, and we have neglected the $\pm\mathbf{P}_W/2$ terms inside the δ-functions in eq. (4.3.18b). Squaring, summing over the initial and final state gauge indices and spins selects the $(\mathbb{3}, 0)$ spin-0 $D\bar{D}$ state, which has three dof. Using eqs. (4.3.4) and (4.3.6), we find

$$\begin{aligned}\frac{1}{3}\sum_{s_1,s_2}\sum_{i,j,a}|(\boldsymbol{\mathcal{M}}^{s_1 s_2})^a_{ij}|^2 \simeq 2^{11}\pi^2\left(\frac{\alpha_2}{\alpha_A+\alpha_R}\right)\left(1+\frac{\alpha_2}{\alpha_A}+\frac{\alpha_H}{\alpha_A}\sqrt{\frac{8\alpha_R}{\alpha_A}}\right)^2\\ \times\left(\frac{\zeta_A^2}{1+\zeta_A^2}\right)S_{\rm vec}\left(\frac{\zeta_1-\zeta_2}{4},\zeta_A\right).\end{aligned} \tag{4.3.20}$$

The cross-section is obtained from eq. (4.3.9a) setting $\alpha_{\mathcal{B}} \to \alpha_A$, and is shown in table 4.7.

$DS \to \mathcal{B}(SS/D\bar{D}) + H$

The perturbative parts of the amplitude are

$$\begin{aligned}\mathbb{i}\mathcal{A}^{s_1 s_2}_{i,h}\left[DS\to(SS)^{\text{spin-0}}_{(\mathbb{1},0)}+H\right] &\simeq -\mathbb{i}\,\delta_{ih}\,\frac{\epsilon^{s_1 s_2}}{\sqrt{2}}\,y\,4m^2\times \\ &\quad\times(2\pi)^3\left[\delta^3(\mathbf{k}'-\mathbf{p}-\mathbf{P}_H/2)+\delta^3(\mathbf{k}'-\mathbf{p}+\mathbf{P}_H/2)\right],\end{aligned} \tag{4.3.21a}$$

$$\mathbb{i}\mathcal{A}^{s_1 s_2}_{i,h}\left[DS\to(D\bar{D})^{\text{spin-0}}_{(\mathbb{1},0)}+H\right] \simeq -\mathbb{i}\,\frac{\delta_{ih}}{\sqrt{2}}\,\frac{\epsilon^{s_1 s_2}}{\sqrt{2}}\,y\,4m^2\,(2\pi)^3\delta^3(\mathbf{k}'-\mathbf{p}+\mathbf{P}_H/2). \tag{4.3.21b}$$

where now the fermion permutations introduced factors $(+1)$ and (-1) for the t- and u-channel $DS \to SS + H$ diagrams respectively, and (-1) for the $DS \to D\bar{D} + H$ diagram. We note that there are two diagrams where an off-shell vector boson (B or W) emitted from one leg and an off-shell Higgs emitted from the other leg fuse to produce the final-state Higgs. In appendix D.3, we show that these diagrams are of higher order, thus we do not consider them here. The full amplitude (4.3.1a) is

$$\mathbb{i}\mathcal{M}^{s_1 s_2}_{i,h} \simeq -\mathbb{i}\,\delta_{ih}\,\epsilon^{s_1 s_2}\sqrt{\frac{2^7\pi\alpha_H}{\alpha_A^3}}\,\frac{\sqrt{\alpha_A}+\sqrt{8\alpha_R}}{\sqrt{\alpha_A+\alpha_R}}\,\mathcal{R}_{\mathbf{k},100}(\alpha_H,\alpha_A), \tag{4.3.22}$$

where we have neglected the $\pm\mathbf{P}_H/2$ terms inside the δ-functions in eqs. (4.3.21). Squaring and summing over the initial and final state gauge indices and spins selects the $(2, 1/2)$ spin-0 DS state, which has two dof. Using the overlap integrals (4.3.4), we find

$$\frac{1}{2}\sum_{s_1,s_2}\sum_{i,h}|\mathcal{M}^{s_1 s_2}_{i,h}|^2 \simeq 2^{14}\pi^2\,\frac{\alpha_H}{\alpha_A^3}\,\frac{\left(\sqrt{\alpha_A}+\sqrt{8\alpha_R}\right)^2}{\alpha_A+\alpha_R}\left(1-\frac{\zeta_H}{\zeta_A}\right)^2\left(\frac{\zeta_A^2}{1+\zeta_A^2}\right)S_{\rm scl}\left(\zeta_H,\zeta_A\right). \tag{4.3.23}$$

The cross-section is obtained from eq. (4.3.9b) setting $\alpha_{\mathcal{B}} \to \alpha_A$, and is shown in table 4.7.

Bound-to-bound transition $\mathcal{B}(DS) \to \mathcal{B}(SS/D\bar{D}) + H$

Using the perturbative amplitudes (4.3.21), we may now compute the rate of bound-to-bound transition (4.2.38). Projecting on the spin-0 DS state, and taking into account the bound-state wavefuntions of table 4.4, we find that the full amplitude is, analogously to eq. (4.3.22), given by

$$\mathbb{i}\mathcal{M}_{i,h} \simeq -\mathbb{i}\,\delta_{ih}\, m \sqrt{2^5 \pi \alpha_H}\, \frac{\sqrt{\alpha_A} + \sqrt{8\alpha_R}}{\sqrt{\alpha_A + \alpha_R}}\, \mathcal{R}_{100,100}(\alpha_H, \alpha_A), \tag{4.3.24}$$

Squaring and averaging over the initial and final state gauge indices, and using the overlap integral (4.3.4e), we find

$$\frac{1}{2}\sum_{i,h} |\mathcal{M}_{i,h}|^2 \simeq 2^{11}\pi m^2\ \alpha_H\ \frac{\left(\sqrt{\alpha_A} + \sqrt{8\alpha_R}\right)^2}{\alpha_A + \alpha_R}\ \frac{(\alpha_H \alpha_A)^3}{(\alpha_H + \alpha_A)^6}. \tag{4.3.25}$$

The transition rate is found from eq. (4.3.13) to be

$$\Gamma_{DS\to SS/D\bar{D}} = 2^4 m\, \alpha_H\, (\alpha_A^2 - \alpha_H^2)\, \frac{\left(\sqrt{\alpha_A} + \sqrt{8\alpha_R}\right)^2}{\alpha_A + \alpha_R}\, \frac{(\alpha_A \alpha_H)^3}{(\alpha_A + \alpha_H)^6} \left[1 - \frac{16 m_H^2}{m^2(\alpha_A^2 - \alpha_H^2)^2}\right]^{1/2}. \tag{4.3.26}$$

4.3.3 $D\bar{D}$ bound states: $(\mathbb{1}, 0)$, spin 1, $n\ell m = \{100\}$

The BSF processes are listed in table 4.8, and the radiative parts of the diagrams contributing to these processes are shown in fig. 4.6. For all processes below, we project the bound-state fields on the $SU_L(2)$ singlet via $\delta_{i'j'}/\sqrt{2}$. Moreover, since spin is conserved at working order, as already seen in section 4.3.2, we project both the scattering and the bound states on the spin-1 configuration by contracting the spin indices with $[U^{\sigma}_{\text{spin-1}}]^{s_1 s_2}[U^{\rho\dagger}_{\text{spin-1}}]^{r_2 r_1}$, where the indices $\sigma, \rho = -1, 0, 1$ run through the three states of the spin-1 multiplets. While the Clebsh-Gordan coefficients contained in $U_{\text{spin-1}}$ are well-known, we shall not need them explicitly. We will instead only invoke that the operators $[U^{\sigma\dagger}_{\text{spin-1}}]^{s_1 s_2}$ are symmetric in s_1, s_2, and $[U^{\sigma}_{\text{spin-1}}]^{s_1 s_2}[U^{\rho\dagger}_{\text{spin-1}}]^{s_2 s_1} = \delta^{\sigma\rho}$.

$D\bar{D}$-like $\to \mathcal{B}(D\bar{D}) + B$

Besides the projections mentioned above, here we also project the $D\bar{D}$ component of the scattering state on the $SU_L(2)$ singlet configuration via $\delta_{ij}/\sqrt{2}$. The perturbative parts of the amplitude are

$$\begin{aligned}
\mathbb{i}\boldsymbol{\mathcal{A}}^{\sigma\rho}&\left[(SS)^{\text{spin-1}} \to (D\bar{D})^{\text{spin-1}}_{(\mathbb{1},0)} + B\right] \simeq \\
&\simeq -\mathbb{i}\sqrt{2}\,\delta^{\sigma\rho}\, y^2\, g_1 Y_H\, 4m^2 \left[\frac{2(\mathbf{k}' - \mathbf{p})}{[(\mathbf{k}' - \mathbf{p})^2 + m_H^2]^2} + \frac{2(\mathbf{k}' + \mathbf{p})}{[(\mathbf{k}' + \mathbf{p})^2 + m_H^2]^2}\right], \qquad (4.3.27a) \\
\mathbb{i}\boldsymbol{\mathcal{A}}^{\sigma\rho}&\left[(D\bar{D})^{\text{spin-1}}_{(\mathbb{1},0)} \to (D\bar{D})^{\text{spin-1}}_{(\mathbb{1},0)} + B\right] \simeq \\
&\simeq +\mathbb{i}\,\delta^{\sigma\rho}\, g_1 Y_D\, 2m\, 2\mathbf{p}\, (2\pi)^3 \left[\delta^3(\mathbf{k}' - \mathbf{p} - \mathbf{P}_B/2) + \delta^3(\mathbf{k}' - \mathbf{p} + \mathbf{P}_B/2)\right]. \qquad (4.3.27b)
\end{aligned}$$

In eq. (4.3.27a), the fermion permutations introduced factors (-1) and $(+1)$ for the t- and u-channel diagrams. Upon projection on the symmetric spin-1 eigenstate, their relative sign does not change. The factor $\sqrt{2}$ appearing in the beginning of eq. (4.3.27a) arises from the projection

Bound state $D\bar{D}$: $(\mathbb{1},\mathbf{0})$, **spin 1,** $\{n\ell m\} = \{\mathbf{100}\}$

Scattering state (spin 1)					Rad	Cross-section
State	$U_Y(1)$	$SU_L(2)$	dof	$\ell_{\mathcal{S}}$	boson	$(\sigma_{\rm BSF} v_{\rm rel})/(\pi m^{-2})$
$D\bar{D}$-like	0	$\mathbb{1}$	3	1	B	$\frac{2^7\alpha_1\alpha_{\mathcal{B}}}{3}\frac{\alpha_A^2}{(\alpha_A+\alpha_R)^2}\left[\left(1-\frac{2\alpha_H}{\alpha_{\mathcal{B}}}\sqrt{\frac{\alpha_R}{\alpha_A}}\right)S_{\rm vec}^{1/2}(\zeta_A,\zeta_{\mathcal{B}}) + \left(\frac{\alpha_R}{\alpha_A}+\frac{2\alpha_H}{\alpha_{\mathcal{B}}}\sqrt{\frac{\alpha_R}{\alpha_A}}\right)S_{\rm vec}^{1/2}(-\zeta_R,\zeta_{\mathcal{B}})\right]^2$
SS-like	0	$\mathbb{1}$	3	1	B	$\frac{2^8\alpha_1\alpha_{\mathcal{B}}}{3}\frac{\alpha_A\alpha_R}{(\alpha_A+\alpha_R)^2}\left[\left(1-\frac{\alpha_H}{\alpha_{\mathcal{B}}}\sqrt{\frac{8\alpha_R}{\alpha_A}}\right)S_{\rm vec}^{1/2}(\zeta_A,\zeta_{\mathcal{B}}) - \left(1+\frac{\alpha_H}{\alpha_{\mathcal{B}}}\sqrt{\frac{8\alpha_A}{\alpha_R}}\right)S_{\rm vec}^{1/2}(-\zeta_R,\zeta_{\mathcal{B}})\right]^2$
$D\bar{D}$	0	$\mathbb{3}$	9	1	W	$\frac{2^7\alpha_2\alpha_{\mathcal{B}}}{3}\left(1+\frac{\alpha_2}{\alpha_{\mathcal{B}}}\right)^2 S_{\rm vec}\left(\frac{\zeta_1-\zeta_2}{4},\zeta_{\mathcal{B}}\right)$
DS	$+1/2$	$\mathbb{2}$	6	0	H	$\frac{2^7\alpha_H}{\alpha_{\mathcal{B}}}\left(1+\frac{\alpha_H}{\alpha_{\mathcal{B}}}\right)^2 S_{\rm scl}(-\zeta_H,\zeta_{\mathcal{B}})\,h_H(\omega)$
$\bar{D}S$	$-1/2$	$\mathbb{2}$	6	0	$H^\dagger$	same as above

Table 4.8: Same as table 4.7 for the $D\bar{D}$ bound states. Here, the bound-state coupling is $\alpha_{\mathcal{B}} = (\alpha_1 + 3\alpha_2)/4$, and correspondingly $\zeta_{\mathcal{B}} = (\zeta_1 + 3\zeta_2)/4$. In the first two processes, α_A and α_R should be evaluated from eq. (4.2.21) with $\ell_{\mathcal{S}} = s = 1$ for the scattering state. For the phase-space suppression h_H, here $\omega = m\left[(\alpha_1+3\alpha_2)^2/16 + v_{\rm rel}^2\right]/4$.

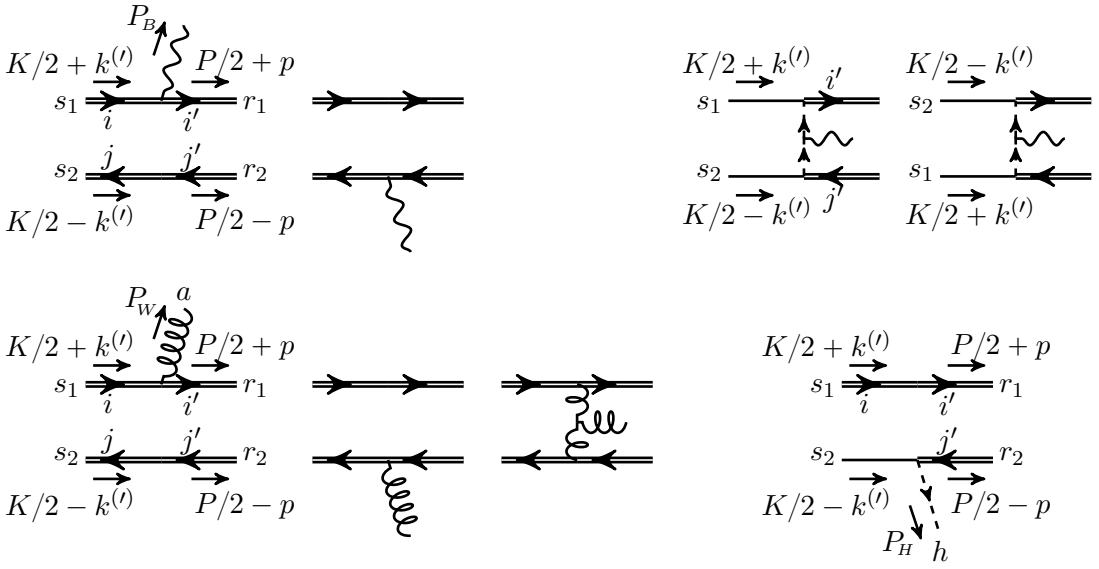

Figure 4.6: Same as in fig. 4.5, for the formation of $D\bar{D}$ bound states. *Top:* $D\bar{D}$-like $\to \mathcal{B}(D\bar{D}) + B$ and SS-like $\to \mathcal{B}(D\bar{D}) + B$. *Bottom left:* $D\bar{D} \to \mathcal{B}(D\bar{D}) + W$. *Bottom right:* $DS \to \mathcal{B}(SS/D\bar{D}) + H$.

onto the $SU_L(2)$ singlet final $D\bar{D}$ state. Using the wavefunctions listed in tables 4.3 and 4.4, we find the full amplitude (4.3.1a) to be

$$\begin{aligned}\mathbb{i}\boldsymbol{\mathcal{M}}^{\sigma\rho} \simeq \mathbb{i}\delta^{\sigma\rho}\,&\frac{2}{\alpha_A+\alpha_R}\sqrt{4\pi\alpha_1\,4m}\,\times\\ &\times\left\{2\sqrt{2\alpha_A\alpha_R}\left[-\boldsymbol{\mathcal{Y}}^H_{\mathbf{k},100}\left(\alpha_A,\frac{\alpha_1+3\alpha_2}{4}\right)+\boldsymbol{\mathcal{Y}}^H_{\mathbf{k},100}\left(-\alpha_R,\frac{\alpha_1+3\alpha_2}{4}\right)\right]\right.\\ &\left.+\alpha_A\boldsymbol{\mathcal{J}}_{\mathbf{k},100}\left(\alpha_A,\frac{\alpha_1+3\alpha_2}{4}\right)+\alpha_R\boldsymbol{\mathcal{J}}_{\mathbf{k},100}\left(-\alpha_R,\frac{\alpha_1+3\alpha_2}{4}\right)\right\},\end{aligned}\tag{4.3.28}$$

where here α_A and α_R should be evaluated from eqs. (4.2.21) for $\ell_{\mathcal{S}}=s=1$ (scattering state). As before, we have neglected the $\pm\mathbf{P}_B/2$ terms inside the δ-functions in eq. (4.3.27b). Next, we square, sum over the spins, and average over the three dof of the incoming spin-1 state. Using the overlap integrals eq. (4.3.4), we find

$$\begin{aligned}\frac{1}{3}\sum_{\sigma,\rho=1}^{3}\left|\boldsymbol{\mathcal{M}}^{\sigma\rho}\right|^2 \simeq\,&\frac{2^{13}\pi^2\alpha_1}{\alpha_{\mathcal{B}}}\frac{\alpha_A^2}{(\alpha_A+\alpha_R)^2}\left(\frac{\zeta_{\mathcal{B}}^2}{1+\zeta_{\mathcal{B}}^2}\right)\times\\ &\times\left[\left(1-\frac{2\alpha_H}{\alpha_{\mathcal{B}}}\sqrt{\frac{\alpha_R}{\alpha_A}}\right)S^{1/2}_{\text{vec}}\left(\zeta_A,\zeta_{\mathcal{B}}\right)+\left(\frac{\alpha_R}{\alpha_A}+\frac{2\alpha_H}{\alpha_{\mathcal{B}}}\sqrt{\frac{\alpha_R}{\alpha_A}}\right)S^{1/2}_{\text{vec}}\left(-\zeta_R,\zeta_{\mathcal{B}}\right)\right]^2,\end{aligned}\tag{4.3.29}$$

where here $\alpha_{\mathcal{B}}=(\alpha_1+3\alpha_2)/4$ and correspondingly $\zeta_{\mathcal{B}}=(\zeta_1+3\zeta_2)/4$. The cross-section is obtained from eq. (4.3.9a), and is shown in table 4.8.

SS-like $\to \mathcal{B}(D\bar{D})+B$

Using the perturbative parts (4.3.27), and the wavefunctions listed in tables 4.3 and 4.4, we find the full amplitude (4.3.1a)

$$\begin{aligned}\mathbb{i}\boldsymbol{\mathcal{M}}^{\sigma\rho} \simeq \mathbb{i}\delta^{\sigma\rho}\,&\frac{2}{\alpha_A+\alpha_R}\sqrt{4\pi\alpha_1\,4m}\,\times\\ &\times\left\{-4\left[\alpha_R\boldsymbol{\mathcal{Y}}^H_{\mathbf{k},100}\left(\alpha_A,\frac{\alpha_1+3\alpha_2}{4}\right)+\alpha_A\boldsymbol{\mathcal{Y}}^H_{\mathbf{k},100}\left(-\alpha_R,\frac{\alpha_1+3\alpha_2}{4}\right)\right]\right.\\ &\left.+\sqrt{2\alpha_A\alpha_R}\left[+\boldsymbol{\mathcal{J}}_{\mathbf{k},100}\left(\alpha_A,\frac{\alpha_1+3\alpha_2}{4}\right)-\boldsymbol{\mathcal{J}}_{\mathbf{k},100}\left(-\alpha_R,\frac{\alpha_1+3\alpha_2}{4}\right)\right]\right\},\end{aligned}\tag{4.3.30}$$

where again α_A and α_R should be evaluated from eqs. (4.2.21) for $\ell_{\mathcal{S}}=s=1$ (scattering state), and with the help of the overlap integrals (4.3.4),

$$\begin{aligned}\frac{1}{3}\sum_{\sigma,\rho=1}^{3}\left|\boldsymbol{\mathcal{M}}^{\sigma\rho}\right|^2 \simeq\,&\frac{2^{14}\pi^2\alpha_1}{\alpha_{\mathcal{B}}}\frac{\alpha_A\alpha_R}{(\alpha_A+\alpha_R)^2}\left(\frac{\zeta_{\mathcal{B}}^2}{1+\zeta_{\mathcal{B}}^2}\right)\times\\ &\times\left[\left(1-\frac{2\alpha_H}{\alpha_{\mathcal{B}}}\sqrt{\frac{2\alpha_R}{\alpha_A}}\right)S^{1/2}_{\text{vec}}\left(\zeta_A,\zeta_{\mathcal{B}}\right)-\left(1+\frac{2\alpha_H}{\alpha_{\mathcal{B}}}\sqrt{\frac{2\alpha_A}{\alpha_R}}\right)S^{1/2}_{\text{vec}}\left(-\zeta_R,\zeta_{\mathcal{B}}\right)\right]^2,\end{aligned}\tag{4.3.31}$$

with $\alpha_{\mathcal{B}}=(\alpha_1+3\alpha_2)/4$ and $\zeta_{\mathcal{B}}=(\zeta_1+3\zeta_2)/4$. The cross-section is obtained from eq. (4.3.9a), and is shown in table 4.8.

$D\bar{D} \to \mathcal{B}(D\bar{D}) + W$

The perturbative part of the amplitude is (cf. eq. (4.3.18b))

$$\begin{aligned}\mathbb{i}(\boldsymbol{\mathcal{A}}^{\sigma\rho})^{a}_{ij}\left[(D\bar{D})^{\text{spin-1}} \to (D\bar{D})^{\text{spin-1}}_{(\mathbb{1},0)} + W\right] \simeq \mathbb{i}\delta^{\sigma\rho}\,\frac{t^{a}_{ji}}{\sqrt{2}}\,g_2\,2m\times \\ \times\left\{2m\;4\pi\alpha_2\;\frac{2(\mathbf{k}'-\mathbf{p})}{(\mathbf{k}'-\mathbf{p})^4} + 2\mathbf{p}\,(2\pi)^3\left[\delta^3(\mathbf{k}'-\mathbf{p}-\mathbf{P}_{W}/2) + \delta^3(\mathbf{k}'-\mathbf{p}+\mathbf{P}_{W}/2)\right]\right\}. \quad (4.3.32)\end{aligned}$$

Using the wavefunctions listed in tables 4.3 and 4.4, and anticipating that the scattering state will be an $SU_{L}(2)$ triplet, we find the full amplitude (4.3.1a),

$$\begin{aligned}\mathbb{i}(\boldsymbol{\mathcal{M}}^{\sigma\rho})^{a}_{ij} \simeq \mathbb{i}\delta^{\sigma\rho}t^{a}_{ji}\sqrt{4\pi\alpha_2\;2^5 m}\times \\ \times\left\{\mathcal{Y}^{W}_{\mathbf{k},100}\left(\frac{\alpha_1-\alpha_2}{4},\frac{\alpha_1+3\alpha_2}{4}\right) + \mathcal{J}_{\mathbf{k},100}\left(\frac{\alpha_1-\alpha_2}{4},\frac{\alpha_1+3\alpha_2}{4}\right)\right\}. \quad (4.3.33)\end{aligned}$$

Squaring and summing over gauge and spin indices, projects the scattering state on the spin-1 $SU_{L}(2)$ triplet that has 9 dof. Using the overlap integrals (4.3.4), we find

$$\frac{1}{9}\sum_{\sigma,\rho}\sum_{i,j,a}\left|[\boldsymbol{\mathcal{M}}^{\sigma\rho}]^{a}_{ij}\right|^2 \simeq 2^{13}\pi^2\;\frac{\alpha_2}{\alpha_{\mathcal{B}}}\left(1+\frac{\alpha_2}{\alpha_{\mathcal{B}}}\right)^2\left(\frac{\zeta_{\mathcal{B}}^2}{1+\zeta_{\mathcal{B}}^2}\right)\,S_{\text{vec}}\left(\frac{\zeta_1-\zeta_2}{4},\zeta_{\mathcal{B}}\right). \quad (4.3.34)$$

The cross-section is obtained from eq. (4.3.9a), and is shown in table 4.8. It agrees with the results of refs. [55, 62] appropriately adjusted.

$DS \to \mathcal{B}(D\bar{D}) + H$

The perturbative part of the amplitude is

$$\mathbb{i}\mathcal{A}^{\sigma\rho}_{i,h}\left[(DS)^{\text{spin-1}} \to (D\bar{D})^{\text{spin-1}}_{(\mathbb{1},0)} + H\right] \simeq \mathbb{i}\delta^{\sigma\rho}\,\frac{\delta_{ih}}{\sqrt{2}}\,y\,4m^2\,(2\pi)^3\delta^3(\mathbf{k}'-\mathbf{p}+\mathbf{P}_{H}/2). \quad (4.3.35)$$

Using the wavefunctions listed in tables 4.3 and 4.4, we find the full amplitude (4.3.1a),

$$\mathbb{i}\mathcal{M}^{\sigma\rho}_{i,h} \simeq \mathbb{i}\delta^{\sigma\rho}\delta_{ih}\sqrt{\frac{2^8\pi\alpha_{H}}{[(\alpha_1+3\alpha_2)/4]^3}}\;\mathcal{R}_{\mathbf{k},100}\left(-\alpha_{H},\frac{\alpha_1+3\alpha_2}{4}\right). \quad (4.3.36)$$

and taking into account the overlap integral (4.3.4a),

$$\frac{1}{6}\sum_{\sigma,\rho}\sum_{i,h}\left|\mathcal{M}^{\sigma\rho}_{i,h}\right|^2 \simeq \frac{2^{14}\pi^2\alpha_{H}}{\alpha_{\mathcal{B}}^3}\left(1+\frac{\alpha_{H}}{\alpha_{\mathcal{B}}}\right)^2\left(\frac{\zeta_{\mathcal{B}}^2}{1+\zeta_{\mathcal{B}}^2}\right)S_{\text{scl}}\left(-\zeta_{H},\zeta_{\mathcal{B}}\right), \quad (4.3.37)$$

with $\alpha_{\mathcal{B}} = (\alpha_1+3\alpha_2)/4$ and $\zeta_{\mathcal{B}} = (\zeta_1+3\zeta_2)/4$. The cross-section is obtained from eq. (4.3.9b), and is shown in table 4.8.

4.3.4 DD bound states: $(\mathbb{1},1)$, spin 1, $n\ell m = \{100\}$

The BSF processes are listed in table 4.9, and the radiative part of the diagrams contributing to these processes are shown in fig. 4.7. In all processes below, we project the bound-state fields on the $SU_{L}(2)$ singlet via $\epsilon_{i'j'}/\sqrt{2}$. Moreover, as in section 4.3.3, we project both the scattering and the bound states on the spin-1 configuration via $[U^{\sigma}_{\text{spin-1}}]^{s_1s_2}[U^{\rho\dagger}_{\text{spin-1}}]^{r_2r_1}$, and invoke that $[U^{\sigma\dagger}_{\text{spin-1}}]^{s_1s_2}$ are symmetric in s_1, s_2, and $[U^{\sigma}_{\text{spin-1}}]^{s_1s_2}[U^{\rho\dagger}_{\text{spin-1}}]^{s_1s_2} = \delta^{\sigma\rho}$.

Bound state DD : $(\mathbb{1},\mathbf{1})$, **spin 1,** $\{n\ell m\} = \{\mathbf{100}\}$

Scattering state (spin 1)					Rad boson	Cross-section $(\sigma_{\rm BSF} v_{\rm rel})/(\pi m^{-2})$
State	$U_Y(1)$	$SU_L(2)$	dof	$\ell_{\mathcal{S}}$		
DD	1	$\mathbb{1}$	3	1	B	0 (due to antisymmetry of DD scattering state)
DD	1	$\mathbb{3}$	9	1	W	$\frac{2^{11}\alpha_{\mathcal{B}}\alpha_2}{3}\left(1+\frac{\alpha_2}{\alpha_{\mathcal{B}}}\right)^2 \; S_{\rm vec}\left(-\frac{\zeta_1+\zeta_2}{4},\zeta_{\mathcal{B}}\right)$
DS	$+1/2$	$\mathbb{2}$	6	0	$H^\dagger$	$\frac{2^{11}\alpha_H}{\alpha_{\mathcal{B}}}\left(1+\frac{\alpha_H}{\alpha_{\mathcal{B}}}\right)^2 \; S_{\rm scl}\left(-\zeta_H,\zeta_{\mathcal{B}}\right)\, h_H(\omega)$

Table 4.9: Same as table 4.7 for the DD bound states. Here, $\alpha_{\mathcal{B}} = (-\alpha_1+3\alpha_2)/4$, $\zeta_{\mathcal{B}} = (-\zeta_1+3\zeta_2)/4$, and $\omega = m\left[(-\alpha_1+3\alpha_2)^2/16 + v_{\rm rel}^2\right]/4$. All processes have conjugate counterparts.

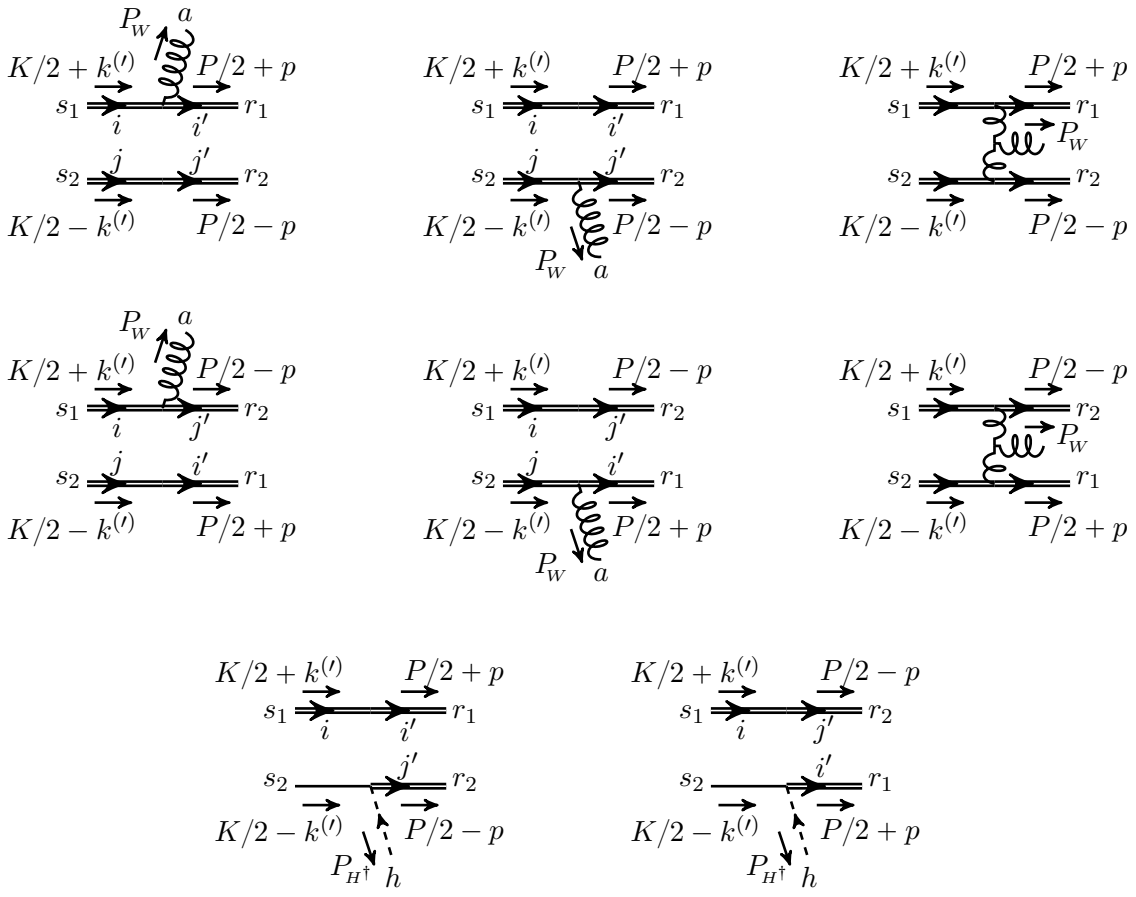

Figure 4.7: Same as fig. 4.5, for the formation of DD bound states. *Top two rows:* $DD \to \mathcal{B}(DD) + W$. *Bottom row:* $DS \to \mathcal{B}(DD) + H^\dagger$.

$DD \to \mathcal{B}(DD) + W$

The perturbative part of the amplitude is

$$\begin{aligned}
&\mathbb{i}(\boldsymbol{\mathcal{A}}^{\sigma\rho})^a_{ij}\left[(DD)^{\text{spin-1}} \to (DD)^{\text{spin-1}}_{(\mathbb{1},0)} + W\right] \simeq \mathbb{i}\delta^{\sigma\rho}\, g_2\, 2m \times \\
&\times \left\{\left[2m\; 4\pi\alpha_2\; \frac{2(\mathbf{k}'-\mathbf{p})}{(\mathbf{k}'-\mathbf{p})^4}\left(-\mathbb{i}f^{abc}t^b_{i'i}t^c_{j'j}\frac{\epsilon_{i'j'}}{\sqrt{2}}\right) + 2\mathbf{p}\,(2\pi)^3\delta^3(\mathbf{k}'-\mathbf{p})\left(t^a_{i'i}\frac{\epsilon_{i'j}}{\sqrt{2}} - t^a_{j'j}\frac{\epsilon_{ij'}}{\sqrt{2}}\right)\right]\right. \\
&\left.-(i \leftrightarrow j,\; \mathbf{k} \to -\mathbf{k})\right\}, \qquad (4.3.38)
\end{aligned}$$

where the last line accounts for the u-channel diagrams. The different number of fermion permutations in the t- and u-channel diagrams introduces a relative (-1) factor between the two, while the projection on the symmetric spin-1 state does not. Here we have neglected the $\pm\mathbf{P}_W/2$ terms inside the δ-functions already at the level of the perturbative amplitude.

It is easy to check that the gauge factors in eq. (4.3.38) are symmetric in $i \leftrightarrow j$, as expected, since the scattering state must be an $SU_L(2)$ triplet. Convoluting with the scattering state wavefunction and setting $\mathbf{k} \to -\mathbf{k}$ for the u channel renders the latter identical to the t-channel up to the extra factor $-(-1)^{\ell_S} = +1$ since $\ell_S = 1$. Thus, the t and u channels add up, and we find the full amplitude (4.3.1a) to be

$$\begin{aligned}
\mathbb{i}(\boldsymbol{\mathcal{M}}^{\sigma\rho})^a_{ij} \simeq \mathbb{i}\delta^{\sigma\rho}\sqrt{4\pi\alpha_2\, 2^8 m} \times \Bigg[&2\boldsymbol{\mathcal{Y}}^W_{\mathbf{k},100}\left(-\frac{\alpha_1+\alpha_2}{4}, \frac{-\alpha_1+3\alpha_2}{4}\right)\left(-\mathbb{i}f^{abc}t^b_{i'i}t^c_{j'j}\frac{\epsilon_{i'j'}}{\sqrt{2}}\right) \\
&+\boldsymbol{\mathcal{J}}_{\mathbf{k},100}\left(-\frac{\alpha_1+\alpha_2}{4}, \frac{-\alpha_1+3\alpha_2}{4}\right)\left(t^a_{i'i}\frac{\epsilon_{i'j}}{\sqrt{2}} - t^a_{j'j}\frac{\epsilon_{ij'}}{\sqrt{2}}\right)\Bigg], \qquad (4.3.39)
\end{aligned}$$

where we also took into account the symmetry factors of the scattering and bound state wavefunctions, as stated in tables 4.3 and 4.4. Considering the relation (4.3.4c) between the overlap integrals, the above simplifies to

$$\mathbb{i}(\boldsymbol{\mathcal{M}}^{\sigma\rho})^a_{ij} \simeq \mathbb{i}\delta^{\sigma\rho}\sqrt{4\pi\alpha_2\, 2^8 m} \times \boldsymbol{\mathcal{J}}_{\mathbf{k},100}\left(-\frac{\alpha_1+\alpha_2}{4}, \alpha_{\mathcal{B}}\right) G^a_{ij}, \qquad (4.3.40)$$

where here $\alpha_{\mathcal{B}} = (-\alpha_1 + 3\alpha_2)/4$, and G^a_{ij} is the gauge factor

$$G^a_{ij} \equiv t^a_{i'i}\frac{\epsilon_{i'j}}{\sqrt{2}} - t^a_{j'j}\frac{\epsilon_{ij'}}{\sqrt{2}} + \frac{\alpha_2}{\alpha_{\mathcal{B}}}\left(-\mathbb{i}2f^{abc}t^b_{i'i}t^c_{j'j}\frac{\epsilon_{i'j'}}{\sqrt{2}}\right), \qquad (4.3.41)$$

with

$$G^a_{ij}G^{a\,*}_{ij} = 3\left(1 + \frac{\alpha_2}{\alpha_{\mathcal{B}}}\right)^2. \qquad (4.3.42)$$

Squaring eq. (4.3.40) and summing over gauge indices and spins projects the scattering state on the spin-1 $SU_L(2)$ triplet configuration that has nine dof. Considering the overlap integral (4.3.4b), we find

$$\frac{1}{9}\sum_{\sigma,\rho}\sum_{i,j,a}|(\boldsymbol{\mathcal{M}}^{\sigma\rho})^a_{ij}|^2 \simeq 2^{17}\pi^2\frac{\alpha_2}{\alpha_{\mathcal{B}}}\left(1+\frac{\alpha_2}{\alpha_{\mathcal{B}}}\right)^2\left(\frac{\zeta_{\mathcal{B}}^2}{1+\zeta_{\mathcal{B}}^2}\right)S_{\text{vec}}\left(-\frac{\zeta_1+\zeta_2}{4}, \zeta_{\mathcal{B}}\right). \qquad (4.3.43)$$

The cross-section is obtained from eq. (4.3.9a) and is shown in table 4.9.

$DS \to \mathcal{B}(DD) + H^\dagger$

The perturbative part of the amplitude is

$$\begin{aligned}\mathbb{i}\mathcal{A}^{\sigma\rho}_{i,h}\left[(DS)^{\text{spin-1}} \to (DD)^{\text{spin-1}}_{(\mathbb{1},0)} + H\right] \simeq &- \mathbb{i}\delta^{\sigma\rho}\,\frac{\epsilon_{ih}}{\sqrt{2}}\,y\,4m^2\,(2\pi)^3\delta^3(\mathbf{k}' - \mathbf{p} + \mathbf{P}_H/2)\\ &+ \mathbb{i}\delta^{\sigma\rho}\,\frac{\epsilon_{hi}}{\sqrt{2}}\,y\,4m^2\,(2\pi)^3\delta^3(\mathbf{k}' + \mathbf{p} + \mathbf{P}_H/2),\end{aligned} \tag{4.3.44}$$

where the fermion permutations alloted factors $(+1)$ and (-1) to the t and u channels respectively. As seen from eq. (4.3.44), the resulting relative sign is canceled upon contraction of the bound-state fields on the $SU_L(2)$ singlet state. Convoluting eq. (4.3.44) with the scattering and bound state wavefunctions found in tables 4.3 and 4.4, and setting $\mathbf{p} \to -\mathbf{p}$ renders the u-channel contribution the same as t-channel, with the extra factor $(-1)^\ell = +1$ for $\ell = 0$. Thus the t and u channels add up, and we find

$$\mathbb{i}\mathcal{M}^{\sigma\rho}_{i,h} \simeq -\,\mathbb{i}\delta^{\sigma\rho}\,\epsilon_{ih}\sqrt{\frac{2^{12}\pi\alpha_H}{\alpha_{\mathcal{B}}^3}}\,\mathcal{R}_{\mathbf{k},100}(-\alpha_H, \alpha_{\mathcal{B}}). \tag{4.3.45}$$

Here $\alpha_{\mathcal{B}} = (-\alpha_1 + 3\alpha_2)/4$, and we have included the symmetry factors of the scattering and bound state wavefunctions. Squaring and summing over the gauge indices and spins, and using the overlap integral eq. (4.3.4a), we find

$$\frac{1}{6}\sum_{\sigma,\rho}\sum_{i,h}|\mathcal{M}^{\sigma\rho}_{i,h}|^2 \simeq \frac{2^{18}\pi^2\alpha_H}{\alpha_{\mathcal{B}}^3}\left(1 + \frac{\alpha_H}{\alpha_{\mathcal{B}}}\right)^2\left(\frac{\zeta_{\mathcal{B}}^2}{1+\zeta_{\mathcal{B}}^2}\right)S_{\text{scl}}(-\zeta_H, \zeta_{\mathcal{B}}), \tag{4.3.46}$$

where we averaged over the six dof of the spin-1 $SU_L(2)$ doublet scattering state. The cross-section is obtained from eq. (4.3.9b) and is shown in table 4.9.

4.3.5 DS bound states: $(\mathbb{2}, 1/2)$, spin 0, $n\ell m = \{100\}$

The BSF processes are listed in table 4.10, and the radiative part of the diagrams contributing to these processes are shown in fig. 4.8. We project the bound-state fields on the spin-0 state via $U^{s_1s_2}_{\text{spin-0}}[U^{-1}_{\text{spin-0}}]^{r_2r_1} = (\epsilon^{s_1s_2}/\sqrt{2})(\epsilon^{r_1r_2}/\sqrt{2})$.

$DS \to \mathcal{B}(DS) + B$

The perturbative part of the amplitude is

$$\begin{aligned}\mathbb{i}\boldsymbol{\mathcal{A}}_{i,i'}\left[(DS)^{\text{spin-0}} \to (DS)^{\text{spin-0}} + B\right] \simeq &\ \mathbb{i}\delta_{ii'}\,g_1Y_D\,2m\,2\mathbf{p}\,(2\pi)^3\delta^3(\mathbf{k}' - \mathbf{p} - \mathbf{P}_B/2)\\ &+ \mathbb{i}\delta_{ii'}\,g_1Y_H\,y^2\,4m^2\,\frac{2(\mathbf{k}'+\mathbf{p})}{[(\mathbf{k}+\mathbf{p})^2 + m_H^2]^2},\end{aligned} \tag{4.3.47}$$

where the fermion permutations alloted factors $(+1)$ and (-1) to the t and u channels. Upon projection on the spin-0 states, the u channel acquired another factor (-1). Using the wavefunctions of tables 4.3 and 4.4, we find the full amplitude (4.3.1a) to be

$$\mathbb{i}\boldsymbol{\mathcal{M}}_{i,i'} \simeq \mathbb{i}\delta_{ii'}\sqrt{4\pi\alpha_1\,4m}\left[\boldsymbol{\mathcal{J}}_{\mathbf{k},100}(-\alpha_H, \alpha_H) + 2\boldsymbol{\mathcal{Y}}^H_{\mathbf{k},100}(-\alpha_H, \alpha_H)\right], \tag{4.3.48}$$

Next we square, sum over the gauge indices and average over the two dof of the spin-0 scattering state. Using the overlap integrals (4.3.4), we obtain

$$\frac{1}{2}\sum_{i,i'}|\boldsymbol{\mathcal{M}}_{i,i'}|^2 \simeq \frac{2^{11}3^2\pi^2\alpha_1}{\alpha_H}\left(\frac{\zeta_H^2}{1+\zeta_H^2}\right)S_{\text{vec}}(-\zeta_H, \zeta_H). \tag{4.3.49}$$

The cross-section is found from eq. (4.3.9a) for $\alpha_{\mathcal{B}} = \alpha_H$ and is shown in table 4.10.

Bound state DS : $(\mathbb{2},\mathbf{1/2})$, spin 0, $\{n\ell m\}=\{\mathbf{100}\}$

Scattering state (spin 0)					Rad	Cross-section
State	$U_Y(1)$	$SU_L(2)$	dof	$\ell_{\mathcal{S}}$	Boson	$(\sigma_{\rm BSF}v_{\rm rel})/(\pi m^{-2})$
DS	$+1/2$	$\mathbb{2}$	2	1	B	$2^5 3\,\alpha_H\alpha_1\,S_{\rm vec}(-\zeta_H,\zeta_H)$
DS	$+1/2$	$\mathbb{2}$	2	1	W	$2^5 3^2\alpha_H\alpha_2\,S_{\rm vec}(-\zeta_H,\zeta_H)$
SS-like	0	$\mathbb{1}$	1	0	$H^\dagger$	$\frac{2^{12}\alpha_A^2}{(\alpha_A+\alpha_R)^2}\left[\left(1+\sqrt{\frac{\alpha_R}{8\alpha_A}}\right)\left(1+\frac{\alpha_R}{\alpha_H}\right)S_{\rm scl}^{1/2}(-\zeta_R,\zeta_H)\right.$ $\left.-\left(\frac{\alpha_R}{\alpha_A}-\sqrt{\frac{\alpha_R}{8\alpha_A}}\right)\left(1-\frac{\alpha_A}{\alpha_H}\right)S_{\rm scl}^{1/2}(\zeta_A,\zeta_H)\right]^2 h_H(\omega)$
$D\bar{D}$-like	0	$\mathbb{1}$	1	0	$H^\dagger$	$\frac{2^8\alpha_A^2}{(\alpha_A+\alpha_R)^2}\left[\left(\frac{\alpha_R}{\alpha_A}-\sqrt{\frac{8\alpha_R}{\alpha_A}}\right)\left(1+\frac{\alpha_R}{\alpha_H}\right)S_{\rm scl}^{1/2}(-\zeta_R,\zeta_H)\right.$ $\left.+\left(1+\sqrt{\frac{8\alpha_R}{\alpha_A}}\right)\left(1-\frac{\alpha_A}{\alpha_H}\right)S_{\rm scl}^{1/2}(\zeta_A,\zeta_H)\right]^2 h_H(\omega)$
$D\bar{D}$	0	$\mathbb{3}$	3	0	$H^\dagger$	$2^8\left(1-\frac{\alpha_1-\alpha_2}{\alpha_H}\right)^2 S_{\rm scl}\left(\frac{\zeta_1-\zeta_2}{4},\zeta_H\right)h_H(\omega)$
DD	1	$\mathbb{1}$	1	0	H	0 (due to antisymmetry of DD scattering state)
DD	1	$\mathbb{3}$	3	0	H	$2^{11}\left(1+\frac{\alpha_1+\alpha_2}{\alpha_H}\right)^2 S_{\rm scl}\left(-\frac{\zeta_1+\zeta_2}{4},\zeta_H\right)h_H(\omega)$

Table 4.10: Same as table 4.10 for the DS bound states. For the SS-like and $D\bar{D}$-like states, α_A and α_R should be evaluated from eq. (4.2.21) for $\ell_{\mathcal{S}}=s=0$. Here, $\omega=m(\alpha_H^2+v_{\rm rel}^2)/4$. All processes have conjugate counterparts.

$DS\to\mathcal{B}(DS)+W$

The perturbative part of the amplitude is

$$\begin{aligned}\mathbb{i}\boldsymbol{\mathcal{A}}^a_{i,i'}\left[(DS)^{\text{spin-0}}\to(DS)^{\text{spin-0}}+W\right]\simeq{}&\mathbb{i}t^a_{i'i}\,g_2\,2m\,2\mathbf{p}\,(2\pi)^3\delta^3(\mathbf{k}'-\mathbf{p}-\mathbf{P}_B/2)\\&+\mathbb{i}t^a_{i'i}\,g_2\,y^2\,4m^2\,\frac{2(\mathbf{k}'+\mathbf{p})}{[(\mathbf{k}+\mathbf{p})^2+m_H^2]^2},\end{aligned}\tag{4.3.50}$$

where the signs are determined as in eq. (4.3.47). The full amplitude is

$$\mathbb{i}\boldsymbol{\mathcal{M}}^a_{i,i'}\simeq\mathbb{i}t^a_{i'i}\sqrt{4\pi\alpha_2\,2^4m}\left[\boldsymbol{\mathcal{J}}_{\mathbf{k},100}(-\alpha_H,\alpha_H)+2\boldsymbol{\mathcal{Y}}^H_{\mathbf{k},100}(-\alpha_H,\alpha_H)\right],\tag{4.3.51}$$

and

$$\frac{1}{2}\sum_{i,i',a}|\boldsymbol{\mathcal{M}}^a_{i,i'}|^2\simeq\frac{2^{11}3^3\pi^2\alpha_2}{\alpha_H}\left(\frac{\zeta_H^2}{1+\zeta_H^2}\right)S_{\rm vec}(-\zeta_H,\zeta_H),\tag{4.3.52}$$

where we used $\mathrm{Tr}(t^at^a)=3/2$. The cross-section is found from eq. (4.3.9a) for $\alpha_{\mathcal{B}}=\alpha_H$ and is shown in table 4.10.

SS**-like** $\to\mathcal{B}(DS)+H^\dagger$

The perturbative parts of the amplitude are

$$\begin{aligned}\mathbb{i}\mathcal{A}_{i'h}\left[(SS)^{\text{spin-0}}\to(DS)^{\text{spin-0}}+H^\dagger\right]\simeq{}&-\mathbb{i}\delta_{ih}\,y\,4m^2\,(2\pi)^3\delta^3(\mathbf{k}'-\mathbf{p}-\mathbf{P}_{H^\dagger}/2)\\&-\mathbb{i}\delta_{ih}\,y\,4m^2\,(2\pi)^3\delta^3(\mathbf{k}'+\mathbf{p}+\mathbf{P}_{H^\dagger}/2)\end{aligned}\tag{4.3.53a}$$

$$\mathbb{i}\mathcal{A}_{ij,i'h}\left[(D\bar{D})^{\text{spin-0}}\to(DS)^{\text{spin-0}}+H^\dagger\right]\simeq\mathbb{i}\delta_{ii'}\delta_{jh}\,y\,4m^2(2\pi)^3\delta^3(\mathbf{k}'-\mathbf{p}+\mathbf{P}_{H^\dagger}/2).\tag{4.3.53b}$$

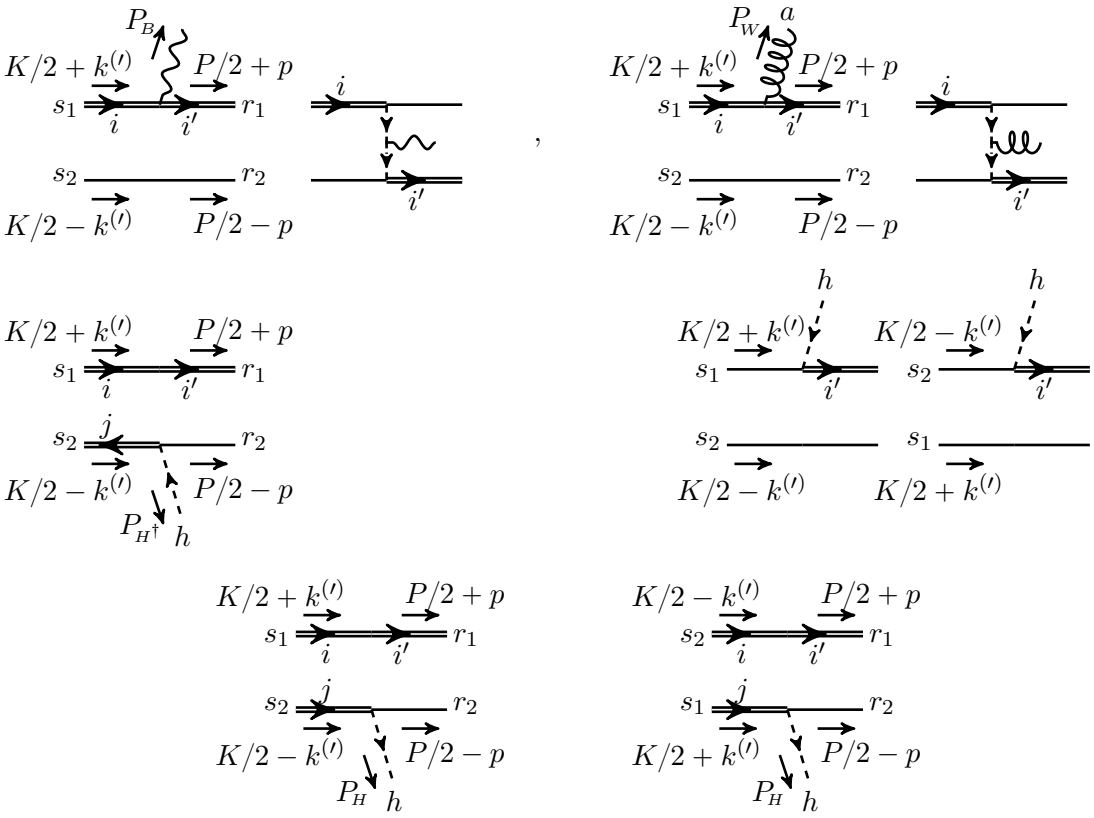

Figure 4.8: Same as fig. 4.5, for the formation of DS bound states. *Top row:* $DS \to \mathcal{B}(DS) + B$ (left) and $DS \to \mathcal{B}(DS) + W$ (right). *Middle row:* $D\bar{D}$-like $\to \mathcal{B}(DS) + H^\dagger$ and SS-like $\to \mathcal{B}(DS) + H^\dagger$. The diagram on the left gives also $D\bar{D} \to \mathcal{B}(DS) + H^\dagger$. *Bottom row:* $DD \to \mathcal{B}(DS) + H$.

In eq. (4.3.53a), the fermion permutations alloted signs $(+1)$ and (-1) factors to the t and u channels. Upon projection on the spin-0 state, the u channel acquired another factor (-1). We now project the $D\bar{D}$ component of the scattering state in eq. (4.3.53b), on the $SU_L(2)$ singlet configuration via $\delta_{ij}/\sqrt{2}$,

$$\mathbb{i}\mathcal{A}_{i'h}\left[(D\bar{D})^{\text{spin-0}}_{(\mathbb{1},0)} \to (DS)^{\text{spin-0}} + H^\dagger\right] \simeq \mathbb{i}\,\frac{\delta_{i'h}}{\sqrt{2}}\, y\, 4m^2(2\pi)^3\delta^3(\mathbf{k}' - \mathbf{p} + \mathbf{P}_{H^\dagger}/2). \tag{4.3.53c}$$

Considering the wavefunctions of tables 4.3 and 4.4, the full amplitude (4.3.1a) is

$$\begin{aligned}\mathbb{i}\mathcal{M}_{i'h} \simeq -\mathbb{i}\delta_{i'h}\sqrt{\frac{2^{12}\pi}{\alpha_H^2}}\left(\frac{\alpha_A}{\alpha_A+\alpha_R}\right)\times \\ \times\left[\left(1+\sqrt{\frac{\alpha_R}{8\alpha_A}}\right)\mathcal{R}_{\mathbf{k},100}(-\alpha_R,\alpha_H) - \left(\frac{\alpha_R}{\alpha_A}-\sqrt{\frac{\alpha_R}{8\alpha_A}}\right)\mathcal{R}_{\mathbf{k},100}(\alpha_A,\alpha_H)\right],\end{aligned} \tag{4.3.54}$$

where α_A and α_R should be evaluated from eq. (4.2.21) for $\ell_{\mathcal{S}} = s = 0$. Using the overlap integrals (4.3.4),

$$\begin{aligned}\sum_{i',h}|\mathcal{M}_{i'h}|^2 \simeq \frac{2^{19}\pi^2}{\alpha_H^2}\left(\frac{\alpha_A}{\alpha_A+\alpha_R}\right)^2\left(\frac{\zeta_H^2}{1+\zeta_H^2}\right)\times \\ \times\left[\left(1+\sqrt{\frac{\alpha_R}{8\alpha_A}}\right)\left(1+\frac{\alpha_R}{\alpha_H}\right)S^{1/2}_{\text{scl}}(-\zeta_R,\zeta_H) - \left(\frac{\alpha_R}{\alpha_A}-\sqrt{\frac{\alpha_R}{8\alpha_A}}\right)\left(1-\frac{\alpha_A}{\alpha_H}\right)S^{1/2}_{\text{scl}}(\zeta_A,\zeta_H)\right]^2.\end{aligned} \tag{4.3.55}$$

The cross-section is found from eq. (4.3.9b) for $\alpha_{\mathcal{B}} = \alpha_H$ and is shown in table 4.10.

$D\bar{D}$-like $\to \mathcal{B}(DS) + H^\dagger$

Starting from the perturbative parts (4.3.53a) and (4.3.53c), and considering the wavefunctions of tables 4.3 and 4.4, the full amplitude (4.3.1a) is

$$\begin{aligned}\mathbb{i}\mathcal{M}_{i'h} \simeq\ & \mathbb{i}\delta_{i'h}\sqrt{\frac{2^8\pi}{\alpha_H^2}}\left(\frac{\alpha_A}{\alpha_A+\alpha_R}\right)\times \\ & \times\left[\left(\frac{\alpha_R}{\alpha_A}-\sqrt{\frac{8\alpha_R}{\alpha_A}}\right)\mathcal{R}_{\mathbf{k},100}(-\alpha_R,\alpha_H)+\left(1+\sqrt{\frac{8\alpha_R}{\alpha_A}}\right)\mathcal{R}_{\mathbf{k},100}(\alpha_A,\alpha_H)\right],\end{aligned} \tag{4.3.56}$$

where again α_A and α_R should be evaluated from eq. (4.2.21) for $\ell_{\mathcal{S}} = s = 0$. Using the overlap integrals (4.3.4),

$$\begin{aligned}\sum_{i',h}|\mathcal{M}_{i'h}|^2 \simeq\ & \frac{2^{15}\pi^2}{\alpha_H^2}\left(\frac{\alpha_A}{\alpha_A+\alpha_R}\right)^2\left(\frac{\zeta_H^2}{1+\zeta_H^2}\right)\times \\ & \times\left[\left(\frac{\alpha_R}{\alpha_A}-\sqrt{\frac{8\alpha_R}{\alpha_A}}\right)\left(1+\frac{\alpha_R}{\alpha_H}\right)S^{1/2}_{\rm scl}(-\zeta_R,\zeta_H)+\left(1+\sqrt{\frac{8\alpha_R}{\alpha_A}}\right)\left(1-\frac{\alpha_A}{\alpha_H}\right)S^{1/2}_{\rm scl}(\zeta_A,\zeta_H)\right]^2.\end{aligned} \tag{4.3.57}$$

The cross-section is found from eq. (4.3.9b) for $\alpha_{\mathcal{B}} = \alpha_H$ and is shown in table 4.10.

$D\bar{D} \to \mathcal{B}(DS) + H^\dagger$

The perturbative part of the amplitude is given in eq. (4.3.53b). We project it the $D\bar{D}$ scattering state on the $SU_L(2)$ triplet configuration via $t^a_{ji}/\sqrt{C(2)} = \sqrt{2}t^a_{ji}$, where $C(2) = 1/2$ is the Casimir of the $SU_L(2)$ doublet representation, and obtain

$$\mathbb{i}\mathcal{A}^a_{i'h}\left[(D\bar{D})^{\text{spin-0}}_{(\mathbb{3},\mathbb{0})} \to (DS)^{\text{spin-0}}_{(\mathbb{2},\mathbb{1}/2)} + H^\dagger\right] \simeq \mathbb{i}\sqrt{2}t^a_{hi'}\, y\, 4m^2\,(2\pi)^3\delta^3(\mathbf{k}' - \mathbf{p} + \mathbf{P}_{H^\dagger}/2). \tag{4.3.58}$$

Considering the wavefunctions of tables 4.3 and 4.4, the full amplitude (4.3.1a) is

$$\mathbb{i}\mathcal{M}^a_{i'h} \simeq \mathbb{i}(\sqrt{2}t^a_{hi'})\sqrt{\frac{2^9\pi}{\alpha_H^2}}\,\mathcal{R}_{\mathbf{k},100}\left(\frac{\alpha_1-\alpha_2}{4},\alpha_H\right). \tag{4.3.59}$$

Squaring, summing over the final state gauge indices, and averaging over the three dof of the scattering state, we obtain

$$\frac{1}{3}\sum_{i',h,a}|\mathcal{M}^a_{i'h}|^2 \simeq \frac{2^{15}\pi^2}{\alpha_H^2}\left(1-\frac{\alpha_1-\alpha_2}{\alpha_H}\right)^2\left(\frac{\zeta_H^2}{1+\zeta_H^2}\right)S_{\rm scl}\left(\frac{\zeta_1-\zeta_2}{4},\zeta_H\right), \tag{4.3.60}$$

where we used $\mathrm{Tr}(\sqrt{2}t^a\sqrt{2}t^a) = 3$. The cross-section is found from eq. (4.3.9b) for $\alpha_{\mathcal{B}} = \alpha_H$ and is shown in table 4.10.

$DD \to \mathcal{B}(DS) + H$

The perturbative part of the amplitude is

$$\begin{aligned}&\mathbb{i}\mathcal{A}_{ij,i'h}\left[(DD)^{\text{spin-0}} \to (DS)^{\text{spin-0}} + H\right] \simeq \\ &\qquad \simeq -\mathbb{i}y\,4m^2\left[\delta_{ii'}\delta_{jh}(2\pi)^3\delta^3(\mathbf{k}'-\mathbf{p}+\mathbf{P}_H/2)+\delta_{ji'}\delta_{ih}(2\pi)^3\delta^3(\mathbf{k}'+\mathbf{p}-\mathbf{P}_H/2)\right],\end{aligned} \tag{4.3.61}$$

where the fermion permutations alloted signs $(+1)$ and (-1) factors to the t and u channels. Upon projection on the spin-0 state, the u channel acquired another factor (-1). We now project the DD scattering state on the $SU_{L}(2)$ triplet configuration via the symbolic operator $(U_{\mathbb{3}})^{a}_{ij} = (U_{\mathbb{3}})^{a}_{ji}$, which satisfies $(U_{\mathbb{3}})^{a}_{ij}(U^{\dagger}_{\mathbb{3}})^{b}_{ji} = \delta^{ab}$,

$$\begin{aligned}\mathbb{i}\mathcal{A}^{a}_{i'h}\left[(DD)^{\text{spin-0}}_{(\mathbb{3},1)} \to (DS)^{\text{spin-0}}_{(\mathbb{2},1/2)} + H\right] \simeq \\ \simeq -\mathbb{i}(U_{\mathbb{3}})_{i'h}\, y\, 4m^{2}\left[(2\pi)^{3}\delta^{3}(\mathbf{k}' - \mathbf{p} + \mathbf{P}_{H}/2) + (2\pi)^{3}\delta^{3}(\mathbf{k}' + \mathbf{p} - \mathbf{P}_{H}/2)\right].\end{aligned} \tag{4.3.62}$$

Considering the wavefunctions of tables 4.3 and 4.4, the full amplitude (4.3.1a) is

$$\mathbb{i}\mathcal{M}^{a}_{i'h} \simeq -\mathbb{i}(U_{\mathbb{3}})_{i'h}\sqrt{\frac{2^{12}\pi}{\alpha_{H}^{2}}}\,\mathcal{R}_{\mathbf{k},100}\left(-\frac{\alpha_1+\alpha_2}{4}, \alpha_{H}\right), \tag{4.3.63}$$

where we included the symmetry factor of the DD wavefunction. Squaring, summing over the final state gauge indices, and averaging over the three dof of the scattering state, and using the overlap integral (4.3.4a), we obtain

$$\frac{1}{3}\sum_{i',h,a}|\mathcal{M}^{a}_{i'h}|^{2} \simeq \frac{2^{18}\pi^{2}}{\alpha_{H}^{2}}\left(1+\frac{\alpha_1+\alpha_2}{\alpha_{H}}\right)^{2}\left(\frac{\zeta_{H}^{2}}{1+\zeta_{H}^{2}}\right)S_{\text{scl}}\left(-\frac{\zeta_1+\zeta_2}{4}, \zeta_{H}\right). \tag{4.3.64}$$

The cross-section is found from eq. (4.3.9b) for $\alpha_{\mathcal{B}} = \alpha_{H}$ and is shown in table 4.10.

4.3.6 Unitarity and BSF via Higgs emission

The unitarity of the S matrix implies an upper limit on the partial-wave inelastic cross-sections, $\sigma^{\text{inel}}_{\ell} \leqslant \sigma^{\text{uni}}_{\ell} = (2\ell+1)\pi/k^{2}$, where ℓ is the partial wave and k is the momentum of either of the interacting particles in the CM frame. In the non-relativistic regime, $k = \mu v_{\text{rel}}$ with μ being the reduced mass, thus

$$\sigma^{\text{uni}}_{\ell} v_{\text{rel}} \simeq \frac{(2\ell+1)\pi}{\mu^{2} v_{\text{rel}}}. \tag{4.3.65}$$

As already discussed in ref. [2], the high efficiency of BSF via charged scalar emission implies that the unitarity limit (4.3.65) may be saturated already for rather small values of α_{H}. If the incoming particles interact via an attractive long-range force, then this occurs for the continuum of velocities $v_{\text{rel}} \lesssim \alpha_{\mathcal{B}}$, otherwise only for a finite range or discrete values of v_{rel} (cf. fig. 4.11.) The apparent violation of unitarity at larger α_{H} by the computations of sections 4.3.2 to 4.3.5, whether it occurs for an infinite or finite range of v_{rel}, indicates that these computations must be amended. At small values of α_{H}, higher order corrections to the perturbative transition amplitudes $\mathcal{A}_{T}$ are expected to be insignificant. Restoring unitarity in perturbative calculations in the non-relativistic regime necessitates instead that the two-particle interactions at infinity are resummed [46].

The results of sections 4.3.2 to 4.3.5 already include the resummation of the (leading-order) long-range interaction between the incoming particles, computed in section 4.2.1. However, according to the optical theorem, all elastic and inelastic processes to which the incoming state may participate contribute to its self-energy. Typically, contact-type interactions can be neglected, as they do not distort significantly the wavefuctions of the interacting particles. Nevertheless, if a contact-type interaction is very strong – as is the case when the corresponding cross-section approaches (or even appears to exceed) the unitarity limit (4.3.65) – then its contribution to the two-particle self-energy may be significant.

The contributions to the 2PI kernels arising from inelastic processes that involve Higgs emission are shown in fig. 4.10. These diagrams include both scattering and bound intermediate states of the S, D and $\bar{D}$ particles, and therefore include bremsstrahlung, BSF and bound-to-bound transitions. Note that in fig. 4.10 we have not included the resummation of the long-range kernels of section 4.2.1 in the incoming and outgoing pairs, as this would result in double-counting; only 2PI diagrams must be included in the kernels that determine the potential.

The proper resummation of the diagrams of fig. 4.10 requires developing suitable formalism, and is beyond the scope of the present work. To ensure that our cross-sections are consistent with partial-wave unitarity, we shall instead adapt the result of ref. [133] that resummed the box diagrams arising from the perturbative part of s-wave annihilation into radiation (hard scattering), to compute the effect on the scattering-state wavefunctions and ultimately on the full cross-sections for s-wave annihilation into radiation. This procedure regulates the annihilation cross-sections as follows [133, eq. (40)],

$$\sigma^{\text{reg}}_{s\text{-wave}}(i \to f) = \frac{\sigma_{s\text{-wave}}(i \to f)}{\left(1 + \dfrac{\sum_{f'} \sigma_{s\text{-wave}}(i \to f')}{4\sigma^{\text{uni}}_{s\text{-wave}}}\right)^2}, \tag{4.3.66}$$

where we have generalised the result of ref. [133] to multiple annihilation channels. Equation (4.3.66) ensures that the unitarity limit is respected by the total s-wave inelastic cross-section, since it implies $r^{\text{reg}} = r/(1 + r/4)^2 \leqslant 1$, with $r^{(\text{reg})} \equiv \left[\sum_f \sigma^{(\text{reg})}_{s\text{-wave}}(i \to f)\right] / \sigma^{\text{uni}}_{s\text{-wave}}$.

We emphasise that the assumptions made in deriving eq. (4.3.66) are not strictly satisfied in our case, for at least two reasons: (i) Reference [133] assumed that for the resummed inelastic processes (hard scattering), σv_{rel} is independent of v_{rel}. For BSF via Higgs emission, the corresponding cross-sections can be found from tables 4.7 to 4.10 by setting $\zeta_{\mathcal{S}} \to 0$; eq. (4.3.6a) then shows that they depend on v_{rel} for $v_{\text{rel}} \gtrsim \alpha_{\mathcal{B}}$. (ii) In the present case, the new contributions to the kernel may affect both the initial (scattering) and final (bound) state wavefunctions, while only the former is relevant for annihilation into radiation in the analysis of ref. [133]. Nevertheless, we shall adopt eq. (4.3.66) as a perscription that regulates the inelastic cross-sections in the velocity range where the base calculation violates unitarity, while leaving them essentially unaffected outside that range. We leave a more precise treatment for future work.

In fig. 4.11, we show how the prescription (4.3.66) adjusts the inelastic cross-sections for the scattering states that may participate in BSF via Higgs emission. We include the total inelastic cross-section (BSF plus annihilation) in the resummation, although only BSF is significant. However, both BSF and annihilation are regulated by the same factor, which implies that the annihilation cross-sections are affected significantly even while themselves being well below the unitarity limit.

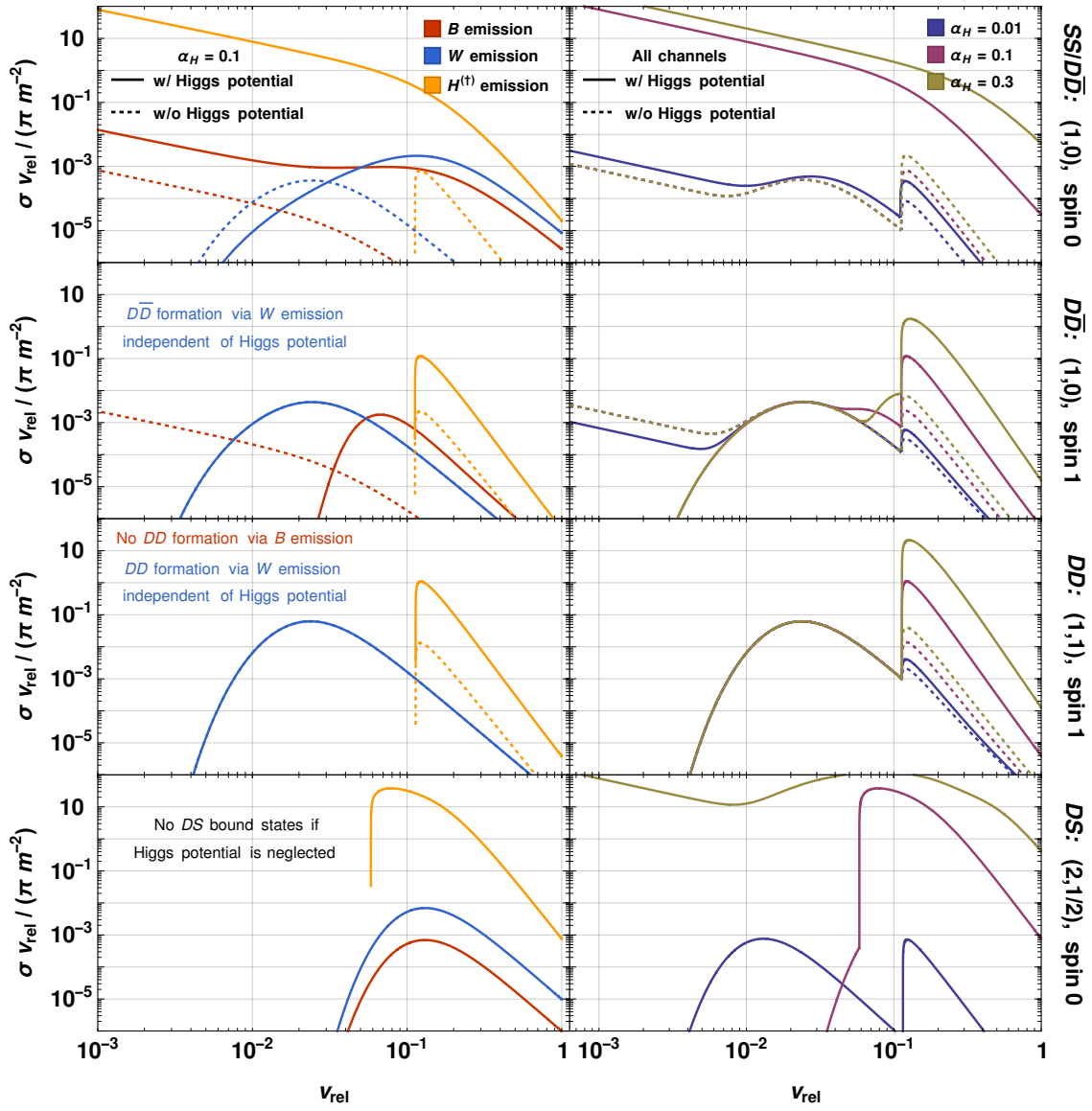

Figure 4.9: The radiative BSF cross-sections vs relative velocity. The four rows correspond to capture into the ground levels of the bound states marked on the right. In the DD and DS panels, we have included the capture into the conjugate bound states, and all BSF channels have been weighted with the number of DM particles eliminated in each process as estimated upon thermal averaging (cf. section 4.5.) *Left column*: The contributions of B, W and $H^{(\dagger)}$ emission, for $\alpha_H = 0.1$. Comparing with fig. 4.3 at $v_{\rm rel} \sim 0.1$ relevant for DM freeze-out, BSF can be comparable to or significantly faster (in the case of $H^{(\dagger)}$ emission) than annihilation, $\sigma_{\rm ann} v_{\rm rel}/(\pi m^{-2}) \sim 10^{-3}$. *Right column*: The sum of the B-, W- and $H^{(\dagger)}$-emission contributions, for different values of α_H. In both columns, we show the cross-sections considering and neglecting the Higgs-mediated potential. The various $\sigma v_{\rm rel}$ normalised to πm^{-2} are independent of the DM mass, except for the cutoff on BSF via $H^{(\dagger)}$ emission due the Higgs mass; for this purpose, we have used $m = 50$ TeV and temperature $T = 300$ GeV which sets $m_H \simeq 168$ GeV. Note that we take the Higgs potential to be Coulombic (see text for discussion.)

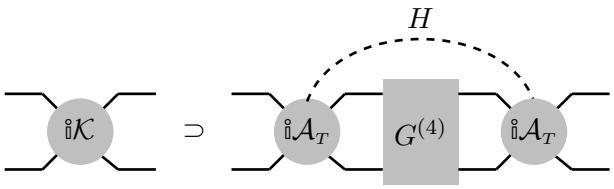

Figure 4.10: The contributions to the 2PI kernels arising from inelastic processes that involve Higgs emission. The solid lines stand for any of the S, D or $\bar{D}$ particles, and $G^{(4)}$ includes their scattering and bound states. The dashed line represents the Higgs doublet. $\mathcal{A}_T$ are the perturbative transition amplitudes with $H^{(\dagger)}$ emission, computed in sections 4.3.2 to 4.3.5.

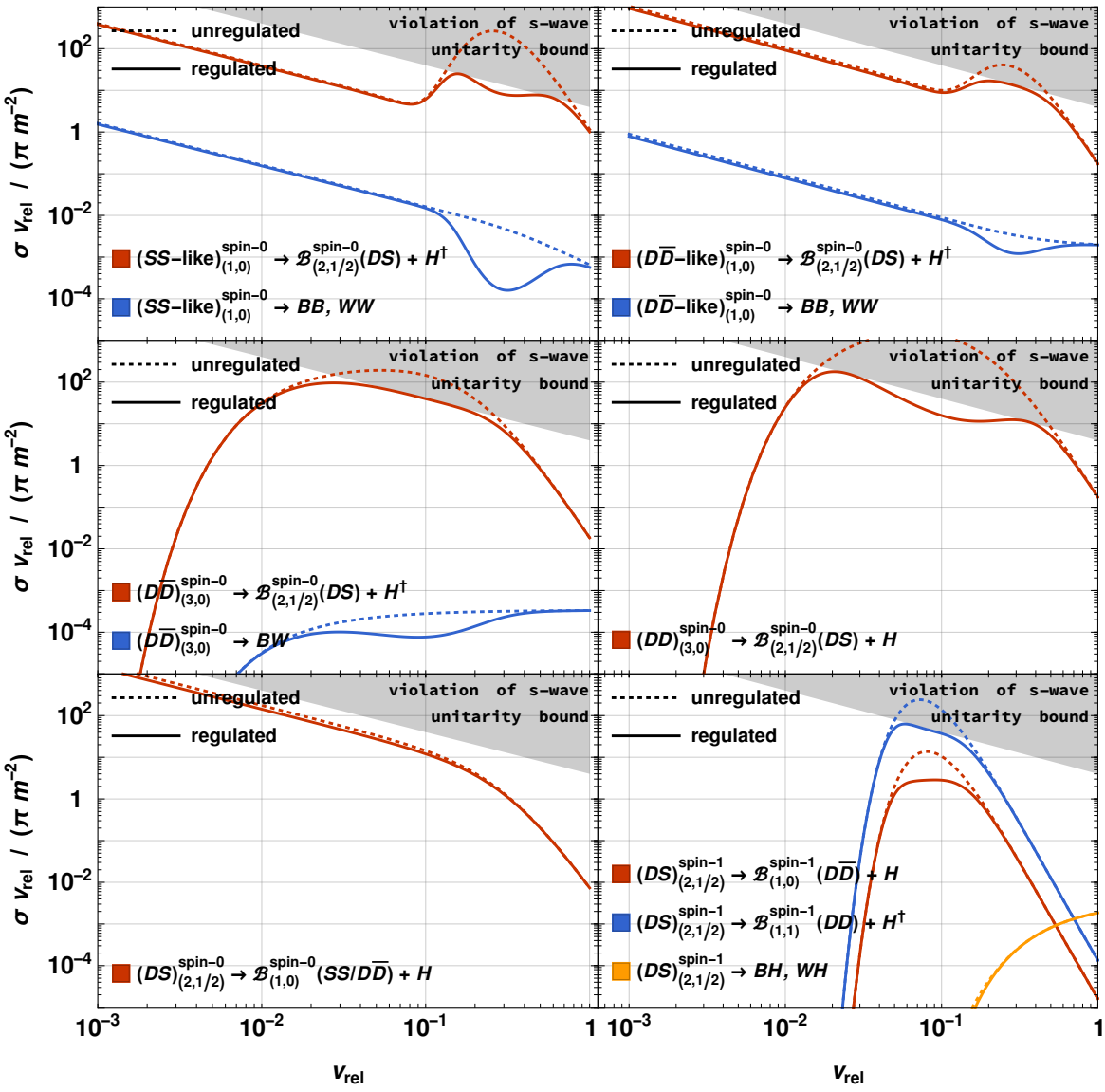

Figure 4.11: The effect of the perscription (4.3.66) on the inelastic cross-sections. While only BSF via Higgs emission approaches or appears to violate the unitarity limit, the regurarisation affects all cross-sections with the same intial state. We have used $\alpha_H = 0.2$, $m = 50$ TeV and $T = 300$ GeV which corresponds to $m_H \simeq 168$ GeV.

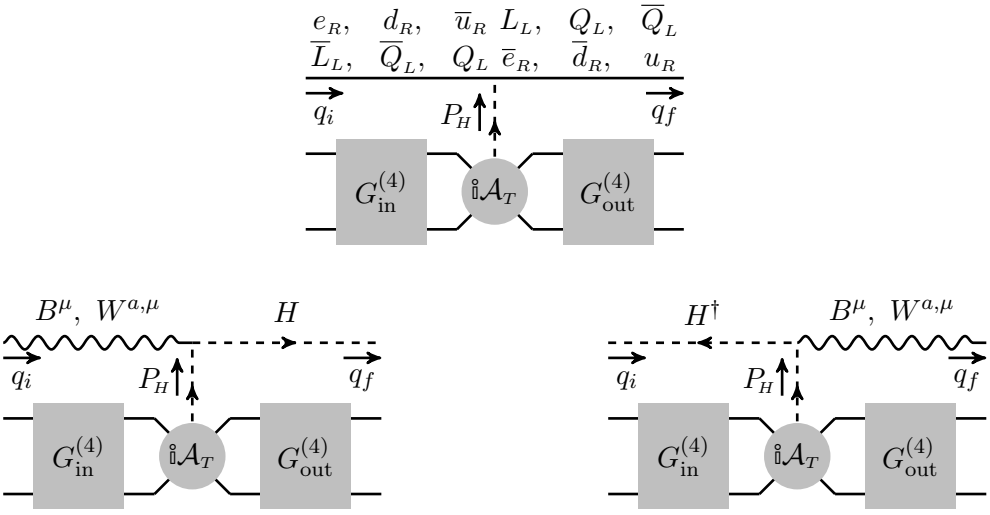

Figure 4.12: Bound-state formation or bound-to-bound transitions via exchange of an off-shell Higgs doublet with the SM particles. The arrows on the field lines denote the flow of Hypercharge. All processes have their conjugate counterparts that occur via $H^\dagger$ exchange.

4.4 Bound-state formation and bound-to-bound transitions via scattering

The dissipation of energy necessary for the capture into bound states or transitions between bound levels, may occur via exchange of an *off-shell* mediator with particles of the thermal bath [61, 64, 65, 102, 134].[4] References [102, 134] showed, in the context of a $U(1)$ model, that the cross-sections for BSF via scattering factorise into the radiative ones (with any phase-space suppression due to the mass of the emitted vector removed), and a factor that depends on the thermal bath and the interaction that mediates the scattering.

In the following, we consider BSF and bound-to-bound transitions via off-shell Higgs exchange. We derive a similar factorisation and then compute the BSF cross-sections and transition rates. We also adapt the results of refs. [102, 134] to our model, for BSF and transitions via off-shell B and W exchange.

4.4.1 H exchange

Factorisation of the effective BSF cross-sections and transition rates

For simplicity, we lay out the discussion in terms of the BSF cross-sections only. The derivation for bound-to-bound transition rates is analogous.

The thermally averaged rate per unit volume for BSF via off-shell Higgs exchange is

$$\frac{d\langle \Gamma^{H^*\text{-BSF}}_{n\ell m}\rangle}{dV} = g_1 g_2 \int \frac{d^3k_1}{(2\pi)^3}\frac{d^3k_2}{(2\pi)^3} f_+(k_1^0) f_+(k_2^0)[1+f_-(\omega_{\mathbf{k}\to n\ell m})]\ \sigma^{H^*\text{-BSF}}_{\mathbf{k}\to n\ell m} v_{\rm rel}, \tag{4.4.1}$$

where we defined

$$\sigma^{H^*\text{-BSF}}_{\mathbf{k}\to n\ell m} v_{\rm rel} \equiv \frac{[1+f_-(\omega_{\mathbf{k}\to n\ell m})]^{-1}}{2k_1^0 2k_2^0}\int \frac{d^3P}{(2\pi)^3 2P^0}\frac{d^3q_i}{(2\pi)^3 2q_i^0}\frac{d^3q_f}{(2\pi)^3 2q_f^0} f_\pm(q_i^0)[1\mp f_\pm(q_f^0)]\times$$
$$\times (2\pi)^4\delta^4(k_1+k_2+q_i-P-q_f)\frac{1}{g_1 g_2}|\mathcal{M}^{H^*\text{-BSF}}_{\mathbf{k}\to n\ell m}|^2. \tag{4.4.2}$$

[4] Other rearragement processes have been considered in ref. [63].

Here, the indices 1,2 correspond to the two incoming DM fields, while q_i and q_f denote the initial and final bath particle momenta. We consider scattering only on relativistic species, whose density in a thermal environment is large, and set $q_i^0 = |\mathbf{q}_i|$ and $q_f^0 = |\mathbf{q}_f|$. $f_\pm(E) = (e^{E/T} \pm 1)^{-1}$ are the phase-space occupation numbers for fermions (+) and bosons (−), and in eq. (4.4.2) the upper and lower signs correspond to scattering on fermionic or bosonic dof respectively.

$\omega_{\mathbf{k}\to n\ell m}$ is the energy dissipated by the DM fields in the capture process, given by eq. (4.3.8). When the DM particles are non-relativistic, it depends only on the relative momentum of the incoming DM particles and the binding energy of the bound state, but is independent of the momenta of the bath particles. (We note that this does not hold for the 3-momentum exchange $|\mathbf{q}_f - \mathbf{q}_i|$ along the off-shell mediator.) The factor $[1 + f_-(\omega_{\mathbf{k}\to n\ell m})]$ in eq. (4.4.1) is compensated by the inverse factor in eq. (4.4.2); this definition ensures that the thermal averaging of the cross-section (4.4.2) is the same as that of its radiative counterpart, which includes a Bose-enhancement factor for the radiated boson (cf. section 4.5.)

Next, we conjecture that the amplitude for off-shell H exchange, $\mathcal{M}^{H^*\text{-BSF}}_{\mathbf{k}\to n\ell m}$, can be factorised into the corresponding amplitude with on-shell H emission, $\mathcal{M}^{H\text{-BSF}}_{\mathbf{k}\to n\ell m}$, and a function of the momenta of the bath particles, as follows[5]

$$\sum_{i,f \text{ dof}} |\mathcal{M}^{H^*\text{-BSF}}_{\mathbf{k}\to n\ell m}|^2 \simeq |\mathcal{M}^{H\text{-BSF}}_{\mathbf{k}\to n\ell m}|^2 \times R_0(q_i \cdot q_f), \tag{4.4.3}$$

where the sum on the left side runs over the dof (spin and gauge) of the initial and final bath particles. $\mathcal{M}^{H\text{-BSF}}_{\mathbf{k}\to n\ell m}$ may depend only on the momentum exchange $\mathbf{q} \equiv \mathbf{q}_f - \mathbf{q}_i$ rather than on $\mathbf{q}_i$ and $\mathbf{q}_f$ separately. R_0 must be Lorentz invariant since the amplitudes are. It may thus depend only on the 4-vector products $q_i^2 = q_f^2 = 0$ and $q_i \cdot q_f$; in eq. (4.4.3) we have denoted its dependence on the latter. The R_0 factors will be specified in section 4.4.1 for the processes shown in fig. 4.12. Switching the integration from $\mathbf{q}_f$ to $\mathbf{q}$, eq. (4.4.2) gives

$$\begin{aligned}\sigma^{H^*\text{-BSF}}_{\mathbf{k}\to n\ell m} v_{\rm rel} = {} & [1 + f_-(\omega_{\mathbf{k}\to n\ell m})]^{-1} \int \frac{d^3 q_i}{(2\pi)^3 2|\mathbf{q}_i|} \\ & \times \frac{1}{2k_1^0 2k_2^0} \int \frac{d^3 P}{(2\pi)^3 2P^0} \frac{d^3 q}{(2\pi)^3 2q^0} (2\pi)^4 \delta^4(k_1 + k_2 - P - q) \frac{1}{g_1 g_2} |\mathcal{M}^{H\text{-BSF}}_{\mathbf{k}\to n\ell m}|^2 \\ & \times \frac{2q^0}{2|\mathbf{q} + \mathbf{q}_i|} f_\pm(|\mathbf{q}_i|) \left[1 \mp f_\pm(|\mathbf{q} + \mathbf{q}_i|)\right] R_0(q_i \cdot q_f),\end{aligned} \tag{4.4.4}$$

where

$$q^0 \equiv q_f^0 - q_i^0 \simeq |\mathbf{q} + \mathbf{q}_i| - |\mathbf{q}_i|. \tag{4.4.5}$$

The second line of eq. (4.4.4) would form the BSF cross-section via on-shell emission, except for two complications: (i) The dispersion relation of the radiated momentum is given by eq. (4.4.5) rather than the on-shell condition of the radiated boson, and depends on the variable $\mathbf{q}_i$. (ii) The last line of eq. (4.4.4) depends on $\mathbf{q}$. These complications are resolved within the non-relativistic approximation, where the cross-section of BSF via scattering can be shown to be proportional to that of radiative BSF, as we shall now see.

Non-relativistic approximation

Similarly to radiative BSF, if the incoming particles are non-relativistic and the final state particles are weakly bound, we may neglect the recoil of the bound state. Then, the energy-momentum conservation implies $q^0 \simeq \omega$ with ω given by eqs. (4.3.8) and (4.3.12) for BSF and

[5] For BSF via vector exchange/emission, the amplitude-squared does not factorise as in eq. (4.4.3). However, it is still possible to obtain a factorisation formula similar to eq. (4.4.9) below, for an effective cross-section, at leading order in the non-relativistic approximation [102, 134]. (See also footnote 7.)

bound-to-bound transitions. (Here we drop the ω indices for simplicity.) The dispersion relation (4.4.5) yields

$$|\mathbf{q}| \simeq \omega \left[\sqrt{1 + \frac{2|\mathbf{q}_i|}{\omega} + \frac{|\mathbf{q}_i|^2 \tau^2}{\omega^2}} - \frac{|\mathbf{q}_i|\tau}{\omega} \right], \tag{4.4.6}$$

with $\tau \equiv \hat{\mathbf{q}}_i \cdot \hat{\mathbf{q}}$. It is also easy to show that $q_i \cdot q_f = (\mathbf{q}^2 - \omega^2)/2$. Using the δ^4-function to perform the integration over $d^3P\, d|\mathbf{q}|$ (as is standard in the computation of 2-to-2 cross-sections), eq. (4.4.4) gives

$$\begin{aligned} \sigma^{H^*\text{-BSF}}_{\mathbf{k}\to n\ell m} v_{\rm rel} \simeq\ & [1 + f_-(\omega)]^{-1} \int \frac{d^3 q_i}{(2\pi)^3 2|\mathbf{q}_i|} \frac{\omega}{\omega + |\mathbf{q}_i|} f_\pm(|\mathbf{q}_i|) \left[1 \mp f_\pm(\omega + |\mathbf{q}_i|)\right] \\ & \times \frac{1}{2k_1^0 2k_2^0} \frac{1}{2P^0 2\omega} \int \frac{d\Omega_{\mathbf{q}}}{4\pi^2}\ \mathbf{q}^2 \left(\frac{\omega + |\mathbf{q}_i|}{|\mathbf{q}| + |\mathbf{q}_i|\tau} \right)\ \frac{1}{g_1 g_2} |\mathcal{M}^{H\text{-BSF}}_{\mathbf{k}\to n\ell m}|^2 \\ & \times R_0 \left(\frac{\mathbf{q}^2 - \omega^2}{2} \right), \end{aligned} \tag{4.4.7}$$

with $P^0 \simeq 2m$ and $|\mathbf{q}|$ given by eq. (4.4.6). Note that the second line of eq. (4.4.7) differs from $(\sigma^{H\text{-BSF}}_{\mathbf{k}\to n\ell m} v_{\rm rel})$ by the factor $\dfrac{\omega + |\mathbf{q}_i|}{|\mathbf{q}| + |\mathbf{q}_i|\tau} \Big/ \dfrac{\omega}{|\mathbf{q}|}$ due to the different dispersion relation of the radiated momentum q, here given by eq. (4.4.5).

The radiative BSF amplitudes are typically computed by expanding in powers of the radiated momentum $\mathbf{q}$ [43].[6] As seen in section 4.3, the dominant contribution to the various $\mathcal{M}^{H\text{-BSF}}_{\mathbf{k}\to n\ell m}$ amplitudes arises from the zeroth order term [2], i.e. $\mathcal{M}^{H\text{-BSF}}_{\mathbf{k}\to n\ell m}$ are independent of $\mathbf{q}$ (and therefore τ) at leading order. Reshuffling the various factors, eq. (4.4.7) becomes

$$\begin{aligned} \sigma^{H^*\text{-BSF}}_{\mathbf{k}\to n\ell m} v_{\rm rel} \simeq\ & \frac{1}{8\pi^2} \frac{1}{2k_1^0 2k_2^0} \frac{\omega}{2P^0} \int d\Omega_{\mathbf{q}}\ \frac{1}{g_1 g_2} |\mathcal{M}^{H\text{-BSF}}_{\mathbf{k}\to n\ell m}|^2 \times \\ & \times [1 + f_-(\omega)]^{-1} \int \frac{d^3 q_i}{(2\pi)^3 2|\mathbf{q}_i|} f_\pm(|\mathbf{q}_i|) \left[1 \mp f_\pm(\omega + |\mathbf{q}_i|)\right] \frac{|\mathbf{q}|^2}{\omega(|\mathbf{q}| + |\mathbf{q}_i|\tau)} R_0 \left(\frac{\mathbf{q}^2 - \omega^2}{2} \right). \end{aligned} \tag{4.4.8}$$

The integration over $d^3 q_i$ in the second line of eq. (4.4.8) eliminates any dependence of the integrand on the orientation of the vector $\mathbf{q}$, allowing us to identify the first line as the cross-section for on-shell Higgs emission with the phase-space suppression removed (cf. eqs. (4.3.7b) and (4.3.9b).) Thus, the effective cross-section for off-shell Higgs exchange can be factorised at leading order as follows[7]

$$\boxed{\sigma^{H^*\text{-BSF}}_{\mathbf{k}\to n\ell m} v_{\rm rel} \simeq \frac{\sigma^{H\text{-BSF}}_{\mathbf{k}\to n\ell m} v_{\rm rel}}{h_H(\omega_{\mathbf{k}\to n\ell m})} \times R_H(\omega_{\mathbf{k}\to n\ell m}),} \tag{4.4.9}$$

[6] The expansion is in effect in the dimensionless combination $|\mathbf{q}|/\sqrt{\kappa^2/n^2 + \mathbf{k}^2} = |\mathbf{q}|/\sqrt{2\mu\omega}$. For BSF via on-shell emission, the radiated momentum is limited by the available energy, $|\mathbf{q}| \leqslant \omega$, thus the expansion parameter is always $\sqrt{\omega/(2\mu)} \ll 1$. However, for BSF via scattering, $|\mathbf{q}|$ can be comparable to or larger than $\sqrt{2\mu\omega}$, particularly at $T \gtrsim \kappa/n$, which puts in question the validity of the expansion. Nevertheless, for the purposes of DM freeze-out, BSF typically reaches ionisation equilibrium at high T, where the DM destruction rate via BSF is independent of the BSF cross-sections [106] (cf. section 4.5.) At lower T, where the magnitude of the BSF cross-sections matters, the $|\mathbf{q}|$ expansion is a valid approximation.

[7] Note that eq. (4.4.9) holds for the effective cross-section of BSF via off-shell Higgs exchange as defined in eq. (4.4.2). Since $\mathcal{M}^{H\text{-BSF}}_{\mathbf{k}\to n\ell m}$ is presumed to be independent of $\mathbf{q}$ and therefore $\mathbf{q} \cdot \mathbf{k}$, it has not been necessary to integrate over the angular variables of $\mathbf{k}$ in order to obtain a factorised expression for the cross-section. This is in contrast to the case of vector exchange, where the amplitude does not factorise as in eq. (4.4.3) and in fact depends on $\mathbf{q}_i \cdot \mathbf{k}$ and $\mathbf{q}_f \cdot \mathbf{k}$. A factorisation similar to eq. (4.4.9) is obtained only for the cross-section averaged over the $\mathbf{k}$ solid angle [102, 134] (cf. section 4.4.2.)

where $h_H(\omega)$ is the phase-space suppression (4.3.10) of the on-shell emission due to the Higgs mass, with $\omega_{\mathbf{k}\to n\ell m}$ being the dissipated energy (4.3.8), and we restored the indices for concreteness. The dimensionless factor $R_H(\omega)$ is

$$R_H(\omega) \equiv \int \frac{d^3q_i}{(2\pi)^3 2|\mathbf{q}_i|} \frac{\mathbf{q}^2}{\omega(|\mathbf{q}|+|\mathbf{q}_i|\tau)} \frac{f_\pm(\mathbf{q}_i)\left[1\mp f_\pm(\omega+|\mathbf{q}_i|)\right]}{1+f_-(\omega)} R_0\left(\frac{\mathbf{q}^2-\omega^2}{2}\right). \tag{4.4.10}$$

We recall that $|\mathbf{q}|$ is given by eq. (4.4.6). Since the entire integrand is rotationally invariant (recall that R_0 is Lorentz invariant), we perform the d^3q_i integration by setting $\mathbf{q}$ on the z axis. Then the azimuthal angle is parametrised by τ defined above. Changing integration variables from $|\mathbf{q}_i|$ and τ to $u \equiv |\mathbf{q}_i|/\omega$ and $z \equiv \mathbf{q}^2/\omega^2 - 1$, eq. (4.4.10) simplifies to

$$R_H(\omega) = \frac{\omega^2}{16\pi^2}\int_0^\infty du\ \frac{f_\pm(\omega u)\left[1\mp f_\pm\left(\omega(1+u)\right)\right]}{1+f_-(\omega)} \int_0^{4u(1+u)} dz\, R_0\left(z\omega^2/2\right). \tag{4.4.11}$$

We compute R_H next. The final result can be found in eqs. (4.4.19) to (4.4.21).

Following the same steps, we find that the bound-to-bound transition rate via off-shell Higgs exchange is related to the radiative one via

$$\boxed{\Gamma^{H^*\text{-BSF}}_{n'\ell'm\to n\ell m} \simeq \frac{\Gamma^{H\text{-BSF}}_{n'\ell'm'\to n\ell m}}{h_H(\omega_{n'\ell'm'\to n\ell m})} \times R_H(\omega_{n'\ell'm'\to n\ell m}),} \tag{4.4.12}$$

where $\omega_{n'\ell'm'\to n\ell m}$ is the dissipated energy (4.3.12).

Amplitudes

Similarly to their radiative analogues, the amplitudes for BSF and bound-to-bound transitions via scattering consist of the perturbative transition amplitudes that encode the scattering on the bath particles, convoluted with the initial and final state wavefunctions. Focusing again on BSF (cf. eq. (4.3.1a)),

$$\mathbb{i}\mathcal{M}^{H^*\text{-BSF}}_{\mathbf{k}\to n\ell m} = \int \frac{d^3\mathbf{k}'}{(2\pi)^3}\frac{d^3\mathbf{p}}{(2\pi)^3}\ \frac{[\psi_{n\ell m}(\mathbf{p})]^\dagger}{\sqrt{2\mu}}\ \mathbb{i}\mathcal{A}_T^{H^*\text{-BSF}}(\mathbf{k}',\mathbf{p})\ \phi_{\mathbf{k}}(\mathbf{k}'). \tag{4.4.13}$$

We now compute $\mathcal{A}_T^{H^*\text{-BSF}}(\mathbf{k}',\mathbf{p})$ for the scattering processes shown in fig. 4.12, and deduce from eq. (4.4.11) the corresponding R factors.

Scattering on fermions

The Higgs couples to the SM fermions via the operators

$$\delta\mathcal{L} = -y_e(\delta_{ab}\bar{L}_{L\,a}H_b)e_R - y_d(\delta_{ab}\bar{Q}_{L\,a}H_b)d_R - y_u(\epsilon_{ab}\bar{Q}_{L\,a}H_b^\dagger)u_R + \text{h.c.}, \tag{4.4.14}$$

where the a,b superscripts indicate the $SU_L(2)$ contractions, while the family indices are suppressed. These couplings give rise to the scattering processes shown in fig. 4.12 (top). The corresponding BSF perturbative transition amplitudes (projected on the desired spin and gauge, scattering and bound states) are[8]

$$\mathbb{i}\left[\mathcal{A}_T^{H^*\text{-BSF}}(\mathbf{k}',\mathbf{p})\right]_h = \mathbb{i}\left[\mathcal{A}_T^{H\text{-BSF}}(\mathbf{k}',\mathbf{p})\right]_{h'} \times \frac{\mathbb{i}}{q^2-m_H^2}\bar{u}_f(-\mathbb{i}y_F^*)\delta_{hh'}\left(\frac{1-\gamma_5}{2}\right)u_i, \tag{4.4.15}$$

[8] In eq. (4.4.15), the sign of the γ_5 term and whether the Yukawa coupling should be y_F or y_F^* depend on the exact process we are considering. For scattering on antifermions, the spinors u_i, u_f become v_i, v_f. In addition, for a scattering involving an up-type right-handed (anti)quark, $\delta_{hh'}$ should be replaced by $\epsilon_{hh'}$. However, all these differences do not affect the R_0 factors.

where h, h' are the $SU_L(2)$ indices of the left-handed SM fermion field and the exchanged Higgs, respectively. The scattering and bound states gauge indices, if any, are left implicit. We use y_F to denote collectively the SM Yukawa couplings of eq. (4.4.14). Inserting eq. (4.4.15) into (4.4.13), squaring and summing over the bath particle spin and gauge dof, we arrive at the R_0 factors (cf. eq. (4.4.3)),

$$R_0 = 2 \times |y_F|^2 \, \frac{2q_i \cdot q_f}{(2q_i \cdot q_f + m_H^2)^2}, \tag{4.4.16}$$

where we introduced a factor 2 to account for the partner process controlled by the same coupling, where the initial (final) fermion becomes the final (initial) antifermion.

Scattering on bosons

The perturbative transition amplitude for scattering on gauge bosons (fig. 4.12, bottom left), projected on the desired spin and gauge, scattering and bound states, is

$$\mathring{\imath}\left[\mathcal{A}_T^{H^*\text{-BSF}}(\mathbf{k}', \mathbf{p})\right]_h^{a,\mu} = \mathring{\imath}[\mathcal{A}_T^{H\text{-BSF}}(\mathbf{k}', \mathbf{p})]_{h'} \times \frac{\mathring{\imath}}{q^2 - m_H^2} \times \mathring{\imath} g \, T^a_{hh'} \, (q_f + q)^\mu, \tag{4.4.17}$$

where h, h' and a are the $SU_L(2)$ indices of the outgoing and exchanged Higgs bosons and the incoming gauge boson respectively. T^a and g stand for the generators and the gauge coupling of the gauge group under consideration. Inserting eq. (4.4.17) into (4.4.13), squaring and summing over the bath particle polarisations and gauge dof, we find the R_0 factors

$$R_0 = 2 \times 4\pi\alpha \, C_2(\mathbb{R}_H) \, \frac{4q_i \cdot q_f}{(2q_i \cdot q_f + m_H^2)^2}, \tag{4.4.18}$$

where, as before, we introduced a factor 2 to account for the partner process where $H^\dagger$ is the incoming bath particle (fig. 4.12, bottom right). $C_2(\mathbb{R}_H)$ is the quadratic Casimir of the Higgs representation under the gauge group considered; here, $C_2(\mathbb{R}_H) = Y_H^2 = 1/4$ for Hypercharge and $C_2(\mathbb{R}_H) = 3/4$ for $SU_L(2)$.

BSF cross-sections and transition rates

Both eqs. (4.4.16) and (4.4.18) depend only on $q_i \cdot q_f$, as presumed in eq. (4.4.3), and in fact in the same fashion. Inserting them into eq. (4.4.11), and carrying out the integration over z, we find the contributions of scattering on fermions and bosons to BSF,

$$\boxed{\begin{aligned} R_H^F &= 2 \times \frac{|y_F|^2}{4\pi} \frac{1}{2} \times R_+ \,, && \text{(4.4.19a)} \\ R_H^{BH} &= 2 \times (1/4)\alpha_1 \times R_- \,, && \text{(4.4.19b)} \\ R_H^{WH} &= 2 \times (3/4)\alpha_2 \times R_- \,, && \text{(4.4.19c)} \end{aligned}}$$

where $R_\pm$ are dimensionless functions of two parameters, ω/T and m_H/ω,

$$\boxed{R_\pm \equiv \frac{1}{2\pi} \int_0^\infty du \frac{e^{u\,\omega/T}}{e^{u(\omega/T)} \pm 1} \frac{e^{\omega/T} - 1}{e^{(1+u)\omega/T} \pm 1} \left\{ \ln\left[1 + \frac{4u(1+u)}{m_H^2/\omega^2}\right] - \frac{4u(1+u)}{4u(1+u) + m_H^2/\omega^2} \right\}.} \tag{4.4.20}$$

The factor 1/2 in eq. (4.4.19a) is due to the SM fermions being chiral. The R_H factor that determines the BSF via scattering cross-section (4.4.9) is

$$\boxed{R_H = \sum_F R_H^F + R_H^{BH} + R_H^{WH}.} \tag{4.4.21}$$

Among the SM fermions, the top quark yields the largest contribution as long as it remains relativistic.

The $R_\pm$ factors (4.4.20) diverge at $m_H \to 0$, which for our purposes occurs around the EWPT (cf. section 4.5.) This divergence can be removed by a full next-to-leading-order calculation, as done in ref. [134] in the context of a $U(1)$ gauge theory. Performing such a computation for the model considered here is beyond the scope of this work. However, comparing the results of refs. [102] and [134] for a massive and massless vector mediator respectively, we find that, upon thermal averaging, the former approximates well the latter at temperatures higher than the binding energy if the screening scale (i.e. the mediator mass) is set to $0.74\,\omega$.[9] Considering this, in eq. (4.4.20) we shall do the replacement

$$m_H \to \max(m_H, \omega). \tag{4.4.22}$$

We present $R_\pm$ and R_H in fig. 4.13. It is clear that they are more significant for $\omega/T \ll 1$. This implies that for bound-to-bound transitions, they enhance the rates at $T \gg \omega_{n'\to n} = |\mathcal{E}_{n'} - \mathcal{E}_n|$. For BSF via scattering, the $R_\pm$ factors weigh preferentially the contribution of DM pairs with low relative velocity. We note that even though in a thermal bath $\langle \omega_{\mathbf{k}\to n\ell m}\rangle = |\mathcal{E}_n| + (3/2)T > T$ (cf. eq. (4.3.8)), lower values of $\omega_{\mathbf{k}\to n\ell m}$ may still incur in a sizeable portion of the DM collisions while $T \gtrsim |\mathcal{E}_n|$.

Even when the R_H factor (4.4.21) is less than 1, BSF via scattering may potentially be (i) faster than radiative BSF, which is suppressed by the $h_H(\omega_{\mathbf{k}\to n\ell m})$ phase-space factor (4.3.10), becoming entirely inaccessible for $m_H/\omega_{\mathbf{k}\to n\ell m} > 1$, and (ii) significant with respect to direct annihilation and BSF via vector emission, since these processes are suppressed by one (two) extra power(s) of couplings compared to BSF via $H^{(\dagger)}$ off-shell exchange (on-shell emission.) Analogously, bound-to-bound transitions via scattering may dominate over their radiative counterparts and/or the direct bound-state decay into radiation.

To assess realistically the impact of BSF and bound-to-bound transitions via scattering we must thermally average the cross-sections and rates of eqs. (4.4.9) and (4.4.12), and consider the interplay of bound-state formation, decay, ionisation and transition processes in the thermal bath. We do so in section 4.5 and figs. 4.14 and 4.15.

4.4.2 B and W exchange

References [102, 134] showed in the context of a $U(1)$ gauge theory that the effective cross-section for BSF via off-shell vector exchange, defined via the thermally averaged rate per volume (cf. footnote 7)

$$\frac{d\langle \Gamma^{V^*\text{-BSF}}_{n\ell m}\rangle}{dV} = n_1 n_2 \left(\frac{2\mu^3}{\pi T^3}\right)^{1/2} \int dv_{\rm rel}\, v_{\rm rel}^2\, e^{-\mu v_{\rm rel}^2/(2T)} \left(1 + \frac{1}{e^{\omega_{\mathbf{k}\to n\ell m}/T} - 1}\right) (\sigma^{V^*\text{-BSF}}_{\mathbf{k}\to n\ell m} v_{\rm rel}), \tag{4.4.23}$$

[9] Reference [134] found that using the binding energy as the minimum screening scale provides a good approximation. While this is indeed so, the above prescription ensures that the R factor depends only on ω/T as predicted by the full computation, besides being a somewhat better approximation.

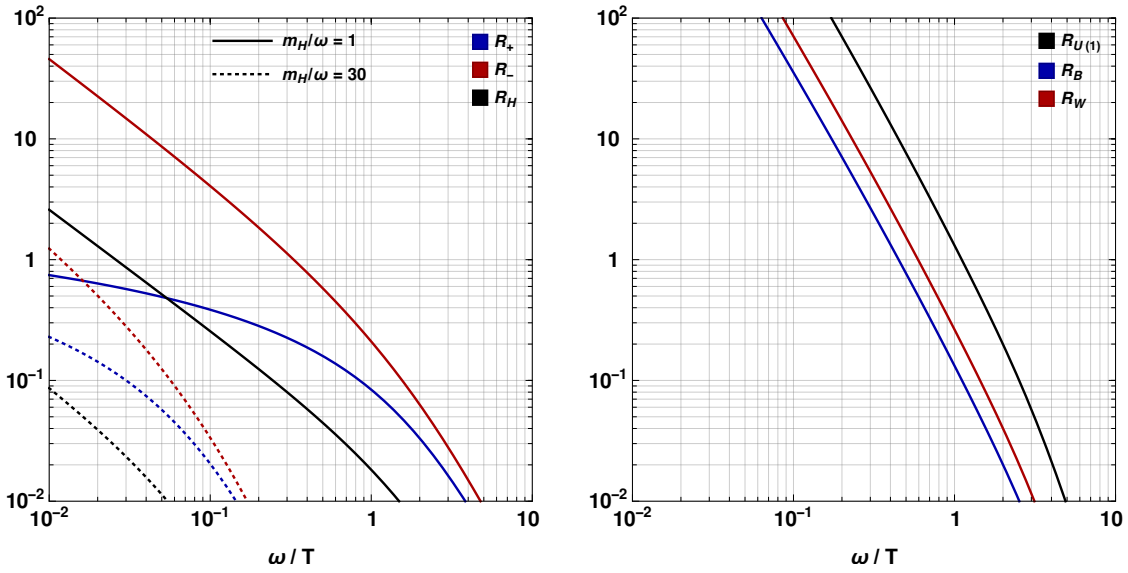

Figure 4.13: *Left*: The $R_\pm$ and R_H factors of eqs. (4.4.20) and (4.4.21) that determine the ratio of BSF via off-shell $H^{(\dagger)}$ scattering over on-shell $H^{(\dagger)}$ emission. *Right*: The R_B and R_W factors of eqs. (4.4.25) that determine the ratio of BSF via off-shell B or W scattering on fermions over on-shell B or W emission. Also shown, the $R_{U(1)}$ factor from [134] (cf. footnote 10.)

is, at leading order in the non-relativistic regime, proportional to the cross-section for on-shell emission, $\sigma^{V^*\text{-BSF}}_{\mathbf{k}\to n\ell m} v_{\rm rel} = (\sigma^{V\text{-BSF}}_{\mathbf{k}\to n\ell m} v_{\rm rel}) \times R_V$, where $R_V = 2 \times \alpha \times R_{U(1)}$. As in section 4.4.1, the factor 2 accounts for the partner processes related via exchanging the initial (final) bath particle with the final (initial) bath antiparticle, and α is the fine structure constant of the group. The factor $R_{U(1)}$ depends only on ω/T provided that V is massless, and has been derived in [134] via a next-to-leading order calculation where the colinear and infrared the divergences are cancelled. For a massive V, a simple analytical formula that depends on ω/T and m_V/ω has been computed in [102]. We define $R_{U(1)}$ to correspond to scattering on one species of relativistic Dirac fermions with charge unity, and use the results of [134].[10]

Adapting the result to the present model, the cross-sections for BSF via off-shell B and W exchange are related to those of on-shell emission as follows

$$\sigma^{B^*\text{-BSF}}_{\mathbf{k}\to n\ell m} v_{\rm rel} \simeq (\sigma^{B\text{-BSF}}_{\mathbf{k}\to n\ell m} v_{\rm rel}) \times R_B(\omega_{\mathbf{k}\to n\ell m}/T), \tag{4.4.24a}$$

$$\sigma^{W^*\text{-BSF}}_{\mathbf{k}\to n\ell m} v_{\rm rel} \simeq (\sigma^{W\text{-BSF}}_{\mathbf{k}\to n\ell m} v_{\rm rel}) \times R_W(\omega_{\mathbf{k}\to n\ell m}/T), \tag{4.4.24b}$$

where

$$R_B(\omega/T) = 2 \times c_B \alpha_1 \times R_{U(1)}(\omega/T), \tag{4.4.25a}$$

$$R_W(\omega/T) = 2 \times c_W \alpha_2 \times R_{U(1)}(\omega/T). \tag{4.4.25b}$$

The factors c_B and c_W account for scattering on the relativistic SM fermions. The contribution of a chiral fermion F transforming under the representation $\mathbb{R}_F$ of a gauge group is $c^F = C(\mathbb{R}_F)/2$, where C is the Casimir operator. When all the SM fermions are relativistic, $c_B = (1/2)\sum_F Y_F^2 = 5$ and $c_W = (1/2)C(\mathbb{2}) \times 12 = 3$, where $C(\mathbb{2}) = 1/2$ for $SU_L(2)$.

Note that eq. (4.4.25b) includes only scattering on SM fermions via off-shell W exchange. However, non-Abelian gauge bosons may also scatter on themselves due to the trilinear gauge

[10] $R_{U(1)}$ is related to $R_{2002.07145}$ defined in ref. [94, eq. (4.13) and fig. 14] as $R_{U(1)} \equiv R_{2002.07145}/(2\pi)$. We thank Tobias Binder for providing the numerical values of $R_{2002.07145}$.

coupling. Estimating this effect necessitates a dedicated next-to-leading order computation that is beyond the scope of this work. We shall thus neglect this contribution.

Formulae analogous to eqs. (4.4.25) hold for bound-to-bound transitions via off-shell B and W exchange, however no such transition is of interest here.

We present the R_B and R_W factors in fig. 4.13.

4.5 Dark matter thermal decoupling: Boltzmann equations

4.5.1 Coupled Boltzmann equations

Let $Y_j \equiv n_j/s$ and $Y_{\mathcal{B}} \equiv n_{\mathcal{B}}/s$ be the number-density-to-entropy-density ratios of the free species i and the bound state $\mathcal{B}$ respectively. In our model, $j = S$, D, $\bar{D}$ and $\mathcal{B} = SS/D\bar{D}$, $D\bar{D}$, DD, DS. We are ultimately interested in the total DM yield

$$Y \equiv Y_S + Y_D + Y_{\bar{D}} = Y_S + 2Y_D. \tag{4.5.1}$$

Note that the bound states are metastable and their abundance becomes eventually negligible, so we do not include them in eq. (4.5.1). As is standard, we will use the time parameter

$$x \equiv m/T. \tag{4.5.2}$$

The entropy density of the universe is $s = (2\pi^2/45) g_{*S} T^3 = (2\pi^2/45) g_{*S} m^3/x^3$. We denote by g_{*S} and g_* the entropy and energy dof respectively, and define

$$g_{*,\text{eff}}^{1/2} = \frac{g_{*S}}{\sqrt{g_*}} \left(1 - \frac{x}{3 g_{*S}} \frac{dg_{*S}}{dx}\right). \tag{4.5.3}$$

The evolution of Y_j and $Y_{\mathcal{B}}$ is governed by the coupled Boltzmann equations

$$\begin{aligned}
\frac{dY_j}{dx} =& -\frac{\lambda}{x^2} \sum_i \langle \sigma_{ji}^{\text{ann}} v_{\text{rel}} \rangle \left(Y_j Y_i - Y_j^{\text{eq}} Y_i^{\text{eq}}\right) - \frac{\lambda}{x^2} \sum_i \sum_{\mathcal{B}} \langle \sigma_{ji\to\mathcal{B}}^{\text{BSF}} \, v_{\text{rel}} \rangle \left(Y_j Y_i - \frac{Y_{\mathcal{B}}}{Y_{\mathcal{B}}^{\text{eq}}} Y_j^{\text{eq}} Y_i^{\text{eq}}\right) \\
& - \Lambda \, x \sum_i \langle \Gamma_{j\to i} \rangle \left(Y_j - \frac{Y_i}{Y_i^{\text{eq}}} Y_j^{\text{eq}}\right), \qquad (4.5.4a) \\
\frac{dY_{\mathcal{B}}}{dx} =& -\Lambda \, x \left[\langle \Gamma_{\mathcal{B}}^{\text{dec}} \rangle \left(Y_{\mathcal{B}} - Y_{\mathcal{B}}^{\text{eq}}\right) + \sum_{i,j} \langle \Gamma_{\mathcal{B}\to ij}^{\text{ion}} \rangle \left(Y_{\mathcal{B}} - \frac{Y_i Y_j}{Y_i^{\text{eq}} Y_j^{\text{eq}}} Y_{\mathcal{B}}^{\text{eq}}\right) \right. \\
& \left. + \sum_{\mathcal{B}' \neq \mathcal{B}} \langle \Gamma_{\mathcal{B}\to\mathcal{B}'}^{\text{trans}} \rangle \left(Y_{\mathcal{B}} - \frac{Y_{\mathcal{B}'}}{Y_{\mathcal{B}'}^{\text{eq}}} Y_{\mathcal{B}}^{\text{eq}}\right) \right], \qquad (4.5.4b)
\end{aligned}$$

where

$$\lambda \equiv \sqrt{\frac{\pi}{45}} m_{\text{Pl}} m g_{*,\text{eff}}^{1/2} \qquad \text{and} \qquad \Lambda \equiv \frac{\lambda}{s \, x^3} = \sqrt{\frac{45}{4\pi^3}} \frac{m_{\text{Pl}}}{m^2} \frac{g_{*,\text{eff}}^{1/2}}{g_{*,S}}, \tag{4.5.5}$$

and the equilibrium densities in the non-relativistic regime are

$$Y_i^{\text{eq}} \simeq \frac{90}{(2\pi)^{7/2}} \frac{g_i}{g_{*,S}} \, x^{3/2} \, e^{-x} \qquad \text{and} \qquad Y_{\mathcal{B}}^{\text{eq}} \simeq \frac{90}{(2\pi)^{7/2}} \frac{g_{\mathcal{B}}}{g_{*,S}} \, (2x)^{3/2} \, e^{-2x} \, e^{|\mathcal{E}_{\mathcal{B}}|/T}, \tag{4.5.6}$$

where g_i are the spin and $SU_L(2)$ dof of the free species, with $g_S = 2$, $g_D = g_{\bar{D}} = 4$; we also define $g_{\text{DM}} \equiv g_S + g_D + g_{\bar{D}} = 10$. The dof $g_{\mathcal{B}}$ and the binding energies $\mathcal{E}_{\mathcal{B}}$ of the bound states we consider here can be found in table 6.

In the above, $\Gamma_{\mathcal{B}}^{\rm dec}$, $\Gamma_{\mathcal{B}\to ij}^{\rm ion}$ and $\Gamma_{\mathcal{B}\to\mathcal{B}'}^{\rm trans}$ are respectively the rates of $\mathcal{B}$ decay into radiation, ionisation (a.k.a. dissociation) to ij, and transition into the bound level $\mathcal{B}'$. The rates $\Gamma_{j\to i}$ describe the transitions between free particles, due to decays, inverse decays and/or scatterings on the thermal bath; overall, these processes do not change the DM number density. Note that in eqs. (4.5.4) we must use the thermally averaged rates, $\langle\Gamma\rangle$. The thermal average introduces Lorentz dilation factors for decay processes – which however are insignificant in the non-relativistic regime – as well as Bose-enhancement factors in the case of transitions and capture or ionisation processes. We discuss this in more detail in section 4.5.3. The thermally-averaged rates and cross-sections of inverse processes are related via detailed balance that we have already employed in writing eqs. (4.5.4),

$$\langle\Gamma_{\mathcal{B}\to\mathcal{B}'}^{\rm trans}\rangle = \Gamma_{\mathcal{B}'\to\mathcal{B}}^{\rm trans}\times(Y_{\mathcal{B}'}^{\rm eq}/Y_{\mathcal{B}}^{\rm eq}), \tag{4.5.7a}$$

$$\langle\Gamma_{\mathcal{B}\to ij}^{\rm ion}\rangle = s\,\langle\sigma_{ij\to\mathcal{B}}^{\rm BSF}v_{\rm rel}\rangle\times(Y_i^{\rm eq}Y_j^{\rm eq}/Y_{\mathcal{B}}^{\rm eq}), \tag{4.5.7b}$$

$$\langle\Gamma_{i\to j}\rangle = \langle\Gamma_{j\to i}\rangle\times(Y_j^{\rm eq}/Y_i^{\rm eq}). \tag{4.5.7c}$$

The fractional relic DM density is

$$\Omega \simeq (m-\sqrt{4\pi\alpha_H}v_H)Y_\infty s_0/\rho_c, \tag{4.5.8}$$

where Y_∞ is the final yield, and we have included the mass shift of the lightest state that arises after the electroweak symmetry breaking (cf. eq. (4.1.11)); this is significant only for the lower end of the mass range we consider and for large couplings. In eq. (4.5.8), $s_0\simeq 2839.5$ cm^{-3} and $\rho_c\simeq 4.78\cdot10^{-6}$ GeV cm^{-3} are the entropy and critical energy densities of the universe today [7].

4.5.2 Effective Boltzmann equation

The system of coupled Boltzmann eqs. (4.5.4) is numerically difficult to solve. We shall thus adopt an effective method that reduces eqs. (4.5.4) to one equation for the DM yield (4.5.1).

For convenience, we first define the total formation cross-section, ionisation rate and transition rate of every bound state $\mathcal{B}$,

$$\sigma_{\mathcal{B}}^{\rm BSF} \equiv \sum_{i,j}\frac{g_ig_j}{g_{\rm DM}^2}\sigma_{ij\to\mathcal{B}}^{\rm BSF}, \tag{4.5.9a}$$

$$\Gamma_{\mathcal{B}}^{\rm ion} \equiv \sum_{i,j}\Gamma_{\mathcal{B}\to ij}^{\rm ion}, \tag{4.5.9b}$$

$$\Gamma_{\mathcal{B}}^{\rm trans} \equiv \sum_{\mathcal{B}'}\Gamma_{\mathcal{B}\to\mathcal{B}'}^{\rm trans}. \tag{4.5.9c}$$

We begin by assuming that the $i\leftrightarrow j$ interactions are sufficiently rapid to ensure kinetic equilibrium, such that $Y_i/Y_i^{\rm eq}=w$, where w is the same for all $i=S,D,\bar{D}$. Due to their decays, inverse decays and transitions to other bound levels, the bound states are typically close to equilibrium, thus $dY_{\mathcal{B}}/dx\simeq 0$. Under this assumption, eqs. (4.5.4b) yield a system of linear equations for $Y_{\mathcal{B}}$ that can be solved and re-employed in eq. (4.5.4a) [135]. For bound states that do not participate in any bound-to-bound transitions, such as $D\bar{D}$ and DD in our system, it is easy to obtain

$$Y_{\mathcal{B}} = Y_{\mathcal{B}}^{\rm eq}\,\frac{\langle\Gamma_{\mathcal{B}}^{\rm dec}\rangle + w^2\langle\Gamma_{\mathcal{B}}^{\rm ion}\rangle}{\langle\Gamma_{\mathcal{B}}^{\rm dec}\rangle + \langle\Gamma_{\mathcal{B}}^{\rm ion}\rangle}. \tag{4.5.10}$$

For the coupled bound states $SS/D\bar{D}$ and DS, eqs. (4.5.4a) read

$$\begin{pmatrix} \langle \Gamma^{\rm dec}_{SS/D\bar{D}} \rangle + \langle \Gamma^{\rm ion}_{SS/D\bar{D}} \rangle + 2\langle \Gamma^{\rm trans}_{SS/D\bar{D}\to DS} \rangle & -2\langle \Gamma^{\rm trans}_{DS\to SS/D\bar{D}} \rangle \\ -\langle \Gamma^{\rm trans}_{SS/D\bar{D}\to DS} \rangle & \langle \Gamma^{\rm ion}_{DS} \rangle + \langle \Gamma^{\rm trans}_{DS\to SS/D\bar{D}} \rangle \end{pmatrix} \begin{pmatrix} Y_{SS/D\bar{D}} \\ Y_{DS} \end{pmatrix} = \\ = \begin{pmatrix} \left[\langle \Gamma^{\rm dec}_{SS/D\bar{D}} \rangle + w^2 \langle \Gamma^{\rm ion}_{SS/D\bar{D}} \rangle \right] Y^{\rm eq}_{SS/D\bar{D}} \\ w^2 \langle \Gamma^{\rm ion}_{DS} \rangle Y^{\rm eq}_{DS} \end{pmatrix}, \quad (4.5.11)$$

where we set $\langle \Gamma^{\rm dec}_{DS} \rangle \simeq 0$, and we recall that $\langle \Gamma^{\rm trans}_{SS/D\bar{D}\to DS} \rangle = \langle \Gamma^{\rm trans}_{DS\to SS/D\bar{D}} \rangle (Y^{\rm eq}_{DS}/Y^{\rm eq}_{SS/D\bar{D}})$, due to detailed balance eq. (4.5.7a). The factors 2 in the first row account for transitions to and from the two conjugate bound states DS and $\bar{D}S$.

Next, we use eq. (4.5.10) for the $D\bar{D}$ and DD yields and the solution of eq. (4.5.11) for the $SS/D\bar{D}$ and DS yields, in the Boltzmann eq. (4.5.4a). Summing over all free particle species, we find that the evolution of Y is governed by the Boltzmann equation

$$\frac{dY}{dx} = -\sqrt{\frac{\pi}{45}} \frac{m_{\rm Pl}\, m\, g^{1/2}_{*,\rm eff}}{x^2} \langle \sigma v_{\rm rel} \rangle_{\rm eff} \left[Y^2 - (Y^{\rm eq})^2 \right], \quad (4.5.12)$$

where the equilibrium density $Y^{\rm eq}$ is

$$Y^{\rm eq} = \frac{90}{(2\pi)^{7/2}} \frac{g_{\rm DM}}{g_{*,S}}\, x^{3/2}\, e^{-x}. \quad (4.5.13)$$

and we recall that $g_{\rm DM} = g_S + g_D + g_{\bar{D}} = 10$. The DM destruction cross-section receives contributions from direct annihilation and BSF processes,

$$\langle \sigma v_{\rm rel} \rangle_{\rm eff} = \langle \sigma_{\rm ann} v_{\rm rel} \rangle + \langle \sigma_{\rm BSF} v_{\rm rel} \rangle_{\rm eff}, \quad (4.5.14)$$

where

$$\langle \sigma_{\rm ann} v_{\rm rel} \rangle \equiv \sum_{i,j} \frac{g_i g_j}{g^2_{\rm DM}} \langle \sigma^{\rm ann}_{ij} v_{\rm rel} \rangle, \quad (4.5.15)$$

and

$$\langle \sigma_{\rm BSF} v_{\rm rel} \rangle_{\rm eff} = \langle \sigma^{\rm BSF}_{SS/D\bar{D}} v_{\rm rel} \rangle_{\rm eff} + \langle \sigma^{\rm BSF}_{D\bar{D}} v_{\rm rel} \rangle_{\rm eff} + 2\langle \sigma^{\rm BSF}_{DD} v_{\rm rel} \rangle_{\rm eff} + 2\langle \sigma^{\rm BSF}_{DS} v_{\rm rel} \rangle_{\rm eff}, \quad (4.5.16)$$

where the factors 2 in the DD and DS terms account also for the formation of the conjugate bound states, and the individual contributions are found from the following:

$$\frac{\langle \sigma^{\rm BSF}_{SS/D\bar{D}} v_{\rm rel} \rangle_{\rm eff}}{\langle \sigma^{\rm BSF}_{SS/D\bar{D}} v_{\rm rel} \rangle} = \frac{\langle \Gamma^{\rm dec}_{SS/D\bar{D}} \rangle}{\langle \Gamma^{\rm dec}_{SS/D\bar{D}} \rangle + \langle \Gamma^{\rm ion}_{SS/D\bar{D}} \rangle + 2 \dfrac{\langle \Gamma^{\rm ion}_{DS} \rangle \langle \Gamma^{\rm trans}_{DS\to SS/D\bar{D}} \rangle}{\langle \Gamma^{\rm ion}_{DS} \rangle + \langle \Gamma^{\rm trans}_{DS\to SS/D\bar{D}} \rangle} \dfrac{Y^{\rm eq}_{DS}}{Y^{\rm eq}_{SS/D\bar{D}}}}, \quad (4.5.16a)$$

$$\frac{\langle \sigma^{\rm BSF}_{D\bar{D}} v_{\rm rel} \rangle_{\rm eff}}{\langle \sigma^{\rm BSF}_{D\bar{D}} v_{\rm rel} \rangle} = \frac{\langle \Gamma^{\rm dec}_{D\bar{D}} \rangle}{\langle \Gamma^{\rm dec}_{D\bar{D}} \rangle + \langle \Gamma^{\rm ion}_{D\bar{D}} \rangle}, \quad (4.5.16b)$$

$$\frac{\langle \sigma^{\rm BSF}_{DD} v_{\rm rel} \rangle_{\rm eff}}{\langle \sigma^{\rm BSF}_{DD} v_{\rm rel} \rangle} = \frac{\langle \Gamma^{\rm dec}_{DD} \rangle}{\langle \Gamma^{\rm dec}_{DD} \rangle + \langle \Gamma^{\rm ion}_{DD} \rangle}, \quad (4.5.16c)$$

$$\frac{\langle \sigma^{\rm BSF}_{DS} v_{\rm rel} \rangle_{\rm eff}}{\langle \sigma^{\rm BSF}_{DS} v_{\rm rel} \rangle} = \frac{\langle \Gamma^{\rm trans}_{DS\to SS/D\bar{D}} \rangle \times \dfrac{\langle \Gamma^{\rm dec}_{SS/D\bar{D}} \rangle}{\langle \Gamma^{\rm dec}_{SS/D\bar{D}} \rangle + \langle \Gamma^{\rm ion}_{SS/D\bar{D}} \rangle}}{\langle \Gamma^{\rm ion}_{DS} \rangle + \langle \Gamma^{\rm trans}_{DS\to SS/D\bar{D}} \rangle + 2 \dfrac{\langle \Gamma^{\rm ion}_{DS} \rangle \langle \Gamma^{\rm trans}_{DS\to SS/D\bar{D}} \rangle}{\langle \Gamma^{\rm dec}_{SS/D\bar{D}} \rangle + \langle \Gamma^{\rm ion}_{SS/D\bar{D}} \rangle} \dfrac{Y^{\rm eq}_{DS}}{Y^{\rm eq}_{SS/D\bar{D}}}}, \quad (4.5.16d)$$

In eqs. (4.5.16), $\langle \sigma^{\rm BSF}_{\mathcal{B}} v_{\rm rel} \rangle$ are the thermal averages of the actual velocity-weighted formation cross-sections for every bound state, defined in eq. (4.5.9a); we discuss them further in the following section. Note that if the transitions between the $SS/D\bar{D}$ and DS bound states are very rapid, in particular when $\langle \Gamma^{\rm trans}_{DS\to SS/D\bar{D}} \rangle \gg \langle \Gamma^{\rm ion}_{DS} \rangle$, then the branching ratios that weigh their actual BSF cross-sections in eqs. (4.5.16a) and (4.5.16d) are equal.

4.5.3 Effective cross-section

We now consider in more detail the contributions to the effective DM destruction cross-section in our model, based on the computations of sections 4.2 to 4.4. We begin with direct annihilation in section 4.5.3, and then discuss BSF in section 4.5.3. In figs. 4.14 and 4.15 we illustrate the contributions to BSF, while in fig. 4.16 we compare all contributions to the DM destruction cross-section for a chosen set of parameters, showcasing the effect of the Higgs potential and of BSF via Higgs emission.

Annihilation

In our model, the total annihilation cross-section is

$$\sigma_{\rm ann} v_{\rm rel} = \left[g_{SS} (\sigma^{\rm ann}_{SS} v_{\rm rel}) + 2 g_{DD} (\sigma^{\rm ann}_{DD} v_{\rm rel}) + 2 g_{D\bar{D}} (\sigma^{\rm ann}_{D\bar{D}} v_{\rm rel}) + 4 g_{DS} (\sigma^{\rm ann}_{DS} v_{\rm rel}) \right] / g^2_{\rm DM}, \tag{4.5.17}$$

where the dof of the various two-particle states are $g_{SS} = 4$, $g_{DD} = 16$, $g_{D\bar{D}} = 16$, $g_{DS} = 8$. In eq. (4.5.17), the DD and DS contributions carry factors of 2 to account also for the annihilation of the conjugate states, and $D\bar{D}$ and DS carry factors of 2 to account for the two distinguishable particles annihilated in each process.[11] From table 4.5, we find[12]

$$g_{SS} (\sigma^{\rm ann}_{SS} v_{\rm rel}) / (\pi m^{-2}) = 0, \tag{4.5.18a}$$

$$g_{DD} (\sigma^{\rm ann}_{DD} v_{\rm rel}) / (\pi m^{-2}) = 3 \times \frac{4\alpha_H^2}{3} \times S_0 \left(\frac{-\zeta_1 + 3\zeta_2}{4} \right), \tag{4.5.18b}$$

$$\begin{aligned} g_{D\bar{D}} (\sigma^{\rm ann}_{D\bar{D}} v_{\rm rel}) / (\pi m^{-2}) = {} & 1 \times \left(\frac{\alpha_1^2}{2} + \frac{3\alpha_2^2}{2} \right) \times \frac{\alpha_A S_0(\zeta_A) + \alpha_R S_0(-\zeta_R)}{\alpha_A + \alpha_R} \\ & + 3 \times \left[\frac{(\alpha_1 + 2\alpha_H)^2}{12} + \frac{10\alpha_1^2}{3} \right] \times S_0 \left(\frac{\zeta_1 + 3\zeta_2}{4} \right) \\ & + 3 \times \alpha_1 \alpha_2 \times S_0 \left(\frac{\zeta_1 - \zeta_2}{4} \right) \\ & + 9 \times \left[\frac{(\alpha_2 + 2\alpha_H)^2}{12} + \frac{\alpha_2^2}{12} + 2\alpha_2^2 \right] \times S_0 \left(\frac{\zeta_1 - \zeta_2}{4} \right), \end{aligned} \tag{4.5.18c}$$

$$g_{DS} (\sigma^{\rm ann}_{DS} v_{\rm rel}) / (\pi m^{-2}) = 6 \times \left(\frac{\alpha_1 \alpha_H}{6} + \frac{\alpha_2 \alpha_H}{2} \right) \times S_0(-\zeta_H). \tag{4.5.18d}$$

The thermally averaged annihilation cross-section (4.5.15) is found from (4.5.17), (4.5.18) and

$$\langle \sigma_{\rm ann} v_{\rm rel} \rangle = \left(\frac{m}{4\pi T} \right)^{3/2} \int d^3 v_{\rm rel}\, e^{-m v_{\rm rel}^2/(4T)}\, (\sigma_{\rm ann} v_{\rm rel}). \tag{4.5.19}$$

[11] As is well known, for pairs of identical particles (here SS, DD, $\bar{D}\bar{D}$), this factor is canceled upon thermal averaging by the factor 1/2 needed to avoid double-counting of the initial particle states [108].

[12] We recall from section 4.2.3 that, for simplicity, the contribution from the annihilation of the SS-like state has been included in the $D\bar{D}$ state.

Bound state formation

Referring to tables 4.7 to 4.10, and recalling also the results of section 4.4, the cross-sections for the formation of the different bound-state species are

$$\begin{aligned}\sigma^{\rm BSF}_{SS/D\bar{D}} v_{\rm rel} = \frac{1}{g_{\rm DM}^2} \Big\{ & 2 \times 1 \times (1 + R_B) \times \sigma v_{\rm rel}[(D\bar{D})^{\text{spin-0}}_{(\mathbb{1},0)}] \\ & + 2 \times 3 \times (1 + R_W) \times \sigma v_{\rm rel}[(D\bar{D})^{\text{spin-0}}_{(\mathbb{3},0)}] \\ & + 4 \times 2 \times (1 + R_H/h_H) \times \sigma v_{\rm rel}[(DS)^{\text{spin-0}}_{(\mathbb{2},1/2)}] \Big\}, \end{aligned} \tag{4.5.20a}$$

$$\begin{aligned}\sigma^{\rm BSF}_{D\bar{D}} v_{\rm rel} = \frac{1}{g_{\rm DM}^2} \Big\{ & 2 \times 3 \times (1 + R_B) \times \sigma v_{\rm rel}[(D\bar{D}\text{-like})^{\text{spin-1}}_{(\mathbb{1},0)}] \\ & + 1 \times 3 \times (1 + R_B) \times \sigma v_{\rm rel}[(SS\text{-like})^{\text{spin-1}}_{(\mathbb{1},0)}] \\ & + 2 \times 9 \times (1 + R_W) \times \sigma v_{\rm rel}[(D\bar{D})^{\text{spin-1}}_{(\mathbb{3},0)}] \\ & + 4 \times 6 \times (1 + R_H/h_H) \times \sigma v_{\rm rel}[(DS)^{\text{spin-1}}_{(\mathbb{2},1/2)}] \Big\}, \end{aligned} \tag{4.5.20b}$$

$$\begin{aligned}\sigma^{\rm BSF}_{DD} v_{\rm rel} = \frac{1}{g_{\rm DM}^2} \Big\{ & 1 \times 9 \times (1 + R_W) \times \sigma v_{\rm rel}[(DD)^{\text{spin-1}}_{(\mathbb{3},1)}] \\ & + 2 \times 6 \times (1 + R_H/h_H) \times \sigma v_{\rm rel}[(DS)^{\text{spin-1}}_{(\mathbb{2},1/2)}] \Big\}, \end{aligned} \tag{4.5.20c}$$

$$\begin{aligned}\sigma^{\rm BSF}_{DS} v_{\rm rel} = \frac{1}{g_{\rm DM}^2} \Big\{ & 2 \times 2 \times (1 + R_B) \times \sigma v_{\rm rel}[(DS)^{\text{spin-0}}_{(\mathbb{2},1/2)}, \quad B \text{ emission}] \\ & + 2 \times 2 \times (1 + R_W) \times \sigma v_{\rm rel}[(DS)^{\text{spin-0}}_{(\mathbb{2},1/2)}, \quad W \text{ emission}] \\ & + 1 \times 1 \times (1 + R_H/h_H) \times \sigma v_{\rm rel}[(SS\text{-like})^{\text{spin-0}}_{(\mathbb{1},0)}] \\ & + 2 \times 1 \times (1 + R_H/h_H) \times \sigma v_{\rm rel}[(D\bar{D}\text{-like})^{\text{spin-0}}_{(\mathbb{1},0)}] \\ & + 2 \times 3 \times (1 + R_H/h_H) \times \sigma v_{\rm rel}[(D\bar{D})^{\text{spin-0}}_{(\mathbb{3},0)}] \\ & + 1 \times 3 \times (1 + R_H/h_H) \times \sigma v_{\rm rel}[(DD)^{\text{spin-0}}_{(\mathbb{3},1)}] \Big\}, \end{aligned} \tag{4.5.20d}$$

where the square brackets denote the scattering states. In each term in the above, the first factor accounts for the number of DM particles destroyed (upon thermal averaging), as well as the capture of the conjugate scattering state if applicable, in analogy to eq. (4.5.17) for annihilation. The second factor corresponds to the dof of the scattering state. The factors in the brackets sum the radiative and via-scattering contributions to BSF. As noted in section 4.4, for BSF via off-shell H or $H^\dagger$ exchange, the phase-space suppression h_H of the radiative cross-section must be removed. The R_H, R_B, R_W and h_H factors must be evaluated at the value of ω, defined in eq. (4.3.8), that corresponds to each bound state.

Next, we must thermally average eqs. (4.5.20). In BSF, the emitted boson carries away a small amount of energy that can be comparable to the temperature of the primordial plasma during the DM decoupling. The Bose enhancement due to the final state boson can thus be significant, and must be included in thermal averaging the BSF cross-sections to ensure that detailed balance holds [39],

$$\langle \sigma^{\rm BSF}_{\mathcal{B}} v_{\rm rel} \rangle = \left(\frac{m}{4\pi T}\right)^{3/2} \int d^3 v_{\rm rel}\, e^{-m v_{\rm rel}^2/(4T)} \left(1 + \frac{1}{e^{\omega/T} - 1}\right) \, (\sigma^{\rm BSF}_{\mathcal{B}} v_{\rm rel}), \tag{4.5.21}$$

where the dissipated energy ω is given in eq. (4.3.8).[13]

As seen in eq. (4.5.16), the contributions of each bound level to the effective DM destruction cross-section (4.5.14) have to be waited by the appropriate branching fractions that account for the portion of bound states that decay into radiation, thereby reducing the DM density. The bound-state decay and transition rates needed to compute these branching fractions can be found in table 4.6. In thermally averaging these rates, we may neglect the Lorentz dilation factor that is $\simeq 1$ in the non-relativistic regime. However, the low-energy boson emitted in bound-to-bound transitions implies a Bose enhancement that must be included to ensure detailed balance at temperatures higher than the dissipated energy. So,

$$\langle \Gamma_{\mathcal{B}}^{\rm dec} \rangle \simeq \Gamma_{\mathcal{B}}^{\rm dec}, \tag{4.5.22a}$$

$$\langle \Gamma_{DS\to SS/D\bar{D}}^{\rm trans} \rangle \simeq \left[1 + R_H(\omega)/h_H(\omega)\right] \Gamma_{DS\to SS/D\bar{D}}^{\rm trans} \left(1 + \frac{1}{e^{\omega/T}-1}\right), \tag{4.5.22b}$$

where here $\omega = m(\alpha_A^2 - \alpha_H^2)/4$ is the dissipated energy. Finally, the bound-state ionisation rates are computed using the detailed balance eq. (4.5.7b), and summing over all ionised states as in eqs. (4.5.9a) and (4.5.9b); this yields

$$\langle \Gamma_{\mathcal{B}}^{\rm ion} \rangle \simeq \langle \sigma_{\mathcal{B}}^{\rm BSF} v_{\rm rel} \rangle \times \frac{g_{\rm DM}^2}{g_{\mathcal{B}}} \left(\frac{mT}{4\pi}\right)^{3/2} e^{-|\mathcal{E}_{\mathcal{B}}|/T}. \tag{4.5.22c}$$

Ionisation equilibrium

Equation (4.5.22c) implies that at $T \gg |\mathcal{E}_{\mathcal{B}}|$, the ionisation of the bound states tends to be faster than their decays and transitions, $\langle \Gamma_{\mathcal{B}}^{\rm ion} \rangle \gg \langle \Gamma_{\mathcal{B}}^{\rm dec} \rangle, \langle \Gamma_{\mathcal{B}}^{\rm trans} \rangle$, provided that $\langle \sigma_{\mathcal{B}}^{\rm BSF} v_{\rm rel} \rangle$ is sufficiently large. If so, in this regime, the system reaches a state of *ionisation equilibrium*, where the effective BSF cross-sections (4.5.16) become independent of the actual ones [134],

$$\langle \sigma_{\mathcal{B}}^{\rm BSF} v_{\rm rel} \rangle_{\rm eff} \simeq \frac{g_{\mathcal{B}}}{g_{\rm DM}^2} \Gamma_{\mathcal{B}}^{\rm dec} \left(\frac{4\pi}{mT}\right)^{3/2} e^{+|\mathcal{E}_{\mathcal{B}}|/T}, \tag{4.5.23}$$

where for the DS bound state whose direct decay into radiation is suppressed, we must use the effective decay rate (cf. eq. (4.5.16d))

$$\langle \Gamma_{DS}^{\rm dec} \rangle \to \langle \Gamma_{DS\to SS/D\bar{D}}^{\rm trans} \rangle \frac{\langle \Gamma_{SS/D\bar{D}}^{\rm dec} \rangle}{\langle \Gamma_{SS/D\bar{D}}^{\rm ion} \rangle + \langle \Gamma_{SS/D\bar{D}}^{\rm dec} \rangle + 2\langle \Gamma_{DS\to SS/D\bar{D}}^{\rm trans} \rangle (Y_{DS}^{\rm eq}/Y_{SS/D\bar{D}}^{\rm eq})}. \tag{4.5.24}$$

Since the bound-state decay rates are proportional to the annihilation cross-sections of the corresponding scattering states (cf. eq. (4.2.37)), eq. (4.5.23) implies that at high temperatures and while ionisation equilibrium holds, the BSF contribution to the DM destruction rate is negligible in comparison to that of direct annihilation.

However, as T approaches or drops below $|\mathcal{E}_{\mathcal{B}}|$, the ionisation rates become exponentially suppressed and are overcome by the bound-state decay and/or bound-to-bound transition rates. For the uncoupled bound states $D\bar{D}$ and DD, this implies that the effective BSF cross-sections increase exponentially until they saturate to their maximum values, the actual BSF cross-sections. For the $SS/D\bar{D}$ and DS coupled system, $\langle \Gamma_{DS\to SS/D\bar{D}}^{\rm trans} \rangle > \langle \Gamma_{DS}^{\rm ion} \rangle$, occurs before the decay rates surpass the ionisation rates; in this interval, the effective BSF cross-sections (4.5.16) together

[13] We recall from section 4.4 that a factor of $[1 + 1/(e^{\omega/T} - 1)]$ has been pulled out from the definition of the BSF cross-section via scattering, such that eq. (4.5.21) is the appropriate thermal-averaging formula for both radiative BSF and BSF via scattering.

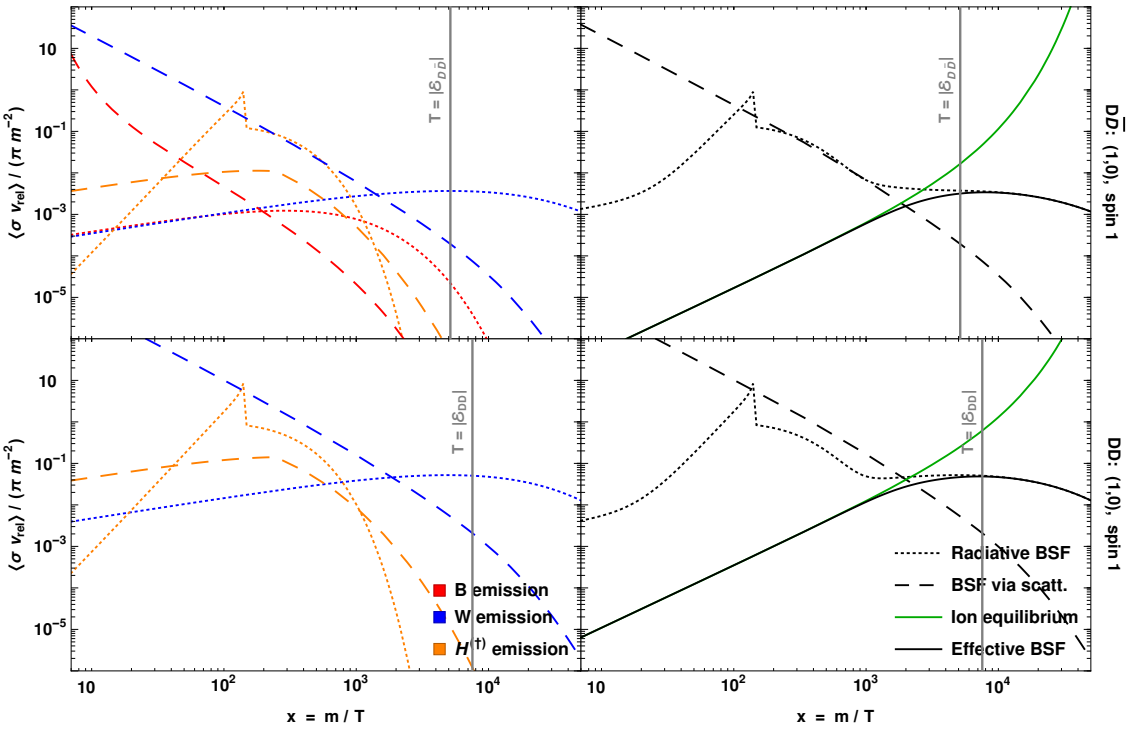

Figure 4.14: Thermally averaged BSF cross-sections for the $D\bar{D}$ and DD bound states; the latter includes the capture into its conjugate. We have used $m = 20$ TeV, $\alpha_H = 0.2$ and the temperature dependent Higgs mass $m_H(T)$; the spikes in the radiative BSF occur at the EWPT, when the Higgs mass tends to zero before becoming $m_h \simeq 125$ GeV. The vertical lines mark the temperatures equal to the binding energies. The cross-sections have been regulated according to section 4.3.6.

with the detailed balance eq. (4.5.22c), imply that ionisation equilibrium holds for the sum of the $SS/D\bar{D}$ and DS contributions,

$$\langle \sigma^{\rm BSF}_{SS/D\bar{D}} v_{\rm rel} \rangle_{\rm eff} + 2\langle \sigma^{\rm BSF}_{DS} v_{\rm rel} \rangle_{\rm eff} \simeq \frac{g_{SS/D\bar{D}}}{g^2_{\rm DM}} \Gamma^{\rm dec}_{SS/D\bar{D}} \left(\frac{4\pi}{mT}\right)^{3/2} e^{+|\mathcal{E}_{SS/D\bar{D}}|/T}, \tag{4.5.25}$$

where again we neglected the $SS/D\bar{D}$ decay against ionisation rate. At even lower temperatures, when ionisation becomes slower than decay, the effective BSF cross-sections reach their actual values.

We illustrate the above in figs. 4.14 and 4.15, where we also compare radiative BSF and BSF via scattering. Two observations are useful more generally for calculations of freeze-out with bound states:

- In some (but not all) cases, BSF via scattering dominates at early times; BSF via Higgs exchange may also dominate at late-times over on-shell emission due to the phase-space suppression of the latter. Nevertheless BSF via scattering does not change significantly the effective BSF cross-section with respect to considering radiative BSF only, because overall it becomes subdominant while the system is still in ionisation equilibrium, or around the time it exits it.

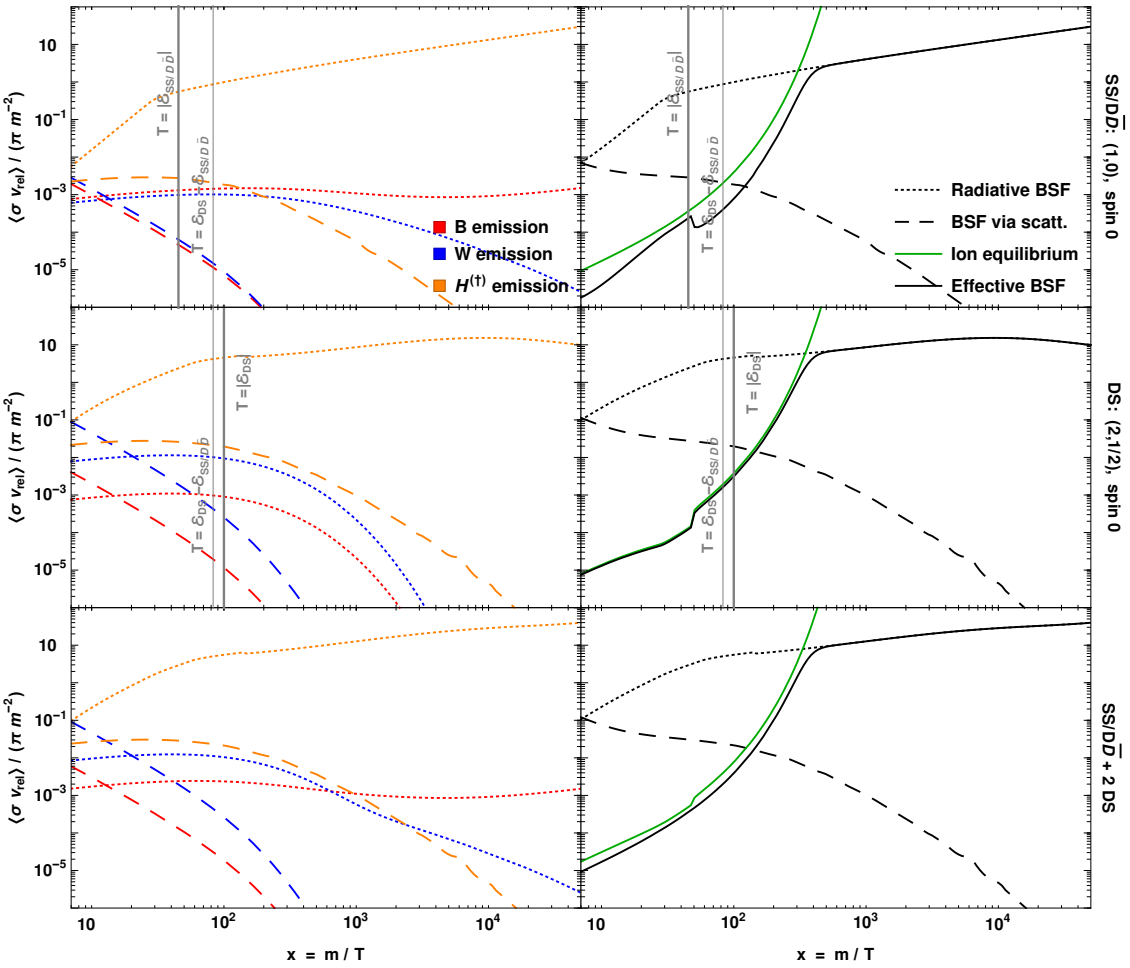

Figure 4.15: As in fig. 4.14, but for the $SS/D\bar{D}$ and DS states that transition into each other via Higgs emission or absorption. The DS panels include the capture into its conjugate. In the bottom row, we show the sum of the $SS/D\bar{D}$, DS and $\bar{D}S$ contributions. The vertical lines mark the temperatures equal to the binding energies and the energy splitting between $SS/D\bar{D}$ and DS. The feature around $x \simeq 50$ occurs when the Higgs doublet mass becomes lower than the energy splitting between the two bound states; this opens up the bound-to-bound transitions via on-shell Higgs emission (at higher T they occur only via off-shell Higgs exchange with the thermal bath), and drives the $SS/D\bar{D}$ bound states somewhat away from ionisation equilibrium.

- For the $D\bar{D}$, DD bound states, ionisation equilibrium ceases at $T > |\mathcal{E}_{\mathcal{B}}|$ (cf. fig. 4.14.)

  In contrast, the bound-to-bound transitions prevent the $SS/D\bar{D}$ and DS coupled system to reach ionisation equilibrium. However, it closely tracks it until much lower temperatures, $T \ll |\mathcal{E}_{\mathcal{B}}|$, due to the largeness of the BSF cross-sections (cf. fig. 4.15.)

  We also note here that the computation of the DM thermal decoupling (cf. section 4.6) shows that much of the BSF effect on the relic density arises after the system exits ionisation equilibrium. (This was also found in ref. [39].)

  The above imply that it is *not* safe to estimate the BSF effect by assuming ionisation equilibrium until $T \sim |\mathcal{E}_{\mathcal{B}}|$ and neglecting any effect thereafter, an approach previously

adopted in refs. [61, 64, 65]. Considering instead the BSF cross-sections is necessary for an accurate computation.

Higgs doublet mass and EWPT

The cross-sections for BSF via H emission depend on the Higgs doublet mass. Taking into account the finite temperature 1-loop corrections to the effective potential (see e.g. [136, 137]), we estimate that before the EWPT of the universe, the Higgs doublet mass was

$$m_H^2(T) \approx -\frac{m_h^2}{2} + \frac{\pi T^2}{4}\left(\alpha_1 + 3\alpha_2 + \frac{2\lambda}{\pi} + \frac{y_t^2}{\pi}\right), \tag{4.5.26}$$

where $m_h \simeq 125$ GeV is the Higgs boson mass at zero temperature, $\lambda = m_h^2/(2v_H^2) \simeq 0.13$ is the Higgs quartic coupling, $V_{\rm SM} \supset -\lambda|H|^4$, and $y_t \simeq 0.994$ is the top quark Yukawa coupling. The EWPT occurs as $m_H^2(T) \to 0$, i.e. at estimated temperature

$$T_{\rm EWPT} \approx \frac{\sqrt{2}m_h}{\sqrt{\pi\alpha_1 + 3\pi\alpha_2 + 2\lambda + y_t^2}} \simeq 151 \text{ GeV}. \tag{4.5.27}$$

In computing the DM decoupling, we use eq. (4.5.26) at $T \geqslant T_{\rm EWPT}$, and set $m_H \to m_h$ at $T < T_{\rm EWPT}$ while still using the annihilation and BSF rates computed under the assumption of electroweak symmetry. We discuss this approximation in section 4.7.

We may now estimate whether or when $m_H(T)$ implies that BSF via Higgs emission is kinematically suppressed. In a thermal distribution, the energy dissipated during BSF, given by eq. (4.3.8), averages to $\langle\omega\rangle = 3T/2 + |\mathcal{E}_\mathcal{B}|$. The first term suffices to provide for $m_H(T)$ for all $T > T_{\rm EWPT}$ since $m_H(T > T_{\rm EWPT}) \leqslant 0.63T$, as well as after the EWPT, down to temperatures $T \sim 2m_h/3 \simeq 83$ GeV. However, since the BSF cross-sections weigh preferentially low values of $v_{\rm rel}$, the kinematic suppression may become important at somewhat larger T than this estimate implies, unless $|\mathcal{E}_\mathcal{B}|$ is sufficient to provide for m_H.

4.6 Results: timeline and relic density

Collecting all the above, we are now ready to compute the DM decoupling and relic density. We will consider and compare the cases described in table 4.11, and repeat that our calculations always assume electroweak symmetry. We discuss this approximation in section 4.7.

In fig. 4.17, we present an example of the time evolution of the effective cross-section and the DM density. For the parameters chosen, the exponential increase of $\langle\sigma v_{\rm rel}\rangle_{\rm eff}$ due to BSF when the ionisation processes cease, gives rise to a second period of DM destruction that decreases the DM density by two orders of magnitude! In fig. 4.18, we show the timeline of the DM thermal decoupling. We define the recoupling period of DM destruction due to BSF as the interval between the two occurrences when $d^2(\ln Y)/d(\ln x)^2 = 0$, and the chemical decoupling as the latest time when $d(\ln Y)/d(\ln x) = 10\%$. In the same plot, we also mark the EWPT, as well as the time beyond which the finite Higgs mass affects its long-range effect. Since in part of the parameter space, the recoupling occurs after the EWPT and the chemical decoupling occurs even later, the effect of BSF via Higgs emission is most important for the range of DM masses where the binding energies exceed the Higgs boson mass, $m_h \simeq 125$ GeV. These ranges are also marked in fig. 4.18. (We discuss the validity of various approximations, including that of electroweak symmetry, in section 4.7).

In fig. 4.19, we show the values of α_H vs. m that reproduce the observed DM density, as well as the impact of the various processes on the relic density. As already seen in fig. 4.17, at

$\mathbf{AnnS}_{BW}$	Annihilation with Sommerfeld effect due to the B, W-mediated potentials.
$\mathbf{AnnS}_{BW}$ + $_{BW}$-$\mathbf{BSF}_{BW}$	Annihilation and BSF via B or W emission or exchange, including the B, W-mediated potentials.
$\mathbf{AnnS}_{BWH}$ + $_{BWH}$-$\mathbf{BSF}_{BWH}$	Annihilation and BSF via on-shell B, W or $H^{(\dagger)}$ emission, including the B, W, H-mediated potentials.

Table 4.11: The combinations of effects we shall compare in the following, in terms of their impact on the DM decoupling. When considering BSF, we always include both radiative BSF and BSF via scattering. However, we have examined their effects separately, and found that the inclusion of BSF via scattering does not change the results obtained when considering radiative BSF only. Moreover, in the present model, considering the Higgs-mediated potential while omitting BSF via Higgs emission, or the reverse, do not result in a significant effect on the relic density (cf. fig. 4.16), we thus do not present these cases separately.

$m \gtrsim$ few TeV, BSF via emission of a Higgs doublet is estimated to decrease the relic density by up to two orders of magnitude. The implications are twofold. For a fixed mass m, the coupling α_H is predicted to be almost up to an order of magnitude smaller than when neglecting BSF via Higgs emission. This should be expected to change (relax) experimental constraints very significantly. Conversely, for a given coupling, a much larger m is anticipated. In fact, DM masses almost up to the unitarity limit can be attained for $\alpha_H < 1$. (We discuss the unitarity limit in more detail in section 4.8.) This motivates experimental searches at very high masses.

To understand better the effect of the various bound states, in fig. 4.20 we show the relation between α_H vs m determined by considering direct annihilation plus each of the four bound states separately. The formation of the spin-1 DD and $D\bar{D}$ bound states has only a small effect because their binding energy is independent of α_H and somewhat small. This implies that ionisations inhibit the DM destruction via their formation until late, when BSF via Higgs emission is kinematically blocked, and BSF via B or W emission is not sufficiently fast to overcome the suppression due to the low DM density. Passing on to the $SS/D\bar{D}$ and DS bound states, for the lower range of m and α_H, their formation destroys DM efficiently after the EWPT. Thus the threshold for their effect being important is set by $|\mathcal{E}_{\mathcal{B}}| > m_h \simeq 125$ GeV, as the grey dotted lines in fig. 4.20 indicate.

Even away from the correlation of parameters that reproduces the observed DM density, the BSF effect on the relic abundance of the stable species can be very large as seen in fig. 4.21. The parameter space where the relic density is cosmologically insignificant is greatly enlarged. This is important for scenarios that do not aspire to explain the DM density, but nevertheless predict the existence of stable particles.

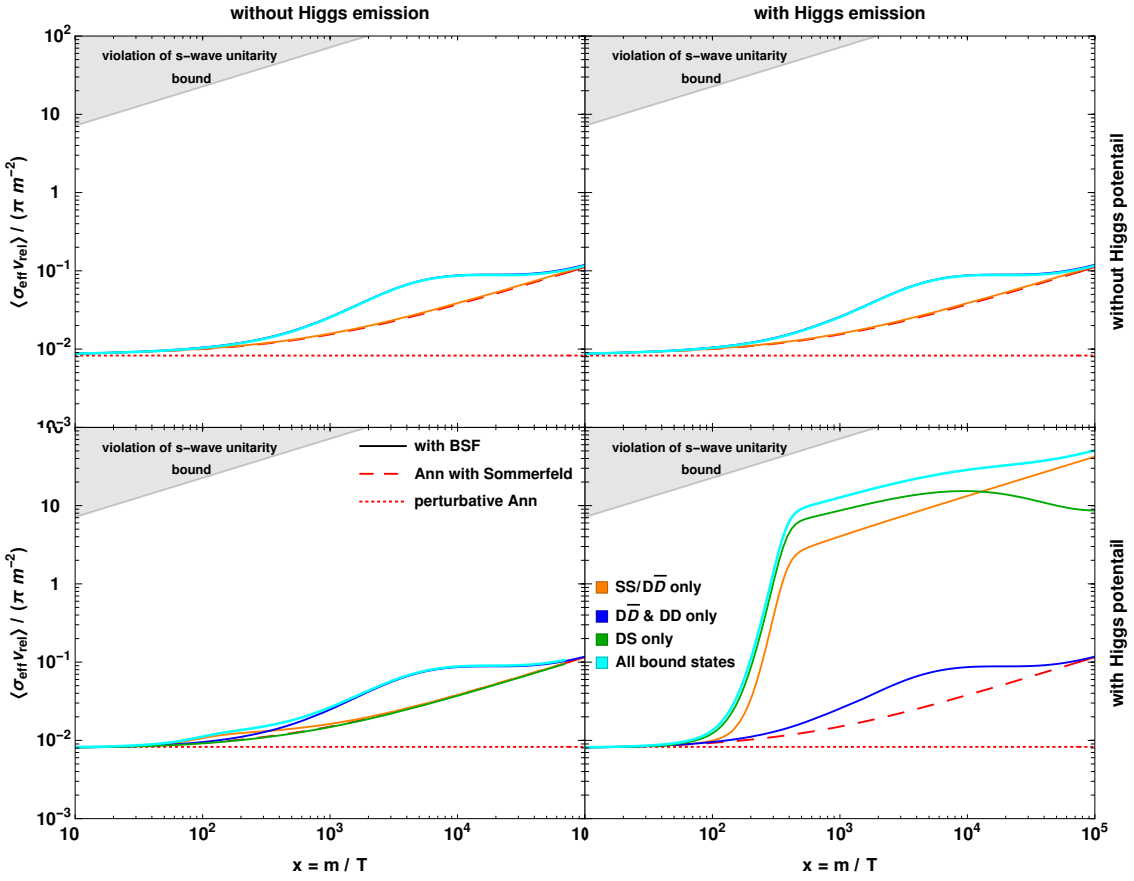

Figure 4.16: Contributions to the effective DM destruction cross-section. The solid lines include direct annihilation with Sommerfeld effect plus BSF according to the colour legend. We have used $m = 20$ TeV, $\alpha_H = 0.2$ and the temperature dependent Higgs mass $m_H(T)$. The cross-sections have been regulated according to section 4.3.6. The binding energy of the $D\bar{D}$ and DD bound states does not depend on the coupling to the Higgs, and their formation via H emission or exchange is always suppressed due the Higgs mass; their contribution is dominated by W emission. Both the $SS/D\bar{D}$ and DS binding energies depend on α_H, which ensures that their formation via H emission is not suppressed when the Higgs-mediated potential is taken into account and provided that α_H is sufficiently large (bottom right panel.) The DS bound states do not exist when neglecting the Higgs-mediated potential (upper row.)

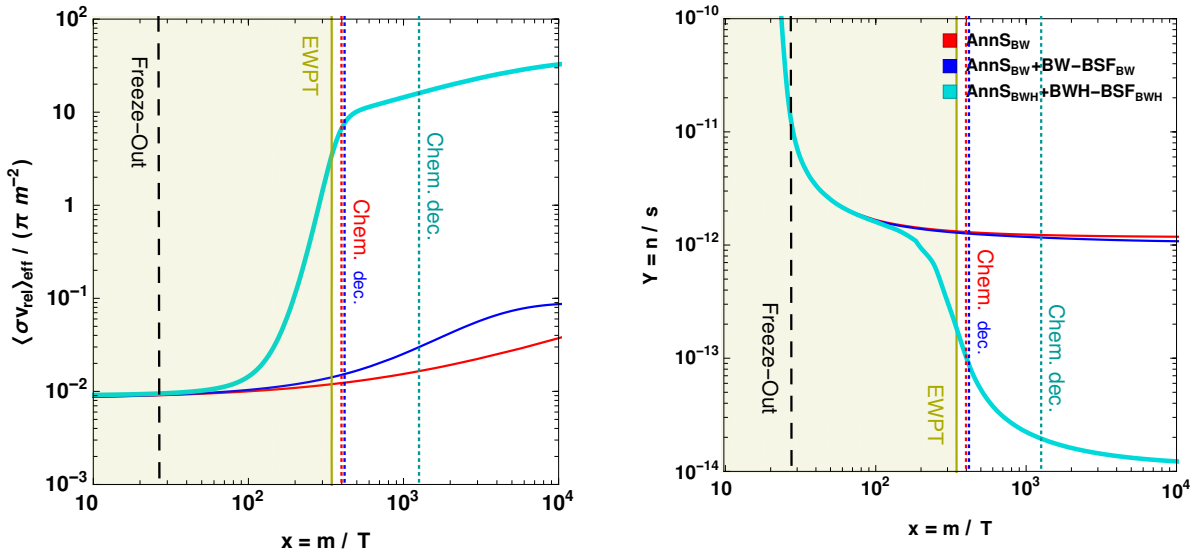

Figure 4.17: The effective cross-section $\langle \sigma v_{\rm rel} \rangle_{\rm eff}/(\pi m^{-2})$ and the dark matter yield $Y \equiv n/s$, vs the time parameter $x = m/T$. We also mark the time of freeze-out, the EWPT, and the chemical decoupling for the three cases in the legend. We have used $m = 50$ TeV and $\alpha_H = 0.2$.

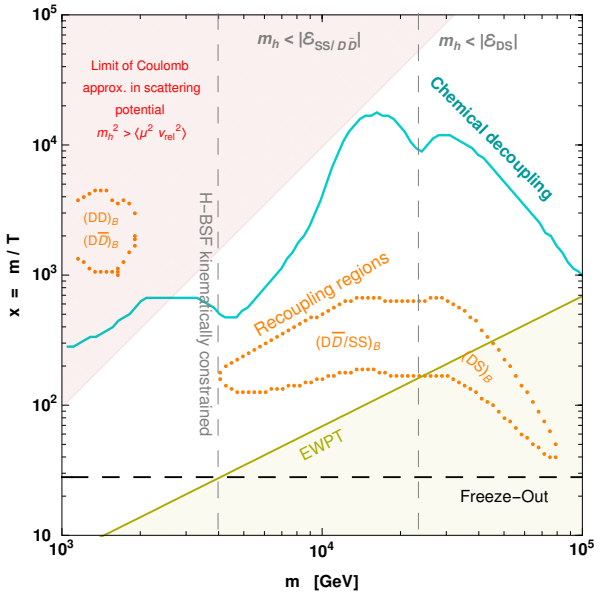

Figure 4.18: Various timeposts in the DM decoupling. See text for discussion. The coupling α_H is chosen as function of the mass m such that the observed DM density is reproduced by the full calculation (cf. cyan line in fig. 4.19.) For the recoupling intervals, we indicate the bound state that has the dominant effect.

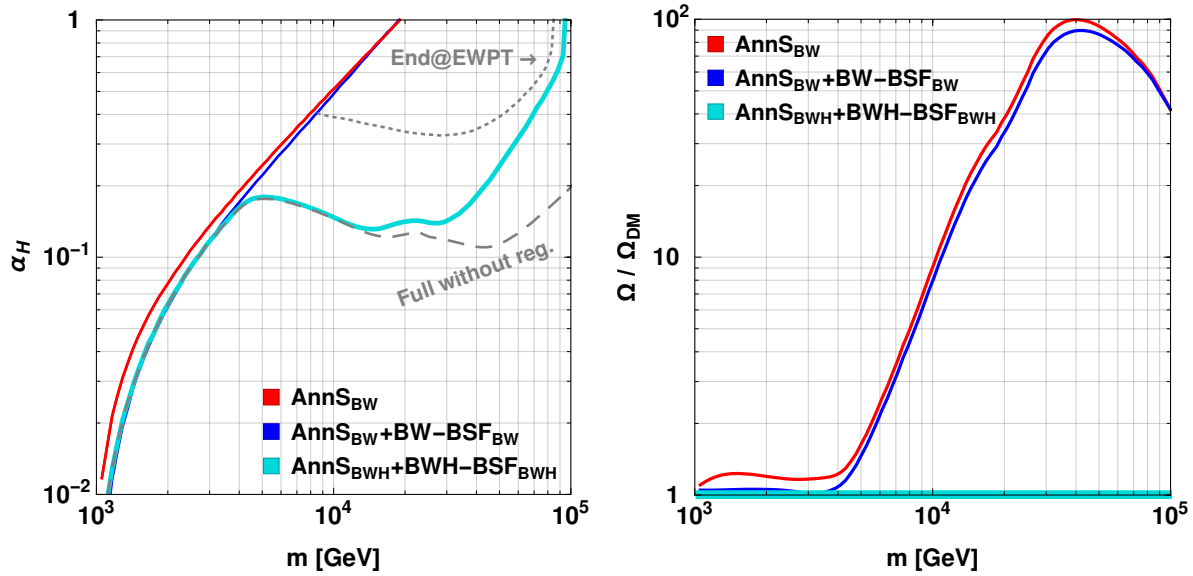

Figure 4.19: *Left:* α_H vs m such that the observed DM density is attained via thermal decoupling, when different combinations of effects are considered, as described in table 4.11. Note that the DM mass is $m_{\rm DM} = m - \sqrt{4\pi\alpha_H} v_H$ with $v_H \simeq 246$ GeV, and does not differ substantially from m along any of the lines. In grey lines, we show the result if the Boltzmann equations are integrated only up until the EWPT (*dotted*), and if the cross-sections are *not* regulated according to section 4.3.6 (*dashed.*) *Right:* The effect of the various processes on the relic density. For all lines, α_H is determined as a function of m by the full computation on the left (cyan line), but for each line here the Boltzmann equations include only the processes indicated in the legend.

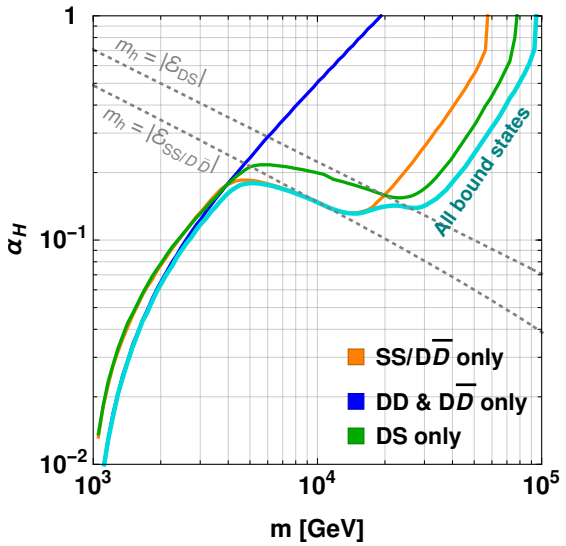

Figure 4.20: α_H vs m such that the observed DM density is attained via thermal decoupling, considering the contributions of the various bound states separately.

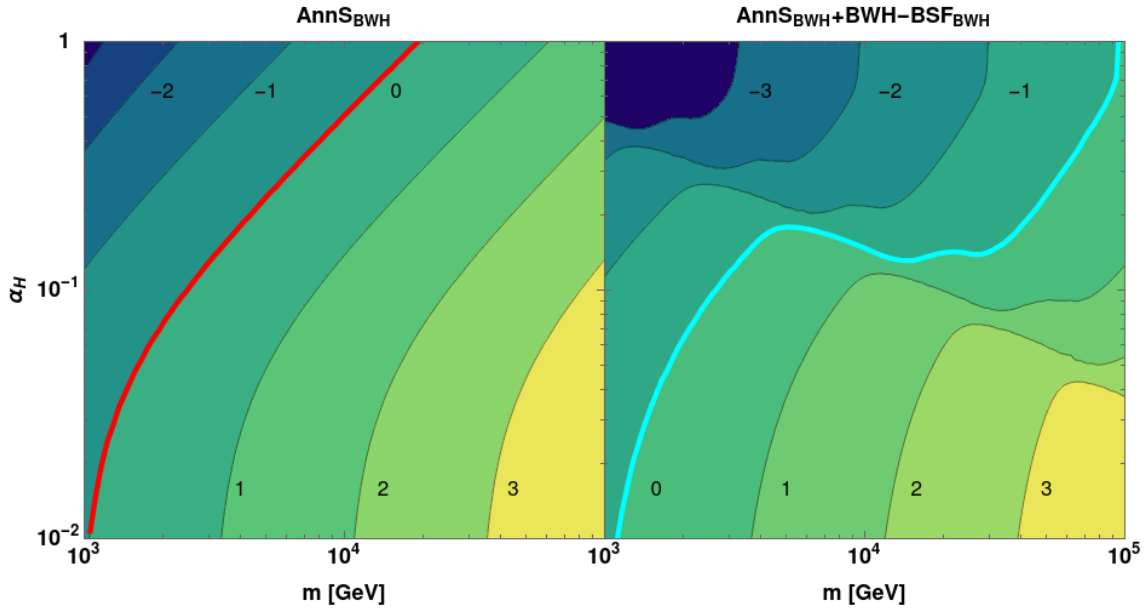

Figure 4.21: Contours of $\log_{10}(\Omega/\Omega_{\rm DM})$ (with the values indicated in black), when considering AnnS$_{BW}$ only (*left*), and AnnS$_{BWH}$ + $_{BWH}$−BSF$_{BWH}$ (*right*.) The red and cyan lines mark $\Omega = \Omega_{\rm DM}$. Note that the DM mass, $m_{\rm DM} = m - \sqrt{4\pi\alpha_H}v_H$, differs significantly from m only at the top left corners of the plots.

4.7 Major approximations and their validity

We now summarise the main approximations made in our analysis and comment on their potential effect on the estimated relic density.

(i) *Considered only ground-level bound states.*

BSF via vector or neutral scalar emission is dominated by dipole and quadrapole moments respectively. In these cases, the capture into the ground state is the dominant BSF process [1, 39, 43, 59, 62], the reason being twofold: it is the most exothermic process, and the overlap of scattering and bound state wavefunctions is larger.

In contrast, BSF via emission of a charged scalar is a monopole transition, and the capture into excited states can be comparable to or faster than the capture into the ground state, despite the latter being more exothermic [2]. This suggests that in the present model, capture into excited states via Higgs emission may be important.

Nevertheless, independently of the BSF cross-sections, the relative effect of the excited states on the relic density is moderated by their smaller binding energy that renders their ionisation efficient until later.

We thus anticipate that excited states may have a significant albeit not dominant effect that would further diminish the relic density and alter the coupling-mass relation along the direction found here. This is worth pursuing in more detail in the future.

(ii) *Regularisation of inelastic cross-sections in parametric regimes where BSF via Higgs emission approaches or appears to exceed the unitarity limit.*

See comments in section 4.3.6. In fig. 4.19 we compare the $\alpha_H - m$ relations with and without regularisation. Clearly, at large m the effect is significant; the regularisation of the cross-sections ensures that m does not exceed the unitarity limit on the mass of thermal relic DM [46, 104], which we discuss in section 4.8. This suggests that working out a more accurate regularisation scheme that would address the issues discussed in section 4.3.6 may be important in order to obtain more accurate results. We leave this for future work.

(iii) *Neglected the Higgs mass in the Higgs-mediated potential.*

Scattering states: In a thermal bath, the condition (4.2.29), $\mu v_{\rm rel} > m_H$, implies $\sqrt{3mT/2} \gtrsim m_H$. Considering the Higgs doublet mass (4.5.26) before the EWPT, this becomes $T \lesssim 3m$, which clearly covers all of the range of interest for the DM freeze-out. Below the EWPT, where $m_H \to m_h \simeq 125$ GeV, the condition is satisfied until after the DM chemical decoupling, as shown in fig. 4.18.

Bound states: The condition (4.2.30) for $n = 1$, $\mu\alpha_H >$ few $\times\, m_H$, becomes $x\alpha_H >$ few before the EWPT, with $x = m/T$. This is satisfied for all relevant x and α_H for which BSF has an effect ($x \gtrsim 50$ and $\alpha_H \gtrsim 0.1$, cf. figs. 4.18 and 4.19.) It is easy to check that the condition (4.2.30) is also satisfied below the EWPT for all relevant DM masses and couplings ($m > 5$ TeV and $\alpha_H \gtrsim 0.1$, cf. fig. 4.19.) Note that this is not coincidental; BSF via Higgs emission does not have a significant effect for lower α_H values because of the phase-space suppression due to the Higgs mass (cf. fig. 4.20.) The estimation here thus confirms the argument of section 4.2.2 that bound states are nearly Coulombic in the parameter space where their formation is kinematically allowed and significant.

(iv) *Assumed electroweak symmetry.*

In fig. 4.18, we see that the DM destruction via BSF may be efficient after the EWPT. The breaking of the electroweak symmetry has several important implications that we now discuss.

a. *The Goldstone modes of the Higgs doublet are absorbed by the $Z, W^\pm$ bosons.*

- BSF via emission of a Higgs doublet in the unbroken electroweak phase corresponds to BSF via emission of h or the longitudinal modes of the $Z, W^\pm$ bosons in the broken electroweak phase. The Goldstone boson equivalence theorem implies that the amplitudes for BSF via emission of the longitudinal $Z, W^\pm$ components are the same as those for the corresponding processes in the unbroken electroweak phase, in the limit that the energy of the emitted vector boson is much larger than its mass, $m_{Z,W}^2/\omega^2 \ll 1$.
  In our computation, the phase-space suppression sets $m_H \to m_h \simeq 125$ GeV after the EWPT, ensuring that $m_h/\omega < 1$ or equivalently $m_{Z,W}^2/\omega^2 < 0.5$. We thus regard the approximation as acceptable, especially in the parameter space away from the phase-space thresholds (cf. fig. 4.20.)
  The importance of monopole BSF processes in a broken gauge phase due to the Goldstone boson equivalence theorem was previously pointed out in ref. [138].
- The potential mediated by the Higgs doublet in the unbroken electroweak phase is mediated by h and the longitudinal $Z, W^\pm$ components in the broken phase. To compute the non-relativistic potential generated by the latter, we need their contribution to the vector boson propagators,

$$\frac{\mathbb{i}}{q^2 - m_V^2} \frac{q^\mu q^\nu}{m_V^2}, \tag{4.7.1}$$

  where q and $m_V = g_V v_H/2$ denote the vector boson momentum and mass, for $V = Z, W^\pm$, with $g_Z = \sqrt{g_1^2 + g_2^2}$ and $g_W = g_2$. In general, the exchange of $Z, W^\pm$ between a pair of $\mathbb{Z}_2$-odd particles may change the mass eigenstate on each leg. (Indeed, in the model under consideration, the $Z, W^\pm$ bosons couple only non-diagonally to the mass eigenstates, cf. eq. (4.1.7).) The contribution from the exchange of the longitudinal $Z, W^\pm$ components to the 2PI kernels (cf. section 4.2.1) is proportional to

$$\begin{aligned} \mathcal{K}_L \propto & [\bar{u}(p_1')\mathbb{i} g_V \not{q} u(p_1)][\bar{u}(p_2')\mathbb{i} g_V \not{q} u(p_2)]/m_V^2 \\ &= (\mathbb{i} g_V)^2 (m_1' - m_1)\bar{u}(p_1')u(p_1)\ (m_2 - m_2')\bar{u}(p_2')u(p_2)/m_V^2, \end{aligned} \tag{4.7.2}$$

  where $q = p_1' - p_1 = p_2 - p_2'$, and we used the Dirac equation $\not{p} u(p) = m u(p)$. Considering the mass splittings $\sim y v_H$, this becomes

$$\mathcal{K}_L \propto g_V^2 (y v_H)^2 (2m)^2/m_V^2 \propto y^2 m^2. \tag{4.7.3}$$

  Equation (4.7.3) shows that the potential generated by the exchange of the longitudinal $Z, W^\pm$ is indeed proportional to the coupling to the Higgs doublet. The screening scale of each contribution is $m_V^{-1} > m_h^{-1}$, thus the arguments presented in item (iii) for the Coulomb approximation remain valid. An analogous result has been obtained in [138] for a broken $U(1)$ model.
  Note that in eqs. (4.7.2) and (4.7.3) we omitted various numerical factors and signs for simplicity, and focused on deriving the scaling of the 2PI kernel. Considering these factors in detail reproduces the Higgs-doublet mediated potential (aside from the screening scale.)

b. *The Weak gauge bosons become massive.*

The non-zero $Z, W^\pm$ masses curtail the range of the potentials generated by the exchange of both their transverse and longitudinal components, and introduce phase-space suppression to the BSF processes occurring via their emission. The validity of the Coulomb

approximation for the $Z, W^{\pm}$ bosons can be assessed as in the preceding discussion for the Higgs. However, in the present model, the B, W-generated potentials and BSF via B or W emission do not have a significant effect, due to the fact that one of the dark multiplets is a gauge singlet and the other belongs to a small representation. We thus do not consider the transverse $Z, W^{\pm}$ components further. The effect of the longitudinal $Z, W^{\pm}$ components was discussed above.

c. *The components of the DM multiplets acquire different masses.*

After acquiring a mass splitting, the various pairs of $\mathbb{Z}_2$-odd particles can oscillate into each other according to the potentials of section 4.2.1 provided that the kinetic energy of their relative motion exceeds their mass difference. This necessitates $mv_{\rm rel}^2/4 > 2yv_H$, which, upon thermal averaging, becomes $T > (4/3)\sqrt{4\pi\alpha_H}v_H$. This condition is not satisfied below the EWPT for the α_H values of interest ($\alpha_H \gtrsim 0.1$.) We thus expect that the rates of some of the processes below the EWPT will be lower than estimated here.

This is probably the most severe limitation of our computation. To assess its impact, in fig. 4.19 we include the coupling-mass relation obtained by integrating the Boltzmann equations only up to the EWPT. Clearly, a proper treatment would result in an $\alpha_H - m$ relation between our this and the result obtained by integrating until late times. We see that even when the integration stops at the EWPT, the Higgs effect is still very significant, even if it appears only for larger α_H values. The impact on the relic density reaches up to a factor of a few.

4.8 Unitarity limit on the dark matter mass

The upper limit (4.3.65) on the inelastic cross-sections implied by unitarity, suggests that for very large masses, annihilations in the early universe may not suffice to reduce the density of thermalised particles to the observed DM value. It thus sets an upper bound on the mass of thermal relic DM annihilating predominantly via a finite number of partial waves in the early universe [104]. For self-conjugate DM in thermal equilibrium with the SM plasma, this is [39, 46][14]

$$m_{{\rm DM},\ell} \lesssim 197 \text{ TeV} \times \begin{cases} \sqrt{2\ell+1}, & \text{solely } \ell, \\ \ell+1, & 0 \leqslant \ell \leqslant \ell_{\max}. \end{cases} \tag{4.8.1}$$

Equation (4.8.1) is modified by $1/\sqrt{2}$ in the case of non-self-conjugate DM.

The parametric dependence of $\sigma_\ell^{\rm uni}$ on μ and $v_{\rm rel}$ implies that the limit (4.3.65) can be attained down to arbitrarily low velocities — thus the upper limit (4.8.1) on the mass of thermal-relic DM can be reached — only if there is an attractive long-range force between the interacting particles, and provided of course that the relevant couplings are sufficiently large [46]. Attractive long-range interactions imply also the existence of bound states, whose formation and subsequent decay may decrease the DM abundance more efficiently than direct annihilation [39]. This means that BSF may essentially be the dominant process that saturates the unitarity limit (4.3.65), and/or that additional partial waves to those dominating in the annihilation processes become important, thereby increasing the upper limit on the DM mass [46].

In general, the Weak interactions of the Standard Model are not sufficiently strong to generate cross-sections that approach the unitarity limit (4.3.65), unless perhaps the interacting particles

[14] If DM annihilates into a dark plasma that has different temperature than the SM plasma or includes many relativistic dof during DM freeze-out, then this value may somewhat change. Moreover, departures from thermal cosmology, such as episodes of entropy injection (see e.g. [98]), imply that larger $m_{\rm DM}$ values may be permissible.

belong to very large $SU_L(2)$ representations. However, BSF via emission of a scalar charged under a symmetry can be very efficient even for small couplings [2]. Here, we have seen that BSF via Higgs emission can raise the predicted WIMP mass very significantly, bringing it potentially close to the unitarity limit.

4.9 Conclusions

In this chapter we studied a renormalisable Higgs portal scenarios in which DM is the lightest mass eigenstate arising from the mixing of two electroweak multiplets that couple to the HiggsIn this context, we have considered the role of the Higgs doublet in the non-perturbative phenomena — the Sommerfeld effect and the formation of bound states — that take place during the thermal decoupling of multi-TeV DM from the primordial plasma.

We have shown that the effect of the Higgs doublet is two-fold: (i) it can mediate a long-range interaction that affects the wavefunctions of both scattering and bound states, and (ii) its emission can precipitate extremely fast monopole transitions, including capture into bound states and transitions between bound levels. In the model considered, these effects may change the relic density of the stable species by up to two orders of magnitude.

From a phenomenological point of view, we see that the effect on the relic density alters the coupling-mass relation that reproduces the observed DM abundance, and, beyond that, it greatly expands the parameter space where the stable relics do not overclose the universe. In the former case, the modified coupling-mass relation implies on one hand that, for a given DM mass, existing constraints may be significantly relaxed, and on the other hand that DM may be much heavier than previously anticipated, potentially approaching the unitarity limit.

In conclusion, while the amplitude for BSF via Higgs-doublet emission can be quite large even for small couplings of the DM multiplets to the Higgs, the Higgs-doublet mass introduces a kinematic suppression to the cross-section that renders this effect relevant for larger DM masses and/or couplings to the Higgs. In the specific singlet-doublet scenario considered here, we found that the effect is significant for $m \gtrsim 5$ TeV and $\alpha_H \gtrsim 0.1$. In models involving larger $SU_L(2)$ representations, the gauge interactions contribute more significantly to the binding energy of the bound states, thereby rendering the phase-space suppression less significant. We thus expect that the effect on the relic density is important even small couplings.

Finally we must notice that the capture into excited bound levels, which we neglected here, may also have a sizeable effect due to the monopole nature of the transitions occurring via Higgs-doublet emission. On the other hand, we have found that including BSF through scattering on the relativistic thermal bath via an off-shell Higgs doublet does not affect the relic density significantly.

Summary and outlook

If DM couples to a force carrier that is much lighter than itself, non-perturbative effects associated with the long-range nature of the interaction impact the DM phenomenology. In this thesis we focused on scalar forces, a particularly compelling possibility in view of the discovery of the Higgs boson, which may itself be the mediator, or provide a portal to DM via an extended scalar sector. If DM possesses a sizeable coupling to the SM Higgs, then it is constrained by current experiments to be significantly heavier than the Higgs. On the other hand, if DM couples to a non-SM scalar mediator that is much lighter than itself, then this coupling may result in significant DM self-scattering inside haloes that can affect the galactic structure and bring theoretical predictions in better agreement with observations [139]. Even outside the self-interacting DM regime, the coupling of DM to a lighter non-SM scalar mediator is a generic possibility within dark sector models.

It is well known that the Sommerfeld effect [37, 38] can influence the DM annihilation and self-scattering rates. This can be the case if the mediator is either a non-SM scalar or the SM Higgs [54]. More recently, it has been realised that the cosmological and astrophysical formation of DM bound states is a generic implication of theories with light mediators. The formation and subsequent decay of unstable bound states can deplete the DM density [39], and contribute to the DM indirect detection signals [40–48, 52]. The formation of stable bound states may quell the DM self-scattering inside haloes [49], and give rise to novel radiative [57, 58, 95, 114] and direct detection signatures [50, 51].

In chapter 2 we saw that, although the capture into bound states via emission of a vector is known to be significant, the capture via neutral scalar emission suffers from cancellations that render it important only within narrow parameter space. In chapter 3 we showed that bound-state formation via emission of a charged scalar is by contrast highly significant. We studied a model where DM is charged under a dark $U(1)$ force and coupled also to a light complex scalar that is charged under the same gauge symmetry. Our results encompass the cross-sections for bound-state formation via emission of the charged scalar, and show that they can exceed those for capture via vector emission, as well as annihilation, by orders of magnitude. This holds even for very small values of the DM coupling to the charged scalar, and remains true in the limit of global symmetry. We then computed DM thermal freeze-out, and found that the capture into meta-stable bound states via emission of a charged scalar can cause a late period of significant DM depletion. We included analytical expressions in the Coulomb limit, that are readily generalisable to non-Abelian interactions.

In chapter 4 we applied the results of chapter 3 in a model considering the Higgs doublet in the thermal decoupling of multi-TeV dark matter coupled to the weak interactions of the Standard Model. We showed that the Higgs doublet can mediate a long-range interaction that binds or strengthens the binding of DM into bound states. More importantly, the emission of a

Higgs doublet precipitates extremely rapid capture processes and bound-to-bound transitions. The formation of metastable bound states via Higgs emission and their decay were found to decrease the relic density very significantly.

In summary, we found that the entire Higgs doublet contributes to the (long-range) potential between the DM multiplets. We also found that the cross-sections for BSF via Higgs emission can exceed those for annihilation or BSF via vector emission by orders of magnitude, and result in a late period of DM chemical recoupling. Consequently, BSF via Higgs emission increases the DM destruction rate in the early universe and, for a given set of couplings, pushes the predicted DM masses to the multi-TeV scale. This, in turn, opens the possibility for thermal-relic WIMP dark mate to be much heavier than anticipated, potentially approaching the unitarity limit, which in the non-relativistic regime implies (or presupposes) the presence of long-range interactions. This is particularly important in view of the numerous existing and upcoming observatories probing high-energy cosmic rays, such as H.E.S.S., IceCube, CTA and KM3Net. The experimental exploration of the multi-TeV scale creates urgency for the comprehensive theoretical understanding of the dynamics and possibilities in this regime.

Looking forward, we note that our calculations are broadly important for scenarios that introduce new stable species in the fashion considered here, even if these species are not anticipated to account for DM. Besides specifying the parameters for which the relic density of the lightest new mass eigenstate matches the observed DM abundance, we showed how the relic density is affected by the new effects within a broader parameter space. As is standard, the relic density of stable particles sets a cosmological constraint of DM for new physics scenarios.

Finally, we leave for future work the capture into excited bound levels, which may also have a sizable effect due to the monopole nature of the transitions occurring via Higgs-doublet emission. Our work may moreover be improved by the introduction of scale-dependent couplings and corrections of the light mediator masses outside the Coulomb limit.

Appendix A

Non-relativistic potential

A.1 Scalar mediator: scalar vs. fermionic interacting particles

The non-relativistic static potential describing the $X_1 - X_2$ interaction is (see e.g. Ref. [59, 140])

$$V(\mathbf{r}) = -\frac{1}{4M\mu}\int \frac{d^3k}{(2\pi)^3}\mathcal{M}_{\text{2PI}}(\mathbf{k})\; e^{i\mathbf{kr}}\,, \tag{A.1.1}$$

where $\mathcal{M}_{\text{2PI}}(\mathbf{k})$ encompasses all 2-particle-irreducible diagrams that contribute to the $X_1 - X_2$ elastic scattering. To leading order, this is the one boson exchange shown in Figure A.1. From

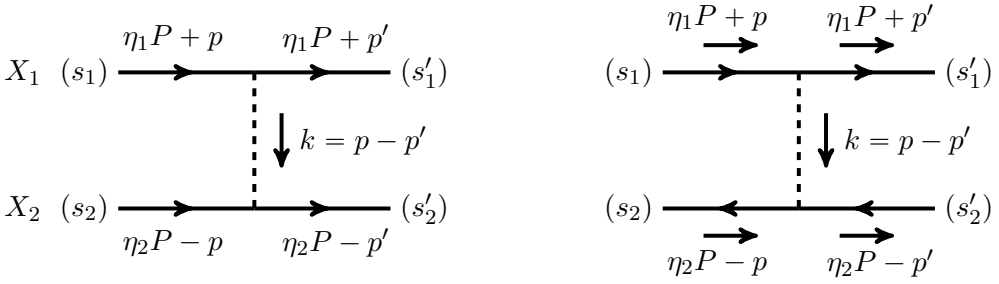

Figure A.1: One boson exchange diagrams that yield the leading order contribution to the non-relativistic potential between two different paticles X_1 and X_2 (*left*), or a particle-antiparticle pair (*right*). The parentheses denote the spin of the incoming and outgoing particles, in the case of fermions.

the Lagrangians of Equations (2.1.1) to (2.1.3), we find for the interaction of a scalar pair X_1X_2, a fermionic pair X_1X_2 and a fermion-antifermion pair $X\bar{X}$,

$$i\mathcal{M}^{sc}_{\text{2PI}}(\mathbf{k}) = (-ig_1m_1)(-ig_2m_2)\,\frac{i}{k^2 - m_\varphi^2} \simeq \frac{ig_1g_2m_1m_2}{\mathbf{k}^2 + m_\varphi^2}\,, \tag{A.1.2}$$

$$\begin{aligned} i\mathcal{M}^{f}_{\text{2PI}}(\mathbf{k}) &= [-ig_1\bar{u}^{s_1'}(\eta_1 P + p')\,u^{s_1}(\eta_1 P + p)][-ig_2\bar{u}^{s_2'}(\eta_2 P - p')\,u^{s_2}(\eta_2 P - p)]\,\frac{i}{k^2 - m_\varphi^2} \\ &\simeq \frac{i4g_1g_2m_1m_2}{\mathbf{k}^2 + m_\varphi^2}\delta^{s_1s_1'}\delta^{s_2s_2'}\,, \end{aligned} \tag{A.1.3}$$

$$\begin{aligned} i\mathcal{M}^{f,X\bar{X}}_{\text{2PI}}(\mathbf{k}) &= (-1)^3[-ig\bar{u}^{s_1'}(P/2 + p')\,u^{s_1}(P/2 + p)][-ig\bar{v}^{s_2}(P/2 - p)\,v^{s_2'}(P/2 - p')]\,\frac{i}{k^2 - m_\varphi^2} \\ &\simeq \frac{i4g^2m_X^2}{\mathbf{k}^2 + m_\varphi^2}\delta^{s_1s_1'}\delta^{s_2s_2'}\,, \end{aligned} \tag{A.1.4}$$

where we made the approximation $k^0 \ll |\mathbf{k}|$. In eq. (A.1.4), the factor $(-1)^3$ arises from the permutation of the fermion fields in the Wick contractions (see e.g. Ref. [140, section 4.7]). For the spinor contractions in eqs. (A.1.3) and (A.1.4), we used

$$\bar{u}^{s'_j}(p'_j)u^{s_j}(p_j) \simeq \bar{u}^{s'_j}(p_j)u^{s_j}(p_j) = +2m_j\delta^{s_j s'_j} \tag{A.1.5}$$

$$\bar{v}^{s_j}(p_j)v^{s'_j}(p'_j) \simeq \bar{v}^{s_j}(p_j)v^{s'_j}(p_j) = -2m_j\delta^{s_j s'_j} \tag{A.1.6}$$

From eqs. (A.1.1) to (A.1.4), we find the well known Yukawa potential

$$V(\mathbf{r}) = -\frac{\alpha}{r}e^{-m_\varphi r}\,, \tag{A.1.7}$$

with $\alpha = \alpha_{sc}$ or $\alpha = \alpha_f$ depending on whether the interacting particles are scalars or fermions respectively, where

$$\alpha_{sc} \equiv \frac{g_1 g_2}{16\pi} \qquad \text{and} \qquad \alpha_f \equiv \frac{g_1 g_2}{4\pi}\,. \tag{A.1.8}$$

The interaction is attractive if $g_1 g_2 > 0$.

A.2 t vs. u channels

We consider a particle-antiparticle pair $XX^\dagger$ and derive the general formula for the non-relativistic potential arising from t-channel and u-channel diagrams. The momentum decomposition for the $XX^\dagger$ interaction is shown in fig. A.2. We begin with the Schrödinger equation in

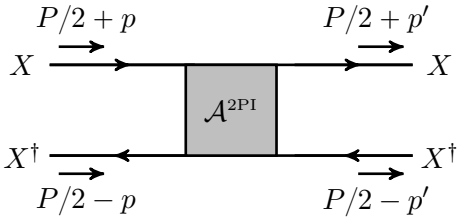

Figure A.2: Momentum decomposition of the 2PI diagrams of the $XX^\dagger$ interaction.

momentum space (see e.g. Ref. [59, eq. (2.78)]),

$$\left(-\frac{\mathbf{p}^2}{2\mu} + \mathcal{E}_{n\ell m}\right)\tilde{\psi}_{n\ell m}(\mathbf{p}) = \frac{\mathbb{i}}{4M\mu}\int\frac{d^3p'}{(2\pi)^3}\,\mathbb{i}\mathcal{A}^{\text{2PI}}(\mathbf{p},\mathbf{p}')\;\tilde{\psi}_{n\ell m}(\mathbf{p}'), \tag{A.2.1}$$

where $\mathcal{A}^{\text{2PI}}(\mathbf{p},\mathbf{p}')$ is the sum of the 2PI diagrams. We will be interested in t-channel and u-channel contributions that have the form

$$\mathbb{i}\mathcal{A}^{\text{2PI}}(\mathbf{p},\mathbf{p}') = \mathbb{i}\mathcal{A}_t^{\text{2PI}}(\mathbf{p}-\mathbf{p}') + \mathbb{i}\mathcal{A}_u^{\text{2PI}}(\mathbf{p}+\mathbf{p}'). \tag{A.2.2}$$

As in Ref. [43, 59, 62], we shall use the Fourier transforms

$$\tilde{\psi}_{n\ell m}(\mathbf{p}) = \int d^3r\;\psi_{n\ell m}(\mathbf{r})\;e^{-\mathbb{i}\mathbf{p}\cdot\mathbf{r}}, \qquad \psi_{n\ell m}(\mathbf{r}) = \int\frac{d^3p}{(2\pi)^3}\;\tilde{\psi}_{n\ell m}(\mathbf{p})\;e^{\mathbb{i}\mathbf{p}\cdot\mathbf{r}}. \tag{A.2.3}$$

Applying the operator $\int d^3p/(2\pi)^3\,\exp(\mathbb{i}\mathbf{p}\cdot\mathbf{r})$ on eq. (A.2.1), we obtain

$$\begin{aligned}
&\left(\frac{\nabla^2}{2\mu} + \mathcal{E}_{n\ell m}\right)\psi_{n\ell m}(\mathbf{r}) = \frac{\mathbb{i}}{4M\mu}\int\frac{d^3p}{(2\pi)^3}\frac{d^3p'}{(2\pi)^3}\,e^{\mathbb{i}\mathbf{p}\cdot\mathbf{r}}\left[\mathbb{i}\mathcal{A}_t^{\text{2PI}}(\mathbf{p}-\mathbf{p}') + \mathbb{i}\mathcal{A}_u^{\text{2PI}}(\mathbf{p}+\mathbf{p}')\right]\tilde{\psi}_{n\ell m}(\mathbf{p}') \\
&= \frac{\mathbb{i}}{4M\mu}\left\{\left[\int\frac{d^3q}{(2\pi)^3}\,e^{\mathbb{i}\mathbf{q}\cdot\mathbf{r}}\;\mathbb{i}\mathcal{A}_t^{\text{2PI}}(\mathbf{q})\right]\psi_{n\ell m}(\mathbf{r}) + \left[\int\frac{d^3q}{(2\pi)^3}\,e^{\mathbb{i}\mathbf{q}\cdot\mathbf{r}}\;\mathbb{i}\mathcal{A}_u^{\text{2PI}}(\mathbf{q})\right]\psi_{n\ell m}(-\mathbf{r})\right\} \\
&= \left[V_t(\mathbf{r}) + V_u(\mathbf{r})\right]\psi_{n\ell m}(\mathbf{r}),
\end{aligned} \tag{A.2.4}$$

where we used that $\psi_{n\ell m}(-\mathbf{r}) = (-1)^\ell \psi_{n\ell m}(\mathbf{r})$, and

$$V_t(\mathbf{r}) \equiv \frac{\mathbb{i}}{4M\mu} \int \frac{d^3q}{(2\pi)^3}\, e^{\mathbb{i}\mathbf{q}\cdot\mathbf{r}}\; \mathbb{i}\mathcal{A}_t^{\text{2PI}}(\mathbf{q}), \tag{A.2.5a}$$

$$V_u(\mathbf{r}) \equiv \frac{\mathbb{i}}{4M\mu}\; (-1)^\ell \int \frac{d^3q}{(2\pi)^3}\, e^{\mathbb{i}\mathbf{q}\cdot\mathbf{r}}\; \mathbb{i}\mathcal{A}_u^{\text{2PI}}(\mathbf{q}). \tag{A.2.5b}$$

We observe that the u-channel contribution depends on the angular momentum mode of the eigenstate. Equation (A.2.4) can now be rewritten in the familiar order

$$\left[-\frac{\nabla^2}{2\mu} + V_t(\mathbf{r}) + V_u(\mathbf{r})\right] \psi_{n\ell m}(\mathbf{r}) = \mathcal{E}_{n\ell m}\psi_{n\ell m}(\mathbf{r}). \tag{A.2.6}$$

Appendix B

Wave functions

B.1 Scattering state and bound state wave functions

The bound state and scattering state wavefunctions obey the Schrödinger equations

$$\left[-\frac{\nabla^2}{2\mu} + V(r)\right]\psi_{n\ell m}(\mathbf{r}) = -\epsilon_{n\ell}\psi_{\{n\ell m\}}(\mathbf{r})\,, \tag{B.1.1}$$

$$\left[-\frac{\nabla^2}{2\mu} + V(r)\right]\phi_{\mathbf{k}}(\mathbf{r}) = +\epsilon_{\mathbf{k}}\phi_{\mathbf{k}}(\mathbf{r})\,. \tag{B.1.2}$$

If there is no long-range interaction: this happens when the mediator φ is very massive, the interacting coupling is very small (e.i condition $m_\varphi < \mu\alpha$ do not fit), or when the mediator does not couple with one of the two particles X_1, X_2. Under one of this conditions, the long-range interacting potential $V(\mathbf{r})$ vanish, the two scattering particles do not feel one each other until the perturbative collision, consequently the scattering solution of the pair is a plane wave and bound state formation is not possible.

If the mediator is massless: the Yukawa potential in eq. (A.1.7) becomes the Coulomb potential

$$V_C(\mathbf{r}) = -\frac{\alpha}{r}, \tag{B.1.3}$$

The solutions of the Schrödinger equations becomes analytical and the two particles interacts at an infinity range. The scattering and bound-state wavefunctions are:

$$\phi_{\mathbf{k}}(\mathbf{r}) = \sum_{\ell=0}^{\infty}(2\ell+1)\left[\frac{\chi_{|\mathbf{k}|,\ell}(\kappa r)}{\kappa r}\right]P_\ell(\hat{\mathbf{k}}\cdot\hat{\mathbf{r}}) \tag{B.1.4}$$

$$\psi_{n\ell m}(\mathbf{r}) = \kappa^{3/2}\left[\frac{\chi_{n\ell}(\kappa r)}{\kappa r}\right]Y_{\ell m}(\Omega_R) \tag{B.1.5}$$

Where $P_\ell(y)$ are the Legendre polynomials and $Y_{\ell m}(\Omega_R)$ are the spherical harmonic polynomials. The sum over the ℓ modes od the scattering state can be also express in the close form

$$\phi_{\mathbf{k}}(\mathbf{r}) = \sqrt{S_0(\zeta)}\ {}_1F_1[\mathbb{i}\zeta; 1; \mathbb{i}(|\mathbf{k}||\mathbf{r}| - \mathbf{k}\cdot\mathbf{r})]e^{\mathbb{i}\mathbf{r}\cdot\mathbf{k}} \tag{B.1.6}$$

where[1]

$$S_0(\zeta) = \frac{2\pi\zeta}{1 - e^{-2\pi\zeta}} \tag{B.1.7}$$

[1] The factor $\sqrt{S_0(\zeta)}$ in eq. B.1.6 often appears in the literature as $e^{\pi\zeta/2}\Gamma(1-\mathbb{i}\zeta)$.

$$\chi_{|\mathbf{k}|,\ell}(x) = \frac{\sqrt{S_0(\zeta)}}{\Gamma(1-\mathbb{i}\zeta)}\frac{\Gamma(1+\ell-\mathbb{i}\zeta)}{(2\ell+1)!}x(2\mathbb{i}x/\zeta)^\ell e^{-\mathbb{i}x/\zeta}{}_1F_1(1+\ell+\mathbb{i}\zeta;2\ell+2;2\mathbb{i}x/\zeta) \tag{B.1.8}$$

$$\chi_{n\ell}(x) = \frac{1}{n}\left[\frac{(n-\ell-1)!}{(n+\ell)!}\right]^{1/2} e^{-x/n}(2x/n)^{\ell+1}L_{n-\ell-1}^{2\ell+1}(2x/n) \tag{B.1.9}$$

Where ${}_1F_1$ is the confluent hypergeometric function of the first kind, and L_b^a are the generalised Laguerre polynomials of degree n.

If the mediator is massive: Hulthen approximation. the solutions of the Schrödinger equation under the Yukawa potential (A.1.7) are not known in a closed form. However, it is possible to obtain analytical solutions for the $\ell = 0$ modes of the wavefunctions, if we replace the Yukawa for the Hulthen potential Ref. [141, 142],

$$V_H(\mathbf{r}) = -\alpha m_* \frac{e^{-m_* r}}{1-e^{-m_* r}}\,. \tag{B.1.10}$$

For $m_* \sim m_\varphi$, the Hulthen potential reproduces the behavior of the Yukawa potential at short and large distances. Both potentials admit bound state solutions provided that the screening length scale is sufficiently large. The thresholds for the n-th bound level in the Hulthen potential are $m_* \leqslant 2\mu\alpha/n^2$, while for the Yukawa potential (A.1.7), bound states exist if $m_\varphi \leqslant \mu\alpha/0.84$ (see Ref. [43]). We shall pick

$$m_* = 1.68 m_\varphi\,, \tag{B.1.11}$$

such that the conditions for the existence of the lowest bound state coincide. The solutions to the Schrödinger equation for the Hulthen potential can be expressed in terms of the two dimensionless parameters

$$\zeta \equiv \alpha/v_{\rm rel} \quad \text{and} \quad \xi \equiv 2\mu\alpha/m_*\,. \tag{B.1.12}$$

Note that ζ and ξ are always defined using the appropriate fermionic or scalar coupling α. ζ compares the average momentum transfer between two unbound particles ($\sim \mu v_{\rm rel}$) with the relative average momentum of the particles inside the bound state ($\sim \mu\alpha$), while ξ compares the Bohr momentum ($\kappa = \mu\alpha$) that determines the size of the bound state, with the screening scale (m_*) that determines the range of the interaction. The interaction manifests as long-range roughly if $\xi \gtrsim 1$; this is the regime where non-perturbative phenomena, the Sommerfeld effect and bound states, emerge. The Coulomb limit is recovered for $\xi \to \infty$. For the ground state, the binding energy is

$$\epsilon_{10} = \frac{\kappa^2(1-1/\xi)^2}{2\mu}\,, \tag{B.1.13}$$

and the wavefunction reads

$$\psi_{100}(\mathbf{r}) = \xi\sqrt{\frac{\kappa^3}{\pi}\left(1-\frac{1}{\xi^2}\right)}\,\frac{\sinh(\kappa r/\xi)\exp(-\kappa r)}{\kappa r}\,. \tag{B.1.14}$$

For the scattering state, we make the partial-wave decomposition

$$\phi_{\mathbf{k}}(\mathbf{r}) = \sum_{\ell_S=0}^{\infty} w_{\ell_S}(m_* r)\; P_{\ell_S}(\hat{\mathbf{k}}\cdot\hat{\mathbf{r}})\,. \tag{B.1.15}$$

It is possible to find an analytical solution for $\ell_S = 0$ only, which suffices for our purposes,

$$w_0(z) = \sqrt{S_0(\zeta,\xi)}\; e^{-i\xi z/(2\zeta)}\;\left(\frac{1-e^{-z}}{z}\right)\;{}_2F_1(a_0,b_0,2;\;1-e^{-z})\,, \tag{B.1.16}$$

where ${}_2F_1$ is the hypergeometric function and

$$a_0 \equiv 1 + \frac{i\xi}{2\zeta}(1 - \sqrt{1 - 4\zeta^2/\xi}), \tag{B.1.17}$$

$$b_0 \equiv 1 + \frac{i\xi}{2\zeta}(1 + \sqrt{1 - 4\zeta^2/\xi}), \tag{B.1.18}$$

$$\sqrt{S_0(\zeta,\xi)} \equiv \frac{i\zeta}{\xi}\left[\frac{\Gamma(a_0)\Gamma(b_0)}{\Gamma(i\xi/\zeta)}\right]^* . \tag{B.1.19}$$

From eq. (B.1.19), we obtain

$$S_0(\zeta,\xi) = \frac{2\pi\zeta\sinh(\pi\xi/\zeta)}{\cosh(\pi\xi/\zeta) - \cosh[(\pi\xi/\zeta)\sqrt{1-4\zeta^2/\xi}]}, \tag{B.1.20}$$

which reduces to eq. (B.1.7) in the limit $\xi \to \infty$.

B.2 Wavefunctions for two different Coulomb potentials

We consider scattering and bound states in two different Coulomb potentials

$$\left(-\frac{\nabla^2}{2\mu} - \frac{\alpha_{\mathcal{S}}}{r}\right)\phi_{\mathbf{k}}(\mathbf{r}) = \mathcal{E}_{\mathbf{k}}\,\phi_{\mathbf{k}}(\mathbf{r}), \tag{B.2.1a}$$

$$\left(-\frac{\nabla^2}{2\mu} - \frac{\alpha_{\mathcal{B}}}{r}\right)\psi_{n\ell m}(\mathbf{r}) = \mathcal{E}_n\,\psi_{n\ell m}(\mathbf{r}). \tag{B.2.1b}$$

The expectation value of the momentum of each particle in the CM frame in the scattering state, and the Bohr momenta for the scattering and bound states are

$$\mathbf{k} \equiv \mu v_{\rm rel}, \tag{B.2.2a}$$

$$\kappa_{\mathcal{S}} \equiv \mu\alpha_{\mathcal{S}}, \tag{B.2.2b}$$

$$\kappa_{\mathcal{B}} \equiv \mu\alpha_{\mathcal{B}}. \tag{B.2.2c}$$

For convenience, we define the parameters

$$\zeta_{\mathcal{S}} \equiv \kappa_{\mathcal{S}}/k = \alpha_{\mathcal{S}}/v_{\rm rel}, \tag{B.2.3a}$$

$$\zeta_{\mathcal{B}} \equiv \kappa_{\mathcal{B}}/k = \alpha_{\mathcal{B}}/v_{\rm rel}, \tag{B.2.3b}$$

as well as the space variables

$$x_{\mathcal{S}} \equiv kr, \tag{B.2.4a}$$

$$x_{\mathcal{B}} \equiv \kappa_{\mathcal{B}} r. \tag{B.2.4b}$$

The energy eigenvalues of the scattering and bound states are

$$\mathcal{E}_{\mathbf{k}} = \frac{\mathbf{k^2}}{2\mu} = \frac{\mu v_{\rm rel}^2}{2}, \tag{B.2.5a}$$

$$\mathcal{E}_n = -\frac{\kappa_{\mathcal{B}}^2}{2\mu\, n^2} = -\frac{\mu\alpha_{\mathcal{B}}^2}{2n^2}, \tag{B.2.5b}$$

and the corresponding wavefunctions are[2]

$$\phi_{\mathbf{k}}(\mathbf{r}) = 4\pi\sqrt{S_0(\zeta_{\mathcal{S}})}\sum_{\ell_{\mathcal{S}}=0}^{\infty}\sum_{m_S=-\ell_{\mathcal{S}}}^{\ell_{\mathcal{S}}} Y^*_{\ell_{\mathcal{S}}m_S}(\Omega_{\mathbf{k}})\, Y_{\ell_{\mathcal{S}}m_S}(\Omega_{\mathbf{r}})$$
$$\times\ \frac{(-\mathbb{i}^{\ell_{\mathcal{S}}})}{(2\ell_{\mathcal{S}}+1)!}\,\frac{\Gamma(1+\ell_{\mathcal{S}}-\mathbb{i}\zeta_{\mathcal{S}})}{\Gamma(1-\mathbb{i}\zeta_{\mathcal{S}})}\, e^{-ix_{\mathcal{S}}}\,(2x_{\mathcal{S}})^{\ell_{\mathcal{S}}}\,{}_1F_1(1+\ell_{\mathcal{S}}+\mathbb{i}\zeta_{\mathcal{S}};\ 2\ell_{\mathcal{S}}+2;\ 2\mathbb{i}x_{\mathcal{S}}), \tag{B.2.6a}$$

$$\psi_{n\ell m}(\mathbf{r}) = \kappa_{\mathcal{B}}^{3/2}\, Y_{\ell m}(\Omega_{\mathbf{r}})\,\frac{2}{n^2(2\ell+1)!}\left[\frac{(n+\ell)!}{(n-\ell-1)!}\right]^{1/2}\times$$
$$\times\, e^{-x_{\mathcal{B}}/n}\,\left(\frac{2x_{\mathcal{B}}}{n}\right)^{\ell}{}_1F_1\left(-n+\ell+1;\ 2\ell+2;\ \frac{2x_{\mathcal{B}}}{n}\right), \tag{B.2.6b}$$

where $S_0(\zeta_{\mathcal{S}}) \equiv 2\pi\zeta_{\mathcal{S}}/(1-e^{-2\pi\zeta_{\mathcal{S}}})$, and in eq. (B.2.6b), we have expressed the bound state wavefunction in terms of the confluent hypergeometric function ${}_1F_1$ rather than the Laguerre polynomials. Note that the wavefunctions (B.2.6) assume *distinguishable* interacting particles. We include the necessary (anti)symmetrization factors for identical particles in Sections 3.1 and 3.2, where we discuss the processes of interest.[3]

[2]For the spherical harmonics, we assume the normalisation $\int d\Omega\, Y_{\ell m}(\Omega) Y^*_{\ell' m'}(\Omega) = \delta_{\ell\ell'}\delta_{mm'}$.

[3]For clarity, in Sections 3.1 and 3.2 we denote the wavefunctions of distinguishable particles with the superscript DP. In this appendix, we have omitted this superscript since there is no risk of confusion.

Appendix C

Overlap integrals

C.1 Neutral scalar emission

For the capture into bound states via emission of two scalars, we need to compute the overlap integrals

$$\mathcal{V}_{\mathbf{k},\{n\ell m\}} \equiv (8\pi\kappa)^{1/2} \int \frac{d^3q}{(2\pi)^3} \frac{d^3p}{(2\pi)^3} \frac{\tilde{\phi}_{\mathbf{k}}(\mathbf{q})\tilde{\psi}^*_{n\ell m}(\mathbf{p})}{(\mathbf{q}-\mathbf{p})^2 + m_\varphi^2}\,, \tag{C.1.1}$$

$$\mathcal{R}_{\mathbf{k},\{n\ell m\}} \equiv (8\pi\kappa^5)^{1/2} \int \frac{d^3q}{(2\pi)^3} \frac{d^3p}{(2\pi)^3} \frac{\tilde{\phi}_{\mathbf{k}}(\mathbf{q})\tilde{\psi}^*_{n\ell m}(\mathbf{p})}{[(\mathbf{q}-\mathbf{p})^2 + m_\varphi^2]^2}\,. \tag{C.1.2}$$

We Fourier transform the wavefunctions as follows

$$\psi_{n\ell m}(\mathbf{r}) = \int \frac{d^3p}{(2\pi)^3}\, \tilde{\psi}_{\{n\ell m\}}(\mathbf{p})\, e^{i\mathbf{pr}}, \qquad \tilde{\psi}_{n\ell m}(\mathbf{p}) = \int d^3r\ \psi_{n\ell m}(\mathbf{r}) e^{-i\mathbf{pr}}\,, \tag{C.1.3}$$

$$\phi_{\mathbf{k}}(\mathbf{r}) = \int \frac{d^3p}{(2\pi)^3}\, \tilde{\phi}_{\mathbf{k}}(\mathbf{p})\, e^{i\mathbf{pr}}, \qquad \tilde{\phi}_{\mathbf{k}}(\mathbf{p}) = \int d^3r\ \phi_{\mathbf{k}}(\mathbf{r}) e^{-i\mathbf{pr}}\,. \tag{C.1.4}$$

The overlap integrals become

$$\mathcal{V}_{\mathbf{k},\{n\ell m\}} = \left(\frac{\kappa}{2\pi}\right)^{1/2} \int d^3r\, \phi_{\mathbf{k}}(\mathbf{r}) \psi^*_{n\ell m}(\mathbf{r}) \frac{e^{-m_\varphi r}}{r}, \tag{C.1.5}$$

$$\mathcal{R}_{\mathbf{k},\{n\ell m\}} = \left(\frac{\kappa^5}{8\pi}\right)^{1/2} \frac{1}{m_\varphi} \int d^3r\, \phi_{\mathbf{k}}(\mathbf{r}) \psi^*_{n\ell m}(\mathbf{r})\, e^{-m_\varphi r} \simeq -\left(\frac{\kappa^5}{8\pi}\right)^{1/2} \int d^3r\, \phi_{\mathbf{k}}(\mathbf{r}) \psi^*_{n\ell m}(\mathbf{r})\, r. \tag{C.1.6}$$

In the second step in eq. (C.1.6), we expanded the decaying exponential inside the integral. The bound-state wavefunction implies that the integrand is significant for $r \lesssim n/(\mu\alpha)$ while the kinematic threshold (2.2.7) for BSF imposes $m_\varphi < \mu\alpha^2/(2n^2)$; therefore $m_\varphi r \lesssim \alpha \ll 1$. The zeroth order term in the expansion vanishes due to the orthogonality of the wavefunctions, leaving the first order term to be the dominant contribution. In the following, we will focus on the capture into the ground state, $\{n\ell m\} = \{100\}$.

While in the Coulomb limit ($m_\varphi \to 0$) it is possible to obtain analytical expressions for the integrals eqs. (C.1.5) and (C.1.6), outside the Coulomb regime they should be evaluated numerically. However, it is possible to obtain an analytical approximation, using the Hulthen potential (cf. appendix B). Since $\xi \equiv 2\mu\alpha/m_* \gg 1$ in all the parameter space where BSF is kinematically allowed to occur [cf. eq. (2.2.7)], the bound state wavefunction $\psi_{100}(\mathbf{r})$ can be well approximated by its Coulomb value. On the other hand, the scattering-state wavefunction $\phi_{\mathbf{k}}(\mathbf{r})$

is close to its Coulomb limit for $r \lesssim 1/m_*$, up to an overall normalisation which, for the $\ell_S = 0$ mode, is determined by the factor $S_0(\zeta, \xi)$ of eq. (B.1.20). Since $\xi \gg 1$, this encompasses all the range in which $\psi_{100}(\mathbf{r})$ and therefore the integrands in eqs. (C.1.5) and (C.1.6) are important, $r \lesssim 1/(\mu\alpha)$. It follows that $\mathcal{V}_{\mathbf{k},\{100\}}$ and $\mathcal{R}_{\mathbf{k},\{100\}}$ – which depend only on the $\ell_S = 0$ mode of the scattering state wavefunction – can be well approximated by their Coulomb values even outside the Coulomb regime provided that we replace $S_0^C(\zeta)$ in eq. (B.1.20) with $S_0(\zeta, \xi)$.

Following ref. [95] (see also [43, 59, 62]), we shall use the identity [143]

$$\int d^3r \frac{e^{i(\mathbf{k}-\mathbf{\Gamma})\mathbf{r}-\kappa r}}{4\pi r} {}_1F_1[i\zeta, 1, i(kr - \mathbf{kr})] = \frac{[\mathbf{\Gamma}^2 + (\kappa - ik)^2]^{-i\zeta}}{[(\mathbf{k}-\mathbf{\Gamma})^{\mathbf{2}} + \kappa^2]^{1-i\zeta}} \equiv f_{\mathbf{k},\mathbf{\Gamma}}(\kappa)\,. \tag{C.1.7}$$

Then, eqs. (C.1.5) and (C.1.6) become

$$\mathcal{V}_{\mathbf{k},\{100\}} \simeq +\sqrt{8\kappa^4 S_0(\zeta,\xi)}\; f_{\mathbf{k},\mathbf{\Gamma}=\mathbf{0}}(\kappa)\,, \tag{C.1.8}$$

$$\mathcal{R}_{\mathbf{k},\{100\}} \simeq -\sqrt{2\kappa^8 S_0(\zeta,\xi)}\; \left[\frac{\partial^2 f_{\mathbf{k},\mathbf{\Gamma}=\mathbf{0}}(\kappa)}{\partial\kappa^2}\right]. \tag{C.1.9}$$

Taking into account that $\kappa/k = \zeta$, we arrive at

$$\mathcal{V}_{\mathbf{k},\{100\}} \simeq \sqrt{8S_0(\zeta,\xi)}\left(\frac{\zeta^2}{1+\zeta^2}\right) e^{-2\zeta\,\mathrm{arccot}\,\zeta}\,, \tag{C.1.10}$$

$$\mathcal{R}_{\mathbf{k},\{100\}} \simeq \sqrt{8S_0(\zeta,\xi)}\left(\frac{\zeta^2}{1+\zeta^2}\right)^2 e^{-2\zeta\,\mathrm{arccot}\,\zeta}\,. \tag{C.1.11}$$

C.2 Charged scalar emission: bound-state formation

We are interested in computing the overlap integral

$$\mathcal{R}_{\mathbf{k},n\ell m} \equiv \kappa_{\mathcal{B}}^{3/2} \int d^3r\; \psi^*_{n\ell m}(\mathbf{r})\,\phi_{\mathbf{k}}(\mathbf{r}) \tag{C.2.1}$$

for the wavefunctions of appendix B.2. Note that the prefactor in eq. (C.2.1) has been chosen such that $\mathcal{R}_{\mathbf{k},n\ell m}$ is dimensionless.

Substituting eqs. (B.2.6) into (C.2.1) and performing the angular integration, picks out the $\ell_{\mathcal{S}} = \ell$ mode of the scattering state. Then, setting $t \equiv 2x_{\mathcal{B}}/n = 2\zeta_{\mathcal{B}}x_{\mathcal{S}}/n$, we obtain

$$\begin{aligned}\mathcal{R}_{\mathbf{k},n\ell m} = {}& \frac{\sqrt{S_0(\zeta_{\mathcal{S}})}}{(\zeta_{\mathcal{B}}/n)^\ell}\, Y^*_{\ell m}(\Omega_{\mathbf{k}}) \times \frac{(-\mathbb{i}^\ell)\pi n}{[(2\ell+1)!]^2}\left[\frac{(n+\ell)!}{(n-\ell-1)!}\right]^{1/2} \frac{\Gamma(1+\ell-\mathbb{i}\zeta_{\mathcal{S}})}{\Gamma(1-\mathbb{i}\zeta_{\mathcal{S}})} \\ & \times \int_0^\infty dt\; t^{2\ell+2}\; e^{-\left(1+\frac{\mathbb{i}\,n}{\zeta_{\mathcal{B}}}\right)\frac{t}{2}}\, {}_1F_1\left(1+\ell-n;\; 2\ell+2;\; t\right) {}_1F_1\left(1+\ell+\mathbb{i}\zeta_{\mathcal{S}};\; 2\ell+2;\; \frac{\mathbb{i}\,n}{\zeta_{\mathcal{B}}}t\right).\end{aligned} \tag{C.2.2}$$

The confluent hypergeometric functions ${}_1F_1$ obey the identity [144, section 7.622]

$$\begin{aligned}&\int_0^\infty dt\; t^{c-1}\; e^{-\rho t}\, {}_1F_1\left(a;\; c;\; t\right) {}_1F_1\left(b;\; c;\; \lambda t\right) = \\ &= \Gamma(c)(\rho-1)^{-a}(\rho-\lambda)^{-b}\rho^{a+b-c}\, {}_2F_1\left[a; b; c;\; \lambda(\rho-1)^{-1}(\rho-\lambda)^{-1}\right] \equiv h(\rho; a, b, c, \lambda),\end{aligned} \tag{C.2.3}$$

for $\mathrm{Re}(c) > 0$ and $\mathrm{Re}(\rho) > \mathrm{Re}(\lambda) + 1$, where ${}_2F_1$ is the ordinary hypergeometric function. For a a non-positive integer, ${}_1F_1(a;\; c;\; t)$ is a finite polynomial in t, and we have checked numerically that

eq. (C.2.3) remains valid for $\mathrm{Re}(c) > 0$ and $\mathrm{Re}(\rho) > \mathrm{Re}(\lambda)$, which encompasses the parameter range of interest. Differentiating (C.2.3) over ρ, and setting

$$a = 1 + \ell - n, \tag{C.2.4a}$$
$$b = 1 + \ell + \mathbb{i}\zeta_{\mathcal{S}}, \tag{C.2.4b}$$
$$c = 2\ell + 2, \tag{C.2.4c}$$
$$\rho = 1/2 + \mathbb{i}\, n/(2\zeta_{\mathcal{B}}), \tag{C.2.4d}$$
$$\lambda = \mathbb{i}\, n/\zeta_{\mathcal{B}}, \tag{C.2.4e}$$

we obtain the integral needed to compute the second line of eq. (C.2.2),

$$-\frac{dh}{d\rho} = 2^{2\ell+4} n (2\ell+1)! \left(1 - \frac{\zeta_{\mathcal{S}}}{\zeta_{\mathcal{B}}}\right) \left(\frac{\zeta_{\mathcal{B}}^2/n^2}{1+\zeta_{\mathcal{B}}^2/n^2}\right)^{\ell+2} e^{-2\zeta_{\mathcal{S}} \operatorname{arccot}(\zeta_{\mathcal{B}}/n)} \times {}_2F_1\left(1+\ell-n;\ 1+\ell+\mathbb{i}\zeta_{\mathcal{S}};\ 2\ell+2;\ \frac{4\mathbb{i}\zeta_{\mathcal{B}}/n}{(1+\mathbb{i}\zeta_{\mathcal{B}}/n)^2}\right) e^{\mathbb{i}2(n-\ell-1)\arctan(\zeta_{\mathcal{B}}/n)}. \tag{C.2.5}$$

Note that the hypergeometric function in eq. (C.2.5) is a finite polynomial in its last argument because its first argument of is a non-positive integer, $1+\ell-n \leqslant 0$. The last factor in eq. (C.2.5) is an unimportant overall phase. Combining eqs. (C.2.2) and (C.2.5), we find

$$\begin{aligned}\sum_{m=-\ell}^{\ell} \int d\Omega_{\mathbf{k}}\ |\mathcal{R}_{\mathbf{k},n\ell m}|^2 = {}& \frac{2^{4(\ell+2)}\,\pi^2 n^4}{2\ell+1}\ \frac{(n+\ell)!}{(n-\ell-1)!}\left[\frac{\ell!}{(2\ell)!}\right]^2 \\ & \times \left(1-\frac{\zeta_{\mathcal{S}}}{\zeta_{\mathcal{B}}}\right)^2 \left[S_0(\zeta_{\mathcal{S}}) \prod_{j=1}^{\ell}\left(1+\frac{\zeta_{\mathcal{S}}^2}{j^2}\right)\right] \frac{(\zeta_{\mathcal{B}}^2/n^2)^{\ell+4}}{(1+\zeta_{\mathcal{B}}^2/n^2)^{2\ell+4}}\ e^{-4\zeta_{\mathcal{S}}\operatorname{arccot}(\zeta_{\mathcal{B}}/n)} \\ & \times \left|{}_2F_1\left(1+\ell-n;\ 1+\ell+\mathbb{i}\zeta_{\mathcal{S}};\ 2\ell+2;\ \frac{4\mathbb{i}\zeta_{\mathcal{B}}/n}{(1+\mathbb{i}\zeta_{\mathcal{B}}/n)^2}\right)\right|^2.\end{aligned} \tag{C.2.6}$$

$\mathcal{R}_{\mathbf{k},n\ell m}$ vanishes if $\zeta_{\mathcal{B}} = \zeta_{\mathcal{S}}$, as expected from the orthogonality of the wavefunctions.

C.3 Charged scalar emission: bound-to-bound transitions

We want to compute the overlap integrals defined in eq. (4.3.3e),

$$\begin{aligned}\mathcal{R}_{n'\ell'm',n\ell m}(\alpha'_{\mathcal{B}},\alpha_{\mathcal{B}}) &\equiv \int \frac{d^3\mathbf{p}}{(2\pi)^3}\ \tilde{\varphi}_{n'\ell'm'}(\mathbf{p};\alpha'_{\mathcal{B}})\ \tilde{\varphi}^*_{n\ell m}(\mathbf{p};\alpha_{\mathcal{B}}) \\ &= \int d^3\mathbf{r}\ \varphi_{n'\ell'm'}(\mathbf{r};\alpha'_{\mathcal{B}})\ \varphi^*_{n\ell m}(\mathbf{r};\alpha_{\mathcal{B}}),\end{aligned} \tag{C.3.1}$$

where the position-space bound-level wavefunctions for the potential $V = -\alpha_{\mathcal{B}}/r$ are

$$\varphi_{n\ell m}(\mathbf{r};\alpha_{\mathcal{B}}) = \left(\frac{2\kappa_{\mathcal{B}}}{n}\right)^{\frac{3}{2}} \left[\frac{(n-\ell-1)!}{2n(n+\ell)!}\right]^{\frac{1}{2}} e^{-x_{\mathcal{B}}/n}\ \left(\frac{2x_{\mathcal{B}}}{n}\right)^{\ell} L^{2\ell+1}_{n-\ell-1}\left(\frac{2x_{\mathcal{B}}}{n}\right) Y_{\ell m}(\Omega_{\mathbf{r}}), \tag{C.3.2}$$

with $\kappa_{\mathcal{B}} \equiv \mu\alpha_{\mathcal{B}}$ being the Bohr momentum and $x_{\mathcal{B}} \equiv \kappa_{\mathcal{B}} r$. Inserting eq. (C.3.2) into (C.3.1),

$$\begin{aligned}\mathcal{R}_{n'\ell'm',n\ell m}(\alpha'_{\mathcal{B}},\alpha_{\mathcal{B}}) = {}& \delta_{\ell\ell'}\delta_{mm'}\left[\frac{(n-\ell-1)!}{2n(n+\ell)!}\ \frac{(n'-\ell-1)!}{2n'(n'+\ell)!}\right]^{1/2}\left(\frac{4\kappa_{\mathcal{B}}\kappa'_{\mathcal{B}}}{nn'}\right)^{\ell+3/2} \times \\ & \times \int_0^{\infty} dr\, e^{-(\kappa_{\mathcal{B}}/n+\kappa'_{\mathcal{B}}/n')\,r}\, r^{2\ell+2}\, L^{2\ell+1}_{n-\ell-1}\left(\frac{2\kappa_{\mathcal{B}}r}{n}\right) L^{2\ell+1}_{n'-\ell-1}\left(\frac{2\kappa'_{\mathcal{B}}r}{n'}\right).\end{aligned} \tag{C.3.3}$$

To compute the integral, ee will use the identity [144, section 7.414, item 4]

$$\int_0^\infty dr\, e^{-\rho r} r^a L_q^a(\lambda r) L_{q'}^a(\lambda' r) = \tag{C.3.4}$$
$$= \frac{\Gamma(q+q'+a+1)}{q!q'!} \frac{(b-\lambda)^q\,(b-\lambda')^{q'}}{b^{q+q'+a+1}} {}_2F_1\left(-q,\ -q';\ -q-q'-a;\ \frac{\rho(\rho-\lambda-\lambda')}{(\rho-\lambda)(\rho-\lambda')}\right)$$
$$\equiv h(a,q,q',\lambda,\lambda',\rho),$$

where ${}_2F_1$ is the ordinary hypergeometric function. Equation (C.3.4) holds for $\mathrm{Re}(a) > -1$ and $\mathrm{Re}(\rho) > 0$. The overlap integral (C.3.3) can be expressed in terms of the h function as

$$\mathcal{R}_{n'\ell'm',n\ell m}(\alpha'_{\mathcal{B}},\alpha_{\mathcal{B}}) = \delta_{\ell\ell'}\delta_{mm'}\left[\frac{(n-\ell-1)!}{2n(n+\ell)!}\,\frac{(n'-\ell-1)!}{2n'(n'+\ell)!}\right]^{1/2}\left(\frac{4\kappa_{\mathcal{B}}\kappa'_{\mathcal{B}}}{nn'}\right)^{\ell+3/2}$$
$$\times\left[-\frac{d}{d\rho}h\left(a,q,q',\lambda,\lambda',\rho\right)\right], \tag{C.3.5}$$

with

$$a = 2\ell+1, \quad q^{(\prime)} = n^{(\prime)} - \ell - 1, \quad \lambda^{(\prime)} = 2\kappa_{\mathcal{B}}^{(\prime)}/n^{(\prime)}, \quad \rho = \kappa_{\mathcal{B}}/n + \kappa'_{\mathcal{B}}/n'. \tag{C.3.6}$$

We find

$$\boxed{\begin{aligned}&\mathcal{R}_{n'\ell'm',n\ell m}(\alpha'_{\mathcal{B}},\alpha_{\mathcal{B}}) = \delta_{\ell\ell'}\delta_{mm'}\frac{(-1)^{n-\ell-1}\,(n+n'-1)!}{\sqrt{nn'(n+\ell)!(n'+\ell)!(n-\ell-1)!(n'-\ell-1)!}}\\ &\times\left(\frac{4\alpha_{\mathcal{B}}\alpha'_{\mathcal{B}}}{nn'}\right)^{\ell+3/2}(\alpha_{\mathcal{B}}-\alpha'_{\mathcal{B}})\left(\frac{\alpha_{\mathcal{B}}}{n}-\frac{\alpha'_{\mathcal{B}}}{n'}\right)^{n+n'-2\ell-3}\left(\frac{\alpha_{\mathcal{B}}}{n}+\frac{\alpha'_{\mathcal{B}}}{n'}\right)^{-(n+n'+1)}\\ &\times{}_2F_1\left[1+\ell-n,\ 1+\ell-n',\ 1-n-n',\ \left(\frac{\alpha_{\mathcal{B}}/n+\alpha'_{\mathcal{B}}/n'}{\alpha_{\mathcal{B}}/n-\alpha'_{\mathcal{B}}/n'}\right)^2\right].\end{aligned}} \tag{C.3.7}$$

Note that eq. (C.3.7) vanishes if $\alpha_{\mathcal{B}} = \alpha'_{\mathcal{B}}$ and $n \neq n'$, but is equal to 1 if $\alpha_{\mathcal{B}} = \alpha'_{\mathcal{B}}$ and $n = n'$, due to the orthonormality of the wavefunctions. Equation (C.3.7) is useful for calculating monopole transitions between bound states of different potentials, i.e. for $\alpha_{\mathcal{B}} \neq \alpha'_{\mathcal{B}}$. This result complements the computation of ref. [2] of scattering-to-bound monopole transitions.

For $n = n' = 1$ and $\ell = 0$, we obtain

$$\mathcal{R}_{100,100}(\alpha'_{\mathcal{B}},\alpha_{\mathcal{B}}) = \frac{8(\alpha_{\mathcal{B}}\alpha'_{\mathcal{B}})^{3/2}}{(\alpha_{\mathcal{B}}+\alpha'_{\mathcal{B}})^3}. \tag{C.3.8}$$

Appendix D

Bound-state formation amplitudes

D.1 Vector emission

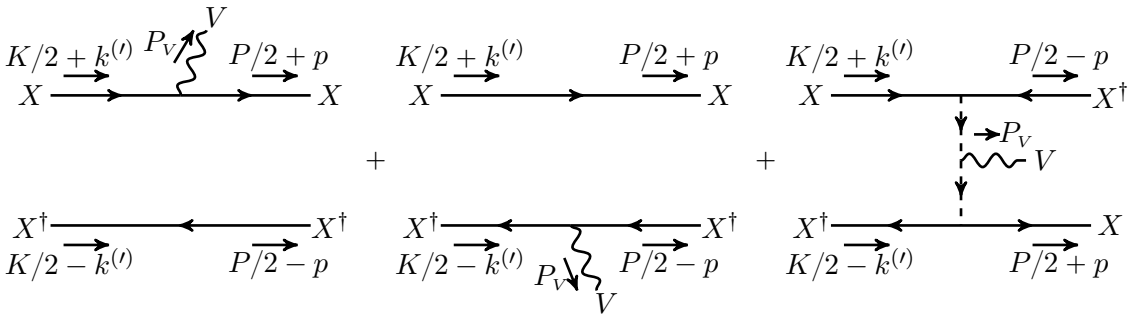

Figure D.1: The leading order contributions to the radiative part of transitions via vector emission $XX^\dagger \to XX^\dagger + V$, in the model of eq. (3.1.1). The arrows on the field lines denote the flow of the $U(1)_D$ charge.

The BSF_V amplitude is Ref. [59]

$$\mathbb{i}\mathcal{M}^V_{\mathbf{k}\to n\ell m} \simeq \int \frac{d^3\mathbf{k}'}{(2\pi)^3}\frac{d^3\mathbf{p}}{(2\pi)^3}\,\tilde{\phi}^{XX^\dagger}_{\mathbf{k}}(\mathbf{k}')\,\mathbb{i}\boldsymbol{\mathcal{A}}^V_T(\mathbf{k}',\mathbf{p})\,\frac{[\tilde{\psi}^{XX^\dagger}_{n\ell m}(\mathbf{p})]^*}{\sqrt{2\mu}}, \tag{D.1.1}$$

where the leading order contributions to the perturbative transition amplitude $\boldsymbol{\mathcal{A}}^V_T(\mathbf{k}',\mathbf{p})$ are shown in Figure D.1. Note that the third diagram does not appear in more minimal $U(1)$ theories where the interacting particles do not couple to a doubly charged scalar. This diagram is akin to the one that appears in non-Abelian theories, where the final-state gluon is radiated from a gluon exchanged between the interacting particles, via the trilinear gluon vertex. Such diagrams seem naively to be of higher order than those with emission directly from one of the interacting particles. However, the momenta exchanged along the propagators scale with the couplings and render these diagrams of the same order as those with emission from the legs Ref. [42]. See also Ref. [1] for analogous contributions arising from couplings in the scalar potential.

Following Ref.[59, 62], we find $\boldsymbol{\mathcal{A}}^V_T(\mathbf{k}',\mathbf{p})$ to be

$$\begin{aligned}\mathbb{i}\boldsymbol{\mathcal{A}}^V_T(\mathbf{k}',\mathbf{p}) \simeq -\mathbb{i}g\Big[&2m_X\,2\mathbf{p}\,(2\pi)^3\delta^3(\mathbf{k}'-\mathbf{p}-\mathbf{P}_V/2)+2m_X\,2\mathbf{p}\,(2\pi)^3\delta^3(\mathbf{k}'-\mathbf{p}+\mathbf{P}_V/2)\\ &+2y^2M\mu\,\frac{2(\mathbf{k}'+\mathbf{p})}{[(\mathbf{k}'+\mathbf{p})^2+m_\Phi^2]^2}\Big],\end{aligned} \tag{D.1.2}$$

where we took into account that $q_X = 1$ and $q_\Phi = 2$. Following Ref. [62], we define

$$\boldsymbol{\mathcal{J}}_{\mathbf{k},n\ell m}(\mathbf{b}) \equiv \int \frac{d^3p}{(2\pi)^3}\, \mathbf{p}\, [\tilde{\psi}^{XX^\dagger}_{n\ell m}(\mathbf{p})]^*\, \tilde{\phi}^{XX^\dagger}_{\mathbf{k}}(\mathbf{p}+\mathbf{b}) = \mathbb{i} \int d^3r\, [\nabla \psi^{XX^\dagger}_{n\ell m}(\mathbf{r})]^*\, \phi^{XX^\dagger}_{\mathbf{k}}(\mathbf{r})\, e^{-\mathbb{i}\mathbf{b}\cdot\mathbf{r}}, \tag{D.1.3a}$$

$$\begin{aligned}\boldsymbol{\mathcal{Y}}_{\mathbf{k},n\ell m} &\equiv 8\pi\mu\alpha_\Phi \int \frac{d^3k'}{(2\pi)^3}\frac{d^3p}{(2\pi)^3}\, \frac{\mathbf{k}'-\mathbf{p}}{(\mathbf{k}'-\mathbf{p})^4}\, [\tilde{\psi}^{XX^\dagger}_{n\ell m}(\mathbf{p})]^*\, \tilde{\phi}^{XX^\dagger}_{\mathbf{k}}(\mathbf{k}') \\ &= -\mathbb{i}\mu\alpha_\Phi \int d^3r\, [\psi^{XX^\dagger}_{n\ell m}(\mathbf{r})]^*\, \phi^{XX^\dagger}_{\mathbf{k}}(\mathbf{r})\, \hat{\mathbf{r}}.\end{aligned} \tag{D.1.3b}$$

Then, the amplitude in eq. (D.1.1) becomes

$$\mathbb{i}\boldsymbol{\mathcal{M}}^V_{\mathbf{k}\to n\ell m} \simeq -\mathbb{i}g\, \frac{4M}{\sqrt{2\mu}} \left[\frac{1}{2}\boldsymbol{\mathcal{J}}_{\mathbf{k},n\ell m}(\mathbf{P}_V/2) + \frac{1}{2}\boldsymbol{\mathcal{J}}_{\mathbf{k},n\ell m}(-\mathbf{P}_V/2) + \frac{(-1)^\ell y^2}{8\pi\alpha_\Phi}\, \boldsymbol{\mathcal{Y}}_{\mathbf{k},n\ell m}\right], \tag{D.1.4}$$

where energy-momentum conservation sets $|\mathbf{P}_V| = \mu(\alpha_\mathcal{B}^2 + v_{\rm rel}^2)/2$ [cf. eq. (3.1.11)]. The leading order terms in the $\boldsymbol{\mathcal{J}}$ integrals are the zeroth order terms in the $\mathbf{P}_V$ expansion Ref. [43]. For capture into the ground state, both the $\boldsymbol{\mathcal{J}}$ and the $\boldsymbol{\mathcal{Y}}$ contributions arise from the $\ell_S = 1$ mode of the scattering state wave function Ref. [43, 62]. In the Coulomb limit Ref. [62]

$$\boldsymbol{\mathcal{J}}_{\mathbf{k},100}(\mathbf{0}) = \hat{\mathbf{k}} \left(\frac{2^6\pi}{k}\, S_0(\zeta_\mathcal{S})\, (1+\zeta_\mathcal{S}^2)\, \frac{\zeta_\mathcal{B}^5\, e^{-4\zeta_\mathcal{S}\,\mathrm{arccot}(\zeta_\mathcal{B})}}{(1+\zeta_\mathcal{B}^2)^4}\right)^{1/2}, \tag{D.1.5a}$$

$$\boldsymbol{\mathcal{Y}}_{\mathbf{k},100} = (\alpha_\Phi/\alpha_\mathcal{B})\, \boldsymbol{\mathcal{J}}_{\mathbf{k},100}(\mathbf{0}), \tag{D.1.5b}$$

where $\zeta_\mathcal{S} \equiv \alpha_\mathcal{S}/v_{\rm rel}$ for the scattering state, $\zeta_\mathcal{B} \equiv \alpha_\mathcal{B}/v_{\rm rel}$ for the bound state, and $S_0(\zeta_\mathcal{S}) \equiv 2\pi\zeta_\mathcal{S}/(1-e^{-2\pi\zeta_\mathcal{S}})$. Considering the potential (3.1.3b), for the process of interest we find

$$\zeta_\mathcal{S} = \zeta_V - \zeta_\Phi \qquad \text{and} \qquad \zeta_\mathcal{B} = \zeta_V + \zeta_\Phi. \tag{D.1.6}$$

Collecting the above, we find the amplitude for capture into the ground state to be

$$|\boldsymbol{\mathcal{M}}^V_{\mathbf{k}\to 100}|^2 \simeq \frac{M^2}{\mu}\alpha_V \left(1+\frac{2\alpha_\Phi}{\alpha_\mathcal{B}}\right)^2\, \frac{2^{11}\pi^2}{k}\, S_0(\zeta_\mathcal{S})\, (1+\zeta_\mathcal{S}^2)\, \frac{\zeta_\mathcal{B}^5\, e^{-4\zeta_\mathcal{S}\,\mathrm{arccot}(\zeta_\mathcal{B})}}{(1+\zeta_\mathcal{B}^2)^4}. \tag{D.1.7}$$

Then, the cross-section Ref. [59, 62]

$$\sigma^V_{100} v_{\rm rel} = \frac{|\mathbf{P}_V|}{2^6\pi^2 M^2 \mu} \int d\Omega \left(|\boldsymbol{\mathcal{M}}^V_{\mathbf{k}\to 100}|^2 - |\hat{\mathbf{P}}_V \cdot \boldsymbol{\mathcal{M}}^V_{\mathbf{k}\to 100}|^2\right) \tag{D.1.8}$$

is found to be

$$\sigma^V_{100} v_{\rm rel} = \frac{2^7\pi}{3\mu^2}\alpha_V\alpha_\mathcal{B} \left(1+\frac{2\alpha_\Phi}{\alpha_\mathcal{B}}\right)^2\, S_0(\zeta_\mathcal{S})\, (1+\zeta_\mathcal{S}^2)\, \frac{\zeta_\mathcal{B}^4}{(1+\zeta_\mathcal{B}^2)^3}\, e^{-4\zeta_\mathcal{S}\mathrm{arccot}(\zeta_\mathcal{B})}. \tag{D.1.9}$$

Note that eq. (D.1.9) holds also for fermionic DM. This has been already established for the two diagrams on the left of Figure D.1. In the third diagram, the contraction of two spinor pairs due to the two fermion-antifermion-scalar vertices gives rise to an extra factor 2^2. Combined with the fact that $y^2 = 4\pi\alpha_\Phi$ for fermions Ref. [1, appendix A], reproduces eq. (D.1.9).

Despite the different potentials in the initial and final states – which in fact occur commonly in BSF_V in non-Abelian theories where the emitted gauge vector boson carries away non-Abelian charge Ref. [62] – BSF_V is suppressed by $\alpha_\mathcal{B}^2$ with respect to the BSF_Φ processes computed in section 3.1, due to the momentum dependence of the vector emission vertices. (For the third diagram of fig. D.1, and its interference with the other two diagrams, the suppression is actually of order α_Φ^2 and $\alpha_\Phi\alpha_\mathcal{B}$ respectively, at the level of the cross-section.).

D.2 Perturbative transition amplitudes: an example

We demonstrate the calculation of diagrams contributing to the perturbative part of the transition amplitudes of section 4.3. We will work out in detail the diagram shown in fig. D.2.

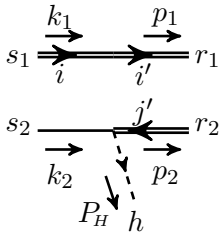

Figure D.2: Example of diagram contributing to the perturbative parts of the amplitudes of various transition processes considered in section 4.3.

We first express the fields in canonical form, following [140],

$$H_j(x) = \int \frac{d^3q}{(2\pi)^3} \frac{1}{\sqrt{2E_H(\mathbf{q})}} \left[a_j(\mathbf{q})\, e^{-\mathbb{i}q\cdot x} + b_j^\dagger(\mathbf{q})\, e^{+\mathbb{i}q\cdot x} \right], \tag{D.2.1a}$$

$$H_j^\dagger(x) = \int \frac{d^3q}{(2\pi)^3} \frac{1}{\sqrt{2E_H(\mathbf{q})}} \left[b_j(\mathbf{q})\, e^{-\mathbb{i}q\cdot x} + a_j^\dagger(\mathbf{q})\, e^{+\mathbb{i}q\cdot x} \right], \tag{D.2.1b}$$

$$S(x) = \int \frac{d^3q}{(2\pi)^3} \frac{1}{\sqrt{2E_S(\mathbf{q})}} \sum_s \left[c(\mathbf{q},s)\, u(\mathbf{q},s) e^{-\mathbb{i}q\cdot x} + c^\dagger(\mathbf{q},s)\, v(\mathbf{q},s) e^{+\mathbb{i}q\cdot x} \right], \tag{D.2.1c}$$

$$\bar{S}(x) = \int \frac{d^3q}{(2\pi)^3} \frac{1}{\sqrt{2E_S(\mathbf{q})}} \sum_s \left[c(\mathbf{q},s)\, \bar{v}(\mathbf{q},s) e^{-\mathbb{i}q\cdot x} + c^\dagger(\mathbf{q},s)\, \bar{u}(\mathbf{q},s) e^{+\mathbb{i}q\cdot x} \right], \tag{D.2.1d}$$

$$D_j(x) = \int \frac{d^3q}{(2\pi)^3} \frac{1}{\sqrt{2E_D(\mathbf{q})}} \sum_s \left[d_j(\mathbf{q},s)\, u(\mathbf{q},s) e^{-\mathbb{i}q\cdot x} + f_j^\dagger(\mathbf{q},s)\, v(\mathbf{q},s) e^{+\mathbb{i}q\cdot x} \right], \tag{D.2.1e}$$

$$\bar{D}_j(x) = \int \frac{d^3q}{(2\pi)^3} \frac{1}{\sqrt{2E_D(\mathbf{q})}} \sum_s \left[f_j(\mathbf{q},s)\, \bar{v}(\mathbf{q},s) e^{-\mathbb{i}q\cdot x} + d_j^\dagger(\mathbf{q},s)\, \bar{u}(\mathbf{q},s) e^{+\mathbb{i}q\cdot x} \right], \tag{D.2.1f}$$

where j is the $SU_L(2)$ index, and the various q^0 inside the integrals are equal to the corresponding on-shell energies,

$$E_H(\mathbf{q}) = \sqrt{m_H^2 + \mathbf{q}^2}, \qquad E_S(\mathbf{q}) = E_D(\mathbf{q}) = \sqrt{m^2 + \mathbf{q}^2}. \tag{D.2.2}$$

The creation and annihilation operators obey the (anti)commutation relations

$$[a_i(\mathbf{p}), a_j^\dagger(\mathbf{q})] = [b_i(\mathbf{p}), b_j^\dagger(\mathbf{q})] = (2\pi)^3 \delta^3(\mathbf{p}-\mathbf{q})\, \delta_{ij}, \tag{D.2.3a}$$

$$\{c(\mathbf{p},r), c^\dagger(\mathbf{q},s)\} = (2\pi)^3 \delta^3(\mathbf{p}-\mathbf{q})\, \delta_{rs}, \tag{D.2.3b}$$

$$\{d_i(\mathbf{p},r), d_j^\dagger(\mathbf{q},s)\} = \{f_i(\mathbf{p},r), f_j^\dagger(\mathbf{q},s)\} = (2\pi)^3 \delta^3(\mathbf{p}-\mathbf{q})\, \delta_{rs}\, \delta_{ij}, \tag{D.2.3c}$$

with all other combinations being zero. The one-particle states are

$$|H_j(\mathbf{q})\rangle = \sqrt{2E_H(\mathbf{q})}\, a_j^\dagger(\mathbf{q},s)|0\rangle, \qquad |H_j^\dagger(\mathbf{q})\rangle = \sqrt{2E_H(\mathbf{q})}\, b_j^\dagger(\mathbf{q},s)|0\rangle, \tag{D.2.4a}$$

$$|S(\mathbf{q},s)\rangle = \sqrt{2E_S(\mathbf{q})}\, c^\dagger(\mathbf{q},s)|0\rangle, \tag{D.2.4b}$$

$$|D_j(\mathbf{q},s)\rangle = \sqrt{2E_D(\mathbf{q})}\, d_j^\dagger(\mathbf{q},s)|0\rangle, \qquad |\bar{D}_j(\mathbf{q},s)\rangle = \sqrt{2E_D(\mathbf{q})}\, f_j^\dagger(\mathbf{q},s)|0\rangle. \tag{D.2.4c}$$

We now return to the diagram of fig. D.2. Its contribution to an amplitude is

$$
\begin{aligned}
&(2\pi)^4\delta^4(k_1+k_2-p_1-p_2-P_H)\,\mathbb{i}\mathcal{A}[DS\to D\bar{D}H]\simeq\\
&\simeq\langle D_{i'}(\mathbf{p}_1,r_1)\,\bar{D}_{j'}(\mathbf{p}_2,r_2)\,H_h(\mathbf{P}_H)|\;(-\mathbb{i}y)\int d^4x\,\bar{S}(x)H^\dagger(x)D(x)\;|D_i(\mathbf{k}_1,s_1)\,S(\mathbf{k}_2,s_2)\rangle\\
&=(-\mathbb{i}y)\sum_{t_S,t_D}\sum_n\int d^4x\int\frac{d^3q_S}{(2\pi)^3}\frac{d^3q_H}{(2\pi)^3}\frac{d^3q_{\bar{D}}}{(2\pi)^3}\frac{\sqrt{2E_D(\mathbf{k}_1)\,2E_S(\mathbf{k}_2)\,2E_D(\mathbf{p}_1)\,2E_D(\mathbf{p}_2)\,2E_H(\mathbf{P}_H)}}{\sqrt{2E_S(\mathbf{q}_S)\,2E_H(\mathbf{q}_H)\,2E_D(\mathbf{q}_{\bar{D}})}}\\
&\times\langle 0|a_h(\mathbf{P}_H)f_{j'}(\mathbf{p}_2,r_2)d_{i'}(\mathbf{p}_1,r_1)\left[c(\mathbf{q}_S,t_S)\,\bar{v}(\mathbf{q}_S,t_S)\,e^{-\mathbb{i}q_S\cdot x}+c^\dagger(\mathbf{q}_S,t_S)\,\bar{u}(\mathbf{q}_S,t_S)\,e^{+\mathbb{i}q_S\cdot x}\right]\\
&\times\left[b_n(\mathbf{q}_H)\,e^{-\mathbb{i}q_H\cdot x}+a_n^\dagger(\mathbf{q}_H)\,e^{+\mathbb{i}q_H\cdot x}\right]\\
&\times\left[d_n(\mathbf{q}_{\bar{D}},t_{\bar{D}})\,u(\mathbf{q}_{\bar{D}},t_{\bar{D}})\,e^{-\mathbb{i}q_{\bar{D}}\cdot x}+f_n^\dagger(\mathbf{q}_{\bar{D}},t_{\bar{D}})\,v(\mathbf{q}_{\bar{D}},t_{\bar{D}})\,e^{+\mathbb{i}q_{\bar{D}}\cdot x}\right]d_i^\dagger(\mathbf{k}_1,s_1)c^\dagger(\mathbf{k}_2,s_2)|0\rangle\\
&=(-\mathbb{i}y)\sum_{t_S,t_{\bar{D}}}\sum_n\int d^4x\int\frac{d^3q_S}{(2\pi)^3}\frac{d^3q_H}{(2\pi)^3}\frac{d^3q_{\bar{D}}}{(2\pi)^3}\frac{\sqrt{2E_D(\mathbf{k}_1)\,2E_S(\mathbf{k}_2)\,2E_D(\mathbf{p}_1)\,2E_D(\mathbf{p}_2)\,2E_H(\mathbf{P}_H)}}{\sqrt{2E_S(\mathbf{q}_S)\,2E_H(\mathbf{q}_H)\,2E_D(\mathbf{q}_{\bar{D}})}}\\
&\times\;\;e^{-\mathbb{i}(q_S-q_H-q_{\bar{D}})x}\times(-1)^2(2\pi)^3\delta^3(\mathbf{k}_2-\mathbf{q}_S)\delta_{t_Ss_2}\,\bar{v}(\mathbf{q}_S,t_S)\times(2\pi)^3\delta^3(\mathbf{P}_H-\mathbf{q}_H)\delta_{hn}\\
&\times(-1)(2\pi)^3\delta^3(\mathbf{p}_2-\mathbf{q}_{\bar{D}})\delta_{t_{\bar{D}}r_2}\delta_{j'n}\,v(\mathbf{q}_{\bar{D}},t_{\bar{D}})\times(2\pi)^3\delta^3(\mathbf{k}_1-\mathbf{p}_1)\delta_{s_1r_1}\delta_{ii'}\\
&=(-1)^3(-\mathbb{i}y)\delta_{s_1r_1}\delta_{ii'}\delta_{hj'}\,\bar{v}(\mathbf{k}_2,s_2)\,v(\mathbf{p}_2,r_2)\sqrt{2E_D(\mathbf{k}_1)\,2E_D(\mathbf{p}_1)}(2\pi)^3\delta^3(\mathbf{k}_1-\mathbf{p}_1)\\
&\times\int d^4x\;e^{-\mathbb{i}(k_2-P_H-p_2)x},
\end{aligned}
\tag{D.2.5}
$$

where in the third step, we did the following contractions, in order,

- $c(\mathbf{q}_S,t_S)$ with $c^\dagger(\mathbf{k}_2,s_2)$,
- $a_n^\dagger(\mathbf{q}_H)$ with $a_h(\mathbf{P}_H)$,
- $f_n^\dagger(\mathbf{q}_{\bar{D}},t_{\bar{D}})$ with $f_{j'}(\mathbf{p}_2,r_2)$,
- $d_i^\dagger(\mathbf{k}_1,s_1)$ with $d_{i'}(\mathbf{p}_1,r_1)$,

and accounted for the signs arising from the permutations of the fermion operators. Considering that $|\mathbf{k}_2-\mathbf{p}_2|=|\mathbf{P}_H|\ll|\mathbf{k}_2|,|\mathbf{p}_2|$, we may set $\bar{v}(\mathbf{k}_2,s_2)\,v(\mathbf{p}_2,r_2)\simeq-2m\delta_{s_2r_2}$. Moreover, we do the following manipulation[1]

$$
\begin{aligned}
(2\pi)^3\delta^3(\mathbf{k}_1-\mathbf{p}_1)\int d^4x\;e^{-\mathbb{i}(k_2-P_H-p_2)x}&=(2\pi)^3\delta^3(\mathbf{k}_1-\mathbf{p}_1)\int d^4x\;e^{-\mathbb{i}(k_1+k_2-P_H-p_1-p_2)x}\\
&=(2\pi)^4\delta^4(k_1+k_2-P_H-p_1-p_2)(2\pi)^3\delta^3(\mathbf{k}_1-\mathbf{p}_1).
\end{aligned}
\tag{D.2.6}
$$

Finally, setting $E_D(\mathbf{k}_1)=E_D(\mathbf{p}_1)\simeq m$, eq. (D.2.5) yields

$$
\mathbb{i}\mathcal{A}[DS\to D\bar{D}H]\simeq(-\mathbb{i}y)\delta_{s_1r_1}\delta_{s_2r_2}\delta_{ii'}\delta_{hj'}\,4m^2(2\pi)^3\delta^3(\mathbf{k}_1-\mathbf{p}_1).
\tag{D.2.7}
$$

[1]Because the diagram of fig. D.2 is disconnected when considered alone, the energy-momentum conservation on the vertex suggests that it vanishes. This is an artifact of having set the incoming and outgoing D, $\bar{D}$ and S particles on shell. In reality, because of their interactions along the ladders (cf. fig. 4.4), the propagating fields are not exactly on-shell. A method for integrating out the virtuality of these particles has been suggested in [59] and employed e.g. in [1, 62].

D.3 Scalar emission via vector-scalar fusion

In many of the BSF processes considered in this work, the radiative parts of the amplitudes receive contributions from diagrams where off-shell vector and Higgs bosons fuse to produce the on-shell radiated Higgs boson; one such diagram is pictured in fig. D.3. These diagrams resemble the ones where an on-shell vector is emitted from an off-shell vector or scalar mediator exchanged between the interacting particles (cf. figs. 4.5 to 4.8.) This suggests that they may be significant. Here we show that the diagrams of the type of fig. D.3 are of higher order than those featuring emission of a vector from an off-shell mediator. Moreover, BSF via vector emission is of higher order than BSF via emission of a charged scalar [2]. Thus, the Higgs emission diagrams of the type of fig. D.3 are very subdominant.

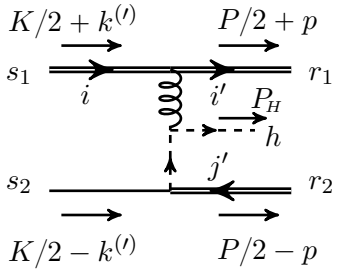

Figure D.3: Scalar emission via vector-scalar fusion.

The contribution from the diagram of fig. D.3 is

$$\begin{aligned} \mathbb{i}\mathcal{A} = \bar{u}(P/2+p, r_1)\, \mathbb{i} g_2 \gamma^\mu t^a_{i'i}\, u(K/2+k', s_1) \left[\frac{-\mathbb{i} g_{\mu\nu}}{(k'-p+P_H/2)^2} \right] \\ \times \mathbb{i} g_2 t^a_{j'j} (3P_H/2 - k' + p)^\nu \, \frac{\mathbb{i}}{(k'-p-P_H/2)^2 - m_H^2} \, \bar{v}(K/2-k, s_2)(-\mathbb{i} y) v(P/2-p). \end{aligned} \tag{D.3.1}$$

Applying the standard approximations due to the scale hierarchies, the above becomes

$$\mathbb{i}\mathcal{A} \simeq \mathbb{i} g_2^2 y\, t^a_{i'i} t^a_{j'j}\, 2m \frac{(k'-p-P_H/2)\cdot[(K+P)/2 + k' + p]}{(\mathbf{k}'-\mathbf{p})^2[(\mathbf{k}'-\mathbf{p})^2 + m_H^2]}. \tag{D.3.2}$$

The 4-vector product in the numerator is of order $\sim m^2(\alpha_s^2 + v_{\rm rel}^2)$, which renders eq. (D.3.2) of higher order than eqs. (4.3.14) and (4.3.18), and even more so that eqs. (4.3.21).

Appendix E

Kernel and wavefunction (anti)symmetrisation for identical particles

E.1 The 2PI kernel

For identical particle (IP) pairs, t-channel diagrams have u-channel counterparts. However, adding them up and resumming them double-counts the loop diagrams because it corresponds to exchanging identical particles in the loops. The proper resummation necessitates using an (anti-)symmetrised kernel, as we will now show. Note that this holds not only for tree-level 2PI diagrams, but more generally for 2PI diagrams involving loops in t- and u-type configurations.

We consider the 4-point function of a pair of identical particles, $G^{\text{IP}}\left(\begin{smallmatrix} p, & s_A, & s_B \\ p', & s'_A, & s'_B \end{smallmatrix}\right)$, where the momentum and spin assignments are shown in fig. E.1. To ease the notation, the dependence of G^{IP} on the total momentum P is left implicit. Let $\mathcal{A}$ be a function of the same variables that stands for the sum of either the t- or u-type 2PI diagrams. Clearly,

$$\mathcal{A}\left(\begin{smallmatrix} p, & s_A, & s_B \\ p', & s'_A, & s'_B \end{smallmatrix}\right) = \mathcal{A}\left(\begin{smallmatrix} -p, & s_B, & s_A \\ -p', & s'_B, & s'_A \end{smallmatrix}\right). \tag{E.1.1a}$$

Then, the sum of complementary 2PI diagrams (u- or t-type respectively) is

$$(-1)^f \mathcal{A}\left(\begin{smallmatrix} p, & s_A, & s_B \\ -p', & s'_B, & s'_A \end{smallmatrix}\right) = (-1)^f \mathcal{A}\left(\begin{smallmatrix} -p, & s_B, & s_A \\ p', & s'_A, & s'_B \end{smallmatrix}\right), \tag{E.1.1b}$$

where $f = 0$ or 1 if the interacting particles are bosons or fermions. This factor arises from the different number of fermion permutations needed in the t- and u-type cases, in order to perform the Wick contractions.

The 4-point function G^{IP} includes the two ladders shown in the two columns of fig. E.1. These ladders are related by exchanging the momenta and spins of the initial (or final) state particles, thus we may write

$$G^{\text{IP}}\left(\begin{smallmatrix} p, & s_A, & s_B \\ p', & s'_A, & s'_B \end{smallmatrix}\right) = G_0^{\text{IP}}\left(\begin{smallmatrix} p, & s_A, & s_B \\ p', & s'_A, & s'_B \end{smallmatrix}\right) + (-1)^f G_0^{\text{IP}}\left(\begin{smallmatrix} -p, & s_B, & s_A \\ p', & s'_A, & s'_B \end{smallmatrix}\right). \tag{E.1.2}$$

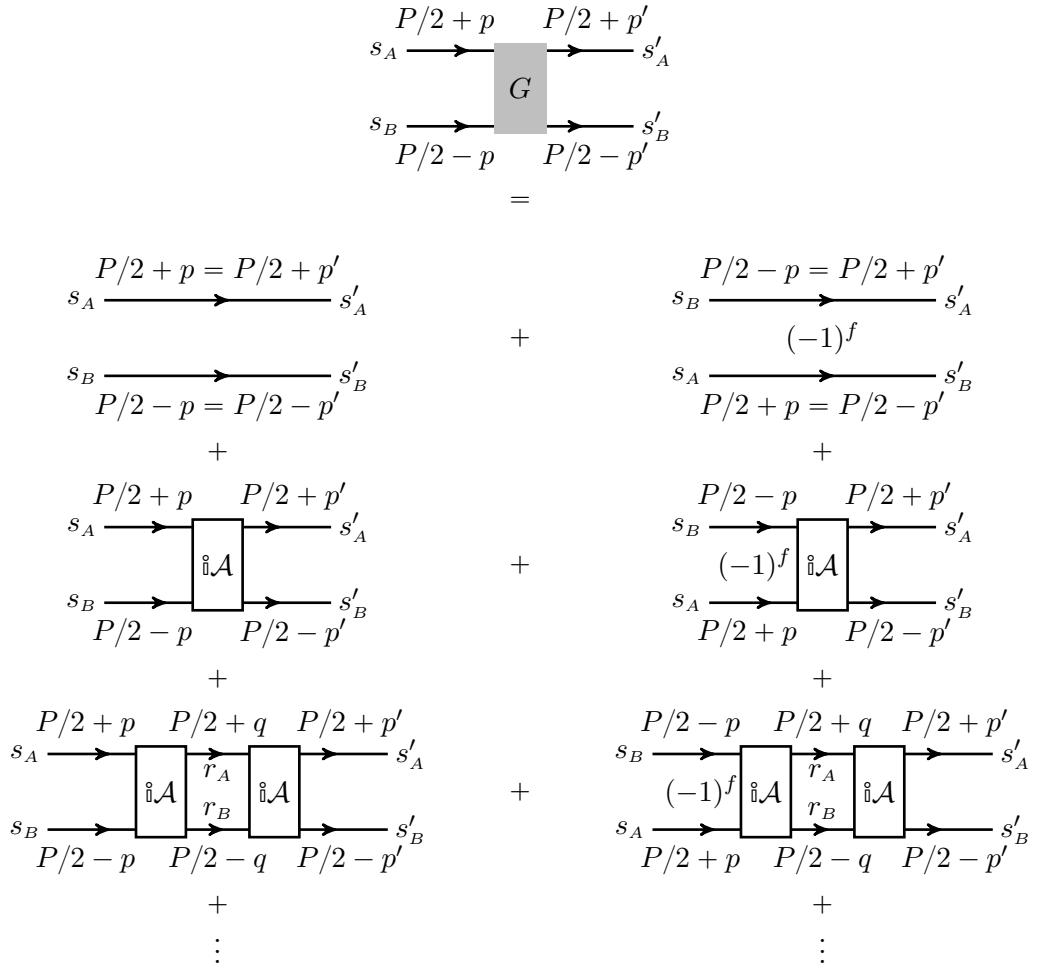

Figure E.1: Resummation of t-type (*left*) and u-type (*right*) 2PI diagrams for pairs of identical particles. Summation over r_A, r_B and integration over q is implied. The u-type diagrams carry extra factors $(-1)^f$ with respect to their t-type counterparts, where $f = 0$ or 1 if the interacting particles are bosons or fermions respectively, due to the different number of fermion permutations needed to perform the Wick contractions.

Let $S(P) \equiv \mathbb{i}/(P^2 - m^2)$. The unamputated function G_0 is

$$\begin{aligned} G_0^{\text{IP}} \begin{pmatrix} p,\, s_A, s_B \\ p',\, s'_A, s'_B \end{pmatrix} &= S(P/2+p')S(P/2-p')\ (2\pi)^4\delta^{(4)}(p-p')\ \delta_{s_A,s'_A}\delta_{s_B,s'_B} \\ &+ S(P/2+p')S(P/2-p')\,\mathbb{i}\mathcal{A}\begin{pmatrix} p,\, s_A, s_B \\ p',\, s'_A, s'_B \end{pmatrix}\ S(P/2+p)S(P/2-p) \\ &+ S(P/2+p')S(P/2-p')\sum_{r_A,r_B}\int\frac{d^4q}{(2\pi)^4}\mathbb{i}\mathcal{A}\begin{pmatrix} q,\, r_A, r_B \\ p',\, s'_A, s'_B \end{pmatrix} S(P/2+q)S(P/2-q) \\ &\times \mathbb{i}\mathcal{A}\begin{pmatrix} p, s_A, s_B \\ q, r_A, r_B \end{pmatrix}\ S(P/2+p)\,S(P/2-p) + \cdots . \end{aligned} \tag{E.1.3}$$

Equation (E.1.3) can be re-expressed as a Dyson-Schwinger equation with $\mathcal{A}$ being the kernel,

$$\begin{aligned} G_0^{\text{IP}} \begin{pmatrix} p,\, s_A, s_B \\ p',\, s'_A, s'_B \end{pmatrix} &= S(P/2+p')\,S(P/2-p')\times \\ \times \left[(2\pi)^4\delta^{(4)}(p-p')\ \delta_{s_A,s'_A}\delta_{s_B,s'_B} + \sum_{r_A,r_B}\int\frac{d^4q}{(2\pi)^4}\,\mathbb{i}\mathcal{A}\begin{pmatrix} p, s_A, s_B \\ q, r_A, r_B \end{pmatrix}\ G_0^{\text{IP}}\begin{pmatrix} q,\, r_A, r_B \\ p',\, s'_A, s'_B \end{pmatrix}\right]. \end{aligned} \tag{E.1.4}$$

In eq. (E.1.4), we can change the integration variable $q \to -q$ and switch $r_A \leftrightarrow r_B$. Adding up the resulting equation with eq. (E.1.4), we obtain

$$G_0^{\mathrm{IP}}\left(\begin{smallmatrix} p,\, s_A, s_B \\ p', s'_A, s'_B \end{smallmatrix}\right) = S(P/2+p')\,S(P/2-p') \times \Big\{(2\pi)^4\delta^{(4)}(p-p')\,\delta_{s_A,s'_A}\delta_{s_B,s'_B} + \frac{1}{2}\sum_{r_A,r_B}\int\frac{d^4q}{(2\pi)^4}\Big[\mathbb{i}\mathcal{A}\left(\begin{smallmatrix} p, s_A, s_B \\ q, r_A, r_B \end{smallmatrix}\right) G_0^{\mathrm{IP}}\left(\begin{smallmatrix} q,\, r_A, r_B \\ p', s'_A, s'_B \end{smallmatrix}\right) + \mathbb{i}\mathcal{A}\left(\begin{smallmatrix} p,\, s_A, s_B \\ -q, r_B, r_A \end{smallmatrix}\right) G_0^{\mathrm{IP}}\left(\begin{smallmatrix} -q, r_B, r_A \\ p',\, s'_A, s'_B \end{smallmatrix}\right)\Big]. \tag{E.1.5}$$

Combining eqs. (E.1.1), (E.1.2) and (E.1.5), we obtain the Dyson-Schwinger equation for G,

$$\begin{aligned} G^{\mathrm{IP}}\left(\begin{smallmatrix} p,\, s_A, s_B \\ p', s'_A, s'_B \end{smallmatrix}\right) &= S(P/2+p')\,S(P/2-p')\times \\ &\times\Big[(2\pi)^4\delta^{(4)}(p-p')\,\delta_{s_A,s'_A}\delta_{s_B,s'_B} + (-1)^f(2\pi)^4\delta^{(4)}(p+p')\,\delta_{s_A,s'_B}\delta_{s_A,s'_B} \\ &+ \sum_{r_A,r_B}\int\frac{d^4q}{(2\pi)^4}\,\mathbb{i}\mathcal{K}\left(\begin{smallmatrix} p, s_A, s_B \\ q, r_A, r_B \end{smallmatrix}\right) G^{\mathrm{IP}}\left(\begin{smallmatrix} q,\, r_A, r_B \\ p', s'_A, s'_B \end{smallmatrix}\right)\Big], \end{aligned} \tag{E.1.6}$$

where we defined

$$\mathbb{i}\mathcal{K}\left(\begin{smallmatrix} p, s_A, s_B \\ q, r_A, r_B \end{smallmatrix}\right) \equiv \frac{1}{2}\Big[\mathbb{i}\mathcal{A}\left(\begin{smallmatrix} p, s_A, s_B \\ q, r_A, r_B \end{smallmatrix}\right) + (-1)^f\mathbb{i}\mathcal{A}\left(\begin{smallmatrix} -p, s_B, s_A \\ q,\, r_A, r_B \end{smallmatrix}\right)\Big]. \tag{E.1.7}$$

Evidently, eq. (E.1.7) is the average of the t- and u-type 2PI diagrams,

$$\mathbb{i}\mathcal{K} = \frac{1}{2}\left(\mathbb{i}\mathcal{A}_t + \mathbb{i}\mathcal{A}_u\right). \tag{E.1.8}$$

The factor $1/2$ ensures that the loop diagrams are not double-counted. From eq. (E.1.7), we can also deduce the following relation

$$\mathbb{i}\mathcal{K}\left(\begin{smallmatrix} p, s_A, s_B \\ q, r_A, r_B \end{smallmatrix}\right) = (-1)^f\mathbb{i}\mathcal{K}\left(\begin{smallmatrix} p,\, s_A, s_B \\ -q, r_B, r_A \end{smallmatrix}\right), \tag{E.1.9}$$

which we use below in the discussion on the (anti-)symmetrisation of the wavefunctions.

Finally, we note that if the interacting particles carry additional conserved numbers, e.g. non-Abelian (gauge) charges, then appropriate factors ensuring their conservation may appear in the 0th order terms of eq. (E.1.6), as well as inside $\mathcal{A}$ and consequently $\mathcal{K}$. However, eq. (E.1.8) remains generally valid as is.

E.2 Wavefunctions

The 0th order terms of the Dyson-Schwinger equations determine the normalisation of the wavefunctions (see e.g. [59, 145].) The two contributions appearing in the second line of eq. (E.1.6) ensure that the wavefunctions of identical particles are properly (anti)symmetrised, as we will now show. Instead of deriving the normalisation conditions from eq. (E.1.6), we shall deduce them by comparing to the case of distinguishable particles (DP), whose wavefunctions are normalised as standard [59, 145].

For DP with equal masses, and incoming and outgoing momenta and spins as in fig. E.1, the Dyson-Schwinger eq. for the four-point function G^{DP} is (compare with eq. (E.1.6))

$$\begin{aligned} G^{\mathrm{DP}}\left(\begin{smallmatrix} p,\, s_A, s_B \\ p', s'_A, s'_B \end{smallmatrix}\right) &= S(P/2+p')\,S(P/2-p')\times \\ &\Big[(2\pi)^4\delta^{(4)}(p-p')\,\delta_{s_A,s'_A}\delta_{s_B,s'_B} + \sum_{r_A,r_B}\int\frac{d^4q}{(2\pi)^4}\mathbb{i}\mathcal{K}\left(\begin{smallmatrix} p, s_A, s_B \\ q, r_A, r_B \end{smallmatrix}\right) G^{\mathrm{DP}}\left(\begin{smallmatrix} q,\, r_A, r_B \\ p', s'_A, s'_B \end{smallmatrix}\right)\Big]. \end{aligned} \tag{E.2.1}$$

We diagonalise eq. (E.2.1) in spin space. The factor $\delta_{s_A,s'_A}\delta_{s_B,s'_B}$ is simply the unity operator, with all its eigenvalues being 1. Thus, the contribution from the spin-s state is

$$G_s^{\rm DP}(p,p') = S(P/2+p')S(P/2-p')\left[(2\pi)^4\delta^{(4)}(p-p') + \int \frac{d^4q}{(2\pi)^4}\mathbb{i}\mathcal{K}_s(p,q)G_s^{\rm DP}(q,p')\right], \quad \text{(E.2.2)}$$

where $\mathcal{K}_s$ is the projected kernel. $G_s^{\rm DP}$ receives contributions from all energy eigenstates that schematically read [59, 145]

$$G_{n,s}^{\rm DP}(p,p') \simeq \frac{\mathbb{i}\tilde{\Psi}_{n,s}^{\rm DP}(p)\ [\tilde{\Psi}_{n,s}^{\rm DP}(p')]^\star}{2P^0(P^0-\omega_{n,s}+\mathbb{i}\epsilon)}, \quad \text{(E.2.3)}$$

where here n denotes collectively all quantum numbers characterising an eigenstate of energy $\omega_{n,s}$. For scattering states, these include a continuous variable that corresponds to the relative momentum of the two interacting particles, while bound states are characterised by a set of discrete quantum numbers. The (momentum space) wavefunctions $\tilde{\Psi}_{n,s}^{\rm DP}(p)$ obey the Schrödinger equation, and have the standard normalisation conditions that emanate from the first term in eq. (E.2.2).

Now we return to IP and the Dyson-Schwinger eq. (E.1.6). For fermions, the operators $\delta_{s_A,s'_A}\delta_{s_B,s'_B}$ and $\delta_{s_A,s'_B}\delta_{s_B,s'_A}$ have eigenvalues 1 and $(-1)^{s+1}$ respectively, while for bosons the eigenvalues are 1. Collectively, this is 1 and $(-1)^{s+f}$. Thus, eq. (E.1.6) yields

$$\begin{aligned} G_s^{\rm IP}(p,p') &= S(P/2+p')S(P/2-p') \\ &\times\left[(2\pi)^4\delta^{(4)}(p-p') + (-1)^s\,(2\pi)^4\delta^{(4)}(p+p') + \int \frac{d^4q}{(2\pi)^4}\mathbb{i}\mathcal{K}_s(p,q)G_s^{\rm IP}(q,p')\right]. \end{aligned} \quad \text{(E.2.4)}$$

The projected kernel is

$$\mathbb{i}\mathcal{K}_s(p,q) = [U^s]_{s_As_B}\ \mathbb{i}\mathcal{K}_s\begin{pmatrix}p, s_A, s_B\\ q, r_A, r_B\end{pmatrix}[U^s]^{-1}_{r_Ar_B}, \quad \text{(E.2.5)}$$

where U^s is the projection operator on the spin-s state, with the symmetry property $[U^s]_{s_As_B} = (-1)^{s+f}[U^s]_{s_Bs_A}$. Equation (E.2.5) combined with eq. (E.1.9) imply

$$\mathbb{i}\mathcal{K}_s(p,q) = (-1)^s\ \mathbb{i}\mathcal{K}_s(p,-q). \quad \text{(E.2.6)}$$

The contribution to the four-point function from the nth energy eigenstate is

$$G_{n,s}^{\rm IP}(p,p') \simeq \frac{\mathbb{i}\tilde{\Psi}_{n,s}^{\rm IP}(p)\ [\tilde{\Psi}_{n,s}^{\rm IP}(p')]^\star}{2P^0(P^0-\omega_{n,s}+\mathbb{i}\epsilon)}, \quad \text{(E.2.7)}$$

where $\tilde{\Psi}_{n,s}^{\rm IP}(p)$ are the IP wavefunctions. We now make the conjecture

$$\tilde{\Psi}_{n,s}^{\rm IP}(p) = \frac{1}{\sqrt{2}}\left[\tilde{\Psi}_{n,s}^{\rm DP}(p) + (-1)^s\tilde{\Psi}_{n,s}^{\rm DP}(-p)\right], \quad \text{(E.2.8)}$$

where $\tilde{\Psi}_{n,s}^{\rm DP}(p)$ are the solutions to the DP Dyson-Schwinger eq. (E.2.2), assuming the kernel is the same as that of eq. (E.2.4). Plugging eq. (E.2.8) into (E.2.7), and considering (E.2.3), we re-express $G_{n,s}^{\rm IP}$ as

$$G_{n,s}^{\rm IP}(p,p') = \frac{1}{2}\left[G_{n,s}^{\rm DP}(p,p') + G_{n,s}^{\rm DP}(-p,-p')\right] + \frac{(-1)^s}{2}\left[G_{n,s}^{\rm DP}(p,-p') + G_{n,s}^{\rm DP}(-p,p')\right]. \quad \text{(E.2.9)}$$

It is now easy to see that, by virtue of the DP Dyson-Schwinger eq. (E.2.2) and the property of the IP kernel (E.2.6), the four-point function $G^{\mathrm{IP}}_{n,s}(p,p')$ of eq. (E.2.9) satisfies the IP Dyson-Schwinger eq. (E.2.4). Therefore, the wavefunctions (E.2.8) are indeed the desired solutions. Expanding in modes of definite orbital angular momentum ℓ, for which

$$\tilde{\Psi}^{\mathrm{DP}}_{n,\ell s}(-p) = (-1)^{\ell}\tilde{\Psi}^{\mathrm{DP}}_{n,\ell s}(-p), \tag{E.2.10}$$

eq. (E.2.8) becomes

$$\tilde{\Psi}^{\mathrm{IP}}_{n,\ell s}(p) = \frac{1+(-1)^{\ell+s}}{\sqrt{2}}\tilde{\Psi}^{\mathrm{DP}}_{n,\ell s}(p). \tag{E.2.11}$$

Note though that, as mentioned in appendix E.1, if the interacting particles carry additional conserved numbers, then appropriate (anti-)symmetrisation factors may appear in eqs. (E.2.10) and (E.2.11) (cf. e.g. DD potential in section 4.2.1.)

Bibliography

[1] R. Oncala and K. Petraki, *Dark matter bound states via emission of scalar mediators*, *JHEP* **01** (2019) 070 [1808.04854].

[2] R. Oncala and K. Petraki, *Dark matter bound state formation via emission of a charged scalar*, *JHEP* **02** (2020) 036 [1911.02605].

[3] R. Oncala and K. Petraki, *Bound states of WIMP dark matter in Higgs-portal models I: cross-sections and transition rates*, 2101.08666.

[4] R. Oncala and K. Petraki, *Bound states of WIMP dark matter in Higgs-portal models II: thermal decoupling*, 2101.08667.

[5] R. Oncala and J. Soto, *Heavy Quarkonium Hybrids: Spectrum, Decay and Mixing*, *Phys. Rev. D* **96** (2017) 014004 [1702.03900].

[6] R. Oncala and J. Soto, *Heavy Hybrids: decay to and mixing with Heavy Quarkonium*, *EPJ Web Conf.* **137** (2017) 06025 [1611.04761].

[7] Planck collaboration, N. Aghanim et al., *Planck 2018 results. VI. Cosmological parameters*, 1807.06209.

[8] WMAP collaboration, E. Komatsu et al., *Seven-Year Wilkinson Microwave Anisotropy Probe (WMAP) Observations: Cosmological Interpretation*, *Astrophys. J. Suppl.* **192** (2011) 18 [1001.4538].

[9] E. Corbelli and P. Salucci, *The Extended Rotation Curve and the Dark Matter Halo of M33*, *Mon. Not. Roy. Astron. Soc.* **311** (2000) 441 [astro-ph/9909252].

[10] Y. Sofue and V. Rubin, *Rotation curves of spiral galaxies*, *Ann. Rev. Astron. Astrophys.* **39** (2001) 137 [astro-ph/0010594].

[11] WMAP collaboration, G. Hinshaw et al., *Five-Year Wilkinson Microwave Anisotropy Probe (WMAP) Observations: Data Processing, Sky Maps, and Basic Results*, *Astrophys. J. Suppl.* **180** (2009) 225 [0803.0732].

[12] Planck collaboration, P. A. R. Ade et al., *Planck 2015 results. XIII. Cosmological parameters*, *Astron. Astrophys.* **594** (2016) A13 [1502.01589].

[13] D. Clowe, M. Bradac, A. H. Gonzalez, M. Markevitch, S. W. Randall, C. Jones et al., *A direct empirical proof of the existence of dark matter*, *Astrophys. J. Lett.* **648** (2006) L109 [astro-ph/0608407].

[14] G. B. Gelmini, *TASI 2014 Lectures: The Hunt for Dark Matter*, 1502.01320.

[15] T. Lin, *Dark matter models and direct detection*, *PoS* **333** (2019) 009 [1904.07915].

[16] G. Bertone, D. Hooper and J. Silk, *Particle dark matter: Evidence, candidates and constraints*, *Phys.Rept.* **405** (2005) 279 [hep-ph/0404175].

[17] Battinelli, P. and Demers, S., *The c star population of ddo 190*, *A&A* **447** (2006) 473.

[18] J. E. Kim and G. Carosi, *Axions and the Strong CP Problem*, *Rev. Mod. Phys.* **82** (2010) 557 [0807.3125].

[19] D. J. H. Chung, P. Crotty, E. W. Kolb and A. Riotto, *On the Gravitational Production of Superheavy Dark Matter*, *Phys. Rev. D* **64** (2001) 043503 [hep-ph/0104100].

[20] M. I. Gresham, H. K. Lou and K. M. Zurek, *Early Universe synthesis of asymmetric dark matter nuggets*, *Phys. Rev.* **D97** (2018) 036003 [1707.02316].

[21] A. Kusenko and M. E. Shaposhnikov, *Supersymmetric Q balls as dark matter*, *Phys. Lett. B* **418** (1998) 46 [hep-ph/9709492].

[22] B. Carr, F. Kuhnel and M. Sandstad, *Primordial Black Holes as Dark Matter*, *Phys. Rev. D* **94** (2016) 083504 [1607.06077].

[23] B. Carr, K. Kohri, Y. Sendouda and J. Yokoyama, *Constraints on Primordial Black Holes*, 2002.12778.

[24] M. Sasaki, T. Suyama, T. Tanaka and S. Yokoyama, *Primordial black holes—perspectives in gravitational wave astronomy*, *Class. Quant. Grav.* **35** (2018) 063001 [1801.05235].

[25] M. M. Flores and A. Kusenko, *Primordial Black Holes from Long-Range Scalar Forces and Scalar Radiative Cooling*, *Phys. Rev. Lett.* **126** (2021) 041101 [2008.12456].

[26] K. Griest and D. Seckel, *Three exceptions in the calculation of relic abundances*, *Phys.Rev.* **D43** (1991) 3191.

[27] G. Arcadi, A. Djouadi and M. Raidal, *Dark Matter through the Higgs portal*, *Phys. Rept.* **842** (2020) 1 [1903.03616].

[28] G. Steigman, B. Dasgupta and J. F. Beacom, *Precise Relic WIMP Abundance and its Impact on Searches for Dark Matter Annihilation*, *Phys.Rev.* **D86** (2012) 023506 [1204.3622].

[29] G. Angloher et al., *Limits on WIMP dark matter using sapphire cryogenic detectors*, *Astropart. Phys.* **18** (2002) 43.

[30] N. Craig and A. Katz, *The Fraternal WIMP Miracle*, 1505.07113.

[31] K. K. Boddy, J. L. Feng, M. Kaplinghat and T. M. P. Tait, *Self-Interacting Dark Matter from a Non-Abelian Hidden Sector*, *Phys.Rev.* **D89** (2014) 115017 [1402.3629].

[32] H. An, B. Echenard, M. Pospelov and Y. Zhang, *Probing the Dark Sector with Dark Matter Bound States*, *Phys. Rev. Lett.* **116** (2016) 151801 [1510.05020].

[33] H. Iminniyaz and M. Kakizaki, *Thermal abundance of non-relativistic relics with Sommerfeld enhancement*, *Nucl.Phys.* **B851** (2011) 57 [1008.2905].

[34] L. Lello and D. Boyanovsky, *The case for mixed dark matter from sterile neutrinos*, 1508.04077.

[35] L. J. Hall, K. Jedamzik, J. March-Russell and S. M. West, *Freeze-In Production of FIMP Dark Matter*, *JHEP* **1003** (2010) 080 [0911.1120].

[36] E. P. Verlinde, *Emergent Gravity and the Dark Universe*, *SciPost Phys.* **2** (2017) 016 [1611.02269].

[37] A. Sommerfeld, *Über die Beugung und Bremsung der Elektronen*, *Ann. Phys.* **403** (1931) 257.

[38] A. D. Sakharov, *Interaction of an Electron and Positron in Pair Production*, *Zh. Eksp. Teor. Fiz.* **18** (1948) 631.

[39] B. von Harling and K. Petraki, *Bound-state formation for thermal relic dark matter and unitarity*, *JCAP* **12** (2014) 033 [1407.7874].

[40] M. Pospelov and A. Ritz, *Astrophysical Signatures of Secluded Dark Matter*, *Phys.Lett.* **B671** (2009) 391 [0810.1502].

[41] H. An, M. B. Wise and Y. Zhang, *Effects of Bound States on Dark Matter Annihilation*, *Phys. Rev.* **D93** (2016) 115020 [1604.01776].

[42] P. Asadi, M. Baumgart, P. J. Fitzpatrick, E. Krupczak and T. R. Slatyer, *Capture and Decay of Electroweak WIMPonium*, *JCAP* **1702** (2017) 005 [1610.07617].

[43] K. Petraki, M. Postma and J. de Vries, *Radiative bound-state-formation cross-sections for dark matter interacting via a Yukawa potential*, *JHEP* **04** (2017) 077 [1611.01394].

[44] M. Cirelli, P. Panci, K. Petraki, F. Sala and M. Taoso, *Dark Matter's secret liaisons: phenomenology of a dark U(1) sector with bound states*, *JCAP* **1705** (2017) 036 [1612.07295].

[45] C. Kouvaris, K. Langaeble and N. G. Nielsen, *The Spectrum of Darkonium in the Sun*, *JCAP* **1610** (2016) 012 [1607.00374].

[46] I. Baldes and K. Petraki, *Asymmetric thermal-relic dark matter: Sommerfeld-enhanced freeze-out, annihilation signals and unitarity bounds*, *JCAP* **1709** (2017) 028 [1703.00478].

[47] I. Baldes, M. Cirelli, P. Panci, K. Petraki, F. Sala and M. Taoso, *Asymmetric dark matter: residual annihilations and self-interactions*, *SciPost Phys.* **4** (2018) 041 [1712.07489].

[48] J. D. March-Russell and S. M. West, *WIMPonium and Boost Factors for Indirect Dark Matter Detection*, *Phys.Lett.* **B676** (2009) 133 [0812.0559].

[49] K. Petraki, L. Pearce and A. Kusenko, *Self-interacting asymmetric dark matter coupled to a light massive dark photon*, *JCAP* **1407** (2014) 039 [1403.1077].

[50] R. Laha and E. Braaten, *Direct detection of dark matter in universal bound states*, *Phys.Rev.* **D89** (2014) 103510 [1311.6386].

[51] A. Butcher, R. Kirk, J. Monroe and S. M. West, *Can Tonne-Scale Direct Detection Experiments Discover Nuclear Dark Matter?*, *JCAP* **1710** (2017) 035 [1610.01840].

[52] H. An, M. B. Wise and Y. Zhang, *Strong CMB Constraint On P-Wave Annihilating Dark Matter*, *Phys. Lett.* **B773** (2017) 121 [1606.02305].

[53] A. Migdal, *Qualitative Methods In Quantum Theory*, Advanced Books Classics. Avalon Publishing, 2000.

[54] J. Harz and K. Petraki, *Higgs Enhancement for the Dark Matter Relic Density*, *Phys. Rev.* **D97** (2018) 075041 [1711.03552].

[55] J. Harz and K. Petraki, *Higgs-mediated bound states in dark-matter models*, *JHEP* **04** (2019) 130 [1901.10030].

[56] W. Shepherd, T. M. Tait and G. Zaharijas, *Bound states of weakly interacting dark matter*, *Phys.Rev.* **D79** (2009) 055022 [0901.2125].

[57] J. M. Cline, Y. Farzan, Z. Liu, G. D. Moore and W. Xue, *3.5 keV x rays as the "21 cm line" of dark atoms, and a link to light sterile neutrinos*, *Phys.Rev.* **D89** (2014) 121302 [1404.3729].

[58] L. Pearce, K. Petraki and A. Kusenko, *Signals from dark atom formation in halos*, *Phys.Rev.* **D91** (2015) 083532 [1502.01755].

[59] K. Petraki, M. Postma and M. Wiechers, *Dark-matter bound states from Feynman diagrams*, *JHEP* **1506** (2015) 128 [1505.00109].

[60] S. Kim and M. Laine, *On thermal corrections to near-threshold annihilation*, *JCAP* **1701** (2017) 013 [1609.00474].

[61] S. Kim and M. Laine, *Rapid thermal co-annihilation through bound states in QCD*, *JHEP* **07** (2016) 143 [1602.08105].

[62] J. Harz and K. Petraki, *Radiative bound-state formation in unbroken perturbative non-Abelian theories and implications for dark matter*, *JHEP* **07** (2018) 096 [1805.01200].

[63] M. Geller, S. Iwamoto, G. Lee, Y. Shadmi and O. Telem, *Dark quarkonium formation in the early universe*, *JHEP* **06** (2018) 135 [1802.07720].

[64] S. Biondini and M. Laine, *Thermal dark matter co-annihilating with a strongly interacting scalar*, *JHEP* **04** (2018) 072 [1801.05821].

[65] S. Biondini and M. Laine, *Re-derived overclosure bound for the inert doublet model*, *JHEP* **08** (2017) 047 [1706.01894].

[66] D. E. Kaplan, G. Z. Krnjaic, K. R. Rehermann and C. M. Wells, *Atomic Dark Matter*, *JCAP* **1005** (2010) 021 [0909.0753].

[67] F.-Y. Cyr-Racine and K. Sigurdson, *The Cosmology of Atomic Dark Matter*, *Phys.Rev.* **D87** (2013) 103515 [1209.5752].

[68] S. J. Lonsdale and R. R. Volkas, *Grand unified hidden-sector dark matter*, *Phys. Rev.* **D90** (2014) 083501 [1407.4192].

[69] K. K. Boddy, J. L. Feng, M. Kaplinghat and T. M. P. Tait, *Self-Interacting Dark Matter from a Non-Abelian Hidden Sector*, *Phys.Rev.* **D89** (2014) 115017 [1402.3629].

[70] G. D. Kribs and E. T. Neil, *Review of strongly-coupled composite dark matter models and lattice simulations*, *Int. J. Mod. Phys.* **A31** (2016) 1643004 [1604.04627].

[71] S. J. Lonsdale, M. Schroor and R. R. Volkas, *Asymmetric Dark Matter and the hadronic spectra of hidden QCD*, *Phys. Rev.* **D96** (2017) 055027 [1704.05213].

[72] S. J. Lonsdale and R. R. Volkas, *Comprehensive asymmetric dark matter model*, *Phys. Rev.* **D97** (2018) 103510 [1801.05561].

[73] M. B. Wise and Y. Zhang, *Stable Bound States of Asymmetric Dark Matter*, *Phys.Rev.* **D90** (2014) 055030 [1407.4121].

[74] M. B. Wise and Y. Zhang, *Yukawa Bound States of a Large Number of Fermions*, *JHEP* **02** (2015) 023 [1411.1772].

[75] M. I. Gresham, H. K. Lou and K. M. Zurek, *Early Universe synthesis of asymmetric dark matter nuggets*, *Phys. Rev.* **D97** (2018) 036003 [1707.02316].

[76] E. Braaten, D. Kang and R. Laha, *Production of dark-matter bound states in the early universe by three-body recombination*, 1806.00609.

[77] C. Itzykson and J. Zuber, *Quantum field theory*. Dover Publications, 1980.

[78] A. Pineda and J. Soto, *Effective field theory for ultrasoft momenta in NRQCD and NRQED*, *Nucl. Phys. Proc. Suppl.* **64** (1998) 428 [hep-ph/9707481].

[79] N. Brambilla, A. Pineda, J. Soto and A. Vairo, *Potential NRQCD: An Effective theory for heavy quarkonium*, *Nucl. Phys.* **B566** (2000) 275 [hep-ph/9907240].

[80] M. Beneke, *Perturbative heavy quark - anti-quark systems*, hep-ph/9911490.

[81] A. V. Manohar and I. W. Stewart, *Renormalization group analysis of the QCD quark potential to order v**2*, *Phys. Rev.* **D62** (2000) 014033 [hep-ph/9912226].

[82] A. V. Manohar and I. W. Stewart, *Running of the heavy quark production current and 1 / v potential in QCD*, *Phys. Rev.* **D63** (2001) 054004 [hep-ph/0003107].

[83] A. Pineda, *Renormalization group improvement of the NRQCD Lagrangian and heavy quarkonium spectrum*, *Phys. Rev.* **D65** (2002) 074007 [hep-ph/0109117].

[84] N. Brambilla, A. Pineda, J. Soto and A. Vairo, *Effective field theories for heavy quarkonium*, *Rev. Mod. Phys.* **77** (2005) 1423 [hep-ph/0410047].

[85] A. Pineda, *Next-to-leading ultrasoft running of the heavy quarkonium potentials and spectrum: Spin-independent case*, *Phys. Rev.* **D84** (2011) 014012 [1101.3269].

[86] A. H. Hoang and M. Stahlhofen, *Ultrasoft NLL Running of the Nonrelativistic O(v) QCD Quark Potential*, *JHEP* **06** (2011) 088 [1102.0269].

[87] E. Braaten, E. Johnson and H. Zhang, *Zero-range effective field theory for resonant wino dark matter. Part II. Coulomb resummation*, *JHEP* **02** (2018) 150 [1708.07155].

[88] E. Braaten, E. Johnson and H. Zhang, *Zero-range effective field theory for resonant wino dark matter. Part I. Framework*, *JHEP* **11** (2017) 108 [1706.02253].

[89] E. Braaten, E. Johnson and H. Zhang, *Zero-range effective field theory for resonant wino dark matter. Part III. Annihilation effects*, *JHEP* **05** (2018) 062 [1712.07142].

[90] K. M. Belotsky, E. A. Esipova and A. A. Kirillov, *On the classical description of the recombination of dark matter particles with a Coulomb-like interaction*, *Phys. Lett.* **B761** (2016) 81 [1506.03094].

[91] T. Bringmann, F. Kahlhoefer, K. Schmidt-Hoberg and P. Walia, *Strong constraints on self-interacting dark matter with light mediators*, 1612.00845.

[92] F. Kahlhoefer, K. Schmidt-Hoberg and S. Wild, *Dark matter self-interactions from a general spin-0 mediator*, *JCAP* **1708** (2017) 003 [1704.02149].

[93] N. F. Bell, Y. Cai, J. B. Dent, R. K. Leane and T. J. Weiler, *Enhancing Dark Matter Annihilation Rates with Dark Bremsstrahlung*, *Phys. Rev.* **D96** (2017) 023011 [1705.01105].

[94] T. Binder, M. Gustafsson, A. Kamada, S. M. R. Sandner and M. Wiesner, *Reannihilation of self-interacting dark matter*, *Phys. Rev.* **D97** (2018) 123004 [1712.01246].

[95] L. Pearce and A. Kusenko, *Indirect Detection of Self-Interacting Asymmetric Dark Matter*, *Phys.Rev.* **D87** (2013) 123531 [1303.7294].

[96] K. Petraki and R. R. Volkas, *Review of asymmetric dark matter*, *Int.J.Mod.Phys.* **A28** (2013) 1330028 [1305.4939].

[97] Y. Kats and M. D. Schwartz, *Annihilation decays of bound states at the LHC*, *JHEP* **04** (2010) 016 [0912.0526].

[98] M. Cirelli, Y. Gouttenoire, K. Petraki and F. Sala, *Homeopathic Dark Matter, or how diluted heavy substances produce high energy cosmic rays*, *JCAP* **1902** (2019) 014 [1811.03608].

[99] H. Fukuda, F. Luo and S. Shirai, *How Heavy can Neutralino Dark Matter be?*, *JHEP* **04** (2019) 107 [1812.02066].

[100] A. Messiah, *Quantum mechanics*. North-Holland Pub. Co., 1962.

[101] S. Cassel, *Sommerfeld factor for arbitrary partial wave processes*, *J.Phys.* **G37** (2010) 105009 [0903.5307].

[102] T. Binder, K. Mukaida and K. Petraki, *Rapid bound-state formation of Dark Matter in the Early Universe*, *Phys. Rev. Lett.* **124** (2020) 161102 [1910.11288].

[103] S. Biondini, *Bound-state effects for dark matter with Higgs-like mediators*, *JHEP* **06** (2018) 104 [1805.00353].

[104] K. Griest and M. Kamionkowski, *Unitarity Limits on the Mass and Radius of Dark Matter Particles*, *Phys.Rev.Lett.* **64** (1990) 615.

[105] S. P. Liew and F. Luo, *Effects of QCD bound states on dark matter relic abundance*, *JHEP* **02** (2017) 091 [1611.08133].

[106] T. Binder, L. Covi and K. Mukaida, *Dark Matter Sommerfeld-enhanced annihilation and Bound-state decay at finite temperature*, *Phys. Rev.* **D98** (2018) 115023 [1808.06472].

[107] L. G. van den Aarssen, T. Bringmann and Y. C. Goedecke, *Thermal decoupling and the smallest subhalo mass in dark matter models with Sommerfeld-enhanced annihilation rates*, *Phys.Rev.* **D85** (2012) 123512 [1202.5456].

[108] P. Gondolo and G. Gelmini, *Cosmic abundances of stable particles: Improved analysis*, *Nucl.Phys.* **B360** (1991) 145.

[109] L. Lopez Honorez, M. H. G. Tytgat, P. Tziveloglou and B. Zaldivar, *On Minimal Dark Matter coupled to the Higgs*, *JHEP* **04** (2018) 011 [1711.08619].

[110] J. Hisano, S. Matsumoto and M. M. Nojiri, *Unitarity and higher order corrections in neutralino dark matter annihilation into two photons*, *Phys.Rev.* **D67** (2003) 075014 [hep-ph/0212022].

[111] J. Hisano, S. Matsumoto and M. M. Nojiri, *Explosive dark matter annihilation*, *Phys.Rev.Lett.* **92** (2004) 031303 [hep-ph/0307216].

[112] J. Hisano, S. Matsumoto, M. M. Nojiri and O. Saito, *Non-perturbative effect on dark matter annihilation and gamma ray signature from galactic center*, *Phys.Rev.* **D71** (2005) 063528 [hep-ph/0412403].

[113] I. Baldes, F. Calore, K. Petraki, V. Poireau and N. L. Rodd, *Indirect searches for dark matter bound state formation and level transitions*, *SciPost Phys.* **9** (2020) 068 [2007.13787].

[114] W. Detmold, M. McCullough and A. Pochinsky, *Dark Nuclei I: Cosmology and Indirect Detection*, *Phys.Rev.* **D90** (2014) 115013 [1406.2276].

[115] R. Mahbubani, M. Redi and A. Tesi, *Indirect detection of composite asymmetric dark matter*, *Phys. Rev. D* **101** (2020) 103037 [1908.00538].

[116] R. Mahbubani and L. Senatore, *The Minimal model for dark matter and unification*, *Phys. Rev. D* **73** (2006) 043510 [hep-ph/0510064].

[117] F. D'Eramo, *Dark matter and Higgs boson physics*, *Phys. Rev. D* **76** (2007) 083522 [0705.4493].

[118] T. Cohen, J. Kearney, A. Pierce and D. Tucker-Smith, *Singlet-Doublet Dark Matter*, *Phys. Rev. D* **85** (2012) 075003 [1109.2604].

[119] C. Cheung and D. Sanford, *Simplified Models of Mixed Dark Matter*, *JCAP* **02** (2014) 011 [1311.5896].

[120] L. Calibbi, A. Mariotti and P. Tziveloglou, *Singlet-Doublet Model: Dark matter searches and LHC constraints*, *JHEP* **10** (2015) 116 [1505.03867].

[121] S. Banerjee, S. Matsumoto, K. Mukaida and Y.-L. S. Tsai, *WIMP Dark Matter in a Well-Tempered Regime: A case study on Singlet-Doublets Fermionic WIMP*, *JHEP* **11** (2016) 070 [1603.07387].

[122] K. Fraser, A. Parikh and W. L. Xu, *A Closer Look at CP-Violating Higgs Portal Dark Matter as a Candidate for the GCE*, 2010.15129.

[123] A. Freitas, S. Westhoff and J. Zupan, *Integrating in the Higgs Portal to Fermion Dark Matter*, *JHEP* **09** (2015) 015 [1506.04149].

[124] J.-W. Wang, X.-J. Bi, P.-F. Yin and Z.-H. Yu, *Impact of Fermionic Electroweak Multiplet Dark Matter on Vacuum Stability with One-loop Matching*, *Phys. Rev. D* **99** (2019) 055009 [1811.08743].

[125] T. Abe and R. Sato, *Current status and future prospects of the singlet-doublet dark matter model with CP-violation*, *Phys. Rev. D* **99** (2019) 035012 [1901.02278].

[126] A. Dedes and D. Karamitros, *Doublet-Triplet Fermionic Dark Matter*, *Phys. Rev. D* **89** (2014) 115002 [1403.7744].

[127] C. E. Yaguna, *Singlet-Doublet Dirac Dark Matter*, *Phys. Rev. D* **92** (2015) 115002 [1510.06151].

[128] T. M. P. Tait and Z.-H. Yu, *Triplet-Quadruplet Dark Matter*, *JHEP* **03** (2016) 204 [1601.01354].

[129] M. Beneke, A. Bharucha, A. Hryczuk, S. Recksiegel and P. Ruiz-Femenia, *The last refuge of mixed wino-Higgsino dark matter*, *JHEP* **01** (2017) 002 [1611.00804].

[130] A. Bharucha, F. Brümmer and N. Desai, *Next-to-minimal dark matter at the LHC*, *JHEP* **11** (2018) 195 [1804.02357].

[131] A. Filimonova and S. Westhoff, *Long live the Higgs portal!*, *JHEP* **02** (2019) 140 [1812.04628].

[132] A. Betancur and O. Zapata, *Phenomenology of doublet-triplet fermionic dark matter in nonstandard cosmology and multicomponent dark sectors*, *Phys. Rev. D* **98** (2018) 095003 [1809.04990].

[133] K. Blum, R. Sato and T. R. Slatyer, *Self-consistent Calculation of the Sommerfeld Enhancement*, *JCAP* **1606** (2016) 021 [1603.01383].

[134] T. Binder, B. Blobel, J. Harz and K. Mukaida, *Dark Matter bound-state formation at higher order: a non-equilibrium quantum field theory approach*, 2002.07145.

[135] J. Ellis, F. Luo and K. A. Olive, *Gluino Coannihilation Revisited*, *JHEP* **09** (2015) 127 [1503.07142].

[136] M. E. Carrington, *The Effective potential at finite temperature in the Standard Model*, *Phys. Rev.* **D45** (1992) 2933.

[137] A. Ahriche, *What is the criterion for a strong first order electroweak phase transition in singlet models?*, *Phys. Rev.* **D75** (2007) 083522 [hep-ph/0701192].

[138] P. Ko, T. Matsui and Y.-L. Tang, *Dark Matter Bound State Formation in Fermionic Z_2 DM model with Light Dark Photon and Dark Higgs Boson*, 1910.04311.

[139] S. Tulin and H.-B. Yu, *Dark Matter Self-interactions and Small Scale Structure*, *Phys. Rept.* **730** (2018) 1 [1705.02358].

[140] M. E. Peskin and D. V. Schroeder, *An Introduction to Quantum Field Theory*. Westview Press, 1995.

[141] L. Hulthén, *Über die eigenlosunger der Schrödinger-gleichung des deuterons*, *Ark. Mat. Astron. Fys.* **28 A** (1942) 1.

[142] L. Hulthén, *On the Virtual State of the Deuteron*, *Ark. Mat. Astron. Fys.* **29 B** (1943) 1.

[143] A. I. Akhiezer and N. P. Merenkov, *The theory of lepton bound-state production*, *Journal of Physics B Atomic Molecular Physics* **29** (1996) 2135.

[144] I. S. Gradshteyn, I. M. Ryzhik, A. Jeffrey and D. Zwillinger, *Table of Integrals, Series, and Products*. Elsevier, 2007.

[145] Z. Silagadze, *Wick-Cutkosky model: An Introduction*, `hep-ph/9803307`.